Diss. ETH No. 18714

Experimental Investigation of the Influence of Flow Structure on Compound Angled Film Cooling Performance

A dissertation submitted to the

SWISS FEDERAL INSTITUTE OF TECHNOLOGY
(ETH ZÜRICH)

for the degree of

DOCTOR OF SCIENCES

presented by

Vipluv Aga

B.Tech/M.Tech, Indian Institute of Technology Madras
born 20 September 1981
citizen of India

accepted on the recommendation of

Prof. Dr. Reza S. Abhari
Prof. Dr. Karen Thole

Zurich 2009

Abstract

Film cooling in turbine blades involves injecting cold air through small holes over the surface of the blade to thermally protect it against the incoming hot freestream. Compound angled film cooling, in which the injected jet is angled laterally with respect to the streamwise flow direction is used in industrial designs owing to their lower cost of manufacture compared to shaped geometries but high coolant spread. The current study incorporates flow structure measurements of film cooling injection flows inclined at 30° to a flat surface and lateral angles of 15°, 45°, 60° and 90° to the freestream. Blowing ratios of 1-2 and density ratios of 1-1.5 are studied. The density ratios are obtained by maintaining the freestream and coolant flows at different temperatures. Three dimensional velocity measurements are carried out through high resolution stereoscopic particle image velocimetry (PIV). It is observed that the typical counter-rotating vortex pair structure associated with streamwise coolant injection is replaced with a single large vortex which causes more lateral spread of the coolant. Infra red thermography measurements are made for the same operating points using the super position principle which allows calculation of adiabatic effectiveness and film heat transfer coefficient. The detrimental effects of jet lift-off at high momentum flux ratios are counteracted by greater coolant spread downstream by the asymmetric vorticity. The streamwise circulation decay with downstream distance for compound angled holes depends on the orientation angle and scales with a momentum flux ratio scaled downstream distance. The boundary layer pile-up is observed to increase with greater lateral orientation of the injection holes. Heat transfer is generally enhanced with greater compound angles and increasing momentum flux ratios. One reason for this enhancement is the increased wall-normal vorticity representing coherent unsteadiness in the near wall region. A blowing ratio pulsation of amplitude 0.3 is applied at two hole diameter based reduced frequencies of 0.01 and 0.017 for a 0° and 60° compound angled injection. The velocity flow structure shows that due to the lateral sweeping motion of the compound angled jet the wake zone is flattened and laterally spread, while the jet is closely attached to the wall. At high blowing ratios, pulsations do not have a very significant effect but cause some enhancement in cooling effectiveness due to lateral coolant spread for compound angled injection. The heat transfer coefficient increases with pulsations compared to a steady jet for all downstream distances as the pulsations enhance coherent unsteadiness. Aerothermal losses are also quantified for pulsating and steady, streamwise and 60° oriented compound angled film cooling jets. The entropy change, derived from pressure and temperature measurements, is calculated by using modified reference conditions to better reflect the losses in both the jet and the freestream. Mass averaged entropy and kinetic energy loss coefficients seem to be apt quantities for comparing aerothermal performance of streamwise and compound angled injection. It is observed that the mass averaged entropy loss coefficient of a streamwise jet doubles when it is pulsated whereas that of a compound angled jet increases by around fifty

percent. It may be conjectured from the measurements shown in this study that streamwise oriented jets suffer most of their entropy change losses at the hole exit due to separation whereas in compound angled jets, downstream thermal mixing between the jet and the freestream, is the dominant mechanism.

Zussamenfassung

Bei filmgekühlten Turbinenschaufeln wird von deren Oberfläche Kühlluft durch kleine Bohrungen in die Hauptströmung eingedüst, um die Schaufeloberfläche thermisch vor der heissen Hauptströmung zu schützen. Gegenüber der Hauptströmung um einen bestimmten Winkel angestellte Bohrungen, den sogenannten compound film cooling Bohrungen, werden auf Grund deren kostengünstigeren Fertigung in Industriegasturbinen profilierten Bohrungen vorgezogen, obwohl diese zu einer weitreichenderen Kühlluftverteilung führen. Im Rahmen der vorliegenden Arbeit wurden Strömungsmessungen zur Auflösung von Strukturen in Filmkühlungsströmungen durchgeführt. Dabei erfolgten die Eindüsungen um einen Neigungswinkel von 30°zu einer flachen Platte und einer seitlichen Anstellung von 15°, 45°, 60°sowie 90°zur Hauptströmung. Die Eindüsungen wurden mit Massenstromverhältnissen von 1 bis 2 sowie Dichteverhältnissen von 1 bis 1.5 betrachtet. Die Dichteverhältnisse wurden durch unterschiedliche Temperaturen im Kühlluftstrom und der Hauptströmung gewährleistet. Mit Hilfe von hochauflösender stereokopischen PIV wurden Messungen des dreidimensionalen Geschwindigkeitsfeldes durchgeführt. Dabei wurde festgestellt, dass an Stelle des typischen Paares von zwei in entgegengesetzte Richtung rotierenden Wirbel, ein einziger grosser Wirbel tritt, welcher zu einer erhöhten seitlichen Verteilung der Kühlluft führt. Unter denselben Bedingungen der PIV Messungen wurden ebenfalls Messungen mittels Infrarot Thermographie durchgeführt. Mit Hilfe des Superpositionsprinzips konnten so die dimensionslose adiabate Wandtemperatur (adiabatic effectiveness) sowie der Filmwärmeübergangskoeffizient (film heat transfer coefficient) ermittelt werden. Den bei hohen Impulsverhältnissen durch Ablösung der eingedüsten Kühlluft hervorgerufenen abträglichen Effekten, wirkt eine durch eine asymetrische Wirbelstärke hervorgerufene stromabwärts weitreichendere Verteilung des Kühlmediums entgegen. Bei angestellten Kühlluftbohrungen (compound film cooling), hängt die Abnahme der Zirkulation in Strömungsrichtung vom Anstellwinkel ab und skaliert mit einer auf das Verhältnis der Impulsflüsse bezogenen stromabwärts angesetzten Strecke. Mit der stärkeren seitlichen Anstellung der Kühlluftbohrungen wächst die Anhäufung von Grenzschichtfluid an. Der Wärmefluss wächst im Allgemeinen bei grösseren Anstellwinkel und höherem Impulsfluss ebenfalls an. Ein Grund dafür ist die Vergrösserung der Wirbelstärke senkrecht zur Wand, welche die kohärente Instationarität in Wandnähe beinhaltet. Pulsierende Eindüsungen mit den beiden Anstellwinkel von 0°(in Richtung der Hauptströmung) und 60°wurden mit einer Amplitude von 0.3 im Massenstromverhältnis für zwei Bohrungsdurchmesser bei den reduzierten Frequenzen von 0.01 und 0.017 untersucht. Die Struktur des Geschwindigkeitsfeldes zeigt, dass der Nachlauf der eingedüsten Kühlluft abgeflacht und seitwärts verdrängt wird, wogegen der Strahl selbst weiterhin an der Wand haftet. Die aero-thermischen Verluste wurden für pulsierende und stationäre Eindüsungen ausgewertet wobei in Richtung der Hauptströmung und unter einem Anstellwinkel von 60°Kühlluft eingedüst wurde. Mit Hilfe von Druck-

und Temperaturmessungen wurde die Entropieänderung unter Referenzbedingungen ausgewertet. Somit können die Verluste sowohl im eingedüsten Medium als auch in der Hauptströmung aufgezeigt werden. Die mit Hilfe des Massenstroms gemittelte Entropie und der Verlustbeiwert der kinetischen Energie erwiesen sich als geeignete Grössen um die aero-thermische Wirkung der Eindüsung in Richtung der Hauptströmung mit derjenigen unter einem Anstellwinkel von 60°zu vergleichen. Es konnte festgestellt werden, dass sich der mit Hilfe der Massenstrom gemittelten Entropie ausgewertete Verlustbeiwert bei pulsierender Eindüsung gegenüber dem für die stationäre Eindüsung verdoppelt falls die Eindüsung in Richtung der Hauptströmung stattfindet. Dieser Verlustbeiwert erhöht sich bei angestellter Eindüsung lediglich um 50%. Die gezeigten Messergebnisse geben Grund zur Vermutung, dass bei der Eindüsung in Hauptströmungsrichtung der grösste Teil aller durch die Entropiezunahme ermittelten Verluste in Folge Strömungsablösungen in unmittelbarer Nähe der Kühlluftbohrung entstehen. Im Gegenzug ist bei der angestellten Eindüsung hauptsächlich die thermische Ausmischung des Kühlmediums in der Hauptströmung für die Verluste verantwortlich.

Acknowledgements

"Experience is the name every one gives to their mistakes"

-Oscar Wilde, 1854-1900

Lady Windermere's Fan, 1892, Act I

Contents

Chapter 1

Introduction

1.1 Motivation

Gas turbine power plant manufacturers, especially those making aircraft engines, face an increasing pressure to reduce fuel consumption and emissions. Aircraft engines also require predictable operation and maintenance schedules such that cost of ownership is reduced without compromising on safety. Reducing fuel consumption requires increasing efficiency within various component parts of a typical turbofan airplane engine, a schematic of which is shown in Fig. 1.1.
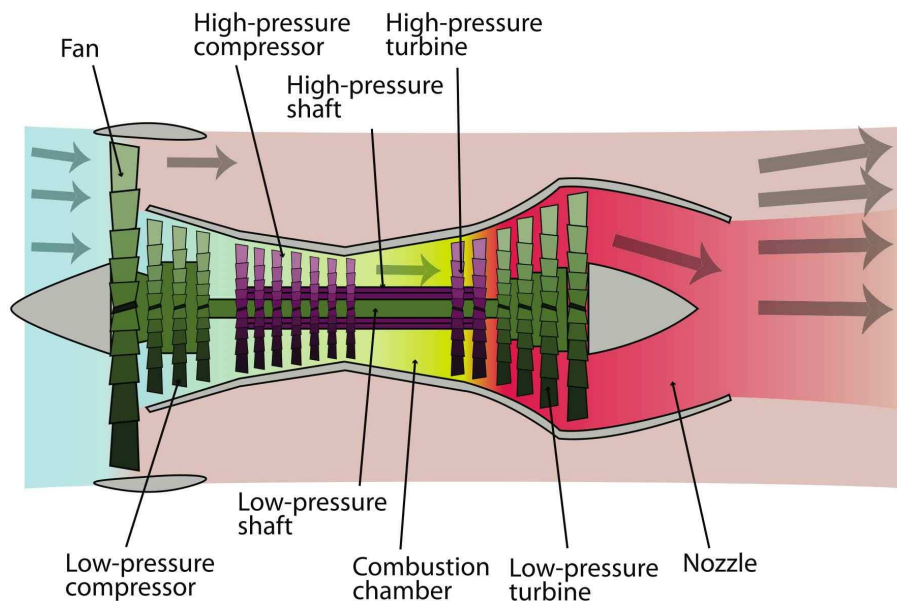
Figure 1.1: Schematic of a typical turbofan engine used in most civilian aircraft in current times
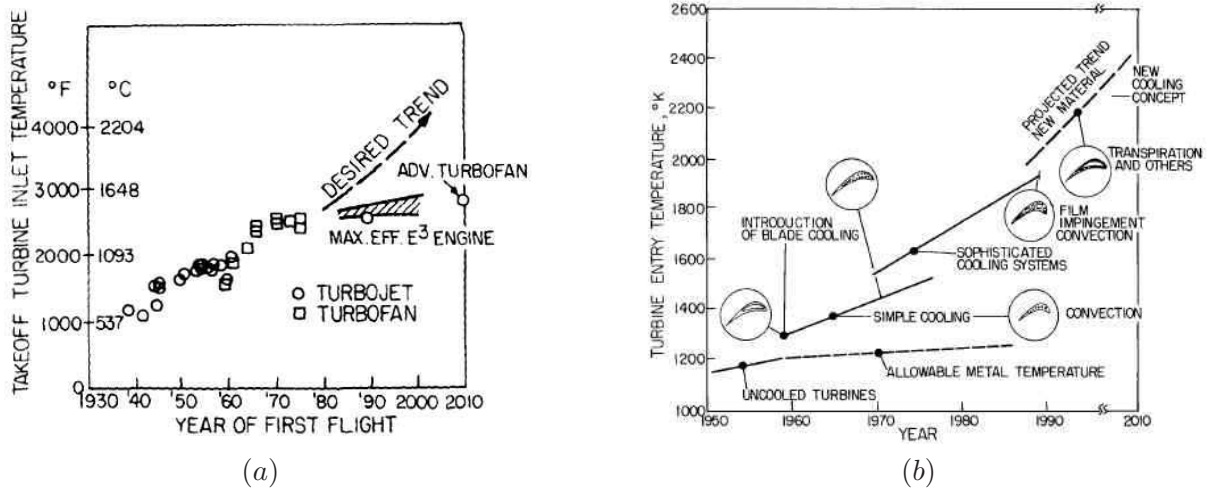
Figure 1.2: (a) Progress in turbine inlet temperature over the years (b) Variation of engine TET over the years due to different forms of cooling. Reproduced from Lakshminarayana [71]
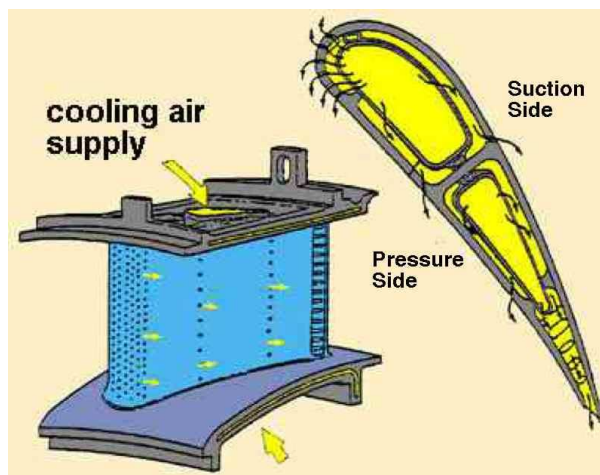
Figure 1.3: Film cooling in a turbine airfoil showing the coolant supply and plenum injection

Some of the highest increases in overall efficiency can be accomplished by improving the efficiencies in the 'hot' parts of the engine namely the combustor and turbine. Airplane engines work on the principle of the Brayton thermodynamic cycle. It is known from the gas turbine cycle analysis that higher cycle temperatures (the highest of which occur just after the fuel is burnt, i.e. at the entry of the turbine) produces a larger amount of work per unit mass flow and improves the weight/power ratio of the gas turbine. A major problem associated in achieving this increased performance is the availability of materials that can withstand the high temperatures and combined stresses due to temperature, rotation and aerodynamic loading. In present times, engines to be deployed on the latest airplanes have achieved turbine inlet temperatures of 2000

Figure 1.4: A film cooled blade from the high pressure turbine of a Pratt and Whitney F135 engine

K. The historical evolution of these turbine inlet temperatures are shown in Fig. 1.2 (a). The materials typically used to make turbine blades are high temperature alloys sometimes equipped with thermal barrier coatings. However, the melting points of these superalloys are still only around 1200 K.

Turbine cooling is employed in most modern gas turbines to achieve the high temperatures above the melting or failure temperature points of the constituent metals. Film and convection cooling allow the blade temperature to be maintained at values much lower that those encountered without cooling. Advances in this area have given rise to considerable improvement in turbine inlet temperature as shown in Fig. 1.2 (b).

As the above figure shows, film cooling currently is the state of the art and widely used in industry until newer cooling concepts become more widespread. In air-cooled turbines, the air is usually drawn from the exit of the compressor and fed into the plenum of every blade. The blade itself has small holes drilled onto the surface through which this cold air is ejected over the surface forming a film and protecting the blade surface from the hot main flow. A schematic showing the principle of film cooling is shown in Fig. 1.3. A picture of a an actual film cooled turbine blade from a Pratt and Whitney F135 engine is shown in Fig. 1.4. Small holes on the surface of the blade are clearly visible.
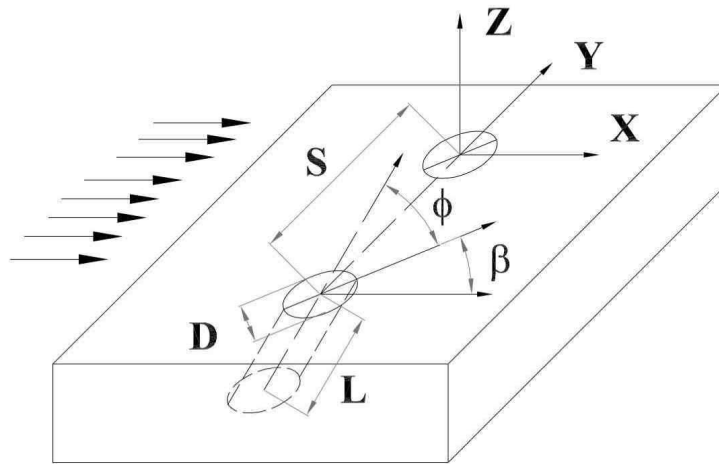
Figure 1.5: Definition of coordinate system and geometrical parameters

The Film Cooling Problem

The mechanism by which film cooling produces a lower blade temperature is considerably different from that of convective cooling. The surface is covered by a thin film of cool air, which acts as a buffer between the high temperature gas and the blade. Film cooling could be effected by slots, a single row of holes or multiple rows of holes as needed. It must be noted that the actual geometry used to deliver the air (round holes, slots etc) is not only determined by cooling performance but also by manufacturability. Drilling hundreds of round holes on a single blade, when each turbine has 40-50 blades, is still economically viable compared to drilling and contouring complex shapes using advanced tooling and extensive labour.

From a heat transfer perspective, film cooling is different from convective cooling because unlike convection which is a two temperature problem, namely the temperature of the fluid and the temperature of the solid being cooled; film cooling is a three temperature problem. The temperature of the hot gas is higher than that of the coolant fluid and their interaction acts to create another temperature for the surface of the metal. A well-behaved boundary layer upstream may undergo dramatic changes, including separation. The injected jet may detach and then reattach subsequently downstream. Since the jets are formed in circular delivery tubes they would have a significant vortical structure. Add to it the fact that multiple jets and rows of jets might be interacting with each other and it is easy to see that a film cooling flow is a very complex three-dimensional problem which has still not been understood very well.

In order to fully understand the aerodynamics and empirically determine the cooling characteristics of film cooling holes, experimental flat plate data has been used predominantly. The geometry parameters determining the film cooling problem and the coordinate system associated

with it are shown in Fig. 1.5. The coolant coverage of film cooling has been investigated with respect to these geometry parameters. In the figure, D is the hole diameter, S is the pitch distance between two holes in a row and L is the length of the delivery pipe through which coolant is fed over the surface. The angles with respect to the streamwise main flow are quite important in film cooling and form the basis of further investigation in the current study. The angle that the delivery pipe makes with the surface is denoted, ϕ and except for the leading edge of the turbine where this may be 90°for showerhead cooling, for all other regions on the pressure and suction side of the turbine airfoil this surface angle is around 30°to 35°. The other angle relevant to the geometry as shown in Fig. 1.5 is β. This is the angle that the delivery pipe makes with the main stream. A traditional jet in crossflow, streamwise angled film cooling jet is one in which $\beta = 0°$. In modern gas turbines which use compound angled film cooling, typically the value of β ranges from 50°to close to 90°.

Measures of Cooling Performance

The film cooling problem is a three temperature system. The main flow or freestream temperature is denoted as T_m or also as T_h in subsequent chapters as it is the hot fluid. The temperature of the coolant is denoted by T_c while the local wall temperature is T_w. To define the heat transfer a datum temperature is required. This datum temperature is called the *adiabatic wall temperature*, T_{aw} and represents the surface temperature of a perfectly insulated surface. If the surface temperature, T_w is non-dimensionalised by the hot and cold stream temperatures it can be denoted by Eq. 1.1, then if the adiabatic wall temperature is also suitably non-dimensionalised it gives the *adiabatic film cooling effectiveness* as given by Eq. 1.2

$$\theta = \frac{T_h - T_w}{T_h - T_c} \tag{1.1}$$

$$\eta = \frac{T_h - T_{aw}}{T_h - T_c} \tag{1.2}$$

The film cooling effectiveness is primarily a function of the blowing parameters, BR, DR and IR which are defined in Table 1.1.

The heat transfer coefficient due to film cooling also needs to be expressed differently from typical convection cases. This *film heat transfer coefficient*, h_f as described by Eq. 1.3 is independent of the actual temperatures of the wall and flow.

$$q_{conv} = h_f \left(T_w - T_{aw} \right) \tag{1.3}$$

Eckert [39] has provided formal proof for the definitions used for cooling effectiveness (Eq. 1.2) and film heat transfer coefficient, (Eq. 1.3). These equations are valid for the following assumptions.

Parameter	Definition	Description
BR, Blowing Ratio	$\frac{\rho_c U_c}{\rho_m U_m}$	Ratio of coolant mass flow rate to main stream mass flow rate
DR, Density Ratio	$\frac{\rho_c}{\rho_m}$	Ratio of coolant density to main flow density
IR, Momentum Flux Ratio	$\frac{\rho_c U_c^2}{\rho_m U_m^2}$	Ratio of coolant momentum flux to main flow momentum flux

Table 1.1: Definition of the parameters affecting cooling performance

1. The coolant has the same property as the main flow, if it was ejected through the holes at the coolant exit temperature

2. The flow is assumed to be steady with constant properties. The aerodynamic heating effects are considered negligible.

3. The assumption of constant fluid property implies that velocities are independent of thermal fields and are assumed known or prescribed.

The above two measures of film cooling performance are used extensively in literature to compare and contrast various film cooling strategies.

1.2   Literature Review

The origins of systematic studies of jets and the vortical structures stretch very far back into fluid mechanics history to the days of Reynolds [96] and Lamb [72] from the late 19th century. As the understanding of fluid mechanics and vorticity in general became more sophisticated, attention was turned towards the classical jet in cross flow problem. A streamwise injected film cooling hole is simply a jet in crossflow with an inclined delivery pipe and hence initial understanding of film cooling was based on fundamental flow physics information of jet in cross flow studies. Some important recent studies like those of Kelso et al. [65], Fric and Roshko [44], Moussa et al. [88] have described many micro and macro flow features of a jet in cross flow in detail. The nature of the counter-rotating vortex pair for this flow has been detailed adequately in Cortelezzi and Karagozian [29]. The separation within the delivery pipe which causes the counter-rotating vortex pair was described in this study. Some of the most recent measurements and analyses of the jet in crossflow problem are described in Smith and Mungal [102], Meyer et al. [86]. The

control of counter-rotating vortex pairs or kidney vortices as they are also called through different geometries was studied by Haven and Kurosaka [56].

However, applying the fundamental flow physics information towards an engineering understanding requires a different kind of treatment. The jet in cross-flow has to be understood in terms of heat transfer. Cooling performance dependance on various blowing and geometry parameters was quantified. Film cooling investigation has mainly been divided into experimental investigation and computational prediction. A thorough review of computational efforts into film cooling investigation and prediction has been made by Burdet [21]. The following paragraphs mainly detail experimental film cooling research with special emphasis on compound angled round hole film cooling.

Streamwise Injection Film Cooling

A large body of literature exists for the canonical streamwise angled film cooling problem. Interestingly, the first use of film cooling through round holes was not for cooling but for heating. Wieghardt [107] described the usage of warm air blown through round holes for de-icing airplane wings in the 40s. However, usage of inclined jets in crossflow was mainly relegated to gas turbine engines. A review was first made by Goldstein [48] into the state of the art in the 1970s. Some of the first measurements and computations about a real turbine blade film cooling problem was presented by Camci [25]. The most up to date literature survey, which covers all the important results and knowledge of film cooling parameters, shapes and strategies is included in Bogard and Thole [15].

Typically film cooling has mainly been studied through heat transfer data. Some instances of flow structure analysis include the LDA measurements of Pietrzyk et al. [91], Rydholm [97] and the eddy diffusivity measurements of Kaszeta2000 using a hot wire anemometer. The turbulent flow structure of streamwise injected jets was observed to possess high degrees of anisotropy of turbulence. They also observed high areas of turbulence in the shear windward sides of the jet and lower turbulence in the wake zone. Recent PIV measurements of Bernsdorf et al. [13, 14] studied the flow structure of the jet at different blowing conditions as well as under pulsations. The effect of large injection angles on the flow structure and thermal fields was quantified by Kohli and Bogard [67]. These studies showed that shallower angles keep the jet attached to the wall and lower the jet lift-off even for high blowing ratios. The entrainment of hot gas from the freestream to the surface due to the effect of the counter rotating vortex pair was also noted.

The operating conditions of blowing and momentum flux ratios have been varied and their influence on adibatic effectiveness has been studied extensively. Initial efforts at demonstrating the most relevant parameters were reviewed by Goldstein [48] who arrived at the conclusion that momentum flux ratio is the most relevant parameter that affects adiabatic effectiveness. A high resolution study into the effect of the various blowing conditions on the effectiveness was performed by Baldauf et al. [8]. The experiments of Yuen and Martinez-Bothas [111, 112] showed

that shallower surface angles provided better film cooling coverage by reducing jet detachment but greater heat transfer coefficient as the wall-turbulence is increased. The assessment of the effect of direction of crossflow in the plenum to the surface performance was also performed by Gritsch et al. [53]. These data were collected together to provide for a correlation for laterally averaged adiabatic effectiveness with downstream distance by Baldauf et al. [9]. Many parameters, like blowing conditions, inclination angle, pitch, freestream turbulence and discharge coefficient accounted for in deriving the correlations. The heat transfer coefficient was also studied for these streamwise geometries notably by Goldstein et al. [50], Eriksen and Goldstein [42] using liquid crystals. Measurements with greater spatial resolution of heat transfer coefficient were performed by Baldauf et al. [7]. These studies confirmed that heat transfer coefficient was a parameter that was very difficult to quantify and its behavior with different blowing conditions could not be readily compared by different research studies as they strongly depended on many factors in combination which could not really be maintained the same from place to place. In spite of these differences, Baldauf et al. [10] brought together many measurements from literature and proposed a correlation for predicting heat transfer coefficient with downstream distance of a coolant injection site.

Many studies looked at second order effects which affect film cooling effectiveness. The effect of freestream turbulence was studied by Bons et al. [17]. They found that higher freestream turbulence increases lateral spread of effectiveness but depresses the value at far downstream positions. Since film cooling is actually used on turbine blades they are subject to pressure gradients which are not present in flat plate studies. The effects of curvature were studied by Ito et al. [62] whereas the effect of pressure gradients on blade cooling were documented by Teekaram et al. [103]. These studies showed that film cooling on a gas turbine blade behaved differently under curvature and pressure gradient effects. However, fundamental first order dependance was still dictated by the momentum flux ratio and the inclination angles of the jet as the jet lift-off and detachment was mainly caused by the operating conditions.

Real turbines operate in an unsteady regime dominated by the periodic unsteadiness from rotor-stator interaction. Measurements on gas turbine blades in real rotating conditions were carried out by Abhari and Epstein [2]. It was observed, that heat transfer increased three to four times in the presence of the unsteadiness causing the local momentum flux to oscillate. In a subsequent study Abhari [1] modeled the impact on film cooling effectiveness along with the measurements on a real turbine facility in the presence of a rotor-stator interaction. Flat plate unsteady flow structure data was recorded through phase resolved PIV measurements by Bernsdorf et al. [14]. The study concluded that at high frequencies a pulsated jet could be approximated as a quasi-steady jet at a slightly lower effective momentum flux ratio.

A recent review on streamwise film cooling which includes computational efforts is found in Bogard and Thole [15]. A review on non-circular cross section delivery holes or shaped holes as they are called has also been published by Bunker [20]. In the industry manufacturing a circular hole on a turbine blade is significantly cheaper then drilling a complex shape. Although it is

known that shaped holes have much better cooling coverage and effectiveness compared to round holes of all orientations, circular holes are still desired to be used in as many regions as possible, simply to reduce the cost of manufacturing a turbine blade.

Compound Angled Film Cooling

Flow Structure

The compound angled flow structure has not been measured often, since film cooling is traditionally viewed as a heat transfer problem and hence a fluid dynamics treatment of it is rather phenomenological. Some visualizations like those of Honami et al. [59] have involved temperature measurements in the flow field of the jet. Some previous efforts in this direction like those of [74] showed the asymmetric vortex flow structure while [63] used the flow structure knowledge to explain the trends on effectiveness due to the combined effect of velocity ratio and orientation angle. Since experimental measurements are hard to come by for these complex flows, some notable computer simulations have been presented which shed some insight into the main features governing compound angled film cooling along with comparisons with streamwise oriented geometry. These computational studies are presented in Walters and Leylek [105], McGovern and Leylek [84]. The conclusions noted some important trends viz. greater orientation angles imply greater average effectiveness due to better spread and mixing, however this difference is most noticeable at higher blowing ratios. It must be noted however, that the quantification and understanding of the vorticity field has never really been investigated in literature.

Effect of Operating Conditions on Cooling Performance

The heat transfer and adiabatic effectiveness measurements of compound angled flow under the influence of many changing parameters have been investigated using different experimental techniques, like thin-film gauges and thermocouples (e.g., Ligrani et al. [77], Ligrani and Ramsey [76]), liquid crystals (e.g., Nasir et al. [89]), and infra-red cameras (e.g., Dittmar et al. [36]). Such studies have primarily concerned themselves with surface heat transfer information rather than the flow structure per se. In order to create a density ratio many studies have used gases of different densities, (Ekkad et al. [40]) and then used the mass transfer analogy to derive heat transfer coefficients using a liquid crystal technique. The effectiveness information for the same operating conditions was also presented in Ekkad et al. [41]. Flat plate compound angled film cooling effectiveness measurements for blowing ratios ranging from 0.5 to 1.5 and density ratios from 1 to 1.6 have been carried out by Schmidt et al. [99]. The corresponding heat transfer studies were also published in Sen et al. [100]. These studies showed that momentum flux ratio was the characteristic parameter for the compound angled flow structure as well and that even at high blowing ratios, compound angled flows had high lateral spread and coolant coverage. The effect of very high Blowing ratios until 4.0 were also investigated by Ligrani and Lee [75]

and it was observed that downstream adiabatic effectiveness significantly reduced for very high
BR as the jet lift-off became prominent. The effect of different orientation angles, i.e. β from
30°to 90°on local and laterally averaged adiabatic effectiveness was presented by Jung and Lee
[63]. The investigation of multiple rows of compound angled holes was investigated by Ligrani
and Ramsey [76]. The above studies laid down a sound experimental database for understanding
compound angled film cooling behavior through surface effectiveness.

The main qualitative observations from the above experiments could be summarized as follows.

- Compound angled injection does not have a counter rotating vortex structure

- A momentum flux ratio increase decreases adiabatic effectiveness but it is still higher than
  streamwise oriented jets due to greater coolant coverage.

- Increasing compound angle orientation increases coolant spread and hence adiabatic effec-
  tiveness

- Heat transfer coefficient increases with increasing momentum flux ratio and compound
  angle orientation

Although, some explanations for these effects were propounded by all the studies a systematic
investigation of both velocity flow structure with special respect to the vortical flow and the
surface performance due to it was still lacking.

Compound Angle Cooling on Curved Surfaces

Although most experiments on film cooling have been performed on a flat plate there have also
been some efforts to quantify the effect of compound angled film cooling on representative turbine
blade surfaces which are curved and have pressure gradients. Waye and Bogard [106] found
that for mild curvature flat plate results were sufficient to predict the effectiveness performance
and that for high blowing ratio a compound angle jet was well suited for enhanced cooling
effectiveness. Hung et al. [60] measured the compound angle effectiveness and heat transfer on
concave and convex surfaces and found that the trends mimicked those of flat plate measurements
except for the local magnitudes of heat transfer and effectiveness due to the pressure gradients.

Effect of Pulsations

The effect of bulk flow pulsations on the flow effectiveness have been studied in cascade tests
using thermocouples by Ligrani et al. [78, 79]. The effect on adiabatic effectiveness and heat
transfer coefficient on streamwise oriented holes was also presented by Coulthard et al. [30, 31].
A slight increase in effectiveness and heat transfer coefficient with jet flow pulsations was noted.
The study also looked at varying duty cycle and frequency parameters. The effect of bulk flow

pulsations specifically with respect to compound angled injection was measured using liquid crystal imaging technique by Lee and Jung [73]. They observed reduced effectiveness due to pulsations but the effective reduction was lower at larger orientation angles. They also observed that at low blowing ratios, pulsations were especially detrimental to coolant spread and adiabatic effectiveness. Although measurements of cooled turbine blade in real rotating turbine test cases have been carried out, (eg. Dunn et al. [38], Abhari and Epstein [2]) they do not deal specifically with compound angled film cooling.

Aerothermal Losses due to Film Cooling

The loss mechanisms that occur in different parts of a turbomachine have been reviewed in a seminal paper by Denton [34]. Among the many loss-producing mechanisms, the ones which involve hot and cold mixing streams, especially those due to cooling had been specifically identified and the prediction of the loss through the usage of an entropy change parameter was proposed. Although, film cooling studies have almost always concentrated on the primary heat transfer issues, engine designers are also concerned with the aero-thermodynamic losses that might be produced when film cooling injection causes mixing losses. This is of particular significance when the aerodynamics are significantly altered in contoured end walls of a turbine due to film cooling. Specifically, studies such as those in Friedrichs et al. [45] have concluded that since the losses generated by film cooling ejection at end walls could be significant, the nature of the 3-D flow field should be accounted for when designing end wall film cooling. The aerodynamic mixing effect due to film cooling ejection was also studied in Wilfert and Fottner [108], in which a mass weighted definition for the reference pressure was used to compute the film cooling pressure loss to take into account, loss from both the freestream and the injected coolant. Other studies like Reiss and Boelcs [95], Lee et al. [74] have also concentrated on the aerothermal performance of film cooling holes. These studies have recognized the need to use the kinetic energy loss coefficient, which is superior to a pressure loss coefficient or an entropy production based only on freestream conditions, as it also takes into account the losses within the film cooling holes. However, it should be noted that most of these studies were performed at conditions when coolant and freestream temperatures were equal, due to the absence of simultaneous temperature and pressure measurements. Thus, the effect of thermal gradients or unsteadiness on kinetic energy loss or entropy has not been properly characterized in previous studies even though almost every film cooling hole is used in an environment where there is periodic unsteadiness due to blade passage in actual machinery.

1.3 Research Objectives

Film cooling is either viewed as a heat transfer problem or a fluid dynamics problem depending on the background of the researcher. An interdisciplinary approach to studying these and other

complex conjugated heat transfer problems is required. The industrial goals of film cooling are not only to devise the strategy with the best cooling performance but a strategy with the best *predictability* and confidence. In the industry such predictions routinely involve computational fluid dynamics (CFD) and it is imperative to be able to quickly and within well defined uncertainty bands, analyze a design change and optimize it if required. This calls for a detailed simulation and resolution of all the flow features of a film cooling jet, which even with today's computing technology is uneconomical in terms of labour (for gridding and meshing), computational cost and large turnaround time for developing a new strategy.

The idea espoused in previous works at ETH Zurich was to develop a film cooling macro model, that would be based on the small scale features which were suitably calibrated from experimental flow structure information. This model would be parametrized according to geometry and blowing conditions. Placing a cooling hole within a computational domain would then require only defining the point on the blade where this hole had to be placed without resolving the plenum and jet pipe flow structure. This immersed boundary condition would then inject all the small scale and macroscopic flow features into the domain required to resolve the downstream flow and heat transfer at a very small fraction of the computational cost. Such a feature based computational model is described in Burdet [21], Burdet et al. [24] for streamwise injection film cooling. The flow structure database used to calibrate this model is described in Bernsdorf [12].

The extension of the ETH film cooling model is desired to predict compound angled flow structure as well. The development of the compound angled flow structure is described in the partner thesis of Fuchs [46]. The research objectives from an immediate application viewpoint therefore are two fold. One, is to provide accurate flow structure data for different orientation angles and operating condition that could be used to tune a feature based model. Secondly, heat transfer experiments involving accurate measurements of effectiveness and heat transfer coefficients at varying momentum flux ratios and hole orientations are required such that they can be compared with the effectiveness predictions using the CFD FCM. This would serve as a validation for establishing confidence in the film cooling model.

Apart from the experimental data serving as an anchor for CFD model development, there are many fundamental flow physics that also need to be investigated. Derived data like vorticity and circulation are important to visualize as well as understand the flow. A correlation between flow structure and their influence on surface heat transfer performance is not clearly understood. A flow physics based understanding can then be used not only to better design new cooling geometries but also help in better predicting the placement of film cooling holes simply by knowing the local flow structure at that part of the blade. Another objective is also to establish certain mean flow quantities as characteristic quantifications which affect heat transfer. The cooling abilities of future geometries may also be evaluated using such quantifications.

The topic of aerothermal loss due to film cooling should also be investigated. An objective of the current study is to compare and contrast different quantification procedures for best evaluating the losses due to film cooling and understanding whether a steady state analysis is adequate to

describe it.

1.4 Thesis Outline

1. The technical and industrial motivation as well as past and current work on film cooling and especially compound angled film cooling is presented in Chapter 1.

2. The experimental rig used in the study along with its important ancillary components for creating the requisite hot main flow and cold coolant flow is described in Chapter 2. The pulsator and wall heating apparatus is also described. Three different measurement techniques, viz. Particle Image Velocimetry (PIV), infrared thermography and fast entropy probes are used. Their setup with respect to the rig and details about their mode of working are described. For computational researchers it is very important to be able to accurately match the flow conditions from experiments and hence a detailed procedure by which the various flow conditions are derived is included in this chapter.

3. The third chapter deals in detail with all the three experimental techniques. An introduction to their usage, their principle of working and practical parameters used during the measurement campaigns are described. The chapter also contains an estimate of the uncertainty analysis of the raw measurements from each of them.

4. Chapter 4 describes in detail the experimental methodology used to reduce the data and obtain the derived quantities. The practical usage of the PIV system is described. Infrared thermography only provides the surface temperatures. These raw data need to be reduced to usable effectiveness and heat transfer data through a superposition method which is described along with the data processing routines and the assumptions made. Finally the chapter ends with a description of the practical parameters used to measure the entropy change in mixing flow. This chapter also contains the uncertainty estimates of all the final quantities like velocity, effectiveness, heat transfer and entropy change that are discussed in later chapters.

5. The description of the main results and their discussion begins with Chapter 5. The velocity data is investigated in detail and the main flow features of a compound angled film cooling flow structure are identified. The main primary vortex core and the wall-normal vorticity which participates in jet-freestream boundary layer mixing are visualized. These quantities are seen in the light of varying orientation angles of $\beta = 15°, 45°, 60°$ and $90°$ as well as varying momentum flux ratio caused by changing the blowing and density ratio. The change in behavior of the flow structures due to these changes are discussed. The magnitude of the streamwise circulation and its decay with downstream distance gives an insight into the mixing behavior of a single vortex dominated flow.

6. A comparison of important flow quantities with the cooling performance indicators like adiabatic effectiveness and film heat transfer coefficient is undertaken in Chapter 6. The shape and extent of the primary vortex core increases increasing compound angled and momentum flux ratio and has a significant effect on the coolant sprea. The wall-normal vorticity is a measure of coherent unsteadiness that increases mixing in the near wall region. The increases in film heat transfer coefficient and wall normal vorticity with higher compound angles and momentum flux ratio is also discussed.

7. Combined measurements of velocity and heat transfer data under the influence of periodic pulsations is described in Chapter 7. The movement of a compound angled jet under oscillations is reported using phase resolved PIV measurements. The comparison of time-averaged effectiveness and film heat transfer coefficient with streamwise and compound angled film cooling under pulsations is also carried out.

8. Three different loss quantification parameters are evaluated to describe aerothermal losses in film cooling in Chapter 8. The entropy change suffered by both main flow and coolant injection is measured for streamwise and compound angled jets under the effect of pulsation.

9. Chapter 9 summarizes the most important conclusions from the experimental observations from all the chapters. A generalized discussion about the main flow physics insight obtained from the current measurements and their impact on cooling performance is provided. A perspective is provided for future work towards the end.

Chapter 2

Experimental Facility

The current research was carried out in the subsonic closed loop wind tunnel facility known as LAVAL situated in ETH Zurich. The measurement campaigns detailed herein were carried out using three different measurement techniques. The velocity flow field was measured using three dimensional Stereoscopic Particle Image Velocimetry (PIV). Then the test configuration was changed considerably for heat transfer measurements using Infra Red Thermography. An
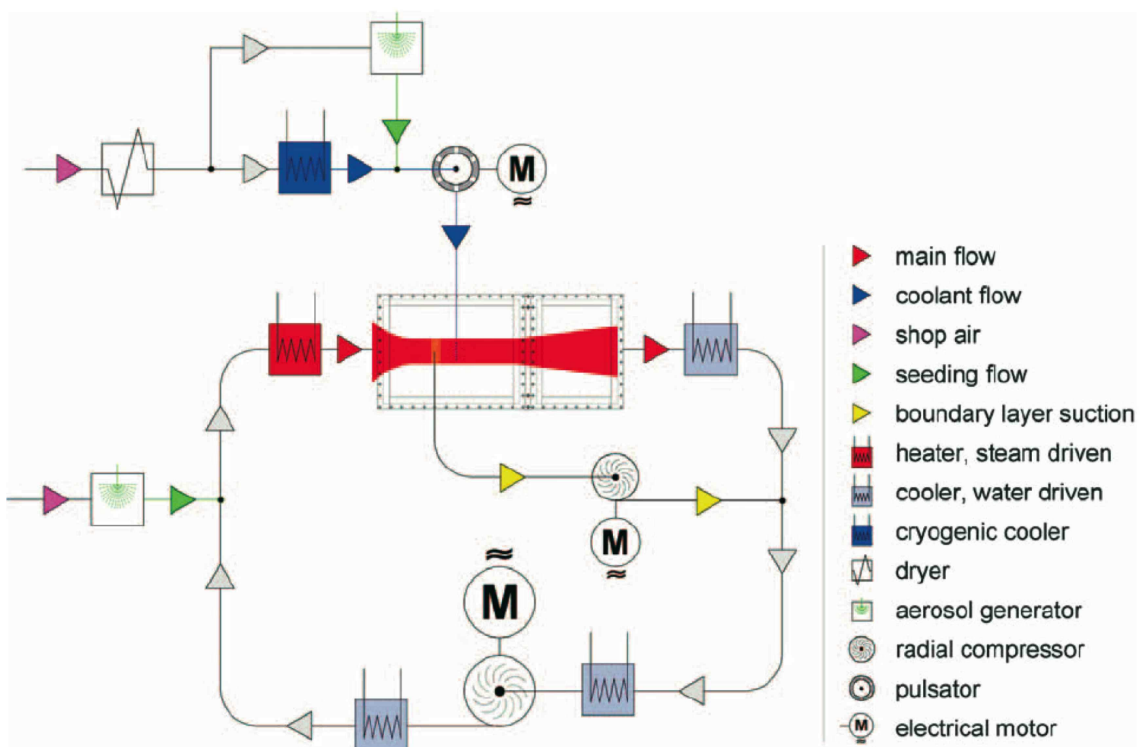
Figure 2.1: Schematic of the LAVAL test facility

Parameter	Main Flow	Coolant Flow
Mass flux [kg/s]	4	0.075
Temperature [°C]	24 to 150	-45 to 25
Test Section Mach No.	0.5	0.6
Test Section Velocity [m/s]	190	180
Pulsator	None	Rotary type, 1000 Hz
Turbulence Intensity	1-2%	-

Table 2.1: Test facility capabilities showing maximum limits

intrusive technique, viz. the Fast Response Entropy Probe (FENT) (Mansour [83]) for measuring simultaneous pressure and temperature also necessitated further modifications on the same basic wind tunnel set up. More details of these measurements are provided in Chapter 3, Section 3.3.

The test facility is the same as detailed in Bernsdorf [12]. It is capable of providing a main flow with a versatile test section, in which the secondary coolant flow may be injected through inserts of varying geometries. A schematic is shown in Fig. 2.1.

2.1   Main Flow

A centrifugal compressor with impeller diameter of 297mm, driven by a 470kW electric motor, creates the main flow in the experimental closed loop facility. The impeller is taken from an ABB VTC 254 turbo charger. The gearbox and periphery are custom made for the application. The pressure level in the system is self-adjusting by a small blow out valve. The resulting pressure in the test section is around the ambient pressure. Temperature is controlled with a water cooled heat exchanger downstream of the compressor, while a second cooler is installed just upstream of the impeller intake for its protection against overheating. That configuration allows a temperature range from 18°C to 40°C in the free stream. The rotational speed of the impeller determines the pressure ratio and with that the resulting mass flow rate in the system. At its maximum speed of 30000 rpm the compressor can deliver up to 4 kg/s. At present, the maximum mass-flow rate required is at about 1.5 kg/s, for free stream Mach number of M=0.5. A stream-air heat exchanger is installed upstream of the test section to raise the main flow temperature up to 120°C. This 180kW heat exchanger with a heat exchanger area of 84 m^2 is fed by 7 bar saturated stream from the house heating system. The heater is controlled with a feedback control loop. The heat is extracted from the main flow downstream of the test section by a watercooled heat exchanger with an exchanger area of 142 m^2. The pipe work containing the main flow is suspended from the ceiling to allow thermal expansion of the steel piping. Additionally, a compensator replaces a section of the pipe to allow angular and lateral displacement of the pipe without causing damage. The hot section of the test rig, between the stream heater and the water cooler, is wrapped in 30mm thermal insulation sheets and the test section is thermally decoupled from the environment by ceramic insulators. Table 2.1 shows the

maximum capabilities for the test section

The boundary layer thickness of the main flow is controlled by a suction arrangement. A centrifugal blower drives the boundary layer suction, extracting throught 327 discrete holes of 1.2mm diameter stacked in 11 arrays over an area of 60x180 mm^2. The extracted air is fed back into the loop far downstram of the cooler. The blower, a Meidinger Witt S-FVR4001, is driven by a 4kW electrical motor. The maximum capacity of the suction is about 50 g/s and is adjusted with a hand valve.

2.2   Cooling Flow

The secondary flow is delivered by the shop air system with a maximum of 75 g/s. First a drier lowers the dew point of the air to -70°C. Two cylinders filled with water absorbing solid particles are alternately drying the air and recuperating inside that drier. Next in line is a fast acting self-controlling pressure control valve, followed by a mass flow measurement section. Downstream is a single cycle cooler, capable of reducing the temperature down to -63°C at cooler exit. The 12mm piping connecting the cooler and the primary wind tunnel is wrapped in 40mm insulation.

2.2.1   Cooling Plant

The cooling plant consists of 2 parts, namely the dryer and the cooler. The dryer is a heat-less regenerating adsorption dryer, Ultrapac MSD-300 manufactured by Deltatherm Hirmer GmbH. The drying of the air is done by the water molecules being physically bound to the large inner surface of the dessicant. The air is alternately dried in one of the two adsorbers while the other one is regenerated. This ensures continuous operation. Regeneration of the moisture laden dessicant is achieved with a partial flow of the dried air. This partial flow enters the adsorber and flows out into the atmosphere. The cryogenic water cooled re-cooler, RKH DE-H1 manufactured by Deltatherm Hirmer GmbH, contains a cooling loop and a closed cryogenic loop. The heat extracted from the air is dumped via the cryogenic medium as it is evaporated in the air-heat exchanger. Afterwards it is compressed and successively liquified in the water cooler. The medium is then fed back to the evaporator thus closing the loop. The air temperature is controlled through a feed-back control loop that keeps the compressor running as long as the set temperature is not reached. As the piping between the cooler and the injection point is more than 15 m, there is some temperature dissipation in the line and hence the temperature is always set lower than the one required in the injection location. The important limits on capabilities of the coolant flow are summarized in table 2.1.
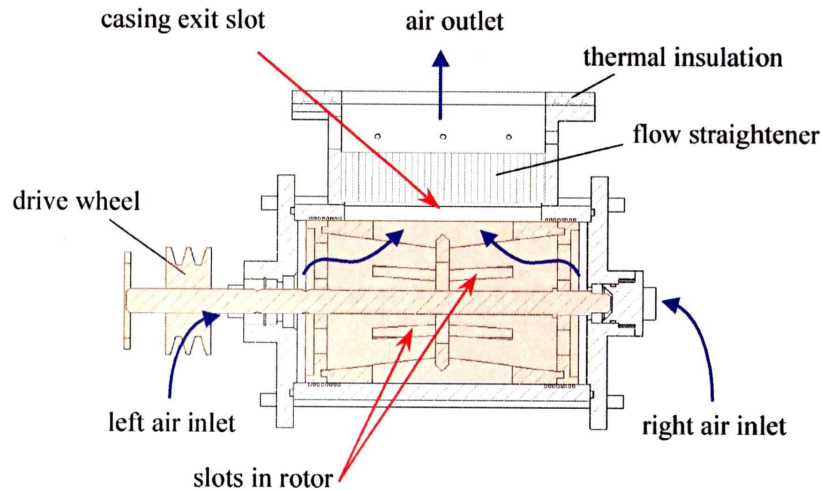
Figure 2.2: A cut-away view of the pulsator used to simulate unsteady blowing of the coolant

2.2.2   Pulsator

In order to study the unsteady effects of a film cooling injection operating in the pulsating wake of a rotating machinery, a pulsator is used to mimic the oscillating blowing ratio coming out from the film cooling injection. A modified rotating valve with slots was designed and built in house (Maerklin [82]). The design was based on an earlier design at the Ohio State University (Giang [47]). A cut through of the pulsator is shown in Fig. 2.2.

Cold air is fed through two air inlets into a plenum between the rotor and the the casing. The rotor has axial inlet holes and six slots on its circumference. The casing has one slot which serves as the air outlet. When the air slots are aligned the air can exit otherwise the flow is stopped much like a rotary valve. A flow straightener is placed in the exit plenum to achieve a uniform flow through the different holes of the cooling array. Sensors to measure pressure and temperature are placed at the exit before the flow enters the coolant injection plenum. These details are covered in Section 2.2.3. The rotor is supported by two ball bearings, one on each side of the rotor body. Three seals are used to suppress air leakage where the shaft penetrates the casing. A clearance of 0.05 mm between the rotor and casing is designed to hold at ambient temperatures. A labyrinth seal is also cut into the casing to further reduce leakage. The pulsator is thermally insulated to reduce thermal leakage when temperatures as low as 220 K are required. Conduction losses are reduced by mounting the pulsator on a wooden plate and the casing is wrapped with thick insulating material.

A 3 kW electrical motor, manufactured by Danfoss, drives the pulsator via a V-belt. The motor speed is continuously variable and hence can be calibrated to obtain the desired pulsation frequency. The relative accuracy of the frequency setting through the speed control is stated by

the manufacturer as 2%. The pulsator is equipped with a safety system that automatically cuts power to the electrical motor when a predefined upper limit of vibration level is exceeded.

The initial design of the pulsator was computationally tested using Finite Element Analysis as the pulsator was designed for long duration continuous operation in the presence of high thermal gradients, very low temperatures and large rotational speeds. The material of the rotor is a low temperature high tensile aluminium alloy ($7075/AlZnMgCu_{1.5}$), which is often used in airplane manufacture. The finite element analysis for this design is detailed in Bernsdorf [12]. A maximum deflection of 11.5 μm was determined at maximum design speed. The maximum von-Mises stress was found to be 70.1 N/mm^2 which is an order of magnitude below the tensile strength of 570 N/mm^2 of the material.

The eigen-frequencies of the rotor using a proprietary software DesignSpace was carried out which showed a rotational eigenmode at 549 Hz. A second eigen-frequency results in a bending mode at 845 Hz. In practice however typical operating frequencies were observed to be well placed away from these eigenmodes. Again, accelerating the pulsator though these eigenmodes do not result in a shut down of the system.

The pulsator was originally designed to produce a fluctuation in blowing ratio which does not change with frequency. However, the functioning of the pulsator involves a pressure build up in the rotor when the slots are closed and then a release of pressure when they open. If the time between opening and closing is above a certain limit dictated by the mass flow and plenum size then the associated pulsating mass flow will have a very large variation from an open position to a closed position. In other words the Blowing Ratio fluctuation becomes a function of the frequency of operation. This effect was first calibrated and then ameliorated.

A fast pressure transducer was attached at the pulsator exit just before the secondary flow enters the main test section through a row of film cooling holes and the subsequent blowing ratio as well as instantaneous blowing ratio fluctuations were measured. The pulsator exit plenum contains a differential fast response pressure transducer manufactured by Endevco model no. 8520A-20. This is calibrated in-situ using the static measurement taps situated there, which are detailed in Section 2.4. The resulting signal is acquired by a fast PC card and a custom LabView program with sampling at 100 kHz to obtain the instantaneous plenum pressure which after assuming a relevant discharge coefficient of 0.8 is converted to a blowing ratio value. The flywheel of the pulsator is also connected with an optical fiber trigger which detects the closed or open state of the pulsator during its rotation.

The blowing ratio behavior at two representative blowing ratios of 1 and 2 at different frequencies is shown in Fig. 2.3 and 2.4 which clearly shows a clear dependance of blowing ratio amplitude variation on frequency. Based on the figures an approximate duty cycle, i.e. the ratio of signal when the pulsator is open to that when it is closed is slightly higher than 50% at all frequencies.

In order to damp the large pressure buildup that causes higher blowing ratio fluctuations at lower frequencies a simple technique was employed. This is detailed in Forrer [43]. A large cylinder of
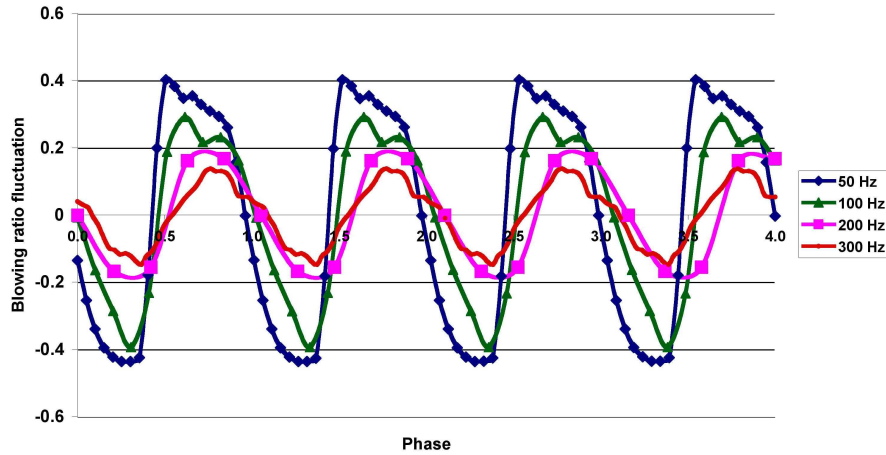
Figure 2.3: Blowing ratio fluctuation for a 30°injection insert with the Main flow at M=0.3 at a mean BR=1 for different pulsator frequencies
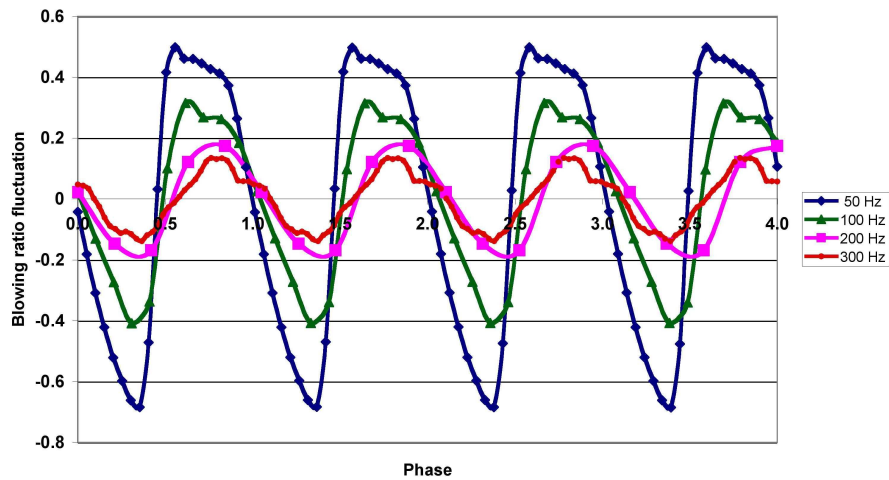
Figure 2.4: Blowing ratio fluctuation for a 30°injection insert with the Main flow at M=0.3 at a mean BR=2 for different pulsator frequencies

110 mm diameter with length of 165 mm is attached at the top end of the pulsator exit. Figure 2.5 shows a photograph of this device attached on top the pulsator viewed from the back side of the wind tunnel. The damping device was seen to ameliorate the large fluctuation at low frequencies whereas at high frequencies the pressure pulsation remained unchanged. The standard deviation of the time varying blowing ratio was used to quantify the amplitude of fluctuations about the
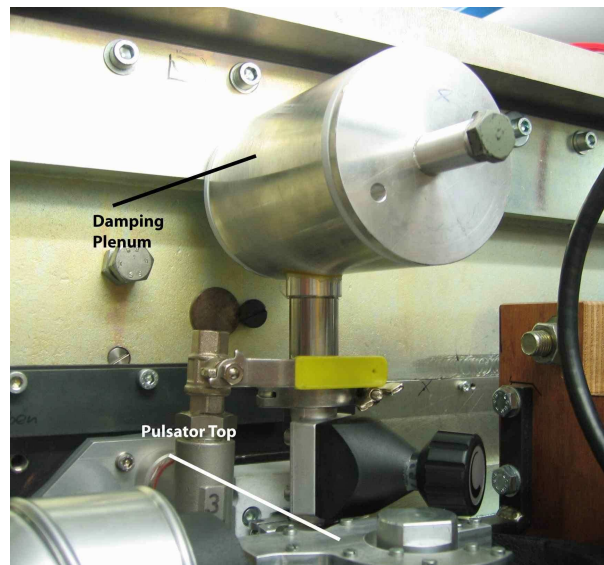
Figure 2.5: Photograph of the damping plenum attached to pulsator to reduce large secondary mass flow fluctuations at low pulsator frequencies
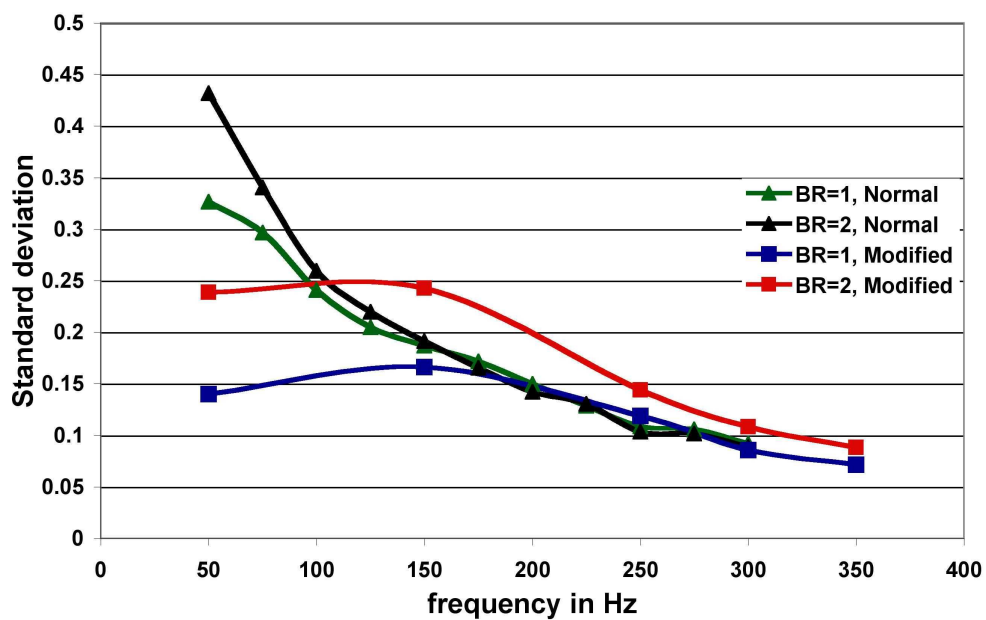
Figure 2.6: Standard deviation of blowing ratio fluctuations for BR=1 and 2 at different frequencies with normal configuration and modified configuration using a damping plenum
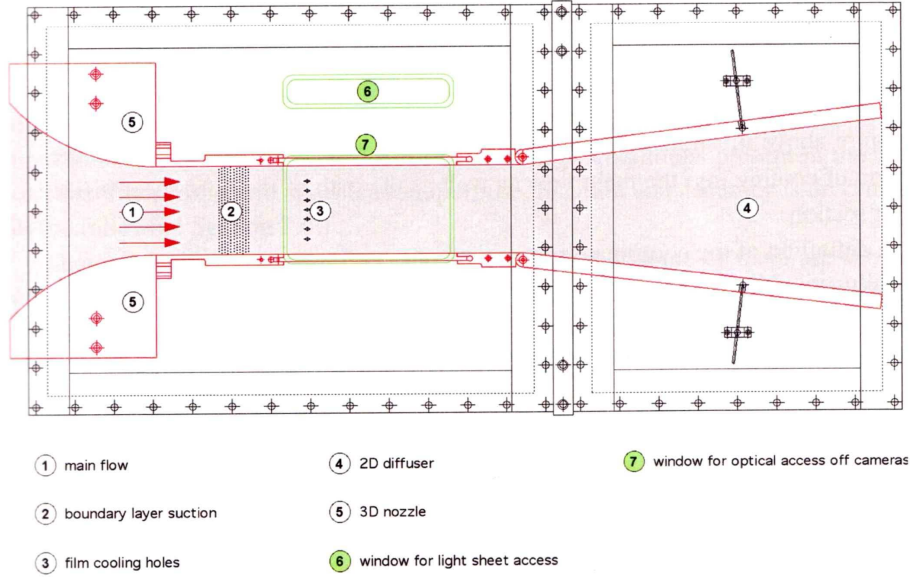
Figure 2.7: A general overview of the test section

mean in order to compare the improvements. The standard deviation was defined by Eq. 2.1.

$$\sigma = \sqrt{\frac{1}{N}\Sigma_{i=1}^{N}(BR_i - BR_{mean})^2} \tag{2.1}$$

This standard deviation of the BR is plotted for the two blowing ratios, 1 and 2 in Fig. 2.6. The effect of the damping plenum uniformly reduces the large fluctuations at low frequencies of 50-150 Hz while the fluctuation is maintained more or less constant for 200 Hz and higher for all cases. However, it must be noted that during high blowing ratio operation some compression waves and expansion waves also travel through to the holes inserts thereby disturbing the assumption of a more or less sinusoidal duty cycle.

2.2.3   Test Section

The entire wind tunnel arrangement schematic is shown in Fig. 2.1. The part labelled 'test section' contains the optical and intrusive access mechanisms for three different kinds of measurement techniques. The window for optical access can be replaced with an infra red transmitting window for infrared thermography access (see Section 2.3.2) or even for probe access (Section 2.3.3) apart from the Particle Image Velocimetry (PIV) setup. For every measurement technique the test section with the cooling holes themselves remains more or less similar but the back plates and front plate are changed.

The test section is built of a vertical frame of 40 x 80 mm^2 steel bars closed by 25 mm steel plates
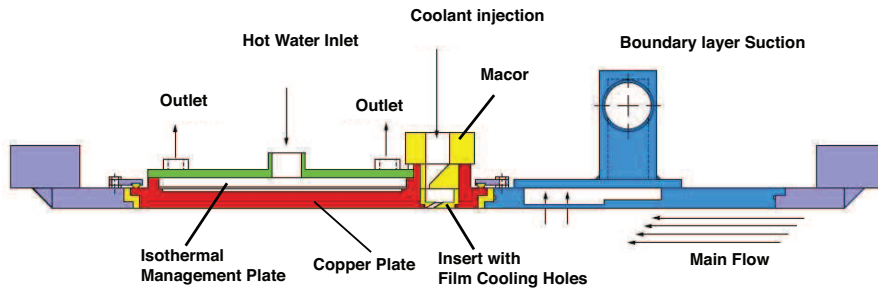
Figure 2.8: A schematic showing the top view of the test section with inserts and isothermal management plate

from the anterior and posterior. The flow path inside the frame is constrained by aluminium and glass elements. A 3-D nozzle accelerates the main flow coming in from the settling chamber. The location of the boundary layer suction is placed upstream of the cooling hole inserts. A 2-D diffuser is located downstream of the test section to recover the dynamic head. The area of the test cross section as shown is 40 x 181 mm^2.

The test section essentially contains a main flow which is carried by the wind tunnel and a secondary flow which is injected in a direction normal to the main flow through inserts which have film cooling holes of different geometries drilled through them. A detailed schematic is shown in Fig. 2.8. The back plate of the test section is made up of a large copper plate measuring 470 mm $\times$ 394 mm. The plate has space for inserts made of a machinable ceramic called MACOR. The inserts have holes drilled into them depending on the geometry being studied. The copper plate has an isothermal management plate with access for hot water to circulate continuously along the entire back surface thus providing a uniform isothermal temperature for heat transfer measurements as shown in Fig. 2.8.

2.3 Rig Setup

2.3.1 Setup for Particle Image Velocimetry (PIV)

The test section can be suitably modified for conducting Particle Image Velocimetry measurements, details of which are provided in Section 3.1. The test section has glass walls of 15 mm thickness on two sides to provide optical access. The front wall is also made for glass for imaging the flow with cameras. The schematic for this is shown in Fig. 2.9. The top and bottom wall allow access for the light sheet. The laser sheet enters the test section normally it but is reflected by a 45°mirror as shown in Fig. 2.9 such that it becomes parallel to the test section and thus illuminates the flow which can then be imaged by a camera viewing it normally.
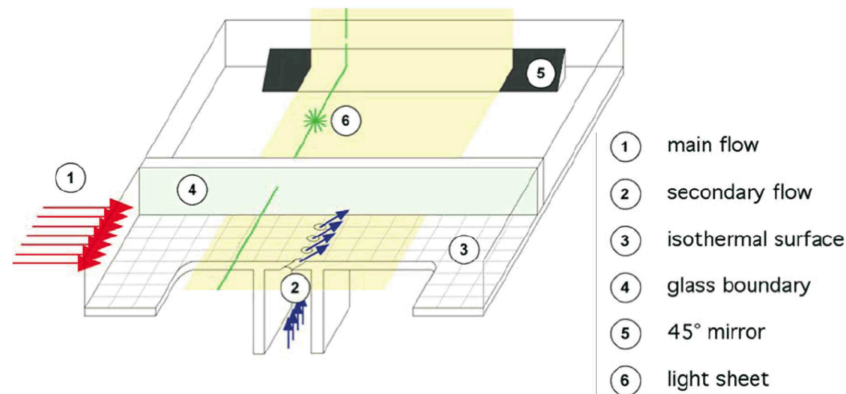
Figure 2.9: A schematic showing the test section setup with optical access to a laser sheet

2.3.2   Setup for Infrared Measurement
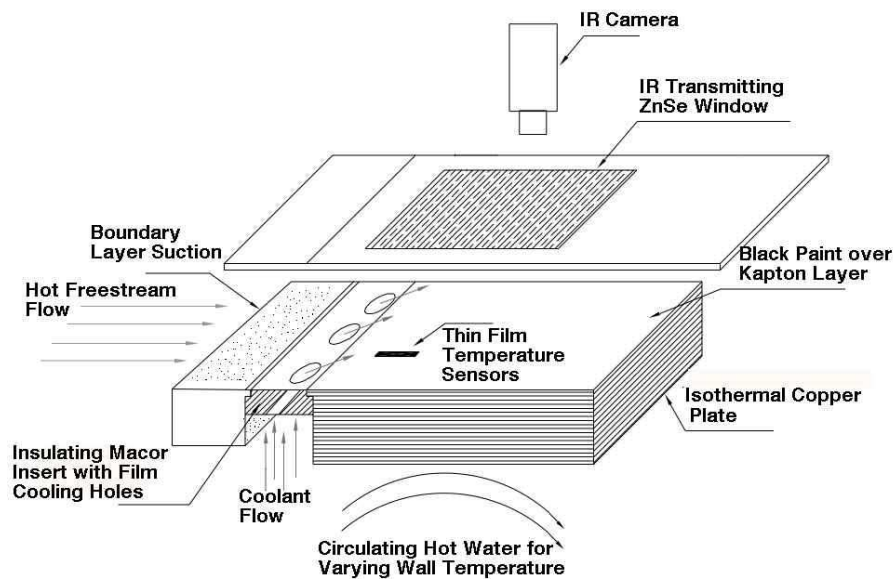
Figure 2.10: A schematic showing the test section setup for infra red measurements

Infrared measurements are used to capture the surface temperature profile from the film cooling jets in a non-intrusive manner. The schematic is shown in Fig. 2.10. The surface of the plate upon which the temperature measurements are taken is first covered with a Kapton insulator. This is a polyamide film manufactured by Dupont. The material used is a 127μm thick KAPTON HN (5 mil). Being very smooth it is essential to strongly cleave it to the smooth copper surface. This is done using a silicon rubber glue, Dow Corning RTV 3140. It is stable and flexible between -50°C and 200°C and so is suitable for the operation. In order to have the best possible
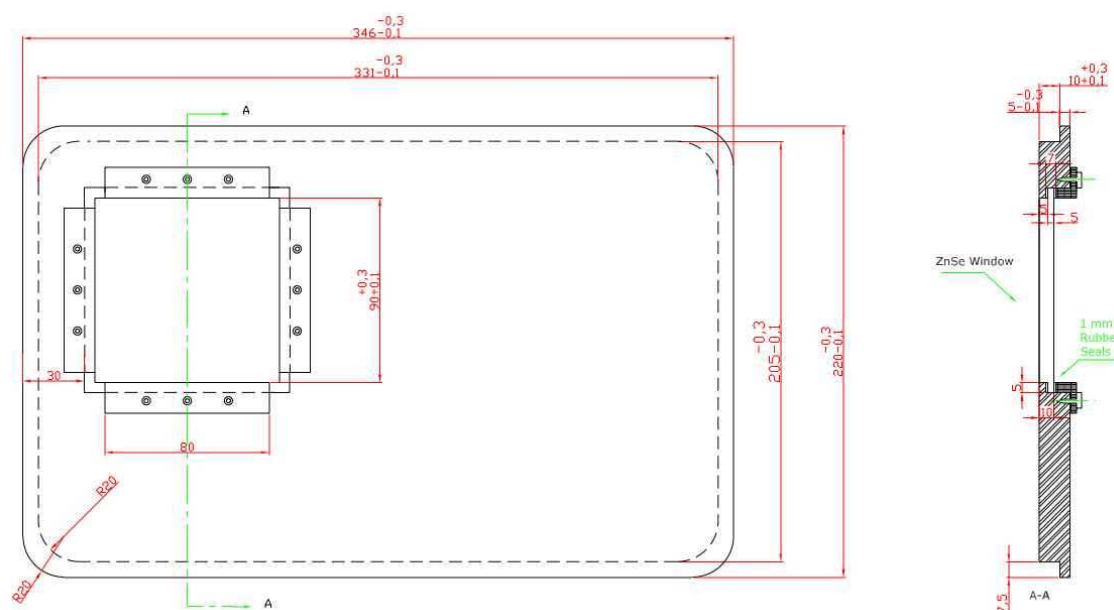
Figure 2.11: A drawing of the ZnSe window placed in a steel window frame

emissivity from the surface, the Kapton foil is spray painted with Nextel Velvet Coating 811-21 Black manufactured by 3M Corporation, having an emissivity of 0.98.. The physical and thermal properties of these three layers is essential for the calculation of heat transfer coefficient and heat flux. These properties are summarized in Table 2.2.

Even with the strong silicon based adhesive it was necessary to first apply a primer and then the adhesive ensuring the absence of air bubbles which would violate the assumption of uniform thermal conditions over the entire surface. The paint was sprayed on top of the dried kapton coating with a spray gun. As Fig. 2.10 shows, some parts of the surface are covered with thin film sensors which are in turn painted by the black paint. These thin film sensors, manufactured by Tao Systems, are known as Senflex sensors and are composed of electron beam deposited nickel elements on a polyamide substrate. After calibration these can be used to measure accurate surface temperature simultaneously with the infra red camera to calibrate the IR camera itself. A 85 kW circulating water heater manufactured by Schniewindt and a Grundfos Magna 50-100 pump is used to circulate hot water. A thermostat allows the setting of temperatures till 85°C. This circulating water provides an isothermal boundary condition for heat transfer calculations.

The outside wall of the wind tunnel was constructed of steel and fitted with a Zinc Selenide window for infrared radiation access. The infrared camera as described in Chapter 3.2 has a spectral range from 7 to 14 microns in wavelength. Zinc Selenide is a binary crystal which has constant transmittance over a wide range of long and medium wavelengths of infrared radiation. The current window was coated with a special anti-reflective coating that boosted the transmit-

Surface element	Thickness	Thermal Conductivity	Density	Specific heat
	$\Delta z\,[m]$	$k\left[\frac{W}{m.K}\right]$	$\rho\left[\frac{kg}{m^3}\right]$	$C_p\left[\frac{J}{kg.K}\right]$
Nextel Velvet 811-21 Paint	0.197	0.13	852	1000
Kapton HN 5	0.12	0.12	1420	1090
RTV 3140 Adhesive	0.14	0.12	1050	326.35

Table 2.2: Material properties of surface elements

(a) (b)
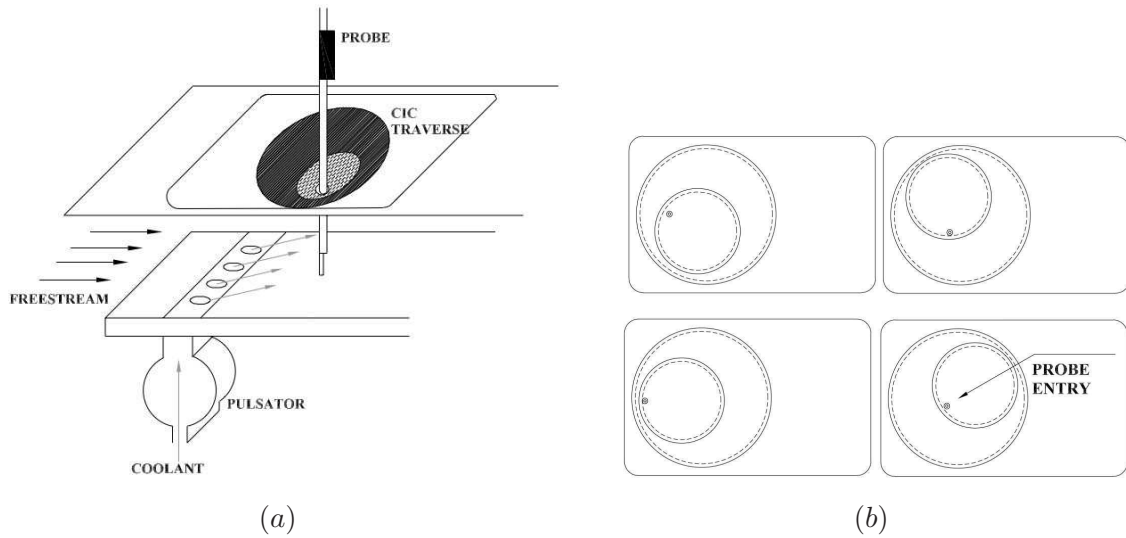
Figure 2.12: A schematic showing (a) Test section setup with probe access (b) Circle in Circle system at different positions

tance to about 0.96 over the range from 7 to 14 microns. Without the anti-reflective coating the ZnSe would have had an average transmittance of around 0.65 as estimated in Kaplan [64]. The ZnSe window was fitted into a steel frame as shown in Fig. 2.11. As the wind tunnel would be operating at high temperatures the thermal expansion of the ZnSe must be considered with respect to its frame. According to Kumar and Sastry [68] the thermal expansion coefficient of ZnSe is not much different from steel and hence the build up of thermal fatigue can be avoided.

2.3.3   Setup for Probe Measurements

In order to adapt the test section for intrusive probe measurements the opposite wall of the copper plate is replaced with a steel plate. The adaptation is shown in the schematic, Fig. 2.12. A novel traversing and probe access technique is used, henceforth referred to as the Circle- In-Circle (CIC) system. This traversing system is made of two circular metal plates fitted onto a flat plate. This is shown in Fig. 2.12. The two non-concentric circular disks can each rotate
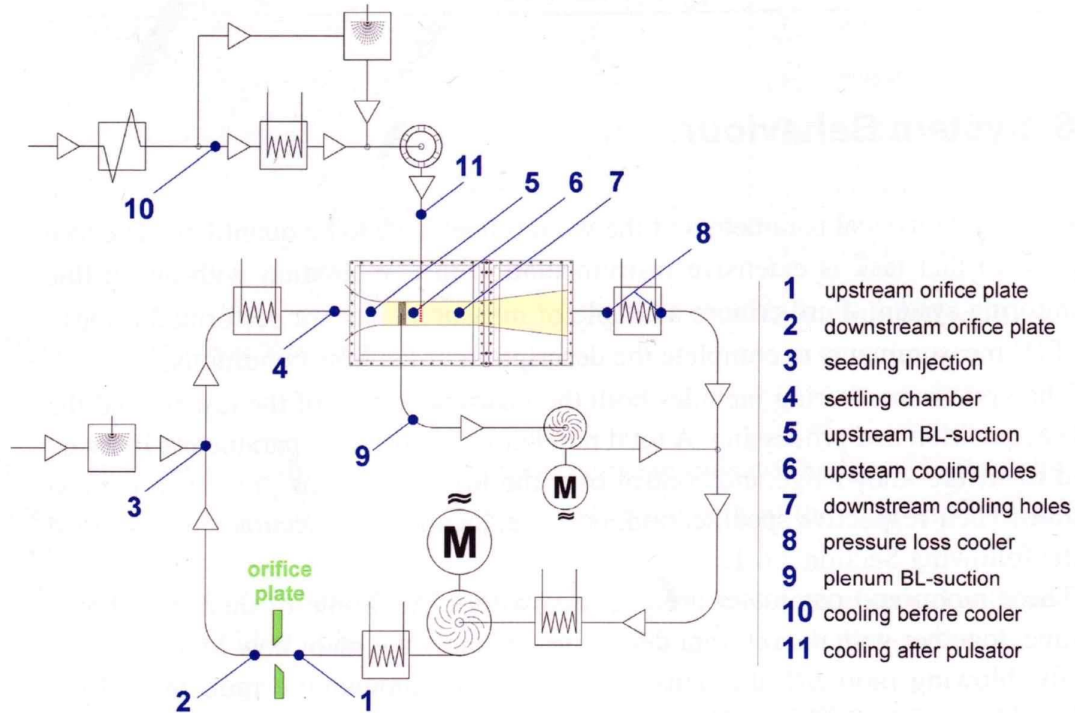
Figure 2.13: A schematic showing location of pressure taps

about their own axes and thereby allow the small probe entry hole, a positioning at any point in the plane. The probe itself can be traversed perpendicular to the plane of the traversing system as shown in Fig. 2.12 thereby allowing an access to any measurement point within the 3D domain. The sealing between the moving circles is effected by tight clamps. The main advantage of such a probe access system, is the ease of manufacture, absolute flexibility in spatial access and ability to move the probe without any other force except that from the four axis traversing system moving the probe assembly itself. This kind of system does not cause any intrusion at the wall, being flush with it and allows a rapid experimental campaign.

2.4   Rig Instrumentation

The LAVAL wind tunnel facility is instrumented with numerous pressure and temperature sensors which are then combined to derive various flow conditions for an online real time adjustment and condition setting. The most important monitored parameters are the main flow Mach number, M, the blowing ratio, BR, the density ratio, DR, the momentum flux ratio, IR, the reduced frequency, f_r and the basic main flow and coolant temperatures. A LabView program records the various parameters onto a rig file every 20 seconds.

Pressure measurement locations for the entire rig are shown in Fig. 2.13. The pneumatic taps
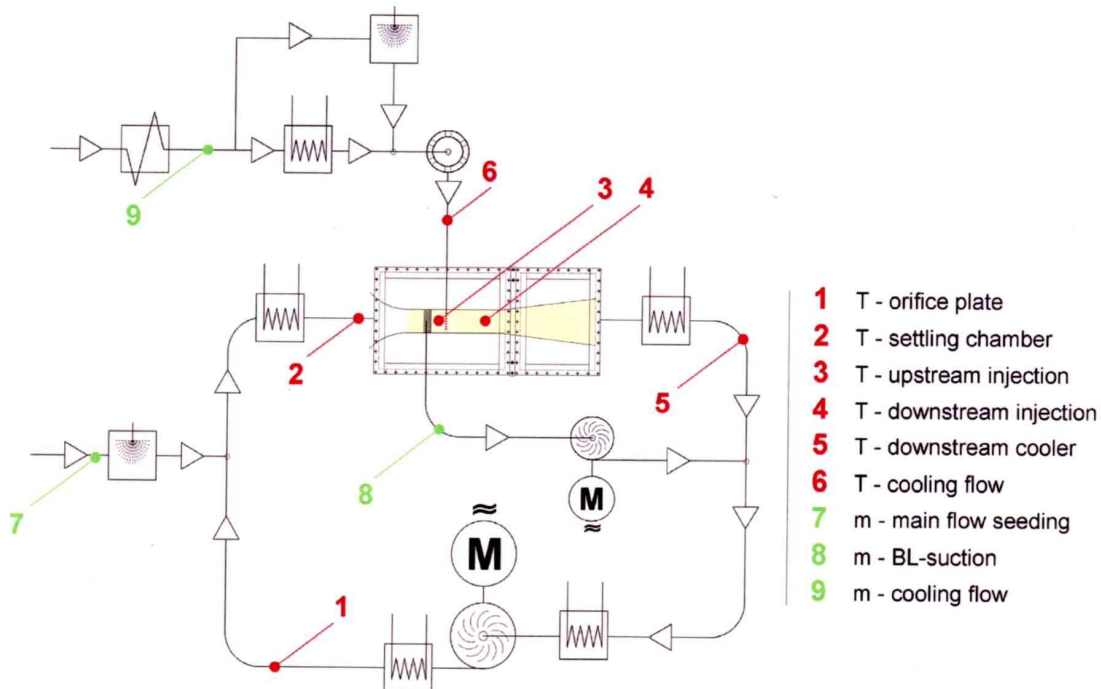
Figure 2.14: A schematic showing location of temperature and mass flow measurement devices

at all the locations shown in the figure are carried to a pressure scanning module PSI 9016 using flexible PVC tubes of 1.5 mm inner diameter. From here the digital signal is fed into a computer. A calibrated orifice plate is used to measure the main flow mass flux using the pressure measurements at points 1 and 2. The other pressure measurement points can be used to calculate the mass flow and velocities in the respective lengths. The atmospheric pressure is continuously scanned with a second pressure scanning module which allows the differential pressure measurements to be recorded. The pressure sensitive modules are calibrated and sealed by the manufacturer PSI. Their stated full scale output (FSO) accuracy is given to be $\pm 0.05\%$ this translates to an uncertainty of 17.5 Pa in the pressure taps located in the test section to 157.5 Pa in the high pressure taps in the coolant flow.

point	accuracy class	FS [K]	deviation [K]
1	B	310	0.5
2	B	400	0.9
3	A	400	0.4
4	A	400	0.4
5	B	310	0.5
6	A	300	0.25

Table 2.3: Accuracy of temperature sensors

point	FSO [g/s]	FSO accuracy [%]	deviation [g/s]
7	18	±2.5	0.45
8	72	±2.5	1.8
9	72	±2.5	1.8

Table 2.4: Accuracy of mass flow sensors
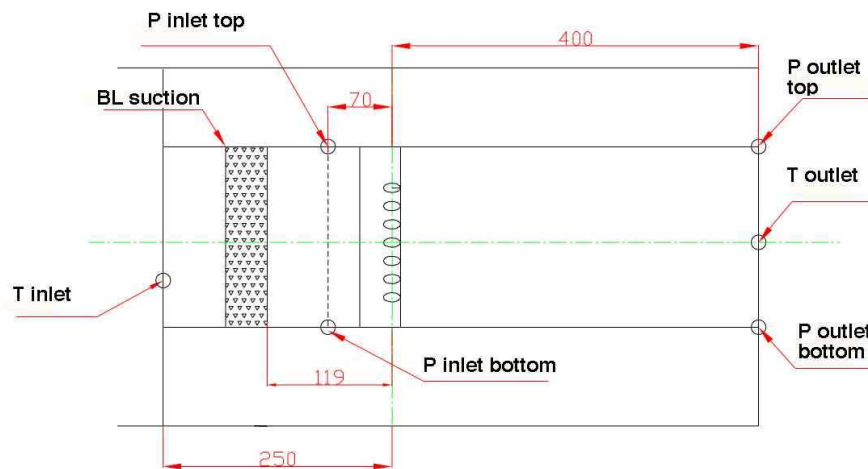
Figure 2.15: Test section schematic showing locations of inlet and outlet pressure and temperature measurement

The temperature is measured at several locations throughout the facility using resistance thermometers. Pt100 temperature sensors are used to measure the inlet and outlet temperature conditions of the test section. The Pt100 thermometers were calibrated against an a water bath using a mercury thermometer to take into account drift and bias introduced by the measurement chain. A schematic with the locations of temperature sensors is shown in Fig. 2.14. This figure also shows the location of three mass flow sensors (nos. 7, 8 and 9). The accuracy classes and stated uncertainty in Kelvin of the different Pt100 thermometers is recorded in Table. 2.3.

The mass flow rate of the cooling, the main flow seeding and the boundary layer suction are each measured with a mass flow measurement device ECOFLOW manufactured by Esters Electronik. The working principle utilizes the mass flow dependancy of convective heat transfer. A Pt100 sensor is kept at a constant temperature difference relative to the flow. A second sensor monitors the flow temperature. The electrical energy required to maintain the temperature difference is therefore directly related to the mass flow. The sensors are calibrated by the manufacturer and their stated accuracy is described in Table 2.4.

2.5 Determination Of Flow Conditions

The determination of the flow and operating conditions is carried out in real time from pressure and temperature measurements by a LabView program. Fig. 2.15 shows the locations and distances of pressure and temperature sensors from the origin of the coordinate system located at the centre of the cooling holes. The inlet and outlet conditions from which the operating conditions are calculated are located in the test section.

2.5.1 Mach Number

The main flow mach number is determined from the temperature and mass flow measurements in the main flow using Eq. 2.2

$$M = \frac{u_m}{a} = \frac{\dot{m}_m}{A_m \rho_m \sqrt{\gamma R T_m}} \tag{2.2}$$

Here A_m is the area of cross section of the main flow and T_m is the inlet temperature measured at point 3 as shown in Fig. 2.14, more accurately the point labeled T_{inlet} in Fig. 2.15. The density ρ_m is calculated from the pressure measurement at the inlet (point 6 in Fig.2.13 or P_{inlet} in Fig. 2.15) according to Eq. 2.3. The pressure P_m is taken to be the inlet pressure averaged from the top and bottom pressure taps.

$$\rho_m = \frac{P_m}{R T_m} \tag{2.3}$$

The mass flow rate $\dot{m}_m$ is derived from the total mass flow measurements at the orifice plate with respective addition of mass flow due to seeding and removal of mass at boundary layer suction. This is shown in Eq. 2.4

$$\dot{m}_m = \dot{m}_{orifice} + \dot{m}_{seed} - \dot{m}_{BLsuction} \tag{2.4}$$

The mass flow rate at the standardized orifice plates is determined by measuring the pressure across it at points 1 and 2 in Fig. 2.13. The orifice plate is standardised according to EN ISO 5167-1:1995 norms and using standard calculation procedures as dictated by DIN Taschenbuch 229 [35]. The seeding and boundary layer suction mass flow rates are determined from the pressure measurements near the points of mass addition or removal.

2.5.2 Blowing Ratio

The blowing ratio is defined as the ratio of mass flux per unit area of the coolant to that of the main freestream flow. It is given by Eq. 2.5

$$BR = \frac{u_c \rho_c}{u_m \rho_m} \tag{2.5}$$

The main flow velocity is determined from the main flow mass flux, the cross section area and the density as shown in Eq. 2.2. Similarly the coolant mean velocity, u_c is given by Eq. 2.6.

$$u_c = \frac{\dot{m}_c}{A_c \rho_c} \tag{2.6}$$

A mass flow meter is installed in the secondary loop which gives the coolant mass flux, $\dot{m}_c$ (point 9 in Fig. 2.14). For some of the heat transfer measurements this mass flow meter was observed to have some drift errors. In those cases a discharge coefficient based mass flow measurement was determined using Eq. 2.7.

$$\dot{m}_c = C_d A_c P_c \left(\frac{P_m}{P_c}\right)^{\frac{\gamma+1}{\gamma}} \sqrt{\frac{2\gamma}{(\gamma-1)\,RT_c}\left[\left(\frac{P_c}{P_m}\right)^{\frac{\gamma-1}{\gamma}} - 1\right]} \tag{2.7}$$

Here the pressure, P_c is the pressure measured in the plenum from which the coolant is injected into the test section. It is indicated by point 11 in Fig. 2.13. C_d is the discharge coefficient which is kept at an average value of 0.8 given the fact that there are many corrections and correlations suggested for film cooling holes (the most recent one being, Gritsch et al. [53]) and the number varies slightly for compound angled holes and different hole diameter based non-dimensional length of injection pipe (L/D).

The coolant density ρ_c is actually the density of the coolant *at the exit plane* into the test section. It is therefore calculated using the coolant temperature T_c but the pressure used is that of the inlet freestream into which the coolant is injecting.

$$\rho_c = \frac{P_m}{RT_c} \tag{2.8}$$

2.5.3 Density Ratio

The ratio of the density of coolant flow to that of the main freestream flow is defined as the density ratio and given by Eq. 2.9. However, because of the definition of the density of the coolant being calculated based on the main flow pressure, the density ratio turns out to be the ratio of the main flow static temperature to coolant temperature (in Kelvin).

$$DR = \frac{\rho_c}{\rho_m} \tag{2.9}$$

2.5.4 Momentum Ratio

The momentum ratio, IR is defined as the ratio of momentum flux of coolant injectant to that of the main flow per unit area. It is given by Eq. 2.10

$$IR = \frac{\rho_c u_c^2}{\rho_m u_m^2} = \frac{BR^2}{DR} \tag{2.10}$$

2.5.5 Reduced Frequency

Using the same kind of non-dimensionalisation typically used for defining a Strouhal number, the reduced frequency is based on the cooling hole diameter as the length scale and the freestream inlet velocity for the velocity scale as shown in Eq. 2.11. Here f is the frequency of pulsation measured at the hole exit.

$$f_r = \frac{f.D}{U_m} \tag{2.11}$$

Often, in literature instead of using the hole diameter as the length scale, the length of the delivery pipe L is used. Since all measurements shown in this study are for a constant, $L/D = 4$, the reduced frequency can be multiplied by 4 to get the comparable number.

2.5.6 Boundary Layer

The boundary layer of the main flow was quantified using a pneumatic probe as described in Bernsdorf [12]. The displacement thickness non-dimensionalised by the hole diameter was measured to be $\delta/D = 0.12$ while the momentum thickness, $\theta/D = 0.05$ giving a high shape factor $H = 2.31$. However the boundary layer followed a 1/7 power law. Equation 2.12 shows the velocity in the boundary layer with respect to wall normal distance, z. Since the test and figures are already detailed in Bernsdorf [12], they are not repeated here.

$$\frac{u}{U_m} = \left(\frac{z}{\delta}\right)^{\frac{1}{7}} \tag{2.12}$$

Hence the boundary layer at the beginning of the test section is still in the developing phase and has not fully developed. In order to have a fully developed turbulent boundary layer a small trip is created by having the cooling hole insert pushed half a mm above the copper flat plate. These numbers are quoted for the case when the boundary layer suction is switched on.

2.6 Uncertainty Analysis

This section only details the uncertainty estimates of the flow parameters that are measured by the rig instrumentation. Uncertainty estimates of the main measured quantities like velocity and

Parameter	Typical Value	Absolute Uncertainty	Relative Uncertainty,[%]
$D_{orifice}$ [mm]	170	0.01	0.006
D_{hole} [mm]	5	0.01	0.2
z [mm]	1	0.1	0.1
A_m[mm]	7240	0.1	0.00014
A_c[mm]	137.4	0.0005	0.0004
$\Delta P_{orifice}$ [Pa]	104500	105	0.1
P_m [Pa]	96400	52.5	0.05
P_c[Pa]	104500	157.5	0.15
$P_{c,tot}$ [Pa]	104500	140	0.13
T_m [K]	297	0.9	0.3
T_c [K]	220	0.25	0.11
m_c [g/s]	45	1.13	2.5
$m_{seeding}$ [g/s]	3	0.08	2.5
$m_{BL-suction}$ [g/s]	51	1.28	2.5
f [Hz]	42	0.05	0.12

Table 2.5: Uncertainty of primary quantities

Parameter	Relative Uncertainty,[%]
M	0.52
DR	0.26
BR	2.6
IR	5
f_r	0.54
δ/D	1.02
θ/D	1.55

Table 2.6: Uncertainty of derived quantities

surface temperature are given in Chapter 4.

The propagation of uncertainty in the derived parameters can be estimated using the methodology described by Kline and McClintock [66]. The uncertainty in estimation of a parameter R with dependance on other parameters X_1, X_2, X_3 can be given by Eq. 2.13.

$$\frac{\delta R}{R} = \sqrt{\left(\frac{\delta X_1}{X_1}\right)^2 + \left(\frac{\delta X_2}{X_2}\right)^2 + \left(\frac{\delta X_3}{X_3}\right)^2 + \cdots} \tag{2.13}$$

Here X_i could represent the pressure or temperature measurement used to derive the quantity and δX_i is the uncertainty in its determination. The uncertainty in measurement of the basic quantities is tabulated in Table 2.5. It must be noted however that this analysis only estimates the statistical uncertainty due to random errors in the measurement chain. The uncertainty of

derived flow conditions based on the calculations in Eq. 2.13 using the uncertainty values from Table 2.5 are shown in Table 2.6.

This table however does not give an idea of the stability of the flow conditions during an experimental campaign. A typical experimental campaign is carried out over a period of a few hours, during which flow conditions like M, BR, DR etc should be maintained constant. However owing to the typical fluctuations in the rig some of the conditions oscillate over a period of time around their set level. This fluctuation is ameliorated by maintaining the same condition for a long time before experiments begin in a warm up mode and then using averaged values over a large period of time.

Chapter 3

Measurement Techniques

The compound angled film cooling problem has traditionally only been treated as a phenomenological empirical understanding of the cooling effectiveness of different geometries. Hence works such Jung and Lee [63], Goldstein and Jin [49], Sen et al. [100], Schmidt et al. [99] have all involved surface temperature measurements for different hole geometries which are then compared with streamwise injection. Film cooling measurement of the flow structure of compound angled cooling on flat plates has not really been investigated much apart from Lee et al. [74] wherein hot wire anemometry was used to measure near hole flow structure. Many of the measurement techniques in literature have employed liquid crystals (eg. Nasir et al. [89]) or more recently infra red cameras (eg. Dittmar et al. [36], Baldauf et al. [9]) to measure surface temperatures.

In order to understand the effect of the flow structure on the surface performance, both the 3-D velocity field as well as the surface temperature were measured for similar flow conditions. A three dimensional stereoscopic Particle Image Velocimetry (3-D PIV) was used. The following sections detail the working principle and the experimental details of the PIV system used to measure the velocities in Section 3.1. This is followed by a description of the infrared thermography equipment and methods used to measure the adiabatic effectiveness in Section 3.2. Lastly the description of the fast response entropy proble, FENT, is given in Section 3.3 which allows measurement of aerothermodynamic performance of film cooling injection.

3.1 Particle Image Velocimetry (PIV)

3.1.1 Operating Principle

Particle Image Velocimetry (PIV) is a whole-flow-field technique providing instantaneous velocity vector measurements in a cross-section of a flow. General and up to date reviews of advances in this technique are detailed in Adrian [3], Prasad [93], Adrian [4]. A practical guide which details all the important factors to consider in PIV are detailed in Raffel et al. [94]. According
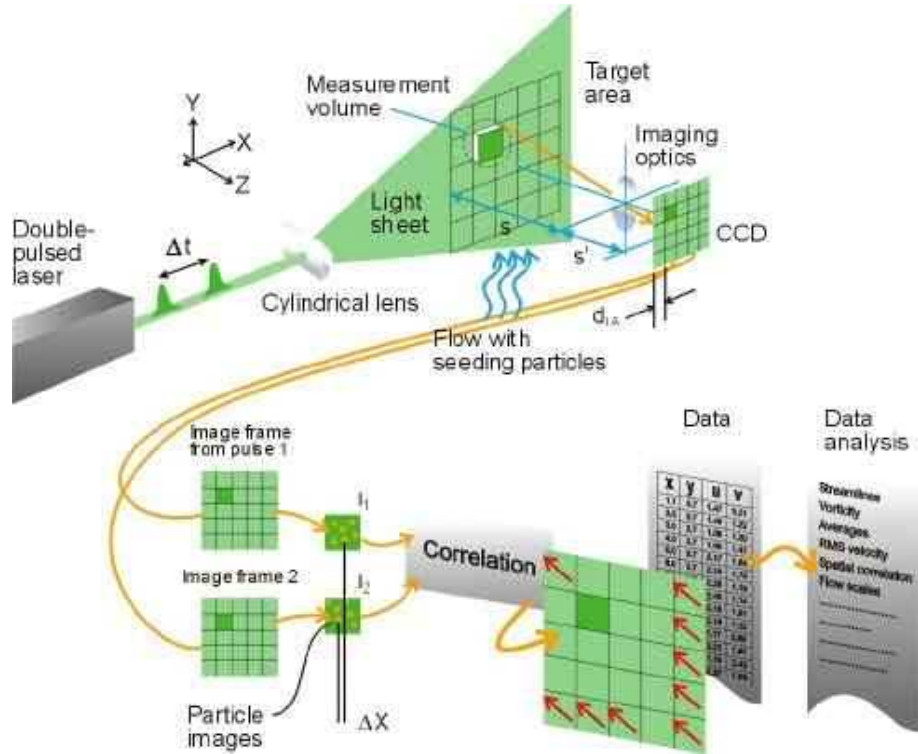
Figure 3.1: A schematic of the PIV process from Dantec Dynamics [32]

to Adrian [4] the important distinction of PIV from typical flow visualization techniques is that it is an *accurate, quantitative measurement of fluid velocity vectors at a very large number of points simultaneously.*

This technique involves the measurement of distance travelled by a tracer particle in a flow and by knowing the time difference between the initial and final positions the velocity may be derived according to Eq. 3.1.

$$\vec{v} = \frac{\Delta \vec{x}}{\Delta t} \tag{3.1}$$

These tracer particles, also known as seeding particles are chosen such that they follow the flow. An area of the flow field is illuminated by a light sheet. Typically these light sheets are produced by pulsed lasers. A charged coupled device (CCD) camera with a capability to take two subsequent pictures in quick succession is used for image capture.

Once a sequence of two light pulses is recorded, the images are divided into small subsections called interrogation areas (IA). The interrogation areas from each image frame, I1 and I2, are cross-correlated with each other, pixel by pixel. The correlation produces a signal peak, identifying the common particle displacement, $\Delta \vec{x}$. An accurate measure of the displacement - and thus also the velocity - is achieved with sub-pixel interpolation. A velocity vector map over the whole target area is obtained by repeating the cross-correlation for each interrogation area over the two
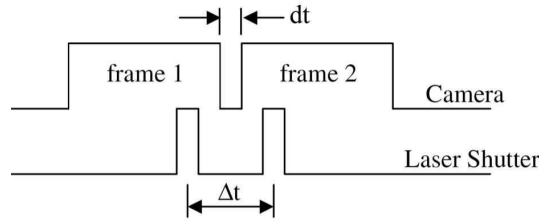
Figure 3.2: Signal diagram showing synchronization of measurements
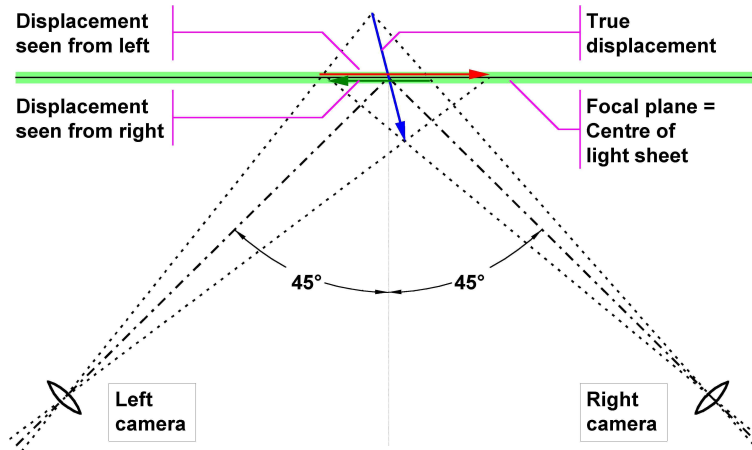
Figure 3.3: A schematic showing the concept of stereoscopic 3 dimensional PIV

image frames captured by the camera. The increase of dynamic range is affected by artificially shifting the interrogation area from the second snap shot, I2 in the mean direction of the fluid flow with a characteristic displacement. This tuning of the PIV system is important to obtain greater accuracy and high dynamic range. The cross correlation peaks can then be decomposed to give velocity vectors. This entire principle is shown in Fig. 3.1.

The synchronization of the laser pulse with the camera shutter is shown in Fig. 3.2. The pulsing light-sheet and the camera are synchronised so that particle positions at the instant of light pulse number 1 are registered in frame 1 of the camera, and particle positions from pulse number 2 are in frame 2. The smaller time of exposure of the laser pulse is important to 'freeze' the flow field in order to capture only instantaneous pictures rather than smeared out traces due to longer exposure of the particles.

When a single camera is used to image the velocity field, only one plane with two cardinal velocity directions can be imaged. In order to extend the 2-D PIV for simultaneous 3 dimensional measurement two cameras at slight angles to the illuminated object plane can be used. The perspective produced is similar to that occurring in human vision for depth perception. A schematic shown in Fig. 3.3 shows how simultaneous images from two cameras can be taken for later recombination into a 3 dimensional particle displacement. An arithmetical model which is

calibrated before an experiment can be used to convert the camera imaged displacements into real displacements using information from both cameras.

3.1.2   PIV System Components

Illumination System   A pulsed Nd:YAG (Neodymium-doped Ytterium Aluminium Garnet, $Nd : Y_3Al_5O_{12}$) solid state laser system has to be chosen as this type of laser delivers sufficient energy to illuminate micron particles in a high speed airflow. The laser SOLO is manufactured by New Wave Research Co. Ltd. Although the power is low with 120 mJ per pluse, an equivalent energy of 12 MW is emitted with each pulse with duration of 10 ns.

The temporal range of pulse separation of this type of pulsed lasers is limited to 15 Hz. The limitation in the range of pulse separations is overcome by using a double cavity Nd:YAG laser system. Two laser cavities are inserted into a housing which contains optics to combine the beam path. Each laser is operated in single Q-Switch mode and electronics control the interval between the emission of laser light from each laser. Using this method the range of pulse separations extends from 300 ns to 300 ms. Communications lines between the pulsed laser and the synchronisation unit in the system unit are required for user control of the data acquisition process. Either the laser can run in a free-run mode where the laser informs the rest of the system that is ready to emit laser light. Alternatively, the synchronisation unit instructs the laser cavities when to fire their flash lamps and when to allow their Q-switches to emit laser radiation.

Nd:YAG lasers emit light with a wavelength of 1064 nm which is in the infrared. For PIV purposes, this wavelength is not very useful since most cameras are not sensitive to it. Generally cameras are most sensitive to the blue-green spectrum. Furthermore, there are many practical difficulties when the laser power is a classified hazard. Therefore, for PIV, Q-switched YAG lasers are frequency-doubled. The wavelength of the laser pulse is halved to 532 nm by a device called a second harmonic generator thus producing a blue-green light. Harmonic generators are not efficient and so there is a need to dump the residual infrared before allowing the pulsing beam to leave the laser. This is done by an optical component called a harmonic separator.

Cameras   The purpose of the camera is to capture the initial and final positions of seeding particles in the flow field. The camera is placed at an angle to the light sheet. Seeding particles scatter light from the first pulse of the light sheet and the camera detects this scattered light, ideally as a bright signal an a dark background. Thus, the camera image map has sampled the initial positions of the seeding particles. The light sheet is switched off and the seeding particles are transported by the movement of the flow field. The second pulse of the light-sheet is fired and the seeding particles scatter light which is imaged onto the camera detector so the final positions of the seeding particles are sampled.

The CCD cameras provide an instantaneous digital signal of the image map of seeding particle

positions. A CCD camera compromises an array of detectors called pixels. Each pixel is a MOS capacitor, being charged by converting incident photons of light into electrons, like in a photo diode. The cells are isolated from each other by potential walls, created by doping of the silicon chip and by applying voltage to a grid of transparent metallic electrodes deposited on the CCD surface. Light falling on a pixel is transformated to a voltage during read-out of the CCD chip and the value of the voltage is seen as a grey scale distribution on the PIV image map. Ideally, images should have a high charge i.e. appear white and the background noise level of the CCD chip should be low i.e. appear dark. Cameras used for PIV have a progressive-scan-interline CCD chip comprises both light-sensitive cells and an equal number of storage cells. The latter are not exposed to light. The first laser pulse is timed to expose the first frame, which is transferred from the light-sensitive cells to the storage cells immediately after the laser pulse. The second laser pulse is then fired to expose the second frame. The storage cells now contain the first frame and the light sensitive cells the second. These two frames are then transferred sequentially to the output shift-register. The storage cells are phisically located adjacent to the light sensitive cells on the surface of the CCD-chip.

The number of vectors in the vector map is dependent upon the number of pixels the CCD camera and the size of the interrogation area used. The array of totally independent vectors is:

$$N_{vectors} = \frac{N_{pixel-CCDrow}}{N_{int}} \cdot \frac{N_{pixel-CCDcolumn}}{N_{int}} \qquad (3.2)$$

where N_{int} is the side of the interrogation area in pixels. In practice, the number of independent vectors is greater. It is highly probable that if a particle has an image near the outer edge of interrogation area its pair may be in the neighbouring interrogation area. That is, the particle images do not contribute to the calculation of a velocity vector. Therefore, successive interrogation areas are overlapped to optimize the use of the information in the image map. By overlapping interrogation areas the use of the avaiable information is maximazed. With 50 % overlapping of interrogation areas the number of vectors obained is:

$$N_{vectors} = \frac{N_{pixel-CCDrow}}{0.5 \cdot N_{int}} \cdot \frac{N_{pixel-CCDcolumn}}{0.5 \cdot N_{int}} \qquad (3.3)$$

The choice of N_{int} is constrained by the conflicting contraints imposed by velocity dynamic range and spatial resolution considerations. Generally, an interrogation area side-length of 32 pixels provides a good compromise.

The dimension of the interrogation area affects the upper limit of the velocity dynamic range, which is determinated by the maximum spacing between successive particle images that can be measured. The displacement vector d_{max} corronding to the maximum velocity vector in a flow field v_{max}, the time between successive pictures t and the object:image scaling factor S is:

$$d_{max} = v_{max}\frac{t}{S} \qquad (3.4)$$

This displacement vector can only be measured if its magnitude is less than the dimension of the interrogation area N_{int}. Furthermore, the displacement vector should be a fraction of the interrogation region to ensure that there is no signal drop-out. The parameters t, S and N_{int} are chosen so that the following relationship is satisfied:

$$d_{max} = v_{max}\frac{t}{S} <= 0.25 \cdot N_{int} \cdot d_{pitch} \tag{3.5}$$

with d_{pitch} being the spacing between the pixel on the CCD array. For a interrogation area with N_{int} the upper velocity limit corrensponds to a pixel pitch of 8 pixels.

A dynamic range of only 9 discrete velocities can be achieved with standard procedures and an interrogation area of 32x32 pixels. The smallest velocity corrensponds to one pixel pitch. With the aid of subpixel interpolation this limitation is improved, with a minimum resolution of 1/64 of one pixel pitch. To allow this, the particles have to appear over at least 3 pixels to satisfy the Nyquist-theorem.

Two PCO SensiCam QE cameras are used in the PIV system. A standard photografic lens, a Nikon AF Micro-Niccor 60mm f/2.8 is mounted on each camera. The dimension of the pixels on the cameras CCD-chip are 6.45x6.45 μm^2, with a total spatial resolution of 1280x1024 pixels on the chip. The camera features a 2-stage peltier cooling of the sensor chip, keeping its temperature as low as -12°C, this improving the signal-to-noise ratio. The interframing time of the cameras can be set between 500 ns to 1000 ns.

System Unit   The system unit Flow Map systemHUB, manufactured by Dantec Dynamics, is the central to the PIV system. It contains special input buffers that can simultaneously read image maps from a CCD camera, store image maps in a memory area and send the entire image to the PC. Furthermore, this process unit provides physical communication and synchronisation links between the processor, the PC, the cameras and the laser. The systemHUB has a Gigabit communcation port that enables the fast delivery of image-data to the PC using the TCP/IP protocol. The HUB is accessed by the FlowManager software which also is an interface for further post processing and exporting of vector files.

Seeding   In PIV it is not actually the velocity of the flow that is measured, but the velocity of particles suspended in the flow. In this respect these seeding particles can be considered to be the actual velocity probes, and seeding consideration are thus important in PIV. The particles must be small enough to scatter sufficient light for the camera to be able to detect them. Ideally, the particles should also be neutrally buoyant in the fluid. Particles whose motion is used to represent that of a fluid continuum should be

- Able to follow the flow

- Good light scatterers
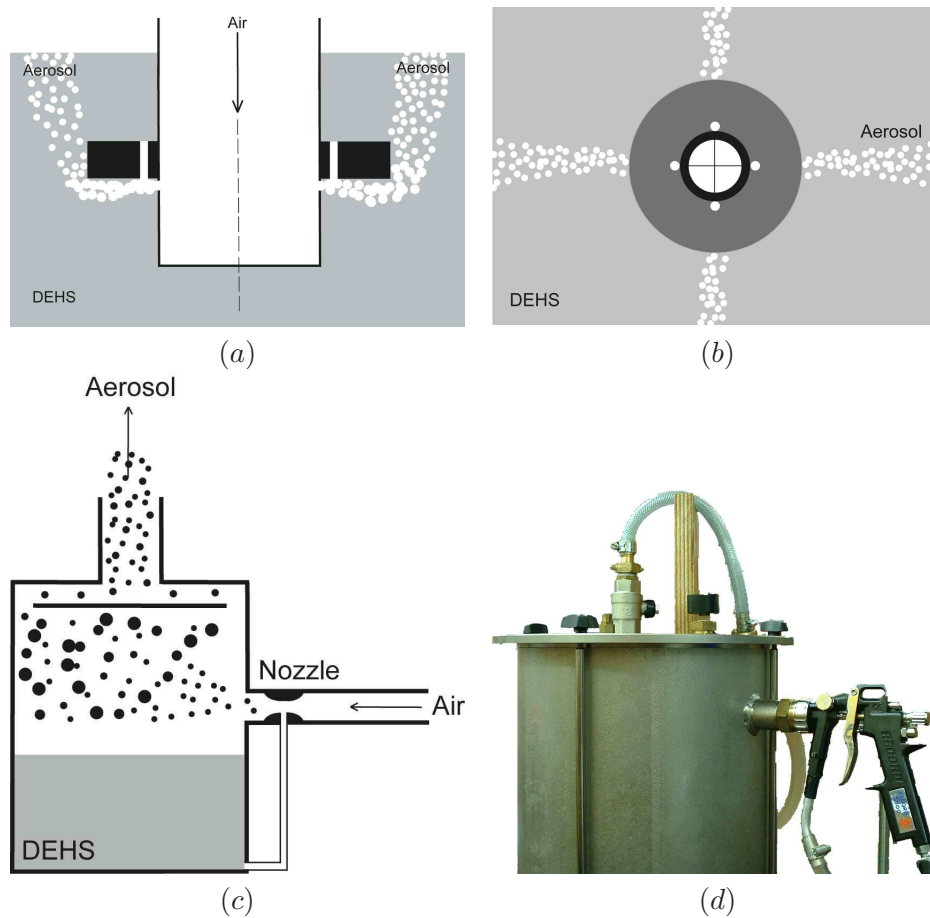
Figure 3.4: Working principle of a Laskin nozzle (a) Side view (b)Top view (c) In-house seeding generator
schematic (d) Photograph of in-house seeding generator

- Conveniently generated

- Cheap

- Non-toxic, non-corrosive, non-abrasive

- Non-volatile, or slow to evaporate

- Chemically inactive

Beside the high requirements on the seeding particles due to the complex flow field furter diffi-
culties due to the thermal conditions of the both flows are considereted in the choice of seeding
material and generation.

The oil Diethyl-hexylsebacat, DEHS is used as the seeding material to be used in aerosol gener-
ators. This material is non-toxic, non-carcinogenic, and only slightly corrosive towards gaskets
and paint. It is of low enough volatility to partly recirculate in the closed loop wind tunnel.

However, unlike other oils it will completely evaporate eventually, reducing the long-lasting contamination. DEHS is an organic material ($C_{26}H_{50}O_4$). It is combustible and open flames have to be prevented. Since the flash point of DEHS is high (ca. 210°C) a danger due to explosion is not present in the current test facility. The lower explosive limit can be calculated from the flash point. The saturated vapour pressure p_d at this temperature is 150.8 Pa and gas constant of DEHS R_{DEHS} is 19.48 $\frac{J}{kgK}$. The explosive limit in vol.% in air is 2.2. DEHS-particles survive in a 120°C environment, are detectable and avaiable in sufficient quantity to allow a sussessful correlation of the recorded images. The seeding for the main flow is generated by an in-house designed and manufactured seeding generator. The seeding for the cooling flow is generated with a Laskin-Nozzle atomizer. Both generators produce particles with a mean diameter of below 4 μm, which fulfil the requirements on tracking capabilities. Injection into the main flow is achivied by means of 2 tubes with many discrete holes that release aerosol far upstream of the test section. The injection of seeding into the coolant flow is done via a T-flange 1.5 m upstream of the pulsator.

Seeding Generation   The main flow and secondary flow are seeded with the same DEHS oil but with different seeding generators. The secondary flow uses a commercially available DLR-40 seeding generator is manufactured by PIVTEC. It is based on the Laskin nozzle technology depicted in Fig. 3.4 (a) and (b). Air is blown throught four holes in a tube in the liquid located in a reservoir. The tube is closed at its lower end. These four sonic jets then suck liquid throught vertical holes in the ring, to produce air bubbles containing finely atomized droplets As the bubbles rise to the liquid surface, the droplets are released into the gas stream. An impactor plate is necessary to remove larger droplets from the polydisperse spray. The DLR seeder thus produced an average particle diameter of 3.43 μm with a minimum and maximum particle diameter of 2.5 to 6 μm.

The particle concentration can be adjusted with the volume air flow within a defined range of inlet pressure between 0.5 bar and 1 bar over pressure, which is governed by the choke limit of the jets and the required jet intensity for particle generation. Other than by the method described the concentration can only be decreased by dilution of the air supply. By adding Laskin nozzles the particle production can be increased. The seeding generation is equipped with 40 Laskin nozzles. Fig. 3.4 (a) and (b) shows the schematic of the laskin nozzles

The main flow is seeded using an in-house developed seeding generator shown in Fig. 3.4 (c) and (d). The generator consists of a pressure vessel with a spray nozzle blowing horizontally into the vessel. DEHS is drawn from the pressure vessel reservoir by the low static pressure of the entraining gas jet and forms a liquid spray. The spray nozzle produces a polydisperse spray. Large droplets are removed with the aid of an impactor, consisting of a plate in front of the aerosol outlet.

The particle concentration proved to be constantly high, independent of pressure levels at the inlet and outlet of the generation. The distribution of particles size is spread slightly wider
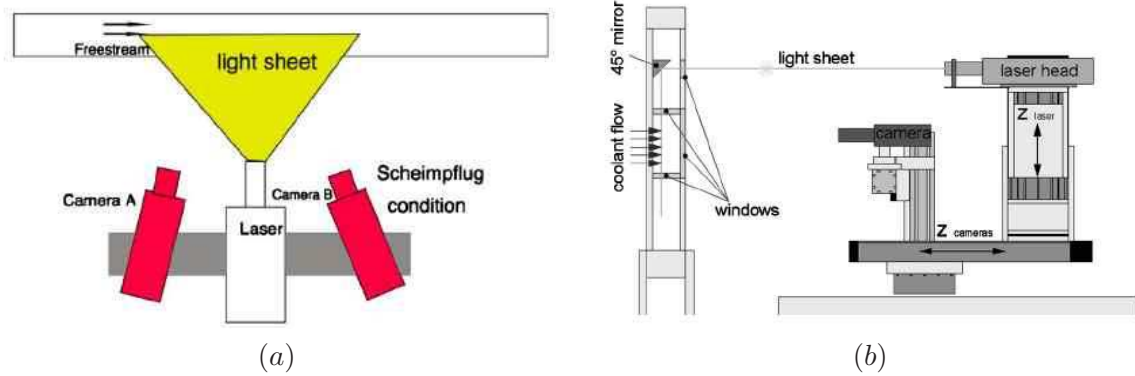
Figure 3.5: Setup of the PIV system (a) Top View (b) Side View

than the one of the DLR seeder, the average diameter is about 1 μm bigger. The mean particle diameter is 4.60 μm, the largest particles are smaller than 6 μm, the smallest relevant particles are larger than 2.5 μm.

3.1.3 PIV Setup

The arrangement of the laser head, cameras, traverse system and test section is shown in Fig. 3.5. A massive cast iron table stands in front of the section of the wind tunnel. This table supports the PIV traverse system. One axis translates the assembly of cameras and laser head parallel to the main flow direction X. The second axis translates the assembly towards the test section, in Z direction. The third axis translates the laser head in vertical direction Z_{laser}. All three axis are aligned to the test section with an accuracy of ± 0.1 mm to ensure the validity of the global calibration approach.

Simultaneous traversing of the laser in vertical direction (Z_{laser} in Fig. 3.5 (b)) with traversing of the cameras in horizontal direction ($Z_{cameras}$) allows the scanning of the flow volume in Z-direction without the need of re-calibration for every light sheet position.

The cameras each rest on a Scheimpflug mount. This device, as shown in Fig. 3.6, is required as the cameras look at an angle on the object plane, the light sheet. Without such a mount the best plane of focus is parallel to the image sensor and not to the plane of the laser light sheet. Therefore the Scheimpflug principle is used. This arrangement where the object plane, the image plane (CCD-plane) and the plane of the imaging lens intersect at a common point realises complete focus at the image plane for all off-axis camera angles (see Figure 3.6).

The Scheimpflug mount makes it possible to tilt the CCD plane relative to the lens-plane around one axis (CCD-axis) and to rotate the connected whole camera set-up around the CCD-axis. The gap between the camera and the lens holder is enclosed by flexible bellows to prevent surrounding light from reaching the CCD-chip. The Scheimpflug arrangement like any other off-
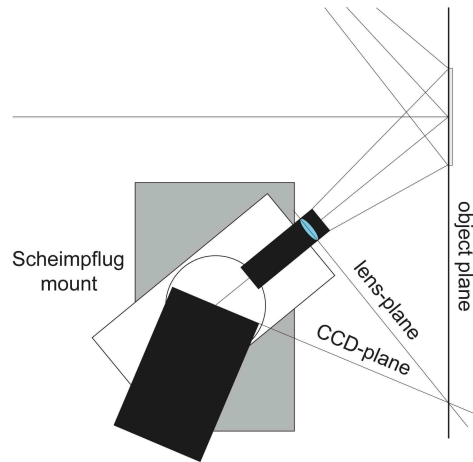
Figure 3.6: Scheimpflug mounting of the camera

axis arrangement introduces perspective distortion. This means that the velocity vectors have to be transformed to convert them from images to non-distorted fluid space velocity vectors. The height of the cameras is adjusted so they look at the centre of the test section. The angle of the cameras is adjusted so that a maximum overlap of both images is achieved. The focus of each camera is adjusted for each camera to obtain best focus on both sides of the centre of each image.

The laser head is mounted on a third traverse axis. The light sheet optics, which are directly connected with the laser, create a light sheet in *XY*-orientation with variable thickness. The lightsheet exits the optics in horizontal orientation and enters the wind tunnel through a 15 *mm* heat resistent quartz window. It then gets reflected downwards via a high precision surface coated silver mirror that is mounted at 45°inside the wind tunnel. The lightsheet enters the test section via another quartz window from top leaves via a third window at the bottom and gets finally dispersed in the cavity below the test section.

The alignment of the lasersheet parallel to the test section is of importance for the accuracy of the reconstruction of the 3D vectors from the two camera images. The positioning of the lightsheet is of importance for the reconstruction of the flow volume from the separate vector planes. The required laser sheet thickness is around twice the size of the interrogation area projected out in object space. The factor 2 is necessary to compensate for the Gaussian distribution of the light intensity.

Calibration The mapping of the displacements from the CCD-plane to the object plane in fluid space can be performed, provided it is known how points in the object plane are imaged onto the CCD-plane. This knowledge is acquired by the calibration procedure. The calibration uses a well defined grid of dots inserted in the test section. The calibration target is aligned with the light sheet and the cameras are traversed relative to the target in several positions.
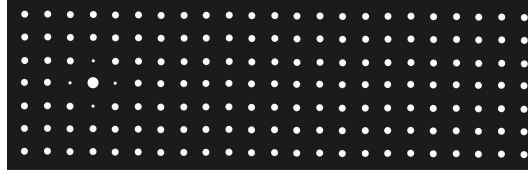
Figure 3.7: Target used for calibrating the cameras

The dots on the calibration target are used to calculate a linear calibration equation for each camera. The linear calibration will compensate for difference in scale and lack of ortogonality (e.g. perspective). An example of such an imaging model is the pinhole camera model, which based on geometrical optics leads to the so-called Direct Linear Transform (DLT):

$$
\begin{bmatrix} kx \\ ky \\ k \end{bmatrix} = \begin{bmatrix} A_{11} & A_{12} & A_{13} & A_{14} \\ A_{21} & A_{22} & A_{23} & A_{24} \\ A_{31} & A_{32} & A_{33} & A_{34} \end{bmatrix} \cdot \begin{bmatrix} X \\ Y \\ Z \\ 1 \end{bmatrix}
\tag{3.6}
$$

Here uppercase symbols X, Y and Z are used for object coordinates, and lowercase symbols x and y represent image coordinates. With imaging models based on physics, calibration coefficients can in principle be calculated from known angles, distances and so on. In practice, however, this approach is not feasible since in the actual experimental set-up in the laboratory it is very difficult to measure the relevant angles, distances and so on with sufficient accuracy. An experimental approach to camera calibration is therefore used. Images of a calibration target are recorded, which contain calibration markers whose true (X,Y,Z) positions are known. Comparing the known marker positions with the positions of their respective images in each camera image, the model paramters are calculated. The calibration target contains a grid of white dots on a black background. It is important to know the exact dot spacing since the grid defines the coordinate system. In the centre of the target is a larger dot surrounded by four smaller dots. By definition the larger dot is the origin of the coordinate system $(0,0,Z)$ and the common fixed point for the two cameras. The four smaller points identify the X- and the Y-axes. Therefore both cameras must be able to see the large dot surrounded by the four smaller ones. As the area of interest varies for the different measurements the calibration targets are self made according to the recommended guidelines by Dantec Dynamics. The target shown in Fig. 3.7 used for all the measurements of film cooling flow has a spacing of the dots of 5 mm, with a centre marker of 3 mm diameter, axis markers of 1 mm diameter and general markers of 2 mm diameter. The number of dots is 385.

In practice a typical calibration process is carried out by placing the calibration target such that the centre large diameter marker corresponds to the desired origin of coordinates. Then it is imaged by both cameras at five different wall-normal positions. The automated FlowManager
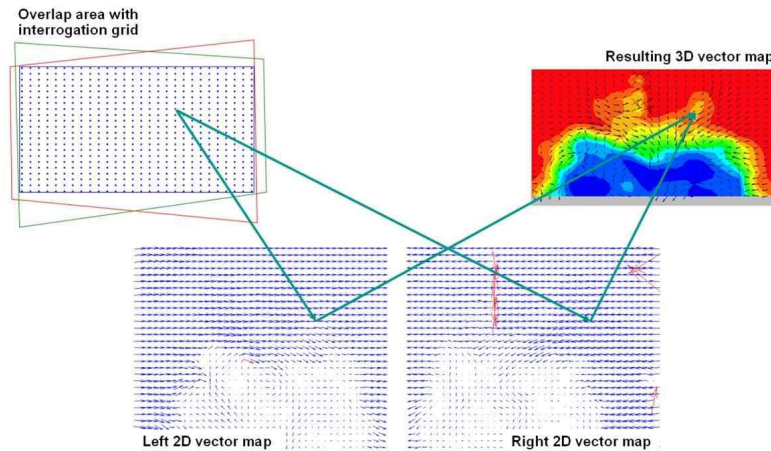
Figure 3.8: Conversion of images from 2D to 3D using FlowManager from Dantec Dynamics [32]

software from Dantec Dynamics [32] then computes the DLT and provides a calibration map. This calibration map when applied to raw velocity vectors as schematically shown in Fig. 3.8 obtains the overlap area and gives all three velocity vectors. With the present setup of straight windows and a rectangular test section it is possible to have a global approach of calibration, enabling a single calibration for all XY-positions of the set-up of cameras and laser head. The calibration is done once at any given location in X and Y direction and is assumed to be valid at all other X and Y locations. The difference of accuracy of the calibration at different X-positions changed less than 0.3%.

3.1.4   Image Processing

The production of velocity vectors from raw double images of particle seeded flows involves intricate post processing in order to capture the large dynamic range of 2 orders of magnitudes. The proprietary softwares FlowMap and FlowManager from Dantec Dynamics [32] contain all the various options which can be carried out by selecting the relevant parameters. These parameters are based on the considerations detailed in Raffel et al. [94].

First the recorded image is separated into interrogation areas. Initially no offset is introduced from the interrogation area in the first image frame to its respective counterpart in the second image frame. Second, the particles in these areas are detected. Third, the particle positions in the first frame are correlated with particle positions in the second frame. This leads to the initial vector map. Fourth, validation procedures are applied to detect and remove faulty vectors. The now obtained vectors are used as an estimate for the window offset for the next correlation. A new run is made, but this time with a smaller interrogation area. The main benefit derived from using the shifted window is capturing the particle images that left the interrogation area during the time between the two light pulses. Loss of these particles reduces signal strength and the

number of successful vectors that can be obtained. This adaptive procedure is performed twice with decreasing window size for each step, until the final interrogation area size of 32×32 pixels is reached. The results obtained proved to give very reliable data, reducing the negative influence of background reflection and non-uniform seeding density strongly.

Cross-Correlation   In PIV two sequential image maps are sub-sampled. The resolution of the sub-sampling is defined as an interrogation area and the interrogation areas from a regular array. Within these interrogation area samples, an average spatial shift of seeding particles may be observed from one sample to its counterpart in the second camera image, provided a flow is present in the illuminated plane. Based on the intensity of light in each interrogation a digital cross correlation is carried out. However, as some particles from the first frame would have exited the second interrogation frame due to high flow speed, the number of truly high cross correlation peaks are not captured. The noise is caused as small cross correlations are observed among different particles between the first and second frame. In order to increase this ratio, a shift in the interrogation area corresponding to the average shift due to the mean flow velocity is affected thereby increasing the chances of finding the same particle in the second interrogation area that was in the first one. The Nyquist sampling criterion associated with the discrete Fourier transform method of cross correlation used here, limits the maximum recoverable spatial displacement in any direction to half the window size in that direction. In reality even this displacement is often too large for the technique to work properly, since the signal-to-noise ratio in the cross-correlation decreases with increasing spatial shift. Given a window size of length N, a maximum particle displacement of $N/4$ is required to ensure a reasonable signal-to-noise ratio. Another important parameter influencing the signal-to-noise ratio is the number of seeding particles within each interrogation area. With a large number of seeding particles, there will be many true correlations ensuring a high signal-to-noise ratio, and in this case an average displacement exceeding $N/4$ may be accepted. With a relatively small number of particles within the interrogation area, the signal-to-noise ratio will decrease, and a minimum of 5 particles/region is required in the software to achieve reasonable results using the cross-correlation technique. The manual of the FlowManager hand book by Dantec Dynamics [32] explains the algorithms used to detect the particles. Then using sub-pixel interpolation and correction the raw vectors are corrected.

Adaptive Correlation   The fundamental principle of the adaptive correlation is an iterative procedure: From an initial guessed value, an offset is introduced from the first window (the interrogation area in the image frame from laser pulse one) to the second window. The obtained vector is validated and is used as a new estimate for the window offset. A new run is made, but this time with a smaller interrogation area. The main benefit derived from using the shifted window is capturing the particle images that left the interrogation area during the time between the two light pulses. Capturing more particle images for each vector permits the interrogation

area to be refined while still obtaining an adequate number of successful vectors without increasing the seeding density in the flow. Using adaptive correlation helps in two ways. First, the signal strength is raised due to the capture of the in-plane dropout. Secondly, a refinement of the interrogation area is possible because an adaptive window offset may be applied, again producing a successful signal.

Window Functions   As Fast Fourier Transforms (FFT) are used to calculate the cross correlation for speed, the method assumes a cyclical input particle pattern. This means that at the edges of the interrogation areas an artifact high cross correlation peak might be recorded due to phantom particles and phantom correlations. A particle's initial position within the interrogation area is correctly correlated with its own image in the next one, but due to the FFT usage it is also correlated with a phantom particle near the edge. This problem is ameliorated by using a windowing function. A spatially Gaussian distribution of weights is used which reduces the intensity at the edges where this problem is stark and increases the intensity in the middle. Since window functions effectively do not use the information near the edges of an interrogation area, interrogation areas are overlapped. The information not used in one interrogation area will thus be used in a different interrogation area, which partly overlaps the first. Overlap applies in both the horizontal and the vertical direction. Without overlapping there is a risk of not using information near interrogation area edges due to loss-of-pairs. Near interrogation area edges it is possible, that either the initial or the final particle position will be outside the interrogation area. Thus, particles near the edges are unlikely to contribute to the velocity calculation. Overlapping interrogation areas increase the chance that all particle pairs are completely within at least one interrogation area. Processing with overlap also produce more vectors, but this does not mean an increase in the fundamental spatial resolution rather than an over-sampling of the flow field. This over-sampling produces additional vectors as suitable interpolations, which are of great help when calculating derived quantities from the vector map. It is better for such "interpolations" to have been produced by over sampling the raw camera images rather than by an artificial interpolation process. The only drawback of overlapping interrogation areas is the processing time, which will increase in proportion to the number of vectors generated.

Dynamic Range and Spatial Resolution   The dynamic range in a PIV measurement may be defined as mean velocity divided by the accuracy of the measurement. Based on a pixel displacement level, it is the displacement divided by the sub-pixel accuracy. For a recording using 32×32 pixel interrogation areas, the displacement is typically 8 pixels. This corresponds to a displacement where the time between the two light pulses is chosen so the displacement is approximately 25% of the interrogation area. The sub-pixel accuracy is a function of many parameters, most of which are beyond the PIV system itself and therefore often unknown. As a rule-of-thumb 0.1 pixel accuracy is a realistic value for a real particle seeded flows with a non-laboratory optical access. This results in a dynamic range of $8/0.1 = 80$.

Zero-Velocity Biasing In PIV there is a tendency to bias measurements toward zero. This is a problem that is worsened with increasing displacements and decreasing seeding density. The problem can be minimased by ensuring that there are always at least 5 seeding particles within each interrogation area. One of the reasons for the zero-velocity biasing is loss-of-pairs. Seeding particles, which move fast, are more likely to have their initial of final position outside the interrogation area, than particles moving slowly. As a result the slow particles will dominate the calculation of average particle displacement and effectively bias results towards zero.

Another reason for zero velocity biasing is the correlation technique itself. The general correlation theory assumes correlation areas to be of infinite size, but in reality interrogation areas are of finite size, and this makes the technique more sensitive to small displacements than large ones. Using an offset of the second interrogation area is another way of reducing the bias. Ideally the selected offset should correspond to the average particle displacement. In this case loss-of-pairs will be minimised, since it will cancel the effect of in-plane motion, leaving out-of-plane motion as the only remaining cause for the problem. Furthermore the optimal offset will ensure that the correct particle displacement will correspond to 100% overlap between the first and the second interrogation area, which is where the correlation technique is most sensitive. If you calculate velocities as an average of several vector maps, outliers will also bias the result towards zero and artificially increase the calculated RMS-values. Outliers are vectors in the vector map, which do not represent true particle displacements. They are a result of random correlations, which have drowned out the true correlation peak because in this particular interrogation area the signal-to-noise ratio is too low. Outliers tend to be longer than the true velocity vectors, but random in direction. This means that the average of several outliers will be zero, while the spread will be large, and this is why the outliers bias measurements towards zero and increase the RMS-value.

3.1.5 Validation

Outliers are incorrect vectors resulting from noise peaks in the correlation function. They may occur in almost any PIV measurement. With FFT-processing it is important to note there will always be an outcome whether the input is meaningful or not. One conceptual difference between the FFT-processing in Particle Image Velocimetry compared to Laser Doppler Anemometry is that in LSA signal conditioners are essentially used to ensure there is a meaningful input. This is possible because it is a time based measurement technique and so you can wait for the input. However, since PIV is an instantaneous measurement technique, all spatial information is sampled at the same time and there is a finite statistical probability there will be some regions where there is really no meaningful input. Therefore, it is necessary to subsequently validate the PIV vector map.

Two validation methods are applied. They are:

- peak height ratios

- moving average (a continuity-type method)

The purpose of validation methods is to recognize, reject and remove these outliers and possibly substitute other vectors instead of the rejected vectors. The reason for removing the outliers is that they might seriously bias the subsequent analysis of the measurement. Substituting a rejected vector with another might appear as some kind of trickery; however, the substitution is not necessarily an arbitrary process. The substituited vector is estimated from the surrounding measured vectors. Thus, the substitution of the rejected vectors is similar to removing noise from a signal by filtering it. The reason to substitute rejected vectors is largely because many subsequent calculation methods require a vector in every point but also for the visual appearance.

Peak Validation   Peak-height validation validates or rejects individual vectors based on the values of the peak heights in the correlation plane where the vector displacement was measured. The highest and the second highest peak in the correlation plane are detected.

The more particles match, the more certain a velocity will be and the higher the measured correlation peak will be. The minimum allowed ratio between the highest peak and the second highest peak is defined by:

$$\frac{highest \ \ peak}{second \ \ highest \ \ peak} \geq k$$

This assumes the measured peak is a signal and the second highest peak is merely noise and the signal should exceed the noise. Thus, if the signal-to-noise ratio is less than a certain threshold the vector is rejected. This criterion is know as the detectability criterion.

Moving Average Validation   Moving-average validation validates or rejects vectors based on a comparison between neighbouring vectors. The rejected vectors may be replaced by vectors estimated from surrounding values. Continuity of the flow field's behaviour is an implicit assumption in the moving-average validation method.

Moving-average validation is a special case of the general class of iterative filtered validation. In moving-average validation the average of the vectors in a rectangular neighbourhood of a vector is calculated and compared with the vector. Consider the vector at position (x, y). If the neighbourhood is of size (m, n), the average is calculated by the formula:

$$\overline{v}(x,y) = \frac{1}{mn} \sum_{i=x-\frac{m-1}{2}}^{i=x+\frac{m-1}{2}} \sum_{j=y-\frac{n-1}{2}}^{j=y+\frac{n-1}{2}} v(i,j) \tag{3.7}$$

The vector is the rejected if:

$$||v(x,y) - \overline{v}(x,y)|| > k \tag{3.8}$$

where k is a variable and the norm is the usual vector distance, i.e.:

$$||v(x,y) - \overline{v}(x,y)|| = \sqrt{\left(v(x,y)_x - \overline{v}(x,y)_x\right)^2 + \left(v(x,y)_y - \overline{v}(x,y)_y\right)^2} \tag{3.9}$$

The idea behind this approach is that the velocity field is slowly changing so that there is not too much change from a vector to its neighbour vectors. In other words, there is a correlation between neighbouring vectors, or equivalently, the vector field is essentially over-sampled. Thus, if a vector deviates too much from its neighbours, it must be an outlier. In the moving average validation calculation method the number k is not given directly. Instead some further calculations are done. First the difference:

$$||v(x,y) - \overline{v}(x,y)|| \tag{3.10}$$

is calculated in all points (x,y) of the grid. The maximum:

$$\max_{x,y} ||v(x,y) - \overline{v}(x,y)|| \tag{3.11}$$

of these is found , and finally k is calculated by:

$$k = \alpha \cdot \max_{x,y} ||v(x,y) - \overline{v}(x,y)|| \tag{3.12}$$

Thus, all vectors that deviate more than a certain percentage of the maximum deviation are rejected. If the acceptance factor α is set to 1, all vectors are validated, while, if it is set to 0, all vectors are rejected. If a vector is rejected, it is replaced by the local average $\overline{v}(x,y)$ in the equation above. The acceptance factor is not a physical parameter; it cannot be given a physical interpretation, and no natural value, related to the flow, can be given. A good choice usually is in the range 0.01-0.1 (for our measurements were set to 0.07). The lower the value, the more vectors will be rejected, and it should be set at least so low that all visible outliers are removed. However, as substitution is used, it is not a critical parameter. If it is set too low, so that some vectors that are actually not outliers are rejected, but the vector that substitues them will be very close to the rejected vector. Therefore, no harm has been done.

To improve the performance of the method an iterative approach is adopted. During the first iteration the most deviating vectors are removed, during the next iteration those a little less deviating are removed and so on. In general, the more iterations are used, the better the method will work, but at the expense of execution time.

3.2 Infrared Thermography

Accurate point measurements of wall temperatures have traditionally been carried out by intrusive devices like contact thermometers, thin film sensors, wall mounted thermocouples etc. However of late due to advancements in infrared sensing and imaging instruments which have made them light weight, easy to use and rugged compared to similar instruments just a few years ago, they are taking up an outstanding place in research laboratories as a measurement device. According to Kaplan [64] the main advantages for using noncontact thermal measurement are given below.

Target in motion Moving targets interfere with the measurement process due to errors from bouncing, rolling etc.

Target electrically conducting Current-conducting equipment and components present a hazard to personnel and instruments alike. Infrared sensors place both out of harms way.

Target fragile If the target is too fragile to be mounted with contact sensors or those sensors would disturb the conditions of the flow then non-intrusive measurements are essential.

Target small When the local measurement area is small enough such that a sensor would conduct away enough heat to change the property being measured an infrared sensor.

Target remote If a target is inaccessible by contact sensors then infrared is the only option.

Target destructive to thermocouples In high temperatures, aggressive environments, thermocouples may become destroyed easily due to burning or erosion.

Multiple measurements required When many points on a target are needed to be measured, especially for full-field measurements, an infrared sensor provides a much cheaper, easier and less cumbersome option than positioning many thermocouples over a target. If the optics are optimised then an infrared sensor can provide a resolution an order of magnitude higher than any comparable sensor.

The only disadvantages of infrared sensing instruments is their relatively higher cost and complexity. Also, because of the fact that the ambient medium may participate in the radiation process, a good calibration is required.

3.2.1 Basic Principles

A simple and practical explanation covering the basics of infrared thermography usage for heat transfer laboratory measurements is given in Buchlin [19].

As soon as the temperature of a body, T exceeds absolute zero, the molecular agitation within the matter results in electromagnetic radiation. The energy released within this radiation increases as the body temperature rises. As an example, the energy of a photon W is related to the wavelength of the radiation, λ by Eq. 3.13. Here c is the speed of light, λ is the wavelength and h_p is the Planck's constant, $h_p = 6.6 \times 10^{-34} \ m^2 kg/s$.

$$W = \frac{h_p c}{\lambda} \tag{3.13}$$

Depending on the material and the conditions the emitted radiation can cover a large continuous range of wavelengths or the energy can be divided into several wave bands of a discrete spectrum. As shown in Fig. 3.9 the wavelength spans a few Angstroms in cosmic radiation to radio waves
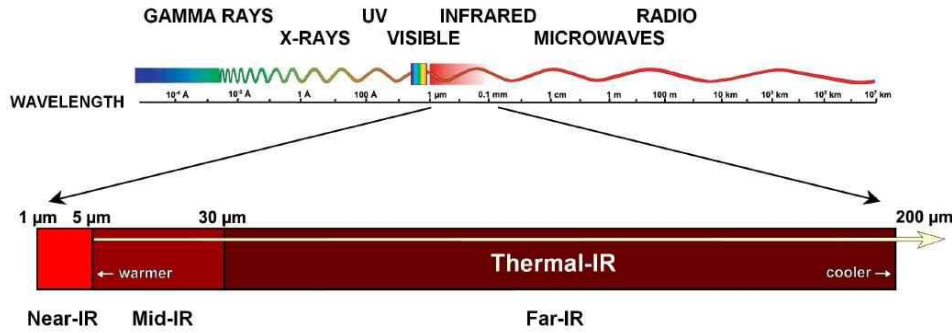
Figure 3.9: Spectrum of electromagnetic radiation showing the infrared band

of 100 km. The electromagnetic spectrum that carries thermal energy is confined to the range $0.1 \leq \lambda \leq 1000\mu m$. Within this the visible range is between 0.4 to 0.7 μm and the infrared spectrum from 0.7 to 1000 μm. Conventionally the infrared spectrum is also sub-divided into the near-infrared or short wave (SW), the mid-infrared or medium wave (MW) and far-infrared or long wave (LW) as shown in Fig. 3.9. Thus, infrared thermography consists of capturing the invisible thermal radiation and transforming it into a visible or grey-scale images. In this sense, the infrared sensor is a detector that converts an incident electromagnetic flux into an electric signal to be adequately treated to yield the temperature of the observed body.

Radiation Exchange

Thermal infrared radiation leaving a surface is called radiosity. It can be emitted from the surface, reflected off it or transmitted through it. Although the total radiosity is equal to the sum of these components, the surface temperature is only related to the emitted component. Kirchoff's law states that the percentage sum of the three components is unity as shown in Eq. 3.14.

$$\alpha + \rho + \tau = 1 \tag{3.14}$$

These percentages or ratios are called absorptivity, α, (this is the same as emissivity, ϵ), reflectance, ρ and transmittance, τ. The description of thermal radiation relies on the concept of a blackbody. In thermodynamic equilibrium, a blackbody is a perfect radiator and it will absorb all the radiant energy of the incident illumination whatever is the wavelength. As a perfect thermal emitter, it will then re-emit all the energy. The spectral distribution of the emissive power of a blackbody emitting in a vacuum is given as a function of wavelength and blackbody's absolute temperature. This relation is known as the Planck's law and given by Eq. 3.16. Here, c is the
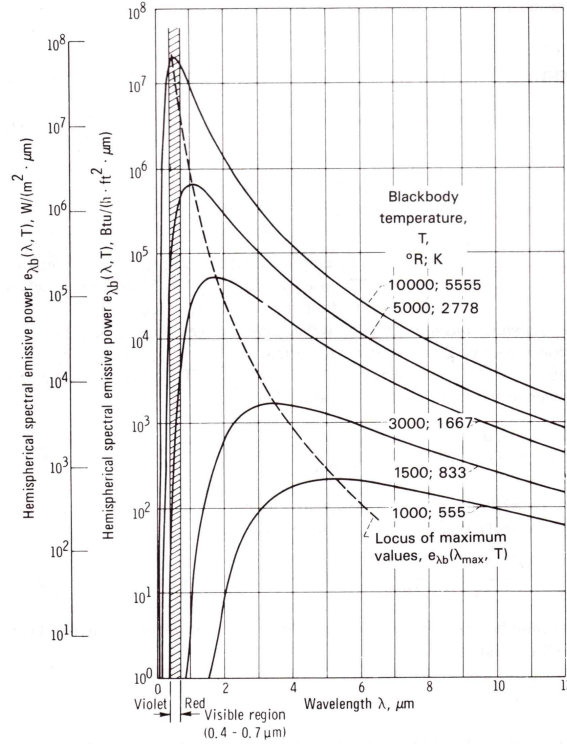
Figure 3.10: Hemispherical spectral emissive power of blackbody for several different temperatures, from Siegel and Howell [101]

speed of light and k_b is the Boltzmann's constant, $k_b = 1.3807 \times 10^{-23}$ J/K.

$$M(\lambda, T) = \frac{C_1}{\lambda^5 \left(e^{\frac{C_2}{\lambda T}} - 1 \right)} \tag{3.15}$$

$$C_1 = 2\pi h_p c^2 \tag{3.16}$$

$$C_2 = \frac{h_p c}{k_b} \tag{3.17}$$

The Planck's law is shown graphically in Fig. 3.10 which is extracted from Siegel and Howell [101]. The dotted line shows the maxima of the emitted power. This maxima follows the Wien's displacement law given by:

$$\lambda_{max}[\mu m] = \frac{e_{\lambda b}}{T} = \frac{2898}{T} \tag{3.18}$$

Emissivity

Real bodies do not behave exactly as a black body. If Eq. 3.16 is integrated over all wavelengths than the blackbody emissive power would only depend on the temperature. However a gray body would have a slightly lesser emissive power. The ratio of the effective emissive power
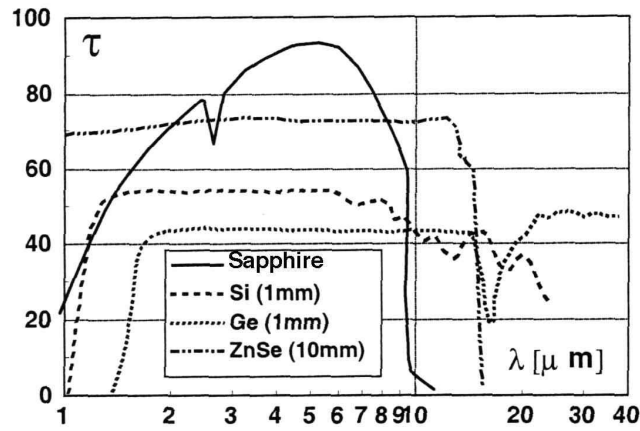
Figure 3.11: Spectral transmittance of Infrared transmitting materials

between a grey body and a blackbody is denoted as emissivity, ϵ. This is given in Eq. 3.19 where $\sigma = 5.67 \times 10^{-8} W / \left(m^2 . K^4 \right)$ is the Stefan-Boltzmann constant.

$$M(T) = \epsilon \sigma T^4 \tag{3.19}$$

For an infrared camera to get the best possible emitted signal with maximally reduced reflective component, the surface should be treated with a layer which has an emissivity of close to 1. Typically, black paints are applied with wavelength independent emissivities at normal test temperatures $T < 500K$ which are $\epsilon = 0.96 - 0.98$.

Transmitting Medium

In wind tunnel experiments an optical access is typically made by using glass or plexiglas windows. However for infrared radiation this is not applicable as glass does not transmit infrared radiation of wavelengths higher than 4 micron. Again a transmitting medium with more or less constant transmittance over required wavelengths and high transmittance, τ are essential for establishing a strong signal in the infrared detector. Figure 3.11 shows the transmission characteristics of most commonly used infrared transmitting materials.

The transmittance characteristics of Zinc Selenide (ZnSe) are largely wavelength independent and constantly high in the mid wave infrared range. It is important to match the transmittance characteristics of the window with the infrared detector. Sapphire is quite expensive and is mainly used for detectors in the short wave range. Other materials like silicon, germanium, calcium flouride etc are quite brittle and fragile. Zinc Selenide is typically grown as a crystal with specialized equipment but can then be cut and polished to a desired shape. Once it is coated
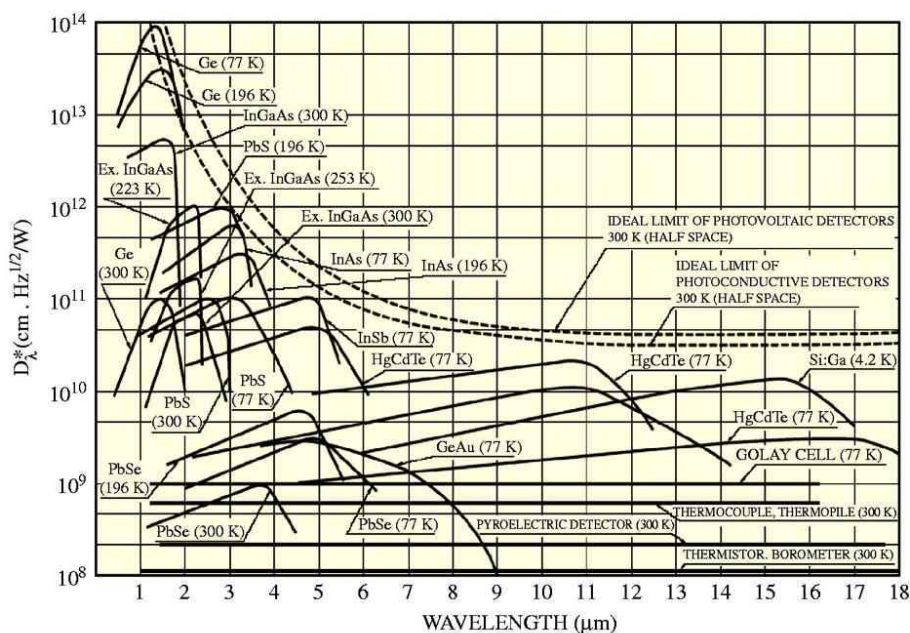
Figure 3.12: Characteristic sensitivity of various infrared detecting materials and their spectral range of operation from Liu and Yang [80]

with an antireflective coating for a desired wavelength band, the transmittance characteristics shown in Fig. 3.11 can be increased to around 0.96.

Infrared Camera

For many years the cost of ownership of an infrared detector was very high due to the complex materials like InSb, HgCdTe etc that could be used as infrared detectors and the associated cooling cycles required. The recent developments in thin film based infrared detectors called microbolometers (see Deb et al. [33]) has significantly reduced this cost, making infrared thermography an economically viable method not only for research and development but also for online monitoring and control. Every detector has a particular spectral band within which it detects infra red radiation. A comparison is shown in Fig. 3.12 which was published originally by Liu and Yang [80].

The camera used in the research shown here is a Focal Plane Array microbolometer based, uncooled camera manufactured by Jenoptik known by its catalogue name, VarioCAM Head. The spectral response of these detectors is from 7.5 to 14 μm. The transmitting medium is matched with the detector spectral response in that it transmits in the same wavelength range. Infrared radiation strikes the detector material known as a microbolometer, heating it, and thus changing its electrical resistance. This resistance change is measured and processed into temperatures which can be used to create an image. Unlike other types of infrared detecting

equipment, microbolometers do not require cooling. These detectors are pre-calibrated by the manufacturer and the camera works with its proprietary software which uses algorithms to make corrections for emissivity, atmospheric temperatures, transmitting medium temperatures. The camera has a stated uncertainty of ± 2 K and a radiation integration time of 0.02 sec. This means that the camera is limited to a 50 Hz recording rate and hence cannot be used for high speed measurements.

As the infrared signature from the test section can be significantly affected by various factors like ambient temperature and reflections as well as the unknown calibration factors within the camera itself which converts radiation signal to electrical signal, it is imperative to perform *in situ* calibration within the test section at similar temperature ranges of operation. The methodology is similar to that used by Dittmar et al. [36] where an intrusive sensor is imaged by an infrared camera at different temperatures and a non-linear fit is applied to convert the infrared readout temperature to the true temperature measured by the thermocouple. In order to have a very thin temperature sensor, a thin film sensor called Senflex manufactured by Tao Systems was used. The thin film sensors are first calibrated with all the leads attached and then affixed onto the measurement plate painted with black paint. The infrared camera can then be calibrated. It is important that a calibration is carried out over all the temperatures that the infrared camera would be expected to detect. Since the relationship between temperature readout and incident radiation is non-linear, a linear extrapolation would significantly affect accuracy.

Apart from the calibration correction, other corrections to the final thermogram required are the corrections due to reflection of the camera itself which distorts the final picture as the camera sees itself. These corrections can be made by imaging a surface of constant temperature without any air flow with the infrared temperature to calculate the background radiation. Additionally multiple reflections from the wind tunnel walls should be reduced by painting them with highly absorbent black paint.

3.2.2 Radiation Correction

The corrections mentioned in the previous section relate to calculating the temperature from an infrared device in the most accurate manner possible. However, the final aim of the temperature measurement is to derive the heat transfer coefficient and from then on the adiabatic effectiveness of cooling. For this information the convective heat transfer coefficient should be calculated. This requires solving the heat balance on the measurement surface. Typically the heat balance is measured by equating the conduction through the substance with the convection from the solid to the fluid, i.e., $\dot{q}_{cond} = \dot{q}_{conv}$. As Fig. 3.13 shows radiation heat transfer must also be accounted for. The radiant heat transfer could be because of irradiation on to the surface from the other wind tunnel components, as well as reflection and heat transfer due to radiation.

The entire wind tunnel section was modeled in CFX Radiation by Vidakovic [104] and divided into discrete elements for a Monte Carlo simulation at laboratory representative conditions to
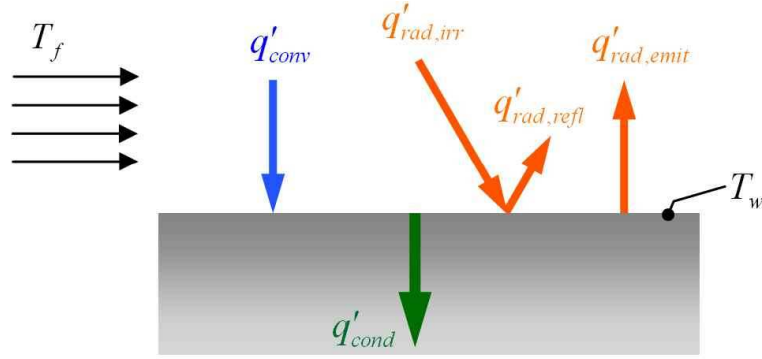
**Figure 3.13:** Schematic of heat balance on the measurement surface

estimate the extent of heat transfer correction required. These simulations were also compared with an analytical method known as the Radiosity method (Siegel and Howell [101]), where the view factors between various interacting components are analytically determined and the radiation energy is analytically calculated according to the temperatures and view factors. The difference in prediction between the Monte Carlo particle tracking methods from the analytical solution was less than 1% of the total heat flux calculated. The study also concluded that for the present configuration and relatively lower operating temperatures until 120°C the radiant heat transfer was 2% of the total heat flux. Calculating the radiation correction for every measurement using radiosity method proves to be extremely time consuming and does not give a marked increase in accuracy for the small radiation correction which can be estimated by Eq. 3.20. Here, the heat flux per unit area $\dot{q}_{rad}$ can be estimated by the Stefan-Boltzmann's law. T_a is the average ambient temperature when the test is being conducted and T_w is the wall temperature.

$$\dot{q}_{rad} = \sigma\epsilon \left(T_w^4 - T_a^4 \right) \tag{3.20}$$

3.3   Fast Response Entropy Probe

3.3.1   Construction

As film cooling involves injecting a jet of cold air into a freestream, the associated mixing causes loss in performance. Quantifying this loss is also necessary for a holistic understanding of film cooling approaches. According to Denton [34] the only comprehensive indicator of loss is the change in entropy. Measuring entropy change requires simultaneous pressure and temperature measurements. This is achieved by using a novel intrusive probe measurement technique known as the Fast Response Entropy Probe (FENT) developed in-house at the ETH Zurich. Comprehensive details are available in Mansour [83]. A close-up photograph is shown in Fig. 3.14.
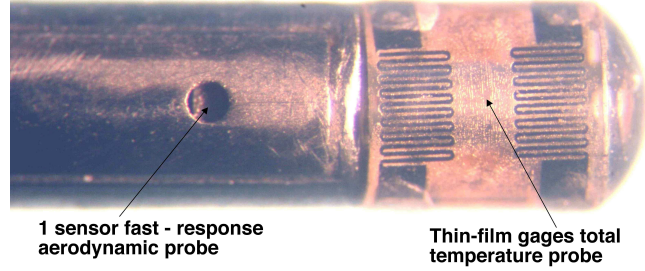
Figure 3.14: Close-up photograph of the Fast Response Entropy Probe (FENT). Diamater of head is
1.8 mm

The principal components of the FENT probe are a fast response aerodynamic probe (FRAP)
and an unsteady total temperature probe. The diameter of the cylindrical probe is 1.8mm. The
design, manufacture and calibration of FRAP is well established at ETH Zurich and detailed in
Kupferschmied et al. [69, 70], Pfau [90], Schlienger [98]. The FRAP is comprised of a miniature
silicon piezoresistive chip, working on the principal of the Wheatstone bridge, which is glued
beneath a pressure tap to measure the unsteady total pressure. The basic element of the unsteady
total temperature probe is a pair of thin-film gages that are deposited onto a semi-cylindrical
fused quartz substrate. The thin-film gages are made of 200nm-thick nickel and are operated as
resistance thermometers. The serpentine shaped sensor is $30\mu m$ wide and covers a rectangular
area of $0.55mm \times 0.85mm$. When the thin-film gauges are electrically heated to two different
temperatures, $T_{f,1}$ and $T_{f,2}$, the convective heat transfer can be expressed as follows:

$$q''_{conv1} = h (T_0 - T_{f,1}) \tag{3.21}$$
$$q''_{conv2} = h (T_0 - T_{f,2}) \tag{3.22}$$

The total temperature T_0 of the flow can therefore be determined by eliminating the heat transfer
coefficient, h between the two equations through Eq. 3.23.

$$T_0 = T_{f,1} + \frac{q''_{conv1} (T_{f,2} - T_{f,1})}{q''_{conv1} - q''_{conv2}} \tag{3.23}$$

The Joulean heating of the thin-film gages is balanced by the conductive and convective heat
losses. Thus the convective heat transfer for each gage is given by Eq. 3.24

$$q''_{conv} = VI - q''_{cond} \tag{3.24}$$

The thin-film gages are operated in a constant current mode, and thus the first term on the
right-hand side of Eq. 3.24 is readily determined. On the other hand, the second term on the
right-hand-side of Eq. 3.24 is estimated using an unsteady, semi-infinite, heat conduction model.

The bandwidth of the conduction model used in the present work is 400Hz to 120kHz with a phase shift of less than 5°. However the FRAP that is integral to the FENT probe limits the bandwidth of the FENT probe to 48 kHz. Pressure and temperature signals are acquired simultaneously at a frequency of 100 kHz over a period of 2 seconds. The offset between the thin-film gauges and the pressure sensor is 2.25mm In the data processing coincident phase-locked measurements of 250 samples of P_0 and T_0 are used to determine the unsteady relative entropy. Therefore when phase-locked averaged data are considered, the spatial resolution of the measurements is given by the area covered by the thin film gages, which is $0.85mm \times 1.77mm$. The probe is calibrated for temperature in a calibration oven and for yaw and pitch angles measurements of the pressure sensor in a freejet calibration facility using aerodynamic calibration models described in Mansour [83].

Chapter 4

Experimental Methodology

The current research involves multiple measurement techniques as was described in Chapter 3. These measurement techniques are used to measure the primary quantities like velocity, surface temperature, pressure etc. However, for the complex flow structure - heat transfer problem studied herein, these quantities need to be reduced to comparable and representative derived quantities. The velocity measurement through 3-D stereoscopic PIV is more or less straight forward. Once a 3-D velocity field is obtained using the parameters described in Section 3.1, local gradients can be calculated to provide the local vorticity from the velocity. Data reduction for temperature measurements requires some effort as the quantities of interest, namely adiabatic effectiveness and temperature independent heat transfer coefficient cannot be directly measured but only derived from well-controlled experimental conditions and raw temperature data. The derivation of loss coefficients for aero-thermodynamic loss measurements, requires suitable data reduction of voltages obtained from the pressure and temperature sensors with respect to their individual calibration files.

4.1   Conducting PIV Measurements

The cameras and lasers are first set up and focussed correctly. Before the experiment starts a sandpaper is used as a virtual object and the cameras are traversed to create a virtual flow of 100 m/s and the entire cross correlation procedure is run to validate the flow vectors. The flow conditions are set after an initial warm up period of the wind tunnel and the seeding is turned on. Care is taken to avoid reflections, by surrounding the entire PIV arrangement and optical access by black sheets and shutting off all illumination from external sources.

Once the flow is established, double pictures are taken separated by a time step of $2.5\mu s$. The corresponding displacement between two frames of a seeding particle traveling with the freestream velocity of 110 m/s is close to 8 pixels. The cameras are adjusted so that they look at the same area of the flow. The light sheet which is parallel to the XY coordinates is set to have a

defined thickness of 1 mm by changing the focussing of the cylindrical lens used in the optical attachment. The calibration is performed with the aid of a single layer calibration target. Both cameras take pictures of the target in 5 distances orthogonal to it. The PIV software detects the points and determines a linear transformation matrix for each camera. This matrix allows the transformation of pixel locations into a flow coordinate system and also for transforming the 2D vector maps into 3-D flow vectors. A single 3-D flow picture typically covers a span of 8 hole diameters laterally and 9 hole diameters in the streamwise direction. Depending on the magnification desired, this span can be changed.

In order to have a reasonable average, 50 double frames are shot for each wall-normal plane and then averaged to provide the 2-D flow vectors. The contrast is improved and background reflections negated by subtracting the average from each double frame and only then subjecting the frames to the cross-correlation procedure described in Section 3.1.4. The final cross-correlation on each image pair is performed with a 32×32 pixel interrogation window. A 50% overlap of the windowing interrogation areas is used to capture out of plane particles. A 1-step iterative refinement of the interrogation are with deforming windows is used along with a high accuracy sub-pixel refinement procedure. A peak validation algorithm is applied with a ratio between the minimum admissible peak height and the second peak of 1.1. A local moving average validation over 3×3 vectors with an acceptance factor of 0.1 is chosen as a local neighborhood validation. A Gaussian weighting function is applied to each interrogation area to deal with the particles at the border of the area which would tend to create a zero velocity bias when they would leave the plane. The flow field is scanned with the camera and laser sheets in the Z direction with steps of 1 mm.

The unsteady measurements are conducted in a similar way, except that the camera and lasers are triggered to using an optical signal from the rotating pulsator. The entire phase is divided in 12 or 8 phases as the smallest time difference that could be set was 0.01 μs. Pictures taken after a predetermined time are grouped together and averaged to create phase-averaged velocity flow fields. The velocity flow field is non-dimensionalised by the inlet free stream velocity, U_m or U_h where h stands for hot stream. All distances are normalized by the hole diameter.

The vorticity in the three cardinal directions is calculated from the 3-D velocity flow field by the following equations.

$$V_x = \frac{\partial W}{\partial Y} - \frac{\partial V}{\partial Z} \tag{4.1}$$

$$V_y = \frac{\partial U}{\partial Z} - \frac{\partial W}{\partial X} \tag{4.2}$$

$$V_z = \frac{\partial V}{\partial X} - \frac{\partial U}{\partial Y} \tag{4.3}$$

This vorticity is also normalized as it is made up of non-dimensionalised velocity and coordinates.

4.1.1 Uncertainty Analysis

The accuracy of the velocity measurement technique can be established in two parts as suggested by Bernsdorf [12]. First an experiment is conducted that allows the estimation of the accuracy of the measurement chain from the light scattered by the seeding particles to the ready processed 3D-vectors field. This includes errors due optics, calibration, correlation and validation. The fact that the seeding particles are of finite size and have a significantly higher density than the fluid leads to additional errors in the measurement of accelerated flow. The effect of vortical acceleration and of fluctuations of the flow are considered in the second part of the error analysis.

Measurement Chain
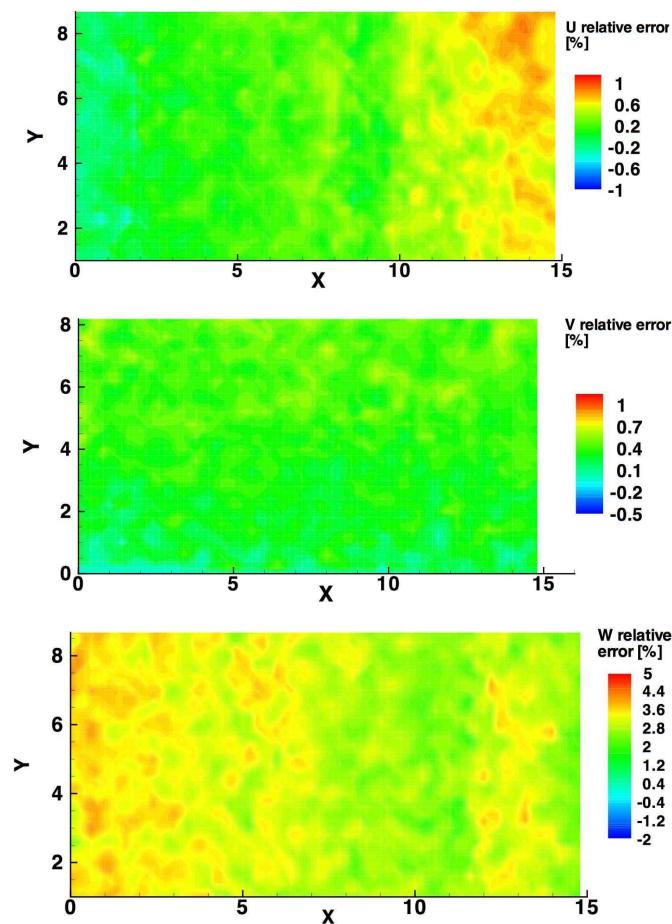
Figure 4.1: The relative random uncertainty in U, V and W [%] for typical PIV measurements

Establishing the accuracy of the measurement chain from raw picture to a 3D-vector field is done with the aid a simple experiment. Sandpaper is placed onto the test surface and lit in a diffuse

way. That way the sendpaper appears to the cameras as a field of seeding particles. The cameras are then traversed relative to the sandpaper over 1 mm while taking the double picture. The timing is set by hand to 10 μs between the two frames, thus creating a virtual velocity of 100 m/s in one direction and 0 m/s in the other directions. The plots showing the local variations in uncertainty of velocity measurements is shown in Fig. 4.1 The relative accuracy obtained with the measurement chain is of order of 1% for the velocities in u and v in respective directions x and y and of order of 4% for the velocity w in z-direction.

Tracking Behaviour of Seeding Particles

The total accuracy of the velocity measurement is influenced by further aspects. The slip between particles and flow due to the difference in density and the finite particle size results in a difference between the flow velocity and the measured particle velocity if the flow is accelerated. The major accelerations present are due to the vortical movement in the kidney vortices and the periodic pulsation of the cooling flow.

Particle Behaviour in a Vortex Structure

Seeding particles of higher density than the fluid are difficult to feed into high intensity vortices as centrifugal forces drive them outwards. A lack of particles occurs in the vortex core. The outwards drift can be estimated for the case of a forced vortex with zero radial fluid velocity in which particles obeying Stokes drag law have reached the tangential fluid velocity. The tangential velocity of a solid body rotation will be calculated as the product of angular velocity ω and the distance from the core R:

$$v_t = \omega R \tag{4.4}$$

Equating the Stokes force and the centrifugal force leads to a formula for the radial velocity v_r.

$$\underbrace{R\frac{1}{6}\pi\omega^2\rho_p d_p^3}_{centrifugal\ force} = \underbrace{3\pi\mu d_p v_r}_{Stokes\ force} \tag{4.5}$$

which can be rewritten as:

$$v_r = \frac{R\omega^2 d_p^2 \rho_p^2}{18\mu} \tag{4.6}$$

The ratio of v_r and v_t is given by:

$$\frac{v_r}{v_t} = \frac{\omega d_p^2 \rho_p}{18\mu} \tag{4.7}$$

The estimation of the absolute error due to vortical movement requires information about the angular and about the tangential velocity. The ratio between radial and tangential velocity is of order of 5-10 %.

Particle Behaviour in a Turbulent Flow

If external forces can be neglected, the tracking capability of suspended particles is influenced only by the particle shape, particle diameter d_p, particle density ρ_p, fluid density ρ_f and fluid dynamic viscosity η or kinematic viscosity ν. Furthermore, a spherical particle shape, low particle concentration of less than 10^{10} $particles/m^3$, which represents an infinite fluid and a high density ratio of particle and a high density ratio of particle and fluid is assumed. For an optimal PIV application 15 particles per interrogation volume (Interrogation area and light sheet thickness $>$ 1 mm^3) are required according to Adrian [3]. This concentration of 1 μm particles results in a suspension with a mean distance between the single particles of 500 diameters.

The following equation describes the unsteady motion of a suspended sphere. Basset [11] derived this equation of motion for a sphere relative to an infinite, stagnant fluid already in 1888, and in Hinze [58] expanded this to a moving fluid, considering the instantaneous velocity $v = u_p - u_f$ of the particle relative to the fluid:

$$\underbrace{\frac{\pi}{6}d_p^3\rho_p\frac{du_p}{dt}}_{accelerating\ force} = \underbrace{-3\pi\mu d_p V}_{Stokes\ viscous\ drag} + \underbrace{\frac{\pi}{6}d_p^3\rho_f\frac{du_f}{dt}}_{pressure\ gradient\ force}$$
$$\underbrace{-\frac{\pi}{12}d_p^3\rho_f\frac{dV}{dt}}_{fluid\ resistance\ to\ accelerating\ sphere} - \underbrace{\frac{3}{2}d_p^2\sqrt{\pi\mu\rho_f}\int_{t0}^{t}\frac{dV}{d\xi}\frac{d\xi}{\sqrt{t-\xi}}}_{dragforce\ associated\ with\ unsteady\ motion}$$

(4.8)

u characterises the instantaneous velocity of the sphere or the fluid, subscript p refers to the seeding particle, and subscript f refers to the fluid. The first term in this equation represents the force required to accelerate the particle, and the second term describe the viscous drag as given by Stokes law. Acceleration of the fluid produces a pressure gradient in the vicinity of the particle, and hence an additional force on the particle as decribed by the third term. The fourth term is the resistance of an inviscid fluid to acceleration of the sphere, and is predicted by potential flow theory. This term is equivalent to the fluid mass which is displaced by the accelerating sphere. The last term is the *Basset history integral* which defines the resistance caused by the unsteadiness of the flow field. Note that when the first, third and fourth terms are combined, the accelerating force is equivalent to that of a sphere whose mass is increased by an additional *virtual mass* equal to half the mass of the displaced fluid.

For the case of particle motion in turbulent gas flows the last three terms on the right side can be neglected due to the high density ratio between particle and fluid. The viscous term (Stokes drag law) dominates due to the small particle Reynolds number $Re \ll 1$ defined as:

$$Re_p = \frac{(u_p - u_f)d_p}{\nu}$$

(4.9)

Now the unsteady motion of a suspended sphere can be expressed as:

$$\frac{du_p}{dt} = -C(u_p - u_f) \tag{4.10}$$

After an algebraic transformation and an implementation of the Stokes number, the non dimensional frequency of the particle response, the expression C can be rewritten and renamed as the characteristic frequency of the particle:

$$C = \frac{18\mu}{\rho_p d_p^2} = \frac{18\omega_c}{S_k \cdot s} \tag{4.11}$$

with the angular frequency:

$$\omega_c = 2\pi f_c \tag{4.12}$$

the Stokes number:

$$S_k = \left(\frac{\omega_c}{\nu}\right)^{1/2} d_p \tag{4.13}$$

and the particle density ratio:

$$s = \frac{\rho_p}{\rho_f} \tag{4.14}$$

Here, ω_c is the angular frequency of the fluctuations of the flow to be observed and f_c is the corrensponding frequency. The occuring turbulent frequency can be estimated with Kolmogorov time scale, but for most flows of practical interest it is not quantifiable with any precision. Estimated by experiment ω_c lies in the range of $f_c = 1 - 10kHz$.

An analytical solution of the equation above gives an expression for the particle response in unsteady flow, which characterizes the fluctuation energies of the time-averaged particle and fluid motion. The criterion for specifying the maximal size of a seeding particle is defined as follows. It is determined from the amplitude ratio of the particle and the fluid velocities, which is set to a minimal value of 0.99, according to Melling et al. [85]:

$$\frac{\overline{u_p^2}}{\overline{u_f^2}} = \left(1 + \frac{\omega_c}{C}\right)^{-1} \neq 0.875 \tag{4.15}$$

For DEHS with a density of 0.914 g/cm^3 with a pressure of 1 bar and a temperature of 20°C is found that the tracking capability for particles of 3.5 μm is very good. The tracking capability of these particles for the turbulent frequencies of 1 kHz and above are not ideal. Smaller particles would resolve those better. The estimation of the relative accuracy due to fluctuations in the flow is of order of 2-3 %.

source	relative accuracy [%]
measurement chain	~ 2
tracking of vortical structure	~ 5
tracking of fluctuation	~ 3
total	~ 8

Table 4.1: Total accuracy of velocity measurement

Total Measurement Accuracy

The total accuracy of the velocity measurement technique is summarized in the following Table 4.1. It should be considered that the error of the measurement chain and of the tracking behaviour of flow fluctuations are of random nature while the tracking of vortical structures is a systematic error. The stated total error is the worst case, where the out-of-plane velocity w measured in the presence of strong vorticity, high tangential velocity and fast flow fluctuation.

4.2 Infrared Thermography Measurements

The measurement of surface temperature with the infrared camera is pretty straight forward. The imaging software commercially obtained with the camera records the temperatures which are then corrected depending on the calibration factors calculated by comparison with the senflex thin film sensor measurements. However, two important derived quantities are required from these temperature measurements, namely the adiabatic effectiveness and the heat transfer coefficient. The effectiveness is a measure of the temperature reduction on the surface whereas the heat transfer coefficient is a measure of the energy transfer due to the cooling. Both these quantities are measured with the same test.

4.2.1 Theoretical Considerations

Commonly in heat transfer studies the heat flux from a hot fluid over a wall (or surface) can be described by Eq. 4.16.

$$q''_{conv} = h_{conv}(T_h - T_w) \tag{4.16}$$

However this definition is realizable and appropriate for two temperature systems. Film cooling flows have three temperatures, viz. hot freestream, coolant and the wall. It is for that reason the concept of the adiabatic wall was proposed by Goldstein [48], which denotes the temperature of the wall if it had been adiabatic, (T_{aw}). The adiabatic effectiveness is then just a non-dimensionalisation of this temperature by the temperatures of the hot freestream and coolant.

$$\eta = \frac{T_{aw} - T_h}{T_c - T_h} \tag{4.17}$$

The concept of the adiabatic wall allows the heat transfer coefficient for a film cooled surface to be defined with no dependance on the wall temperatures. This heat flux can be described by Eq. 4.18.

$$q''_{conv} = h_f \left(T_{aw} - T_w \right) \tag{4.18}$$

However, from an experimental point of view, it is not possible to have an adiabatic wall. Hence, the heat transfer coefficient most readily measured is, h_{conv} from Eq. 4.16. This variable is dependant on the temperature of the wall. For the current case, the local wall temperature may be non-dimensionalised by the hot and cold streams to yield θ.

$$\theta = \frac{T_w - T_h}{T_c - T_h} \tag{4.19}$$

In many references (eg. Baldauf et al. [8], etc), the non-dimensionalised temperature, θ denoted therein is the exact reciprocal of the formula given in Eq. 4.19, because the convective heat transfer coefficient, (h_{conv}) is linearly dependent on $(1/\theta)$. However, it is only a matter of convention. The linearity of h_{conv} with $1/\theta$ for a given flow field arises from the form of the differential energy equation within the boundary layer given by Eq. 4.20 with the effective k and μ for turbulent flow.

$$\rho C_p \left(u \frac{\partial T}{\partial x} + v \frac{\partial T}{\partial y} \right) = \frac{\partial}{\partial y} \left(k \frac{\partial T}{\partial y} \right) + \mu \left(\frac{\partial u}{\partial y} \right)^2 \tag{4.20}$$

Equation 4.20 shows the equivalence of convective energy transport and thermal conduction and dissipation with respect to a differential volume. In incompressible flows, the energy and momentum transport equations of the boundary layer are not coupled. Assuming constant properties, a linear differential equation in T is given which can be solved by superposing two particular solutions of the same flow field. This superposition follows from Duhamel's superposition principle, a proof of which is given in Carslaw and Jaeger [26]. Duhamel's method essentially helps to convert the differential equation for heat conduction into an integral formulation and can then be used to superpose the heat fluxes from hot stream to wall, assuming, $T_c = T_w$ and from cold stream to wall assuming, $T_h = T_w$.

Practically, the heat transfer from the outer hot gas to the wall is described by Eq. 4.16, while the heat flux from the adiabatic wall to the wall is described by Eq. 4.18. Duhamel's superposition method implies that these two fluxes are equal. The two fluxes can be equated to obtain a relationship between the h_f and η by Eq. 4.21.

$$h_{conv} \left(1/\theta \right) = h_f \left(1 - \frac{\eta}{\theta} \right) \tag{4.21}$$

For engine relevant density ratios, the hot and coolant streams need to be maintained at their designated temperatures. Under such experimental conditions with realistic temperature ratios, θ is always non-zero and the wall- temperature independent, h_f cannot be measured directly.

Thus, different experiments are carried out at different θ such that the T_h and T_c are the same, but the wall temperature is changed by changing the heat flux condition into the wall. This involves either using a constant heat flux boundary condition for the wall, or an iso-thermal condition with varying temperatures. It must be noted, that the heat transfer coefficient h_f is measured at different hot and cold fluid temperatures and not the iso-energetic conditions often used in the past (see Choe et al. [28]). The linearity of h vs $1/\theta$ for engine like density ratios and high resolution local h_f measurements was evaluated and validated by Gritsch et al. [52].

This linearity can be exploited for superposition measurements under the conditions detailed in Gritsch et al. [52], namely:

1. The flow field and blowing conditions in terms of the BR and DR are maintained exactly the same

2. The variation in the wall temperature is within the limits of coolant and main flow temperature. This point is important for compressible flows.

3. The coolant to main stream temperature ratio should also be maintained exactly the same for all the different tests.

4. The heat transfer regimes within which the different $h_{conv}(\theta)$ points are measured should span the extremes of near-adiabatic condition to high heat transfer condition for accurate effectiveness and h_f.

5. The change in θ must be affected by changing the wall temperature boundary condition or by changing the temperatures of the jet and freestream such that their density ratio remains exactly the same.

4.2.2   Measurement of η and h_f

In the current study, as discussed in Section 3.2, an isothermal thermally managed copper plate was used to set the isothermal wall boundary conditions. The temperature of the surface at four different conditions but the same blowing conditions was recorded. The surface temperature measurements (T_w) were recorded for four different iso-thermal wall temperatures which were set using the water heater and the temperature recorded. The required operating condition in terms of the BR and DR is maintained exactly the same in terms of absolute temperatures as well for all the four infrared measurements. For post-processing, a three-dimensional finite element mesh with the properties of the multilayer surface and copper and macor interfaces is simulated to calculate the heat flux at the surface. The entire multi-layer surface as well as the copper and macor insert is meshed as shown in Fig. 4.2. The meshing is automatically done from the solid state heat transfer simulation toolbox in the commercial solver MATLAB. In some places the density of unstructured mesh is high as the high gradients would be expected at the interface of the Macor and the copper surfaces. Based on the measured wall temperature,
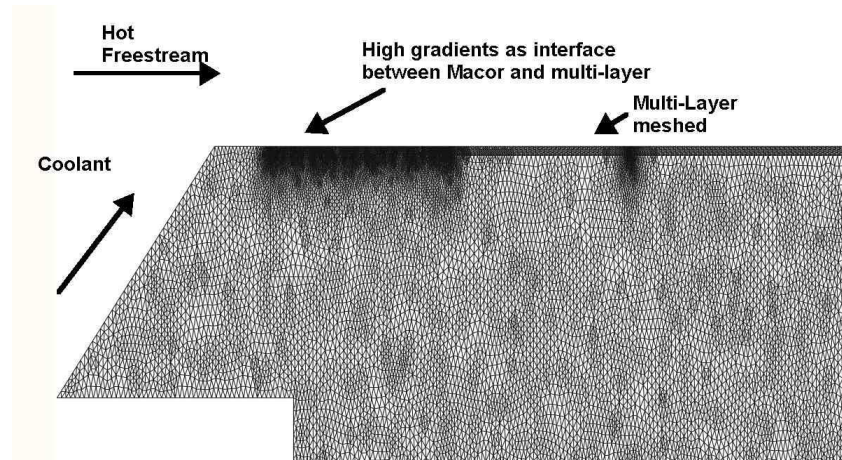
Figure 4.2: The mesh for finite element method (FEM) solution resolving the multi-layer of adhesive, kapton and black paint above the copper plate. The interface with Macor insert through which coolant is injected has higher block density
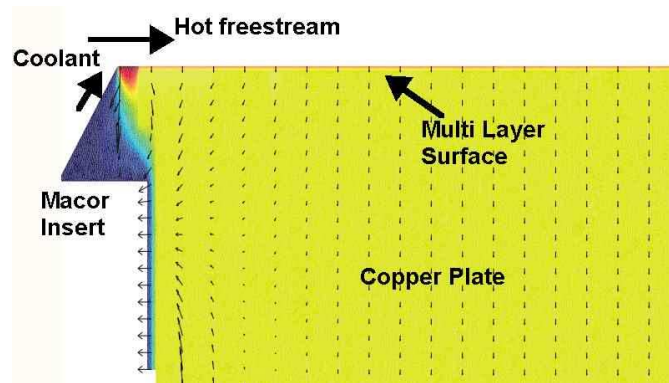
Figure 4.3: Color contours show temperatures and arrows show heat flux transport in steady state during a typical injection. The FEM solution resolves the conduction losses through the copper plate towards Macor insert which is cold due to coolant plenum

the circulating water temperature on the lower side of the copper plate as well as the coolant temperature cooling the Macor plenum and surface the heat flux solution is computed as shown in Fig. 4.3. The temperature are shown in color contours, whereas the heat flux direction is shown as arrows. Based on the temperature of the top most layer just below the kapton and the infrared thermogram of the surface the heat flux through the multi-layer can be further refined even after taking care of radiation losses. The heat flux in the vertical direction is two orders of magnitude higher than that in the lateral direction due to strong conductivity of copper and high insulating effectiveness of kapton which forces the heat flux to be as uni-dimensional as possible.

Based on this calculated heat flux and the infrared thermograms, the local heat transfer coefficients at every point are determined from Eq. 4.16. The four cases are then put together and a
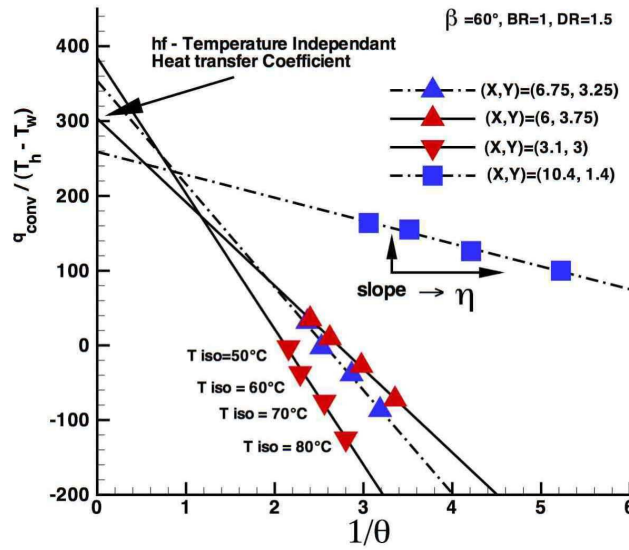
Figure 4.4: Adiabatic effectiveness and heat transfer calculation shown for four different points (X,Y) for $\beta = 60°$, BR=1, DR=1.5

linear regression is applied over every point in the matrix to derive the straight line equation for h vs $1/\theta$.

Based on Eq. 4.21, this linear regression over four representative points in different parts of the surface is shown in Fig. 4.4 for a real measurement condition. The y-intercept would give the h_f while the slope or x-intercept would give the adiabatic effectiveness value, η. Thus, both the quantities can be derived from the same set of four measurement at different isothermal wall temperatures, $T_{iso} = 50°, 60°, 70°$ and $80°$. For very low effectiveness values, it is observed that the linearity suffers slightly due to presence of singularities in the equation.
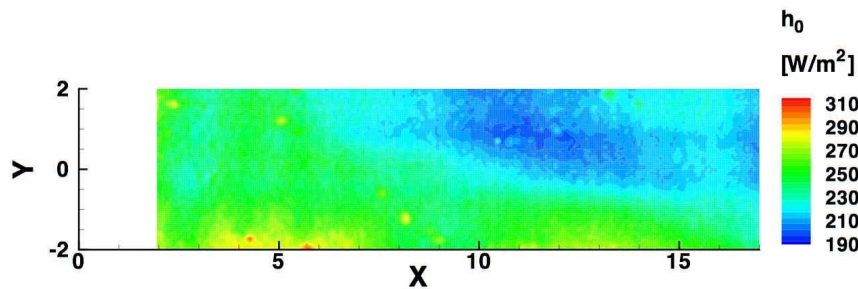
Figure 4.5: The heat transfer coefficient, h_0 for the case without any coolant injection at M=0.3

In order to properly non-dimensionalise the h_f it is important to measure the heat transfer coefficient without any cooling, h_0. This is accomplished by using a blank insert without any outlet from holes and running the wind tunnel at the same main flow temperatures as that in

the normal cooling cases. The surface temperatures are recorded with the infrared camera and the the finite element grid post processing is applied to calculate the uncooled heat transfer coefficient, h_0. As the surface is not completely uniform due to manufacturing defects, care should be taken to accurately map the spatial fluctuations of the local h_0 and not an averaged or one from analytical results. The h_0 distribution is represented in Fig. 4.5. The h_f calculated at every point is non-dimensionlised by the corresponding h_0 at that point.

4.2.3   Uncertainty Analysis

The uncertainty in measurement of temperature is determined by the infrared camera. However, the boundary condition from the thermal management of the copper plate which is supposed to be iso-thremal would also suffer from an uncertainty. The camera itself does not have the same uncertainty as sometimes the transmitting ZnSe window reflects the camera's own imaging chip, which is slightly hotter than ambient surroundings. Some of these external factors can always be corrected by subtracting raw undisturbed temperature information from the final results. The temperature non-uniformaty of the iso-thermal plate at two different temperatures viz. $50.5°C$ and $68°C$ is shown in Fig. 4.6 shown in a non-dimensionalised form. It must be noted that this temperature is also inclusive of the temperature non-uniformity suffered because of the unevenness of the kapton and adhesive layer above the copper plate as well as the black paint that is used to have a high emissivity of the surface. The small variation of less than 2K is comparable to the uncertainty in measurement of the infrared camera itself and is taken into account to calculate the uncertainty in heat transfer coefficients and adiabatic effectiveness.

The errors and uncertainties for the thermal field were calculated based on the terminology and methods described in Moffat [87], Kline and McClintock [66] and reported based on a 95% confidence interval. Equation 4.22 shows the calculation of the uncertainty in adiabatic effectiveness, η. All the independent parameters like temperature of the flow streams, wall temperature, thermal conductivity of the surface etc were perturbed individually based on their uncertainties and the entire post processing regimen involving the four point extrapolation was run to calculate the resulting heat transfer coefficient from which the individual gradient terms were derived. A similar process was also repeated to obtain the uncertainty in heat transfer coefficient, h_f.

$$\Delta \eta = \sqrt{\sum \left[\left(\frac{\partial \eta}{\partial T_h} \Delta T_h \right)^2 + \left(\frac{\partial \eta}{\partial T_c} \Delta T_c \right)^2 + \left(\frac{\partial \eta}{\partial k} \Delta k \right)^2 + \cdots \right]} \qquad (4.22)$$

The derivation of the final quantities was carried out by the running the entire FEM calculation with changed thermal conductivities and thickness for the component layers of kapton, adhesive and black paint. The sensitivity of the final effectiveness to these parameters was an order of magnitude lesser than to the temperature measurement.

The relative uncertainty in laterally averaged h_f varies from 11% in the near hole region $X < 6$
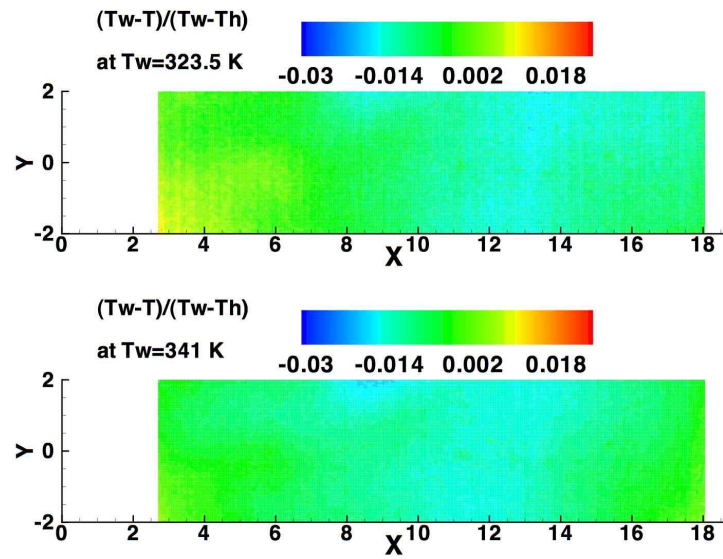
Figure 4.6: The temperature non-uniformity on the iso-thermal plate when it is maintained at $T_w = 323.5$ K or $50.5°$C and $T_w = 341$ K or $68°$C shown non-dimensionalised by the temperature difference form where $T_h = 298$ K
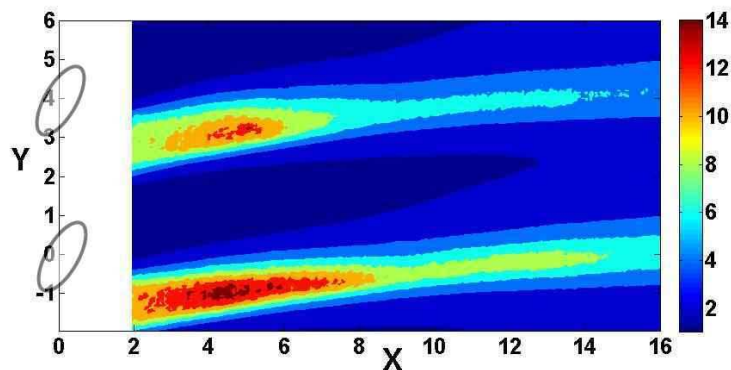
Figure 4.7: The relative uncertainty in adiabatic effectiveness [%] for $\beta = 60°$, BR=1, DR=1.5

to 10.2% downstream. The overall relative uncertainty in a spatially averaged sense for h_f varied from 10.4% for high compound angled holes which had a more uniform surface temperature, to 10.8% for the smaller lateral angles with stronger gradients.

The actual error in the heat flux coefficient h_f is sensitive to the non-linearity in the $h(\theta)$ vs θ curve fit over four different iso-thermal wall temperatures. The non-linearity at every point was calculated using the R^2 condition, which is the ratio of the regression sum of squares to the total sum of squares for a linear fit over the four h_{conv} vs θ points. It was observed to be above 98% for all points except in the uncooled parts of the surface between the jets, where the slope of the line and hence the effectiveness is near 0, causing singularities in the calculation of the R^2

condition.

The relative uncertainties for the thermal field were calculated based on the terminology and methods described in Moffat [87], Kline and McClintock [66] and reported based on a 95% confidence interval. All the independent parameters like temperature of the flow streams, wall temperature, thermal conductivity of the surface etc were perturbed individually based on their uncertainties and the entire post processing regimen involving the four point extrapolation was run to calculate the resulting effectiveness from which the uncertainty was derived. The calibrated infrared thermograms had an uncertainty of ± 1 K, while measurements of other temperatures had an uncertainty of 0.5 K. This resulted in an average uncertainty in h_{conv} of about 10.4%. The uncertainty in effectiveness in a spatially averaged sense varied between 5% to 7% for the different compound angles. Uncertainty in local effectiveness was as high as 18% for very low values ($\eta < 0.05$) using the 4 point extrapolation process as this results in the slope of the h vs θ curve to be near zero. Figure 4.7 shows the distribution of relative uncertainty in adiabatic effectiveness on the surface for a 60°injection at BR=1, DR=1.5. It clearly shows that the uncertainty is high for areas which are between the cooling jets where the effectiveness is low. A similar trend exists for h_f.

4.3   Entropy Probe Measurements

The aerothermal loss measurements were carried out using an in-house developed FENT probe as described in Section 3.3 with the help of a Circle-in-Circle traversing system shown in Fig. 2.12. The large density ratio of 1.5 was not reached due to the temperature limitations on the piezo-resistive chip on the pressure sensor. Hence a density ratio of 1.3 was measured by setting the hot freestream temperature to 393 K and the cold stream at room temperature, 300 K.

The flow field was measured at 6 planes normal to the primary free stream velocity at X/D = 0, 1, 2, 3, 4, 6. The hole centre was used as the origin of the coordinate system. Each normal plane consisted of 19 wall lateral and 15 wall normal points. Owing to the 1.8 mm diameter of the FENT probes, the closest to wall, Z/D measured was around 0.5 in the case of the streamwise, unpulsated case. In pulsated cases, as the temperature sensors are located lower than the pressure sensors, measurements closer to the wall were possible. However, measurement of quantities derived from both pressure and temperature were limited to Z/D = 0.5. It must be noted however that all derived quantities used velocity and temperature measurements from coincident points. This was done by traversing the probe with the same wall normal distance as the distance between the temperature and pressure sensor to obtain signals at coincident points. Pressure and temperature signals were acquired simultaneously at a sampling rate of 100 kHz over 2 seconds. The data sets are processed to obtain time-resolved, total and static temperature, total and static pressure, Mach number, flow angles and velocity by phase-lock averaging over 250 samples.

4.3.1 Uncertainty Analysis

Several sources contribute to the total temperature derived from the unsteady total temperature sensor. The propagation error technique is used to combine the uncertainties in these sources into a composite value. The derivation of the unsteady total temperature is based on Eq. 3.23. Therefore the uncertainty in the unsteady total temperature measurements depends on the uncertainties associated with to the measurements of the thin film total temperatures, $(T_{f,1}, T_{f,2})$, and the convective heat transfer rates, q''_{conv1}, q''_{conv2}. The relative errors in the convective heat transfer and the measured thin film temperatures are $\Delta q''_{conv}/q''_{conv} = \pm 3.77\%$ and $\Delta T_{f,1,f,2}/T_{f,1,f,2} = 1\%$, respectively. These yield to a relative error of 2.5% in the total temperature. The uncertainty in the time resolved total pressure is 100Pa. As change in entropy is defined by Eq. 4.23, where ref refers to the reference quantities, the derived quantity of entropy can also be determined from the relative uncertainties in pressure and temperature. The uncertainty is calculated to be 2.7%.

$$s_{ref} - s = \triangle s = -\mathcal{C}_p \ln\left(\frac{T_t}{T_{t,ref}}\right) + \mathcal{R} \ln\left(\frac{P_t}{P_{t,ref}}\right) \tag{4.23}$$

Chapter 5

Compound Angled Film Cooling Flow Structure

This chapter reports on various flow structure observations through PIV measurements for compound angled film cooling flows. Measurements are carried out for lateral angles, $\beta = 15°$, $45°$, $60°$ and $90°$ at various BR=1 and 2 and density ratios of 1 and 1.5. The distinct flow features that distinguish flows in this regime from streamwise angled injection and the influence of the blowing conditions and orientation angles on them are discussed.

The coordinate system and geometrical parameters are based on the geometry definition shown in Fig. 1.5.

5.1 Velocity

The compound angled film cooling flow structure shares some of the distinct flow features of a jet in crossflow which are modified due to its orientation with the freestream. A typical jet in crossflow as described by Moussa et al. [88], Kelso et al. [65] consists of a counter-rotating vortex pair injected into the freestream which then mixes with the freestream and entrains the fluid towards the centre causing a momentum deficit region and a thinning of the boundary layer at the edges of the jet. In a compound angled injection when the jet ejects at an angle to the freestream the basic flow features so commonly recognized in normal or inclined jets in crossflow are askew. Figure 5.1 shows the real PIV measurements of a 60° injection film cooling flow with the relevant flow features marked. The contours show the horizontal velocity normalised by the freestream velocity U_m whereas the arrows denote the cross plane velocity vectors. The figure shows that the classical counter-rotating vortex pair is instead replaced by only one large streamwise oriented vortex. The trajectory of the stream-traces also shows that the core jet has no line of symmetry and is aligned with the orientation of the jet. The high momentum jet core appears to be aligning itself with the freestream direction with downstream distance but
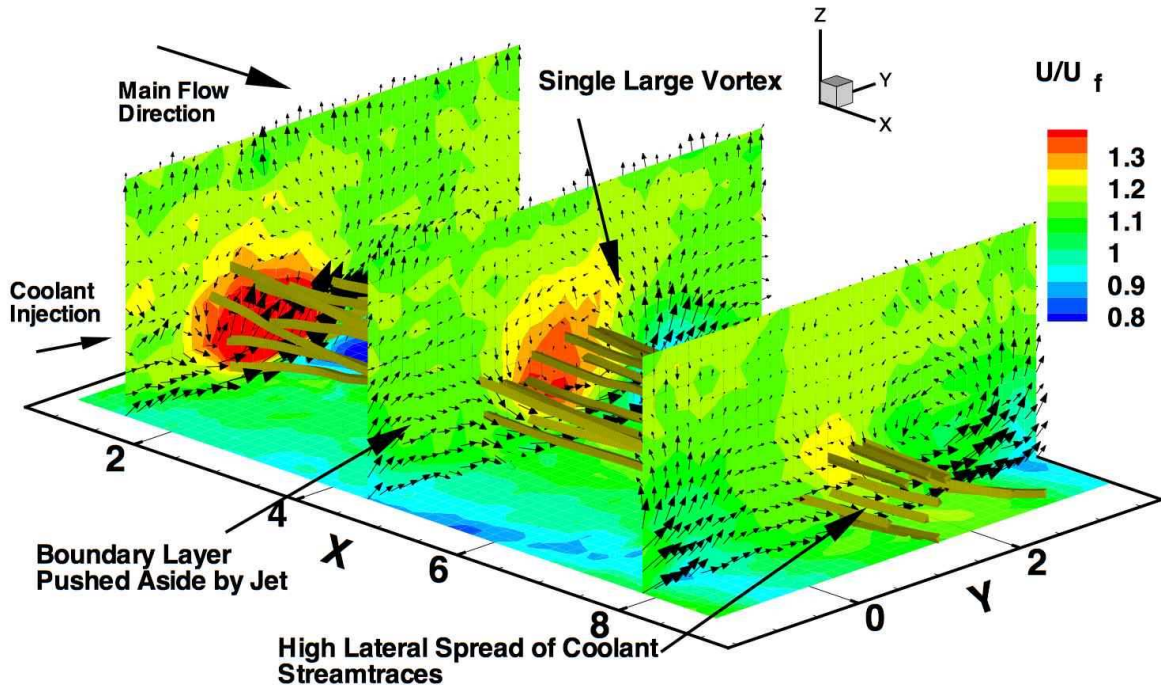
Figure 5.1: Velocity schematic of a 60°injection showing the relevant flow features with Y-Z velocity planes shown at $X = 1.6, 4$ and 8

the primary vortex core continues to keep its trajectory. The boundary layer pile-up is another significant flow feature. Low momentum fluid which makes up the wake in a streamwise injected jet is now piled onto one side of the emanating jet as a boundary layer pile-up. This pile-up is primarily caused due to the asymmetric vortex core as fluid is scooped and heaped to one side.

In the following discussions all distances, X, Y, Z are non-dimensionalised by hole diameter, $D = 5mm$ and all velocities, shown are also non-dimensionalised by the freestream velocity, U_m which vary from 112 m/s to 130 m/s based on the density ratio in order to maintain a Mach no., $M = 0.3$. The hole diameter, $D = 5mm$, based Reynolds number is, $Re_D = 43000$. The surface orientation angle is denoted by ϕ and the lateral angle is β. The origin of the coordinate system is at the hole centre. Unless otherwise stated, in all velocity plots the flow moves from left to right.

A canonical compound angled injection with surface orientation angle, $\phi = 20°$, and lateral angle, $\beta = 45°$ at high blowing ratios of 2 and 3 and different density ratios of 1 and 1.5 was investigated. A three dimensional velocity field was measured and plane cuts were made at $X = 4$. The horizontal velocity U contours are shown in Fig. 5.2 with the cross plane tangential velocities, $\sqrt{V^2 + W^2}$ depicted as vectors. The mixing out of the high momentum coolant core by the time it reaches $X = 4$ visible in all the four operating cases. The higher density ratio cases are clearly seen to have a mainly momentum deficit wake zone which is asymmetrically
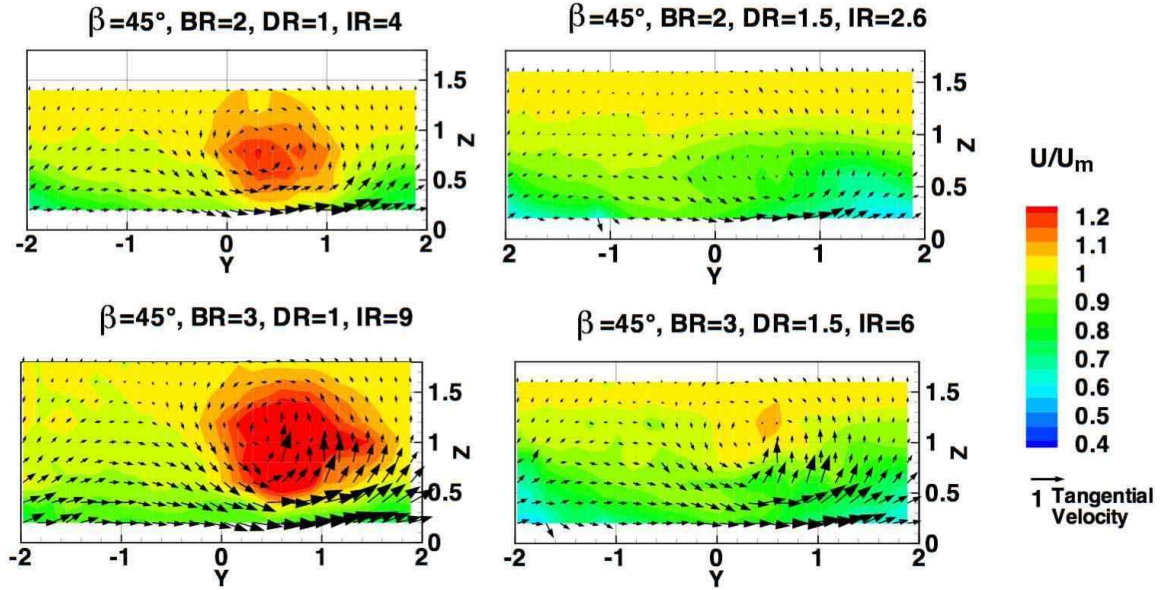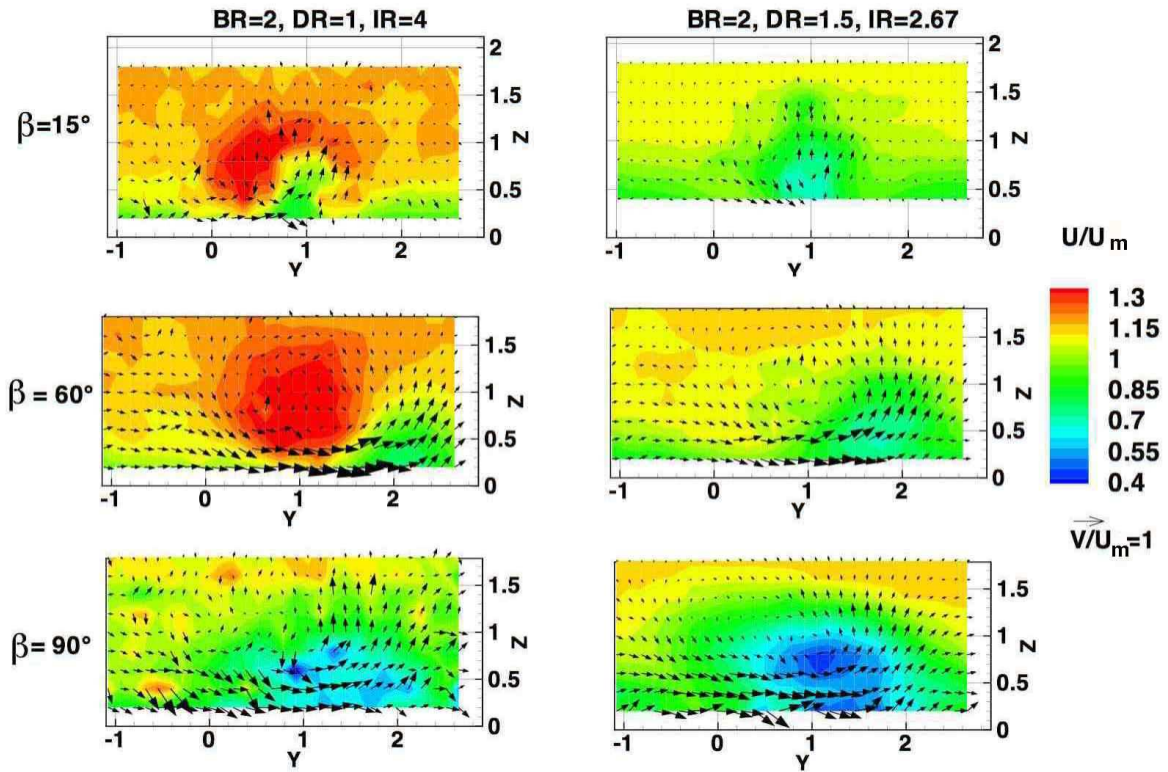
Figure 5.2: Cross plane velocity contours at X=4 of the horizontal velocity at different operating conditions for a $\beta = 45°$ injection

piled up. There is no counter-rotating vortex pair, instead the presence of a single large vortex is visible from the tangential velocity vectors. These vectors are larger for higher momentum flux ratios, IR and hence indicate a stronger streamwise vorticity for these cases. Increased density ratio also causes greater lateral spread primarily due to the decreased momentum ratio.

In most cases, film cooling surface injection angles are oriented at $\phi = 30°$. Based on this reference surface orientation angle, the lateral angle in the geometry was varied to 15°, 60°and 90°. The 15°lateral angle is not normally used but in operating gas turbines the flow angles on a blade are periodically changing as the rotor moves. In those cases a streamwise oriented hole might end up actually being inclined at a small angle during a periodic wake passing. Also the low lateral angle helps to understand the flow in the regime when the counter rotating vortex pair is still not completely diminished but is slowly becoming more and more asymmetric.

In order to compare the three compound angled geometries, plane cuts of the velocity field at $X = 4$ are shown in Fig. 5.3 for BR=2, and DR=1 and 1.5. The growing asymmetry of the size of the two vortices that emanate from the hole are clearly visible as β increases. As was shown in Aga et al. [5], there is only one large vortex present at high compound angles. Figure 5.3 also shows that, the location of the high momentum coolant fluid which is situated at about $Y = 0.2$ for $\beta = 15°$ keeps moving laterally as is seen by its presence near $X = 1$ for $\beta = 60°$.

In Fig. 5.3 the two data sets are shown at two different IR by changing the DR. There exist large momentum regions and asymmetric vortex structures which are stronger at higher IR. At very large compound angles the high momentum jet structure is not present but instead there exists

Figure 5.3: Cross plane velocity contours at X=4 of the horizontal velocity at DR=1 and 1.5 and compound angles, 15°, 60°and 90°at BR=2

a single large vortex emanating from the injection hole because of which the velocity contours of 90° show a very large momentum deficit zone but greater uniformity of velocity. This flow structure information thus explains the trends reported in previous studies. Refs Jung and Lee [63], Schmidt et al. [99] had shown that with greater compounding the adiabatic effectiveness increases, however the adverse effect of higher momentum flux ratios on effectiveness, reduces at higher angles. The flow structure in 5.3 show that the asymmetry of the vorticity increases with larger compounding as well as larger momentum flux ratios, for $\beta = 15°$ and $60°$. For both these angles the difference in size of coolant jet and vorticity change significantly from $IR = 2.67$ to $IR = 4$ even though the blowing ratio is the same. The spread and mixing of the coolant should therefore reduce. The $\beta = 90°$ case does not show a similar trend, rather, the low momentum wake zone appears to be the dominant region in both cases.

5.2   Vorticity

In turbulent flows, local fluid particles are seldom irrotational. This means that the velocity cannot be expressed as a gradient of a scalar function e.g. potential flows. Two key fluid

dynamic concepts associated with rotational flows are *vorticity*, which has to do with the local rate of rotation of a fluid particle and *circulation*, which is a related but more global concept (see Greitzer et al. [51]). Vorticity, ω is formally defined as the curl of velocity.

$$\omega = \bigtriangledown \times \vec{U} \tag{5.1}$$

The primary vorticity ejecting from a round jet is generated as a consequence of the fluid impulse at hole exit which creates a convecting vortex ring. As the angle of injection is inclined to the surface and the shear as well as body force from the crossflow is acting on this ejected vortex ring of the jet, the vortex ring is forced to curve towards the wall. As the vortex ring curves the deformation brought about by this convection and rotation, converts the erstwhile vorticity which was oriented normal to the hole area to now be aligned in the streamwise direction. This results in the formation of two opposite signed vortex rings which are of equal magnitude, having formed from the same ejected vortex ring. This is the typical counter-rotating vortex pair for a jet in crossflow. As visualized by Haven and Kurosaka [55], a backflow of the plate-boundary layer vorticity on the leeside of an emanating jet determines the lateral separation of these two vortices. The two vortices are rotating in an opposite direction and their lateral separation determines whether they induce the jet to lift-off with respect to the wall or stay closer to the surface.

Identifying vorticity locally is the object of much debate as shown in Chakraborty et al. [27]. However, the standard definitions of vorticity are readily understood and the three primary components of vorticity, V_x, V_y, V_z pointing in the cardinal directions are described in Eq. 4.2, 4.3 and 4.3.

As there is shedding of vortices from the interaction of the freestream meeting the jet body, horse shoe vortices are formed which have a wall-normal orientation. These wall-normal or upright vortices (as visualized by Fric and Roshko [44]) are not only the remnants of the shed horse shoe vortices, but also formed as vortices ejected from the jet interact and turn. These are involved in enhancing the mixing between the freestream and the jet. The streamwise oriented vorticity (V_x) and the wall-normal vorticity, (V_z) are derived from the three dimensional velocity field and discussed in subsequent sections.

If the velocities and distances used are all non-dimensionalised then the vorticity will also be a normalized quantity.

5.2.1 Streamwise Vorticity

The non-dimensional streamwise vorticity, $V_{x,n}$ emanating from the injection holes can be visualized by 3-D vorticity iso-surfaces spanning vorticity of equal magnitude but opposite sign. A streamwise injection case would show two parallel tubes of equal shape as shown in Bernsdorf et al. [13]. The freestream flow direction is from left to right, that is from $X = 0$ to $X = 6$.
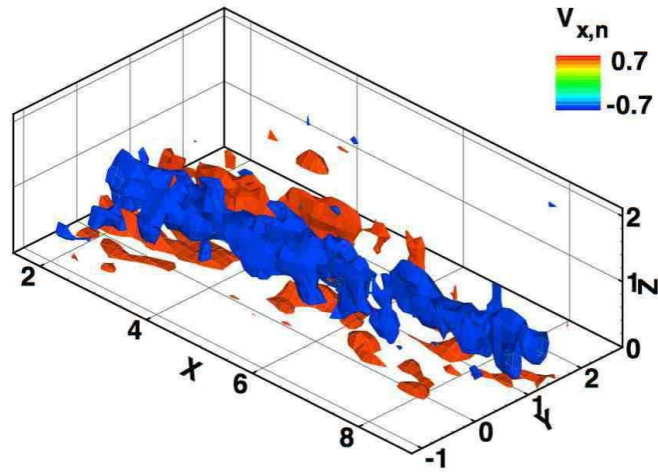
Figure 5.4: Surface iso-contours of normalised streamwise vorticity, $V_{x,n}$ for β=15°at BR=2, DR=1, IR=4
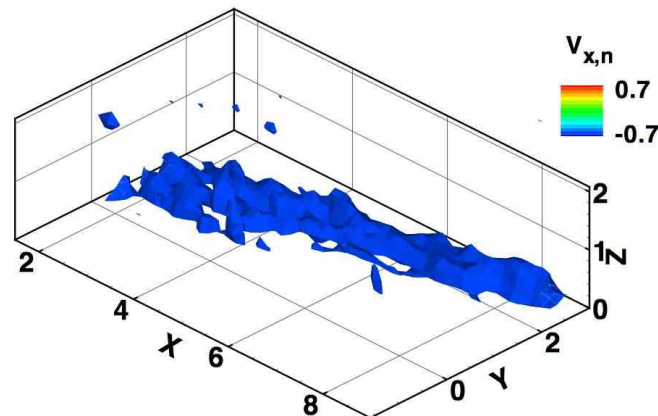
Figure 5.5: Surface iso-contours of normalised streamwise vorticity, $V_{x,n}$ for β=60°at BR=1, DR=1, IR=1

Figure 5.4 exhibits clearly that just after a 15° injection, the streamwise vorticity is of a counter-rotating nature with both the iso-surfaces laterally next to each other. However, with increasing downstream distance because of the skewness of injection angle, the negative signed vorticity (i.e. counter-clockwise rotation when viewed in the direction against the freestream flow) gains preponderance at the expense of the positive signed vorticity. The trajectory of the primary vortex core also deviates with the angle of injection. As discussed in Aga et al. [5], the amount of deviation is directly proportional to the IR. As the angle of compounding is increased, to $\beta = 60°$ in Fig. 5.5 and 5.6, the vorticity is primarily only of one sign. There is no evidence of a counter-rotating vortex pair, which hinders cooling by bringing hot air from the freestream closer to the surface. Instead the single strong vortex core would help to spread the coolant more
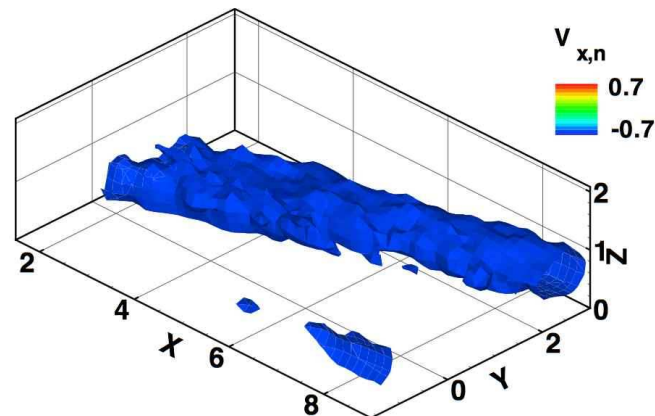
Figure 5.6: Surface iso-contours of normalised streamwise vorticity, $V_{x,n}$ for β=60°at BR=2, DR=1, IR=4
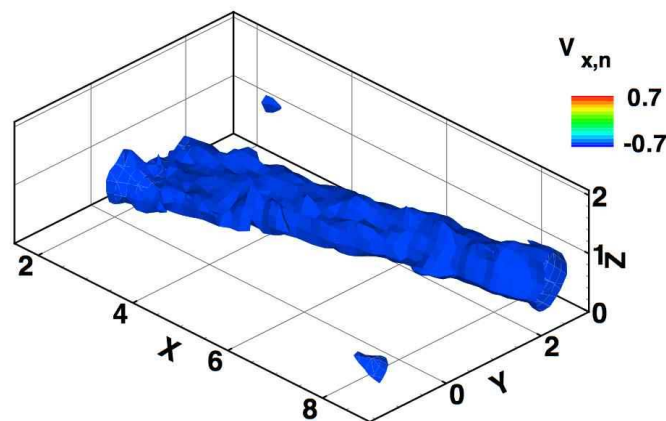
Figure 5.7: Surface iso-contours of normalised streamwise vorticity, $V_{x,n}$ for β=60°at BR=2, DR=1.5, IR=2.67

evenly over the surface. The positive signed partner vortex is seen to have not only reduced in magnitude but also tilted below the primary vortex core and limited only to the boundary layer as the image vortex.

Figure 5.5 shows the vorticity iso-contour of a 60°injection at a lower IR than that in Fig. 5.6. As expected the size of the vortex core is smaller. However, an important difference is also the greater proximity of this vorticity to the wall. The most visible effect is the lesser image vorticity spread in the boundary layer because of the greater attachment of the primary vorticity to the wall. The greater vertical momentum for the BR=2, DR=1, case causes the vorticity to be more detached, but it dissipates faster than in streamwise cases due to the greater mixing because of compounding. Increasing the density ratio simply causes a lowering of the primary vortex core

Figure 5.8: Surface iso-contours of normalised streamwise vorticity, $V_{x,n}$ for β=90°at BR=2, DR=1, IR=4

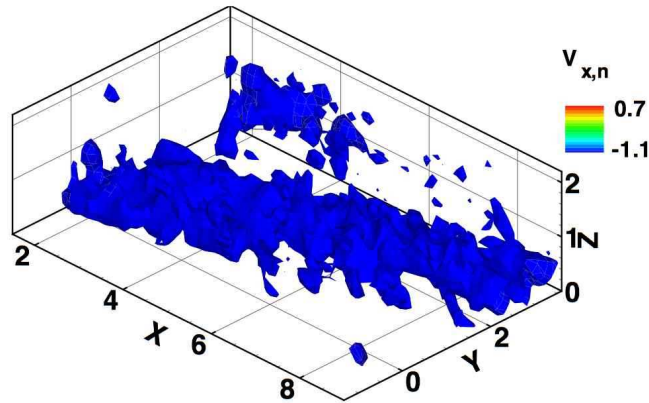**Figure 5.9:** Surface iso-contours of normalised streamwise vorticity, $V_{x,n}$ for β=90°at BR=2, DR=1.5, IR=2.67

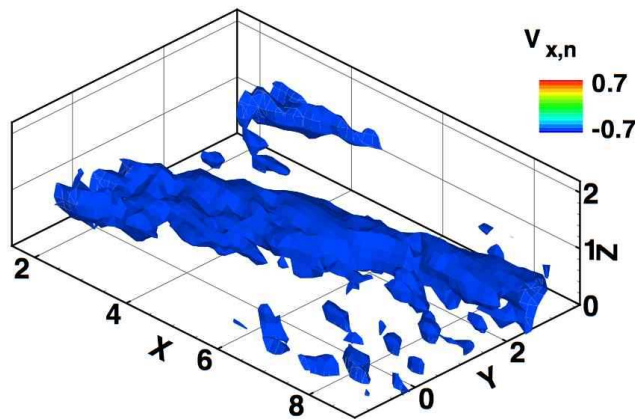magnitude and inclination to freestream as shown in Fig. 5.7. The density ratio mainly affects the primary vortex core indirectly by reducing the effective momentum flux ratio, IR.

As Haven and Kurosaka [56] has shown, a counter-rotating vortex pair enhances jet lift off and entrains hot fluid towards the surface. Of late there have been efforts to design film cooling technologies using cylindrical holes for economy, but with other devices like trenches (e.g. Lu et al. [81]) or anti-vortex designs (e.g. Heidmann and Ekkad [57]) mainly to reduce or eliminate the counter rotating vortex pair from cylindrical injection. Figure 5.6 clearly shows that a moderately high compound angled injection already has these advantages and hence should be treated as the baseline case when comparing new concepts. Figure 5.8 shows the primary vortex core at a very high compound angle of $\beta = 90°$ at a high blowing ratio of 2 and DR=1. The

streamwise vorticity is much larger compared to the smaller compound angles and has a higher magnitude. Increasing the density ratio, DR to 1.5 causes a reduction in the momentum flux ratio, IR and the effect is visible in Fig. 5.9. The vortex core is seen to occupy a larger spanwise region albeit flattened towards the wall, indicating that the coolant jet is not only spread over a larger spanwise region but also more attached to the surface. The image vorticity in the boundary layer is more prominent than for the $\beta = 60°$ case, indicating a greater vortex-boundary layer interaction. The trajectory of the primary vortex core does not show greater deviation than for the $\beta = 60°$. This could be contrasted with the primary vortex cores in $\beta = 15°$ and $60°$ that are aligned along the lateral angle as the primary vortex core is produced within the metering length of the holes as the jet is being ejected. The non-alignment of the $\beta = 90°$ suggests that there after a certain high angle of compounding the resulting vortex core downstream is affected by the interaction of the freestream with the jet rather than being dominated by the initial vorticity emerging from the hole.

From these iso-surface contours it can be concluded that the streamwise vorticity core increases in magnitude and spread with greater compounding and momentum flux ratio of injection. The inclination of the primary vortex cores keeps aligning with the same angle as that of the injection away from freestream direction with increasing IR. However, there is a limit until which the primary vortex follows the injection direction. For 90°injection, the primary vortex though larger is still aligned at an angle of only about 60 to 70°to the freestream.

5.2.2 Streamwise Circulation

The scaling of a counter-rotating vortex pair has often been developed though many parameters like trajectory and circulation. The streamwise circulation in the absolute reference frame (as opposed to local jet aligned reference frame) is often used to quantify the far field dissipation. Many studies like those of Hasselbrink and Mungal [54] have shown a scaling of the streamwise circulation of a jet in crossflow with distance non-dimensionalised as $(x/RD)^{-\frac{1}{3}}$, where $R = U_c/U_m$ is the velocity ratio. For density ratio jets viewed in the near hole region, the momentum flux ratio becomes a more appropriate quantity for scaling. A compound angled jet in crossflow however is somewhat different from a typical jet in crossflow as it has a single laterally angled vortex. For a small compound angled jet, $\beta = 15°$, it would be the growing asymmetry of vorticity that would also be important. As discussed in Greitzer et al. [51] the circulation typically scales with an appropriately reduced downstream distance by a power law for a jet in crossflow. An existing IR scaled distance from film cooling literature may also be used to achieve the same.

Streamwise injection of a film cooling jet has been studied extensively enough to provide a large database to produce data fits and hence correlations involving the various influencing conditions. Previous discrete hole film cooling correlations and approaches which have been detailed in Baldauf et al. [9] have used a non-dimensional downstream distance which is scaled according to the BR or IR. The general agreement, at least, for streamwise cylindrical injection according
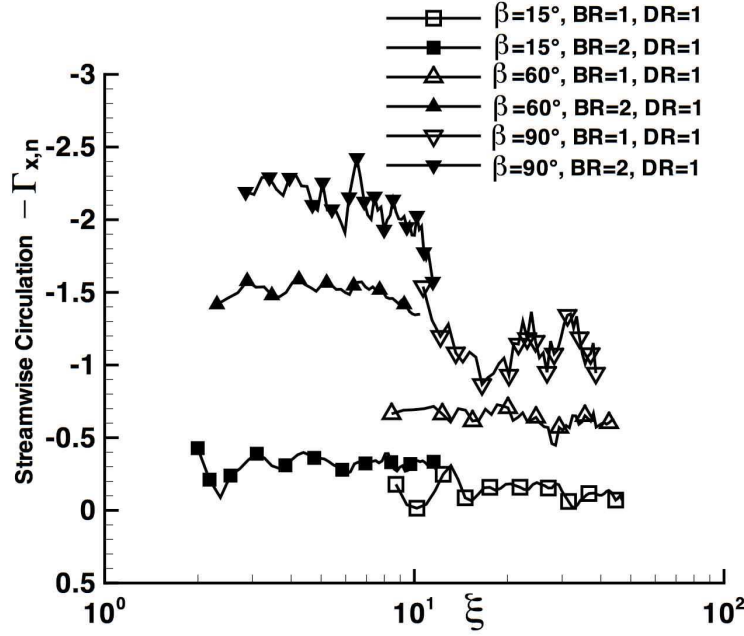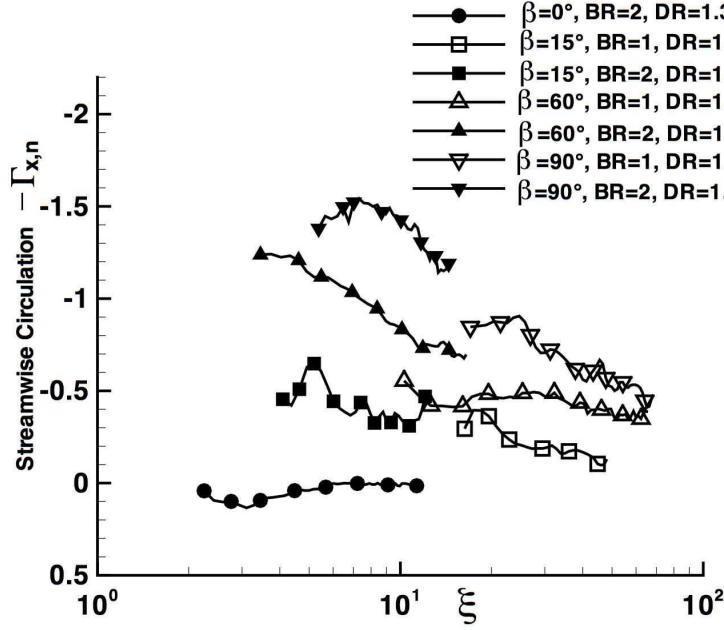
Figure 5.10: Streamwise normalized circulation, $\Gamma_{x,n} = \oint V_{x,n} dA$, plotted on a semi-log scale against $\xi = \frac{4X(S/D)}{IR\pi}$ for different compound angled injection at DR=1

to Baldauf et al. [9] has been that the BR is a better scaling parameter for far downstream correlations ($X > 40$) and the IR for the near field as IR more appropriately dictates jet lift-off. To that effect, a non-dimensional IR-scaled downstream distance, ξ is defined in Eq. 5.2 according to Baldauf et al. [9]. IR is used as the scale since the current data set is confined to the near field and measurements are made at high IR where BR by itself is not that important. The definition stems from a modification of the slot film cooling scaling through the usage of an equivalent slot width as used in Goldstein [48].

$$\xi = \frac{4X(S/D)}{IR.\pi} \tag{5.2}$$

This definition is qualitatively similar to the ones described by Hasselbrink and Mungal [54], with the pitch and momentum flux ratio used instead of an empirical coefficient and the velocity ratio R, respectively.

The asymmetry of the vorticity is quantified in terms of the circulation. The streamwise vorticity is integrated over the cross-section area spread along one pitch at different downstream X planes. The resulting normalised circulation is calculated according to Eq. 5.3, which integrates all the negative as well as positive vorticity, excepting those parts which have been identified as outliers in the streamwise direction over an area plane stretching till $Z = 2$ and for one pitch from $Y = -1$ to $Y = 3$. A higher value of the streamwise circulation would indicate a greater asymmetry in

Figure 5.11: Streamwise normalized circulation, $\Gamma_{x,n} = \oint V_{x,n} dA$, plotted on a semi-log scale against $\xi = \frac{4X(S/D)}{IR\pi}$ for different compound angled injection at DR=1.5

terms of spatial extent as well as strength.

$$\Gamma_{x,n} = \oint_A V_{x,n}.dA \tag{5.3}$$

Figure 5.10 shows the downstream evolution of the streamwise circulation with respect to the IR-scaled downstream distance, ξ. The data separates into two groups, one with the filled symbols showing the higher IR cases and the others indicated with the empty symbols for the lower IR case. Within the IR=4 regime, the average streamwise circulation increases with greater compounding. The 15° compound angle circulation starts from a lower value as the vortex is not very asymmetrical, then by $\xi = 6$ it reaches a peak and then starts dissipating and tilting in other directions, because of which the net circulation drops. However due to high IR, the circulation magnitude remains consistently high even at downstream distances. The higher compound angles show a similar behaviour at both IR=4 and IR=1. It is observed that a sharper drop in asymmetric circulation occurs at high compound angles whereas a higher momentum flux ratio tends to increase the initial magnitude of this circulation. The asymmetric circulation clearly follows a trend wherein the slope of decay on the semi-log scale as shown in Fig. 5.10 is similar for the same compound angles even though the absolute magnitudes depend on the momentum flux ratio.

Figure 5.11 shows the same figure for all the compound angled injection with high density
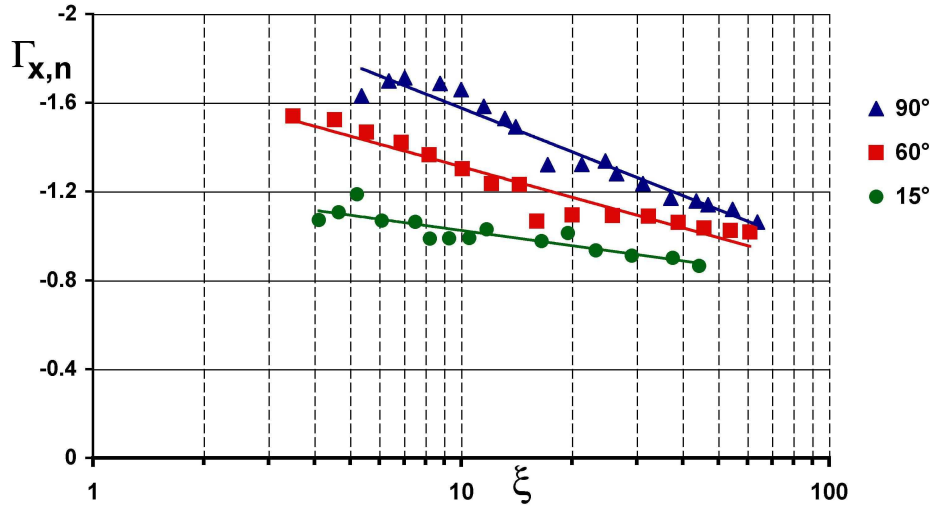
Figure 5.12: Data fits on a semi-log plot for the streamwise circulation evolution for $\beta = 15°$, $60°$and $90°$at DR=1.5 of the form $\Gamma_{x,n} = A\ln(\xi) + B$ or if y-axis is made positive by taking the absolute value of circulation the same fit can be formulated as a power law of the form, $\Gamma_{x,n} = A(\xi)^{-1/B}$, $B > 1$

ratio as well. The streamwise injection case, $\beta = 0°$ shown as a reference indicates almost no net circulation in the single pitch at all distances, which is because the positive and negative vorticity from the CVP cancel each other out. The trends in circulation decay are much clearer due to the lower difference in the two IRs as compared to Fig. 5.10. The IR=2.67 circulation measurements smoothly follow into the IR=0.67 points. The slope of decay clearly increases with the compound angle.

The asymmetric circulation shown in Fig. 5.11 can be fitted with logarithmic trendlines for each of the different orientation angles over the high and low blowing ratio ranges. This is shown in Fig. 5.12. However, if the streamwise circulation was taken as an absolute value (i.e. a positive value), the same fit could also yield a power law of the form $\Gamma_{x,n} = A(\xi)^{-1/B}$ where $B > 1$. This is qualitatively similar to the scaling of $(x/Rd)^{-1/3}$ which has been described for high blowing ratio jets in crossflow by Hasselbrink and Mungal [54].

These trendlines show that the decay in circulation is dominated by the lateral angle, whereas its actual magnitude depends on the momentum flux ratio for a particular geometry. These trendlines also show that a circulation decay scaling that is used for a streamwise jet may also be suitably modified for use with a compound angled jet, with the care taken that the power coefficient which dictates decay is set according to the compound angle.

The exact values of these coefficients can only be defined after many more measurements especially at far downstream conditions to ascertain the effects of large scale mixing on the asymmetric vorticity. Again, it is important to investigate the exact effect of density ratio on streamwise
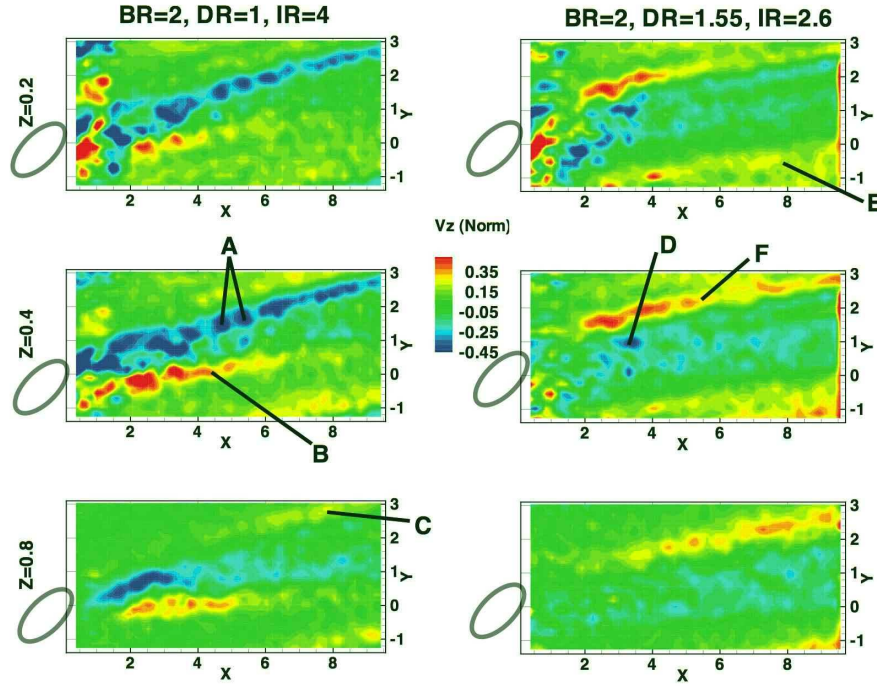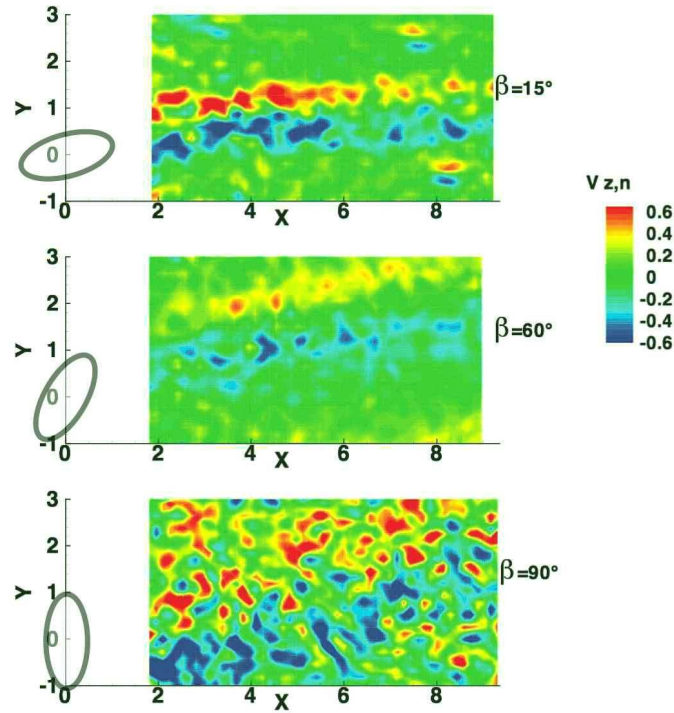
Figure 5.13: Iso-contours of normalised wall-normal vorticity, $V_{z,n}$ for $\beta=45°$ at BR=2 and DR=1 and 1.55

circulation as the trends are not exactly the same for DR=1 and DR=1.5 compound angled flow. It may be conjectured at this point that the effect of baroclinic vorticity $\omega = \bigtriangledown\rho \times \bigtriangledown P$ due to the strong density gradients could also be playing a role.

5.2.3 Wall Normal Vorticity

The normal vorticity formed due to the interaction between the free stream flow and the emanating jet are shown in Fig. 5.13 for a canonical 45°injection. This figure shows the wall-normal vorticity, i.e. vorticity in the Z direction for two different DR at the same BR at different wall normal distances. This normal vorticity consists of the wall-normal component from the jet and the freestream. These may be thought of as analogous to wake vortices in straight jets in cross-flows. Wake vortices have been shown to be responsible for vorticity transport and mixing between the boundary layer and the jet by Fric and Roshko [44]. As a sign convention, in Fig. 5.13, the blue zones are regions of anticlockwise rotation while the warmer colours are those of clockwise rotation. The label "A" shows the vorticity directly involved in the mixing process between the boundary layer and the coolant jet. The region marked "C" is produced on the opposite side of the jet from the origin of "A", and thus has an opposite sign. The region "C", which appears symmetric to "A" in a streamwise injection is seen to have reduced in extent. This dwindling of "C" may be linked to the uneven shear layer due to the skewed surface proffered by the jet
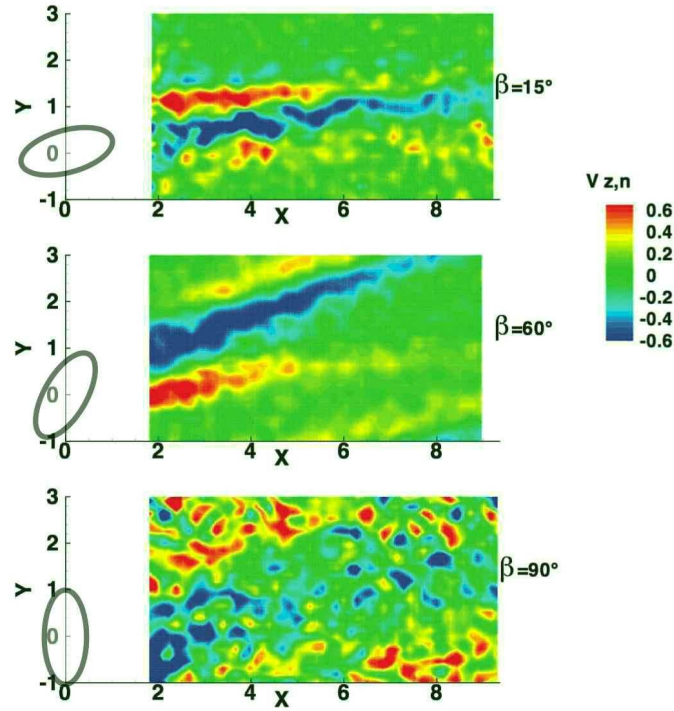
Figure 5.14: Iso-contours of normalised wall-normal vorticity, $V_{z,n}$ for $\beta=15°$, $60°$and $90°$at BR=1 and
DR=1 at Z=0.5

angled to the free stream. Region, "B" on the other hand which was observed as a weak remnant
of the horseshoe vortex for a streamwise injection in Bernsdorf et al. [13] is in this case seen to
be enhanced in size and strength. For the higher DR case, "D" which corresponds to "A" is seen
to be spread out over a spatially larger region as well as subjected to greater deviation from its
initial trajectory and is more aligned with the free stream flow. Zone "E" corresponding to "B"
is much weaker. "F" on the other hand is clearly visible as the vortex street of opposite sign
from that of "D". Unlike "C", "F" strongly participates in the mixing between the boundary
layer and the jet.

The wall-normal vorticity is also an indicator of the mass and momentum transport between the
jet and the freestream and hence would have a direct influence on the heat transfer coefficients.
The coherent structures most responsible for jet and freestream mixing are the upright vortices.
It has also been shown in previous studies by Fric and Roshko [44], that these coherent structures
also cause turbulence intensity enhancement. The turbulence quantities could not be measured
and hence the wall-normal vorticity could serve as a steady state flow structure indication of
sites of turbulence enhancement at different operating conditions.

Although their magnitude is about half that of the primary vortex core, they have an important
effect on heat and momentum transfer. A plane slice at Z=0.5 diameters above the surface is
shown for the three different compound angles for BR=1 and DR=1 (IR=1) in Fig. 5.14. For

Figure 5.15: Iso-contours of normalised wall-normal vorticity, $V_{z,n}$ for β=15°, 60°and 90°at BR=2 and DR=1 at Z=0.5

the low IR, the spatial extent and strength of the upright vortices is lower for all the angles compared to the higher IR contours shown in Fig. 5.15. The trajectory of the wall-normal vortices is along the angle of injection. However, as the compound angle is increased the lateral spread of this vorticity also increases as jet-freestream interaction is increased. The direction of rotation of the wall-normal vorticity (i.e. whether clockwise or anticlockwise in the figures shown) is not significant, but rather the magnitude of these coherent structures is what determines the turbulence enhancement or heat transfer magnitude in this region. At higher blowing ratios as shown in Fig. 5.15 the local magnitude of the vorticity is higher while the spatial spread is mainly due to the compound angle. The 60°injection in Fig. 5.15 can be compared to the 15°plot just above it. The alternating legs of oppositely signed vorticities are still present but their trajectories are widely diverging. This shows a larger lateral mixing at the edges of the jet where the coherent structures are weakening as they spread. The 90°injection contour shows a well mixed out vorticity field, with coherent structures dispersed within the field and well spread out. The jet-freestream interaction is therefore quite substantial.
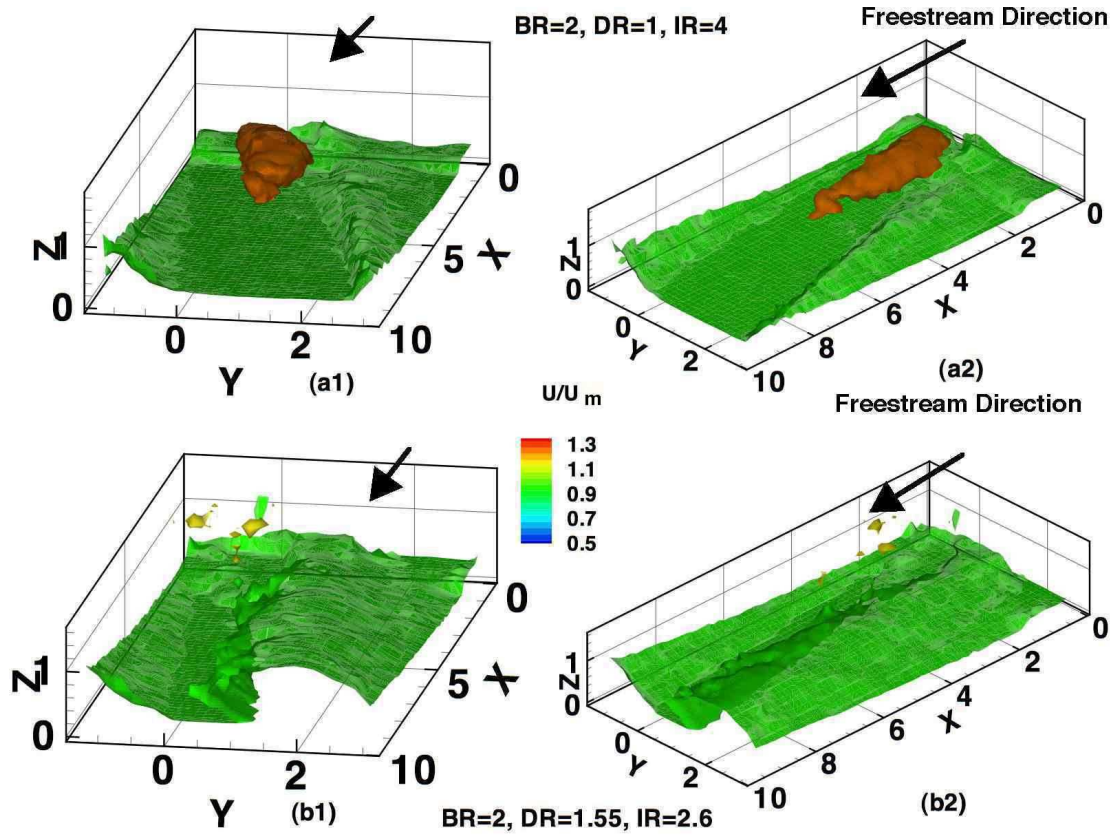
Figure 5.16: Surface iso-contours of normalised horizontal velocity, U/U_m delineating the boundary layer at $U/U_m = 0.95$ and high momentum jet at $U/U_m = 1.25$ for $\beta=45°$ at two different blowing conditions

5.3 Boundary Layer Shape

For an inclined jet in a cross flow, the boundary layer envelope is directly dependent on the primary vorticity. The shape of the boundary layer with respect to its spatial extent and local wall-normal height is relatively complex and has a distinct three-dimensional nature. The strength and orientation of the streamwise vorticity would cause preferential entrainment towards one side of the jet while scouring away the low momentum fluid from the other side. In addition for high compound angled flows, the resulting enhanced mixing also leads to a larger low-momentum fluid area which is within the boundary layer.

Figure 5.16 shows the iso-surface contours of the normalised streamwise velocity, U/U_m for two different levels. The free stream direction is from right to left in this case. One level (green) at $U/U_m = 0.95$ indicates the boundary layer, and the second level (orange) at $U/U_m = 1.25$ delineates the coolant jet. The obvious difference in the trajectories of the wall boundary
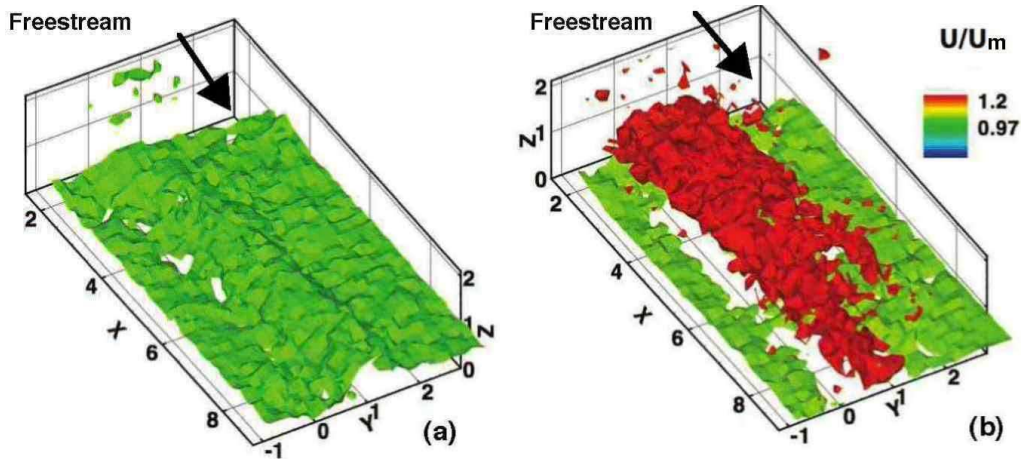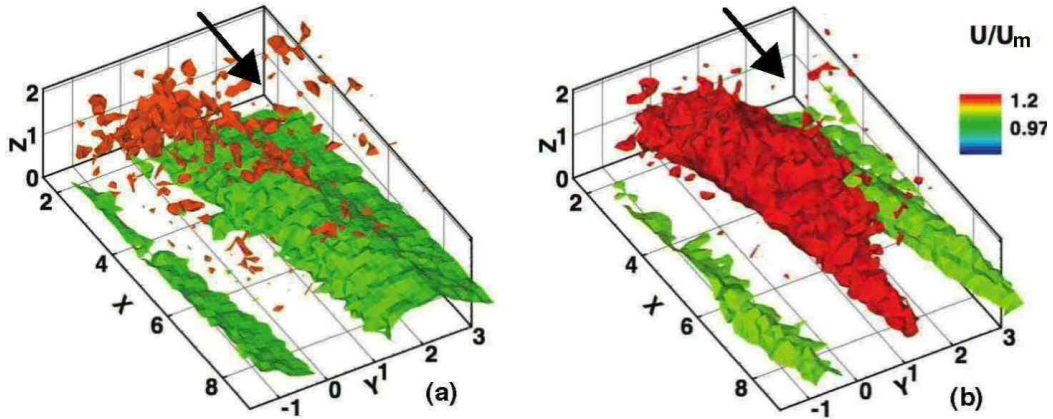
Figure 5.17: Surface iso-contours of normalised horizontal velocity, U/U_m delineating the boundary layer at $U/U_m = 0.97$ and the high momentum jet core, $U/U_m = 1.2$ for β=15°at (a) BR=1, DR=1, IR=1 and (b) BR=2, DR=1, IR=4

layer and the coolant jet can be explained by the combined mixing action of the wake vortices (normal vorticity) and primary vortex core (streamwise jet vorticity). It can be observed that the streamwise vorticity, because of its asymmetrical nature adds a horizontal velocity component to the coolant ow and causes it to swirl as well. This has the net effect of leaching the momentum of the coolant in its original injected direction until it gets aligned with the direction of the free stream. This tendency of alignment is quite apparent in Fig. 5.16 (a1) and (a2).

Additionally, the jets high velocity core becomes very diffuse as visible by the tapering shape of the iso-surface of $U/Um = 1.25$ in Fig. 5.16. The streamwise vorticity causes the boundary layer pile up on one side by entraining uid from the other, as a consequence of its asymmetrical nature. The effect of this is visible as the span wise spreading of the thinned boundary layers in (a1) and (a2). The growth and subsequent entrainment of the vortex increases the area over which this entrainment occurs. For the lower IR case, DR = 1.5 for the same BR = 2 , the coolant is almost enveloped by the wall bounded ow. The lower vorticity combined with the faster diffusion of horizontal momentum from the coolant jet leads to a greater spread of the coolant. For this case, the boundary layer is piled up over a much greater spatial extent, while its trajectory is maintained.

The effect of compounding on the lateral spread and alignment of the boundary layer 3-D profile is to flatten it as well as enlarge it. However, momentum flux ratio also plays an important role. This can be observed in subsequent figures. The coordinate system has its origin at the centre of the injection holes and the direction of freestream flow is always from left to right, i.e. from X=0 to X=8.

Figure 5.17 shows the two iso-surfaces of velocities delineating the boundary layer and jet core for a 15°injection. The density ratio is maintained at 1 and the figure shows BR=1 and 2. The

Figure 5.18: Surface iso-contours of normalised horizontal velocity, U/U_m delineating the boundary layer at $U/U_m = 0.97$ and the high momentum jet core, $U/U_m = 1.2$ for β=60°at (a) BR=1, DR=1, IR=1 and (b) BR=2, DR=1, IR=4

increased IR shows a stronger jet core, while the IR=1, injection has only a wake zone delineated by the boundary layer pile-up along the jet centerline. It clearly shows the entrainment of fluid from the sides of the jet towards the centre and upwards, due to the remnant counter rotating vortex pair. As the compound angle is increased, the primary vorticity is more and more asymmetric. Figure 5.18 (a) shows a 60°injection for BR=1, DR=1. The momentum jet core is not strong but the boundary layer has an asymmetric shape. Figure 5.18 (b) shows the same compound angled injection at a higher IR=4. The jet core is larger and stronger but dissipates quickly with downstream distance, whereas the boundary layer envelope becomes larger with downstream distance. The strong momentum flux causes the boundary layer to be preferentially piled up only on one side of the jet, leaving the path directly below the jet scoured of boundary layer fluid. The boundary layer profile is an important feature for compound angled holes, as it is pushed preferentially towards one side of the injection.

5.4 Summary

The flow structure of a compound angled film cooling is different from that of a simple jet in crossflow as well as from a streamwise injected, inclined jet in crossflow. The relative angle between the injected jet and the cross stream creates different vortical structures and mixing. The two most important flow structures are the asymmetric unpaired streamwise oriented primary vortex core and the asymmetric boundary layer profile. The main observations can be summarized below.

1. The counter-rotating vortex pair (CVP) typically associated with a jet-in-crossflow is absent. Increasing lateral inclination of an injection hole reduces one vortex while enlarges

the other until only one large asymmetric primary vortex core is present.

2. The trajectory boundary layer height enhancement is pushed to the side of the trajectory of the coolant injection. The high momentum jet core aligns itself with the freestream direction at a downstream distance whereas the boundary layer profile is modified due to the primary vortex core which maintains its trajectory in the same direction as initially injected.

3. Increasing the momentum flux ratio increases the size and strength of the asymmetric vorticity for compound angled injection and also aligns the vorticity more in line with the original orientation angle. However the maximum alignment is limited to about 60 to 70°even if the lateral angle was 90°.

4. The streamwise circulation decays along a power law with respect to an IR-scaled downstream distance. The magnitude of decay depends on the compound angle whereas the absolute magnitude for each geometry is directly proportional to the momentum flux ratio.

5. The wall-normal vorticity is responsible for momentum and energy transfer between the jet and the underlying fluid from the freestream. For compound angled injections, this vorticity increases in lateral spread with greater compounding and increases in local magnitude with momentum flux ratio.

6. The trajectory of the wall-normal vorticity follows that of the streamwise vorticity initially but then for higher compound angles, the different tines of the vortical structures diverge laterally and dissipate in strength with downstream distance. This could be due to the increased lateral mixing between jet and the freestream.

Chapter 6

# Influence of Flow Structure on Cooling Performance

The adiabatic effectiveness, η is a measure of the cooling performance from the temperature reduction viewpoint for film cooling flows. Previous studies have generally shown higher compound angled injection to cause greater effectiveness as they spread the coolant better. However, just precisely which flow features causes the greater coolant spread must be examined in tandem with effectiveness measurements to glean correlation and causation. Chapter 5 deals in detail with the flow structures most characteristic of compound angled film cooling flows. It was observed that the streamwise vorticity which is highly spread out and is asymmetric plays an important part in momentum transfer and mixing which would substantially affect the adiabatic effectiveness.

The temperature independent film heat transfer coefficient, h_f as described in Eq. 4.21 is an important parameter to evaluate film cooling performance. This parameter represents the energy transfer capabilities of the injection from the fluid domain to the wall. It is non-dimensionalised by the heat transfer coefficient when there is no cooling flow, h_0. It has been conjectured that the presence of more turbulent flow and mixing leads to a greater heat transfer coefficient as the energy transfer is enhanced. Previous studies on compound angled film cooling heat transfer (eg. Goldstein and Jin [49], Sen et al. [100], etc) have shown that heat transfer coefficient is typically higher for higher compound angles and on an average generally increases with increasing momentum flux ratio. This could be as greater unsteadiness is introduced on to the wall and the boundary layer is energized by the wall-hugging jet. The following sections show detailed local heat transfer coefficient results along with partner flow field measurements showing boundary layer pile-ups and normal vorticity plots to glean the influence of the macroscopic flow structures on the heat transfer coefficient.

The PIV measurements shown henceforth are all for a BR=1, 2 and DR=1.5 with the mainstream velocities, $U_h = 130$ m/s. The infrared thermograms were also captured for the same operating conditions. T_h was maintained at 115°C and T_c at around -15°C. As the density ratio

is maintained constant for the heat transfer studies, the primary aim to change BR is to change the IR. Change in IR is the dominant cause of changes in effectiveness and flow structure for the discussed flow regime.

6.1 Streamwise Vorticity and Adiabatic Effectiveness
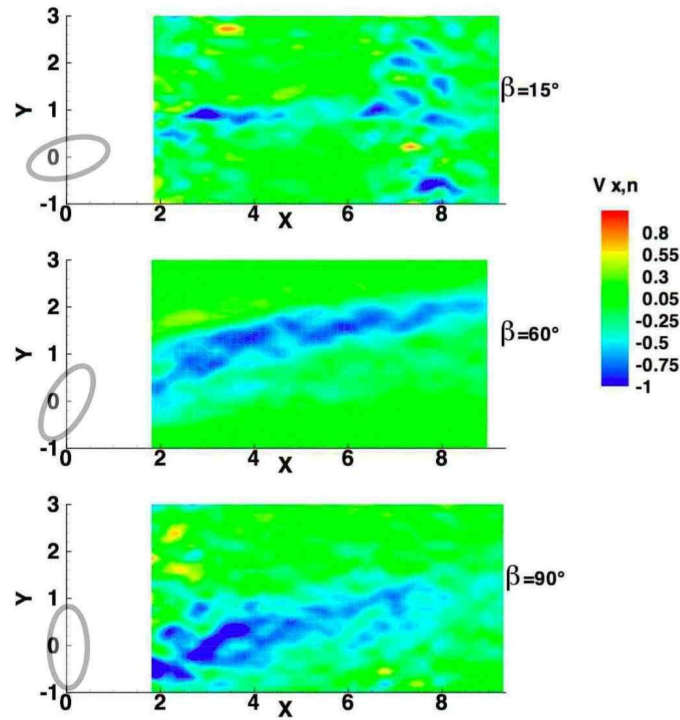
Figure 6.1: Normalised streamwise vorticity iso-contours at Z=0.5 above the wall for BR=1, DR=1.5, IR=0.67

The streamwise vorticity appears to be the predominant flow feature that causes mixing as well as coolant spread. The diminishing of the vortical intensity with downstream distance as well as its trajectory should have an influence on the adiabatic effectiveness. In order to investigate the causal link more clearly the streamwise vorticity was plotted as surface iso-contours of an axially oriented slice of data. The 3-D streamwise vorticity discussed in Section 5.2.1 shows that the primary vortex can be coherently visualized at a $Z = 0.5$ slice as the leg of opposite signed vorticity is tilted under the primary core close to the surface. The change of a skewed vortex structure from $\beta = 15°$ injection to the large swathes of mixed vorticity due to 90° injection dictated by unsteady freestream jet interaction is clearly observed in Fig. 6.1.

Adiabatic effectiveness measurements are obtained for $DR = 1.5$ cases and hence a comparison of the vorticity contours with the surface performance may be carried out. Figure 6.1 shows the
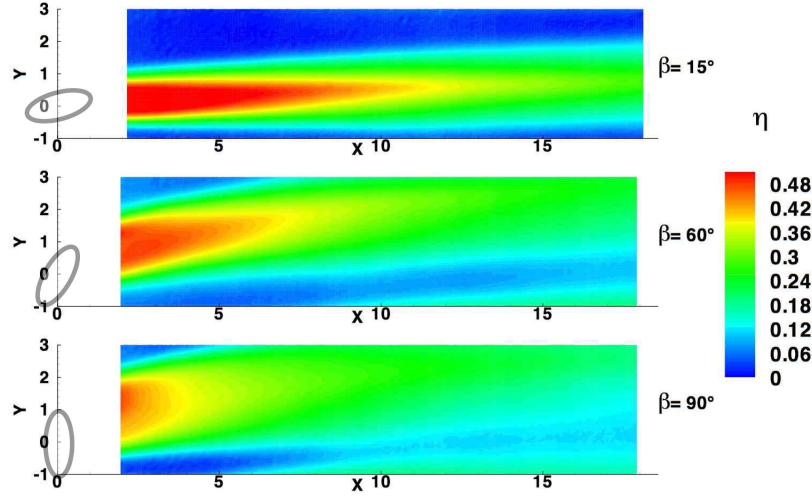
Figure 6.2: Contours of adiabatic effectiveness, $\eta = \frac{T_h - T_{aw}}{T_h - T_c}$ for BR=1, DR=1.5, IR=0.67 for three compound angled injection cases

streamwise vorticity contours for the low $BR = 1$ case. This figure can be compared with Fig. 6.2 which shows adiabatic effectiveness, η contours for the same pitch and conditions. The adiabatic effectiveness is high in the near hole regions and is seen to curve to align with the freestream at downstream distances. The adiabatic effectiveness does not exactly correlate to the asymmetric vorticity but qualitatively the trajectory is similar in that it does not continue in the direction of injection. The vorticity would have an effect of the near wall turbulence which would affect heat transfer. This flow quantity though, has not been measured and so an indirect inference into the main mechanisms affecting the heat transfer through vorticity is attempted.

Many experimental results (e.g. Schmidt et al. [99], Jung and Lee [63]) have reported that increasing the momentum flux ratio (IR) for high compound angles does not affect the laterally averaged effectiveness as starkly as for streamwise angled holes or for those with smaller compound angles. The explanation may be mainly due to the counteracting effects of jet lift off and coolant spread.

The local magnitude of the streamwise vorticity is observed to increase with increasing compound angle for the low IR=0.67 as observed in Fig. 6.1. When these are compared to similar plots at IR=2.67 shown in Fig. 6.3 it is seen that this streamwise vorticity becomes stronger and has great lateral spread at the increased injection rate. Another important observation is the trajectory that is followed by the streamwise vorticity. For the lower injection ratio the vorticity trajectory tends to align itself with the freestream at a short downstream distance, but for the higher momentum flux ratio, it is present along a path in the direction of original injection. The 90°, injection is noteworthy because it shows that there is a limit to how much the streamwise vorticity will follow the injection angle. As shown in Fig. 6.3, the streamwise vorticity for a
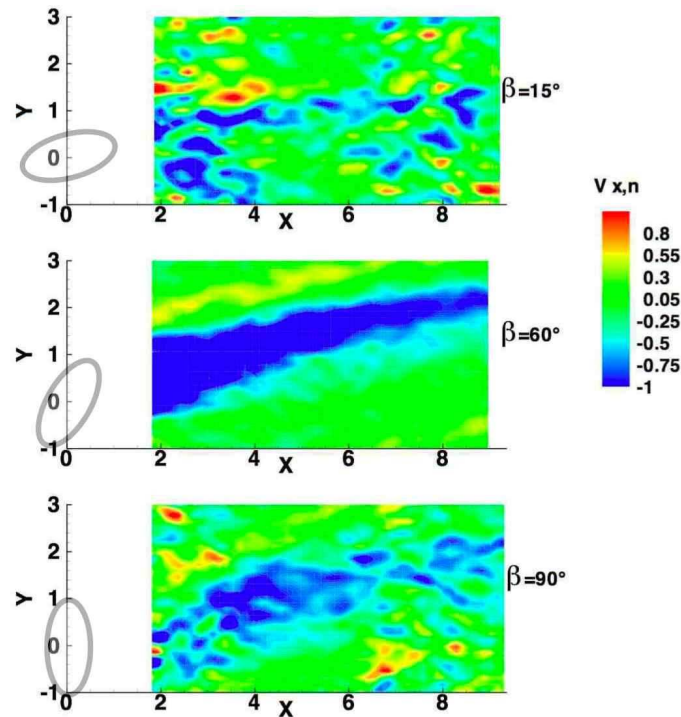
Figure 6.3: Normalised streamwise vorticity iso-contours at Z=0.5 above the wall for BR=2, DR=1.5, IR=2.67

90°injection, though having a larger spread is still aligned roughly along a 65°angle.

The adiabatic effectiveness is plotted for lower IR=0.67 in Fig. 6.2. As the IR is low the jet lift-off is not prominent, high local peaks are visible for a 15°injection as well. The cooling for this lower IR is mainly caused by the proximity of the jet to the wall. The stronger asymmetric vorticity for the higher compound angle holes would be responsible for spreading the coolant in a lateral direction.

As discussed extensively in the discussions of Haven and Kurosaka [56] and Haven and Kurosaka [55], the absence of a kidney vortex causes greater attachment of the jet to the wall as it discourages lift-off. An asymmetric kidney vortex is present for the 15°injection but only a single completely asymmetric vortex is present for the higher compound angles at high IR as observed in Fig. 6.3. This would imply that the coolant proximity of a 60°and 90°is greater than a simple streamwise injection. This is especially visible for the effectiveness plots shown in Fig. 6.4. In the near hole region, due to the jet depressing effect of the asymmetric vortex compared to a kidney vortex, the jet is less lifted off and hence there are local peaks in effectiveness. As the jet travels downstream and wall proximity increases due to the high vertical momentum component, the coolant proximity should also reduce and with it the local peaks. This does happen, but a counteracting effect is spread of coolant laterally for the 60 and 90°injections which compensates for the reduced local magnitudes. This greater spread can be said to be due to the streamwise
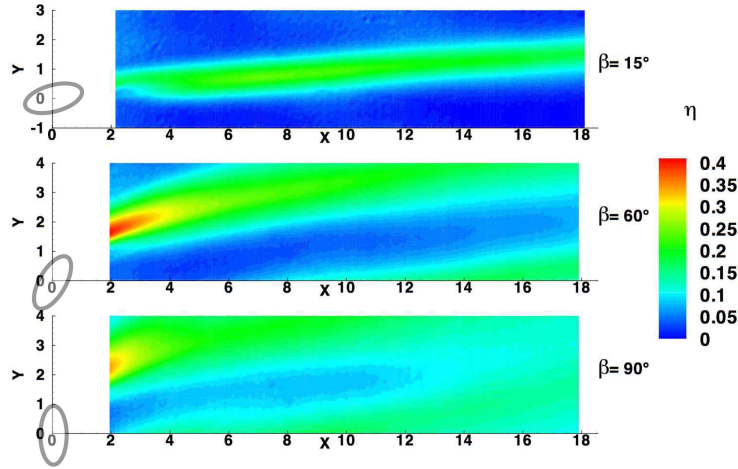
Figure 6.4: Contours of adiabatic effectiveness, $\eta = \frac{T_h - T_{aw}}{T_h - T_c}$ for BR=2, DR=1.5, IR=2.67 or three compound angled injection cases

vorticity which spreads the coolant at downstream distance. Again, the 90°effectiveness contours show that the trajectory of enhanced cooling is roughly along a 60-70°angle with the freestream.

The lateral spread and peak effectiveness hence appear to be caused by two differing mechanisms which are dependent on the compound angle and IR. Firstly, the strength of the streamwise vorticity determines the mixing and spread of the coolant jet. As is clear from the streamwise vorticity contours, the asymmetry of vorticity is determined by the compound angle. Secondly, the momentum flux ratio determines how close to the wall this vorticity will be confined and hence whether more coolant will be present along its trajectory closer to the wall. The peak adiabatic effectiveness is then a direct quantification of the proximity of the coolant film. At greater downstream distances for high momentum flux ratios, the jet has a tendency to travel away from the wall due to higher vertical momentum and so this proximity reduces. The detrimental effect of this jet lift-off is then ameliorated by the coolant spread by the single vorticity.

6.2 Laterally Averaged Adiabatic Effectiveness

The current adiabatic effectiveness results are compared with those from previous published results in Fig. 6.5 and are seen to match within uncertainty bounds. Most data in published literature correspond to a smaller pitch, $S/D = 3$ compared to the larger $S/D = 4$ used in the current results. An experimental data-fit based correlation for describing laterally averaged effectiveness with downstream distance for streamwise angled jets, $\beta = 0°$ is noted in Baldauf et al. [9]. This correlation was fitted with the operating and geometric conditions of the current measurements at the same surface angle and pitch distance. The high and low BR cases match the correlation within the uncertainty associated both with the correlation as well as the experiments
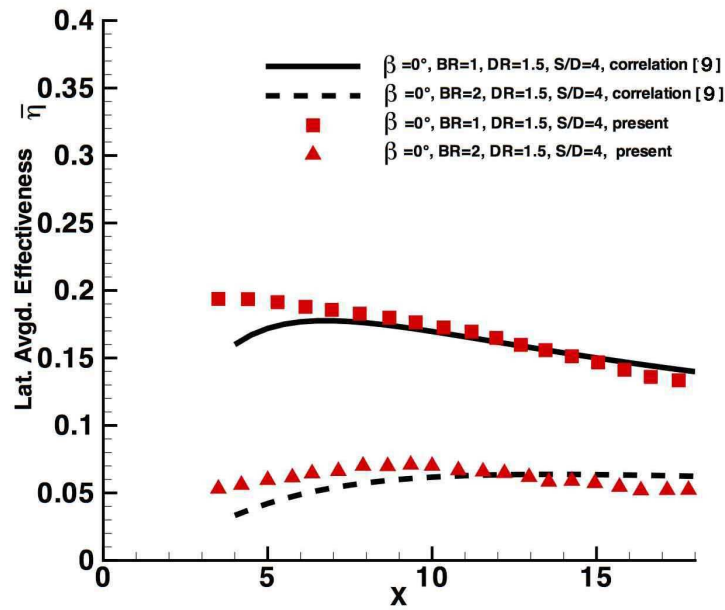
Figure 6.5: Laterally averaged adiabatic effectiveness with downstream distance, X compared to published correlation of Baldauf et al. [9] for streamwise oriented jets
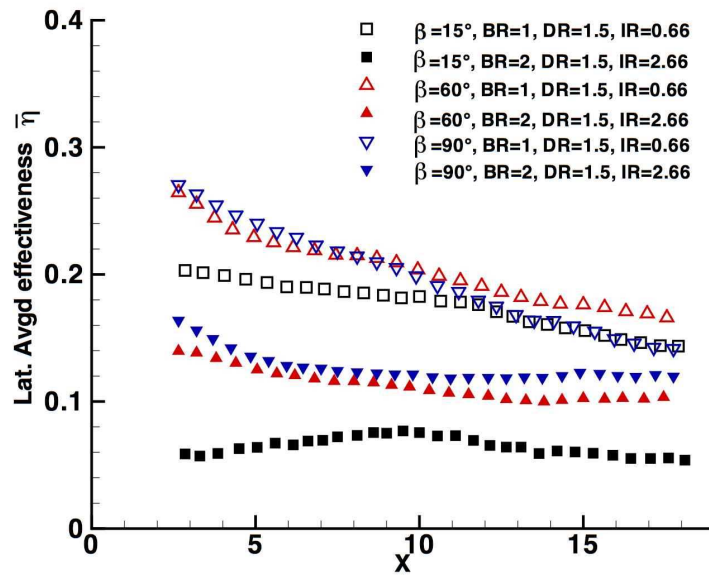

Figure 6.6: Laterally averaged adiabatic effectiveness with downstream distance, X for all compound angled geometries at $DR = 1.5$

thus giving a validation for the correctness of the experimental method. However slight differences in the near-hole regime are observed as the correlations artificially fit a curve that is forced to go to zero at the holes although no measurements can be conducted there. Comparison with previous measurements like Schmidt et al. [99] are incompatible as the pitch distance of $S/D = 4$ used in those measurements would cause a uniformly higher laterally averaged effectiveness than the one used in this study.

A comparison of the laterally averaged adiabatic effectiveness for all blowing ratio cases is shown in Fig. 6.6. In general the higher momentum flux reduces the effectiveness whereas increasing compounding increases it. The 15° injection is seen to have a similar effectiveness curve as a streamwise injection. For $IR = 0.67$, the lower effective penetration leads to greater effectiveness for 60° and 90° cases. However, the IR is lowered by lowering the blowing ratio and so, as the amount of coolant flow is low the decrease in effectiveness for 90° case is pronounced until it drops below that of the 60° case at X=15. For the higher $IR = 2.67$, the high vortex asymmetry and mixing of the 90° and 60°case results in a consistently high effectiveness value. The change in laterally averaged effectiveness for the two high compound angled cases, 60° and 90° is much lesser for the increase in IR as compared to 15° case.

6.3 Boundary Layer Shape

The boundary layer evolution is directly dependent on the streamwise vorticity as the rotating fluid entrains the low momentum fluid over to one side depending on its orientation. However, these features are sensitive to the momentum flux ratio, IR as well. Figures 6.7, 6.8 and 6.9 shows the delineation of the boundary layer through streamwise velocity surface contours. The injection is always at the origin of the coordinate system and the direction of the freestream is from left to right, i.e. from $X = 0$ towards $X = 8$. The iso-contour $U/U_h = 0.98$ delineates the profile of the boundary layer modified by the injection.

One of the reasons that compound angled film cooling is used is because of coolant spread and uniformity. This means that even at moderately high blowing ratios, the coolant core is mostly spread laterally rather than ejected as a high momentum jet. The boundary layer shape with DR=1.5 for a $\beta = 15°$ injection is shown in Fig. 6.7. The high momentum core is absent due to the lower momentum flux ratios and hence only the $U/U_h = 0.98$ velocity iso-contour is visualized. The lower IR=0.67 case in Fig. 6.7 (a) shows a larger spread as most of the coolant is injected within the boundary layer extent causing a larger momentum deficit wake zone nearer to the wall compared to Fig. 6.7 (b). The IR=2.67 case shows a greater pinching of the boundary layer at the sides of the jet due to the stronger remnant counter rotating vortex pair (CVP). One leg of this CVP, though reduced is not completely absent. The net effect is that the boundary layer delineating contour at $Y = 2$ is at a higher wall normal distance than at $Y = -1$ due to asymmetry.
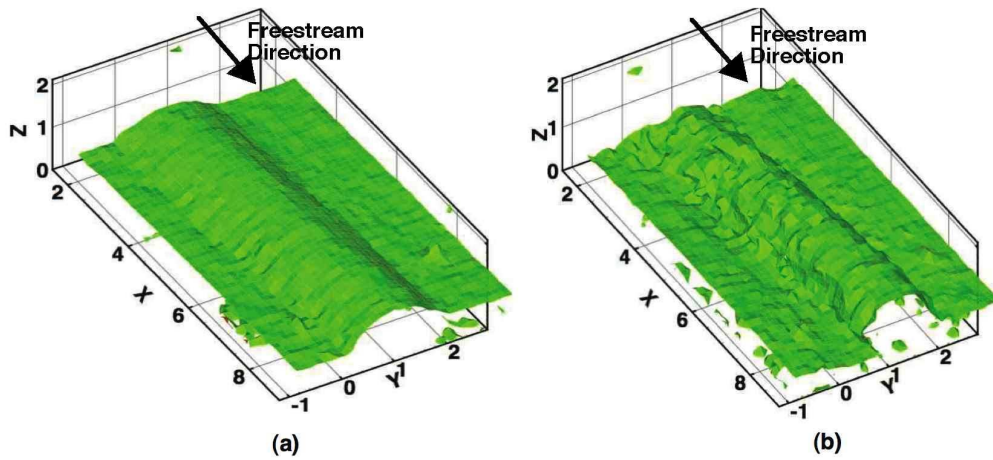
Figure 6.7: Velocity iso-contour $U/U_h = 0.98$ delineating the boundary layer for $\beta = 15°$ at (a) BR=1, DR=1.5, IR=0.67, (b) BR=2, DR=1.5, IR=2.67
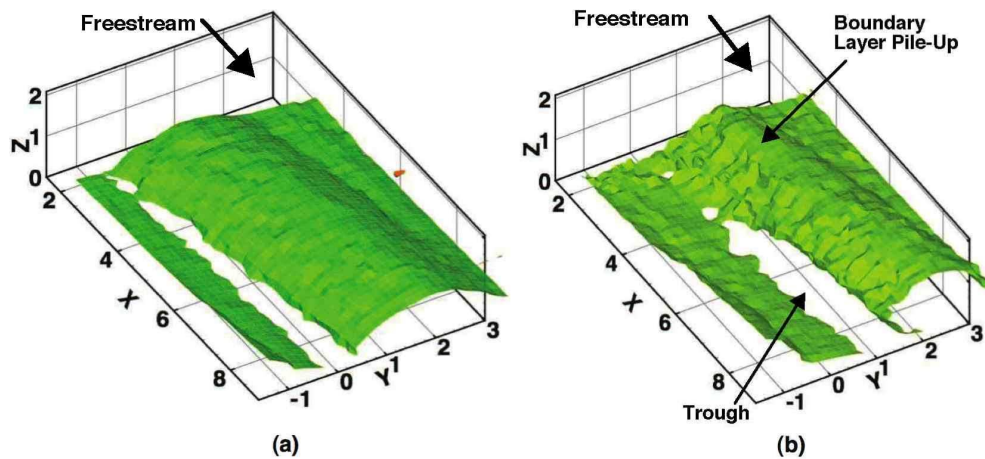
Figure 6.8: Velocity iso-contour $U/U_h = 0.98$ delineating the boundary layer for $\beta = 60°$ AT (a) BR=1, DR=1.5, IR=0.67, (b) BR=2, DR=1.5, IR=2.67

The boundary layer velocity iso-contours for $\beta = 60°$ for the two cases of BR=1 and BR=2 at DR=1.5 are shown in Fig. 6.8 (a) and (b) respectively. The lower blowing case shows a flatter and less disturbed boundary layer profile compared to the higher blowing case. The IR=2.67 case also shows that the delineating contours of the boundary layer profile are at a greater wall-normal distance enclosing not only the primary vortex core under it but also a momentum deficit zone with greater lateral spread. The strong asymmetric vortex core in both cases is seen to have entrained the low velocity boundary layer fluid from one side of the vortex (namely near $Y = 0.5$) causing a trough and deposited it onto the other side near $Y = 2.4$, with the pile-up in Fig. 6.7 (b) especially significant. The heat transfer coefficient beneath the boundary layer pile up could be expected to be higher than at the trough.
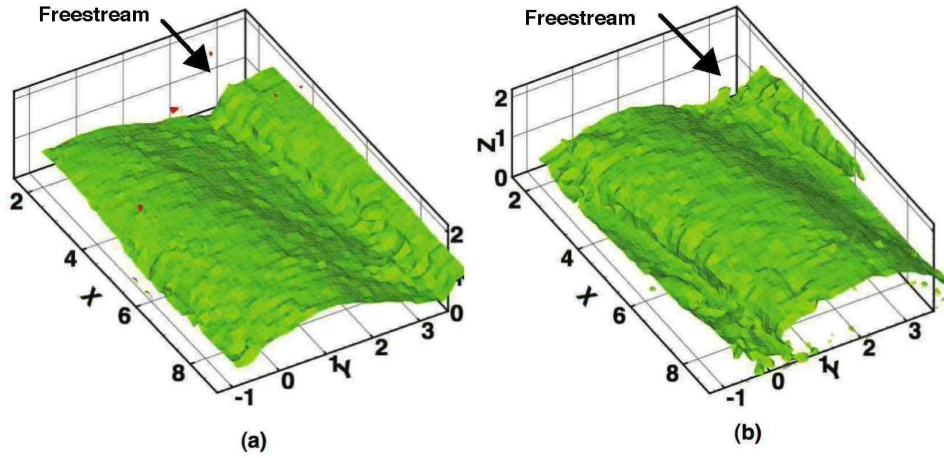
Figure 6.9: Velocity iso-contour $U/U_h = 0.98$ delineating the boundary layer for $\beta = 90°$ AT (a) BR=1, DR=1.5, IR=0.67, (b) BR=2, DR=1.5, IR=2.67

The $\beta = 90°$ injection case for the two different injection rates is shown in Fig. 6.9. Both the blowing cases have a very flat boundary layer profile with a larger pile up of low momentum fluid when there is greater coolant mass injection, as seen in Fig. 6.9 (b). This can be ascribed to the stronger asymmetric vortex core which spreads the coolant strongly and dissipates the strong momentum jet core in lateral directions. Furthermore, the difference in the boundary layer pile-up is not very stark at the two different blowing ratios. In fact it can even be argued that the greatest increase in the boundary layer pile up shape with increasing IR is for the low compound angled injection shown in Fig. 6.7 and this difference reduces with greater compounding as seen in Fig. 6.8 and 6.9.

Boundary layer modification information is also useful from the point of aerodynamic control, as the creation of larger and flatter boundary layers would cause re-energizing especially when there is a concern of separation in film cooled environments. From a heat transfer perspective a boundary layer pile-up could also give an idea of the regions where greater heat transfer enhancement is to be expected, but this is only if it encloses large regions of coherent unsteadiness.

6.4 Wall Normal Vorticity and Heat Transfer Coefficient

One of the conjectures of McGovern and Leylek [84] was that the reason the heat transfer coefficient is higher in compound angles is because the turbulence at the wall is significantly increased where crossflow accelerates underneath the coolant at the edges of the jet. The explanation proffered by Goldstein and Jin [49] was similar but mentioned that the scouring of the boundary layer by the asymmetric vortex core would cause differences in heat transfer along the injection path. The heat transfer augmentation trends for streamwise injection have been well documented and a correlation to predict the same has been shown in Baldauf et al. [10]. Compound angled
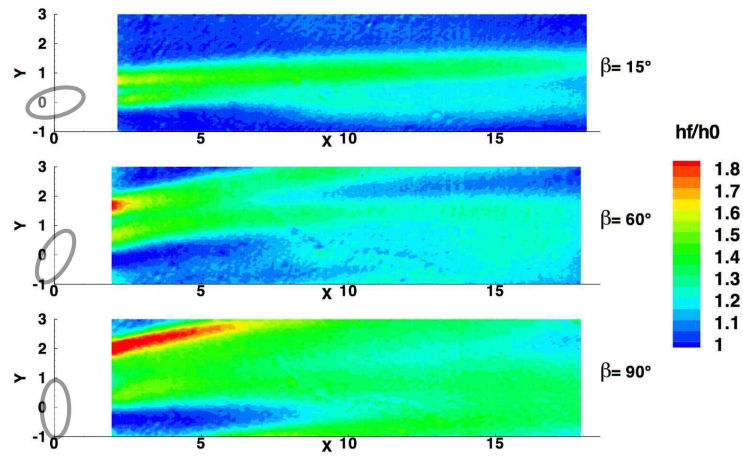
Figure 6.10: Contours of normalized heat transfer coefficient, h_f/h_0 FOR BR=1, DR=1.5, IR=0.67 for three compound angled injection cases
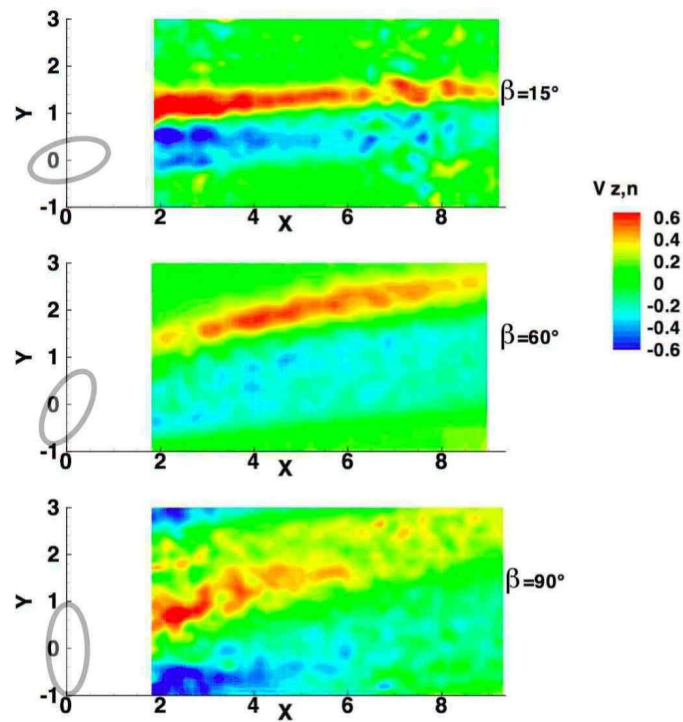
Figure 6.11: Normalized wall-normal vorticity iso-contours at Z=0.5 above the wall for BR=1, DR=1.5, IR=0.67
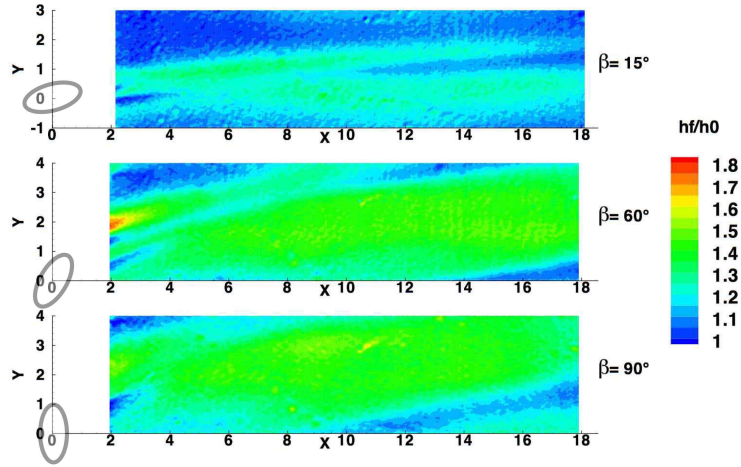
Figure 6.12: Contours of normalized heat transfer coefficient, h_f/h_0 FOR BR=2, DR=1.5, IR=2.67 for three compound angled injection cases

heat transfer however, is relatively less studied and the underlying mechanisms which influence the trends are still unclear.

The shape of the boundary layer is created by the streamwise vorticity, however there is another feature that produces significant mixing in the close to wall region in the form of wall-normal vorticity. As observed by Fric and Roshko [44], these are also known as wake vortices since they are primarily formed in the wake of the jet blockage to the freestream. These vortices are mainly unsteady as they start out by being shed from the horse shoe vortex as the jet obstructs the freestream but then the streamwise vortex also contributes to their development and lateral convection. These wall-vortices are primarily situated as vertically oriented tubes which connect the jet with the near wall fluid and enhance the mixing thereof. Owing to the fact that they are highly unsteady, PIV can only capture time averaged traces of their extent and spread. These wake vortices could indicate the presence of increased unsteadiness and possibly higher heat transfer coefficients. The wake vorticity can also be thought of as the measure of the shear stress in the near wall fluid layer, which directly affects the near wall turbulence and hence the heat transfer coefficient. This conjecture may be tested by plotting the heat transfer coefficient contours and the wake vorticity contours for the same regions.

Figure 6.10 shows the non-dimensionalised heat transfer coefficient, h_f/h_0 for a BR=1 case for all three compound angled geometries. For the 15° case the heat transfer augmentation is not very significant. The $\beta = 60°$ injection shows a high lateral spread of heat transfer augmentation. The $\beta = 90°$ case has an almost uniform heat transfer enhancement over the entire pitch with higher peaks than the 60° case as well as larger augmented heat transfer regions.

The wall-normal vertical oriented vortices or the wake vortices are shown at a wall-normal distance of $Z = 0.5$ for the three geometries at BR=1, DR=1.5 in Fig. 6.11. The $\beta = 15°$ contour
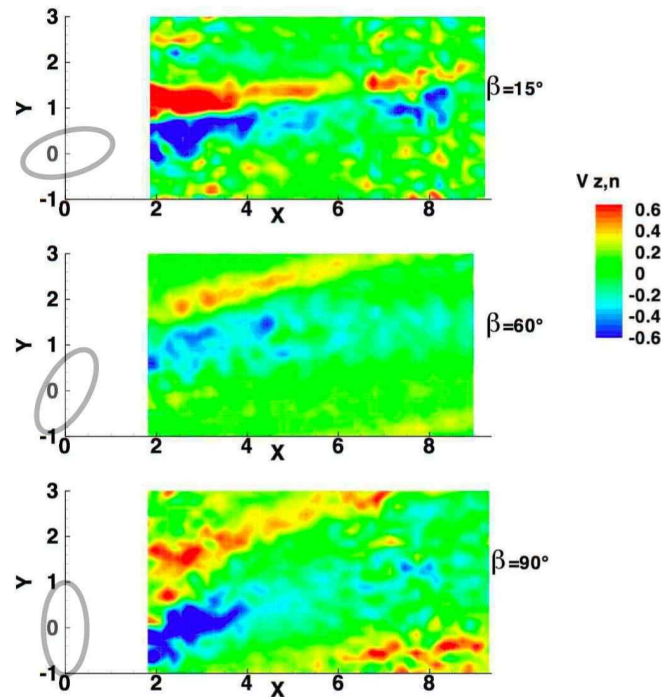
Figure 6.13: Normalized wall-normal vorticity iso-contours at Z=0.5 above the wall for BR=2, DR=1.5, IR=2.67

plot shows the two opposite signed upright vortices emanating from the interaction of the jet with the crossflow. The vorticity extent has larger lateral spread for the 60° case. It must be noted however, that the positively signed vorticity does not get diminished or eliminated like the streamwise vorticity, $V_{x,n}$ with the compounding. The trajectory of the heat transfer augmentation is roughly aligned along the paths of the wall normal vortices, but they *do not correlate exactly* with their local magnitudes. The sign of this vorticity is not important since it is only indicative of greater shear stress and coherent unsteadiness. The 90° injection has large spreads of heat transfer augmentation regions due to the strong and widely distributed wall-normal vorticity visible in Fig. 6.11.

The increased momentum flux results in a stronger asymmetric streamwise vortex core, which in turn also affects the jet-freestream interaction. The strength and size of the wall-normal vorticity is a direct manifestation of this increased interaction.The higher IR case in Fig. 6.13 shows a stronger vorticity for the 15° case with both legs aligned with the injection direction. Figure 6.12 shows the 15° IR=2.67, heat transfer coefficient to be at a peak at the point of reattachment near X=7 and subsequently mixing out. As the compound angle is increased to 60° the vorticity becomes asymmetric, however the negatively signed vorticity is spread over a larger lateral space as well as having higher peaks compared to the lower momentum flux ratio contours shown in Fig. 6.11. This indicates more areas of coherent unsteadiness of similar magnitudes. The areas downstream of 60° show a large and uniform spread of high h_f/h_0.
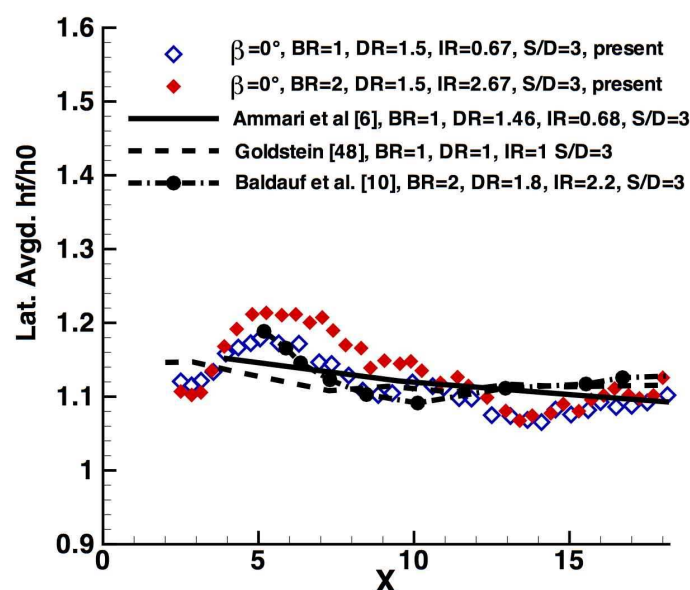
Figure 6.14: Laterally averaged heat transfer coefficient augmentation, h_f/h_0 compared with published results from Ammari et al. [6], Goldstein et al. [50] and Baldauf et al. [10]

It must be added however, that although wall-normal vorticity increases in magnitude and spread for increased IR and compound angle, their local trajectories do not correlate well with the heat transfer coefficient enhancement. This points towards an indirect effect of the flow structure on the heat transfer. The coherent unsteadiness as represented by the wall-normal vorticity is responsible for increasing near-wall turbulence due to the mixing. This turbulence could be conjectured to have increased the heat transfer coefficient. However, since no turbulence measurements could be made for the current tests a direct correlation cannot be ascertained.

The laterally averaged heat transfer coefficients for streamwise oriented film cooling holes have been studied in literature. Figure 6.14 shows a comparison of some test results for streamwise cases for validation with previous measurements. In literature most cases are shown for S/D=3 so a comparison with S/D=3 for streamwise injection is shown for comparison. Heat transfer augmentation measurements even in literature are seen to vary widely for the same blowing conditions as they are dependent on the reference h_0, the method used to derive it, the turbulence levels as well as the set-up of the rig. In spite of these variations, the current results match older studies on streamwise injection geometries by Ammari et al. [6], Goldstein et al. [50] and Baldauf et al. [10] in terms of average levels even though some of the operating conditions are slightly different.

The laterally averaged h_f/h_0 compound angled cases are shown in Fig. 6.15. On an average, increasing compound angle and increasing IR tend to increase the average heat transfer augmentation. The 15° cases are both low and close to the value of a streamwise injection. The 60°,
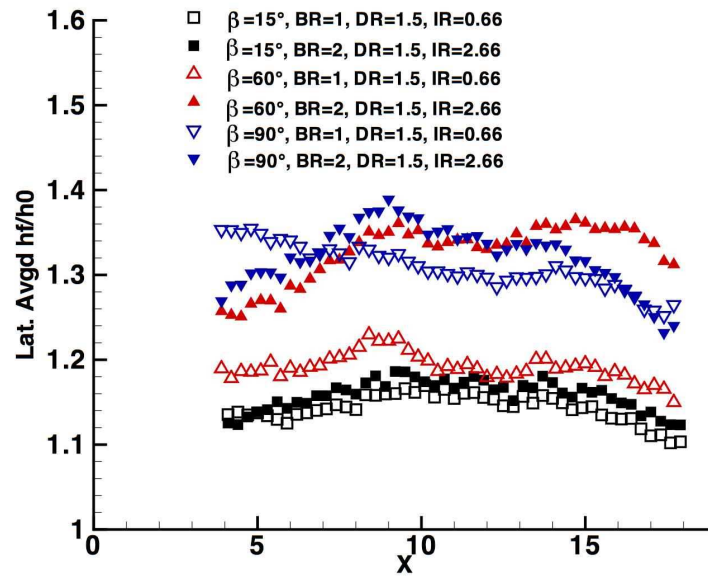
Figure 6.15: Laterally averaged heat transfer augmentation, h_f/h_0 at DR=1.5

IR=0.67 injection has a higher h_f/h_0 which increases significantly at IR=2.67 due to the stronger wall-normal vortices. The heat transfer augmentation is more or less stable with downstream distance as the phenomenon of jet lift off and re-attachment which typically enhances heat transfer coefficient for streamwise injection is absent. The 90° case shows a very high average level of heat transfer augmentation at IR=0.67 which increases a little at BR=2.67. The initial high rate of mixing and and vigorous mixing manifested by the strong wall-normal vorticity for the 90° case leads to the enhanced heat transfer and this does not significantly increase at higher IR.

6.5   Net Heat Flux Reduction

The adiabatic effectiveness is the primary indicator of the performance of a film cooling geometry. Regions with high effectiveness are those where the coolant is present closer to the wall, as well as those where the hot fluid is prevented from coming in contact with the wall. Rather than localized peaks in adiabatic effectiveness, the aim of most film cooling designers is to achieve the largest possible spread for a limited amount of coolant which remains attached to the wall, and compound angled injection succeeds to a degree. The heat transfer coefficients, however increase for compound angled geometry. As these two quantities are both important for film cooling designers a combined quantification was sought by Sen et al. [100] through the use of a Net Heat Flux Reduction (NHFR) given by Eq. 6.1. By putting the value of $1/\theta = 1.6$ for an engine representative value a net performance factor may be found. Typically, these are spatially averaged values over the measurement plate by putting the effectiveness and heat transfer results
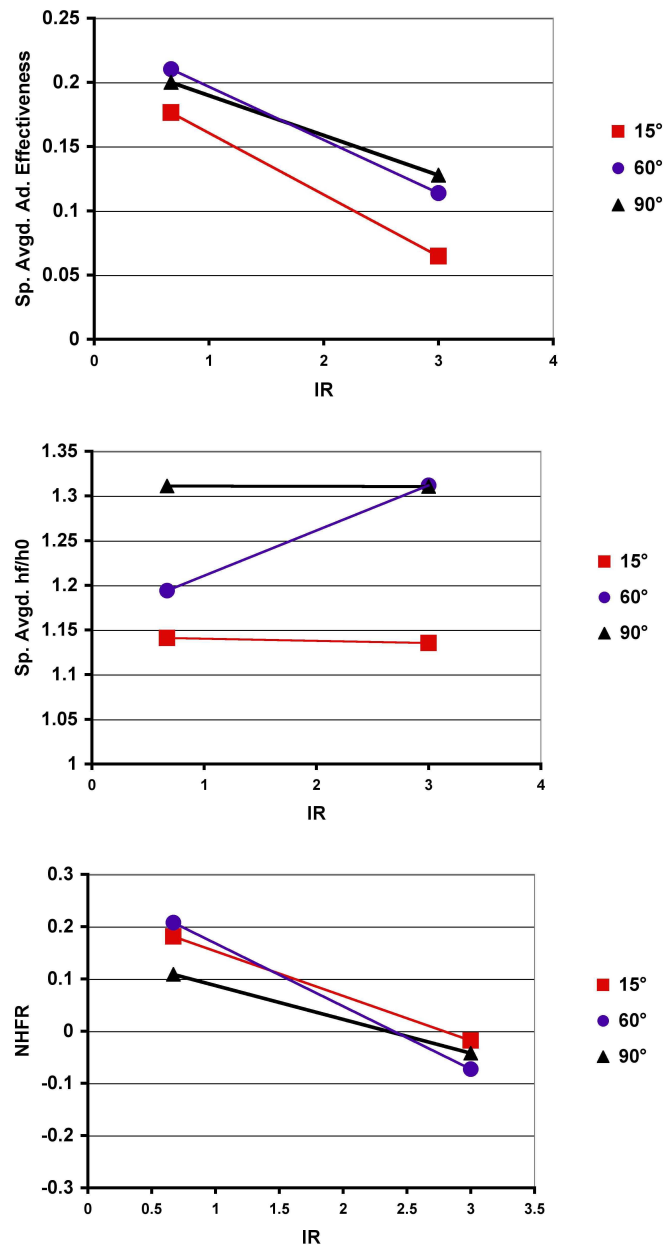
Figure 6.16: Spatially averaged cooling quantities plotted against the momentum flux ratio for 15°, 60°and 90°

together.

$$NHFR = 1 - \frac{h_f}{h_0}\left(1 - \frac{\eta}{\theta}\right) \tag{6.1}$$

This quantity is used to give an overall view and comparison of various strategies. The spatially

averaged quantity of NHFR is used based on the spatially averaged values of adiabatic effectiveness and heat transfer coefficient. All three spatially averaged values are shown in Fig. 6.16. The adiabatic effectiveness in general increases with greater compounding, but the heat transfer coefficient also increases. For the spatially averaged adiabatic effectiveness, the difference between 60 and 90°is lesser than the measurement uncertainty. For a 90°case, the heat transfer coefficient is already quite high even for low blowing and hence the change is not much, however for the 60°injection the increase with momentum flux ratio is substantial as the unsteadiness becomes stronger. The low compound angled of 15°does not have significant heat transfer enhancement at high IR as well. The net heat flux reduction thus behaves accordingly, being a function of the effectiveness and heat transfer coefficient. It must be noted however that since these figures show a spatial average, these quantities must be viewed in light of the fact that they are calculated for a S/D=4, i.e. higher pitch distances than what were previously presented in literature (Sen et al. [100]) and hence the added cooling due to jet merging is reduced. The NHFR value can also be recalculated by changing the non-dimensional metal temperature, θ depending on the application.

6.6   Summary

1. Averaged adiabatic effectiveness is about twice as high than for streamwise injection at large compound angles (60°and 90°) even for high blowing ratios.

2. Effectiveness is high for regions where the coolant is spread over a larger region and hot fluid from the freestream is not strongly entrained towards the surface.

3. At low IR=0.67, the jet is close to the wall causing near hole rise in effectiveness, but due to lower mass injection less bulk coolant is available downstream. A quicker decay of laterally averaged effectiveness with downstream distances is thus observed after initial higher peaks where the coolant is attached to the wall.

4. At high IR=2.67, the absence of a CVP lowers jet lift-off for high compound angled. The asymmetric streamwise vorticity also helps to spread the large bulk coolant laterally over the surface. Due to the strong spreading by the asymmetric vorticity, the effectiveness does not decay substantially with downstream distance as it would have due to the jet lift-off.

5. The boundary layer is preferentially piled up on one side of the emanating jet by the asymmetric primary vortex core. For a higher IR the profile shape becomes thicker on one side of the jet. Increasing the compound angle causes a flatter but more laterally spread boundary layer shape modification. Thus, a higher compound angle geometry re-energizes the boundary layer with lesser lift off.

6. The normalised heat transfer coefficient, h_f/h_0 in general increases with higher compounding mainly due to increased jet-freestream interaction and mixing.

7. Wall-normal vorticity is known to cause mixing between near wall fluid and the jet. These flow structures are also representative of coherent unsteadiness and shear in the near wall region thereby giving an indication of the near wall turbulence enhancement which could not be directly measured.

8. Wall-normal vorticity is asymmetric with one leg laterally spread more than the other. The trajectory roughly follows that of the streamwise vorticity but with added intensity increases along the jet edges. The local heat transfer augmentation does not directly correlate with the local wall-normal vorticity very well.

9. Increasing momentum flux ratios tend to increase the laterally averaged heat transfer coefficient. The increase in spatially averaged heat transfer coefficient is much greater for a 60°injection rather than the 90°injection. This is because the unsteadiness and proximity to the wall for a 90°jet is already quite high even at low IR, but for a 60°injection a stronger streamwise vorticity at higher IR tends to increase the heat transfer.

10. Mid range compound angled (45-70°) film cooling would be useful for areas on the pressure side of a turbine where there is strong IR fluctuation as the effectiveness is less sensitive to change in IR. However very high compound angles (80-90°) can be used for having a high effectiveness at all IR too, but on the other hand they have high heat transfer coefficient and hence low NHFR.

Chapter 7

Pulsated Compound Angled Film Cooling

Film cooling has traditionally been studied as a steady flow problem. In fact many of the industry standard empirical "cooling curves", that designers use to place film cooling holes according to the heat load, are all based on steady tests. However, in rotating machinery there is significant periodic unsteadiness that a film cooling injection regime would have to operate in. The periodic wakes emanating from rotor-stator interaction would significantly affect the flow structure and hence cooling performance of a film cooling hole. Experimental measurements showing the effect of this periodic unsteadiness was shown for the first time by Abhari [1]. The primary flow effect due to periodic unsteadiness is that the momentum flux ratio pulsates. This is so because the plenum is provided with a constant mass flow but the external cross flow pulsates with respect to traveling pressure wakes. In the near hole region this amounts to a periodic unsteadiness of the momentum flux ratio. Studies by Bons et al. [16] showed that for streamwise tests, at high momentum flux ratios, periodic unsteadiness doesn't have much effect on effectiveness, but at lower blowing ratio there is a slight reduction, possibly due to some extra jet lift off. In the current measurements the main comparison is between a pulsated jet and a steady jet for compound angled film cooling and so change in other important parameters like amplitude, duty cycle and large variations in frequency are not studied.

Reduced Frequency

In the current experimental campaign, the periodic pulsations in momentum flux ratio are simulated by means of a rotary valve which causes a periodic pressure fluctuation in the plenum. This arrangement is discussed in Section 2.2 and the pulsator arrangement is shown in Fig. 2.2. The amplitude of oscillations cannot be changed and is typically less than 25% of the mean blowing ratio. The main flow remains steady but the injected jet oscillates, mimicking the periodic oscillations due to the rotating turbomachinery regime. A reduced frequency based on freestream

conditions and coolant hole diameter was described in Bernsdorf et al. [14] as $f_r = fD/U_m$. The characteristic reduced frequency based on the coolant conditions and using the length of the jet pipe (in all present measurements this is 4 hole diameters, L=4D), $f_c = fL/U_c$ is according to the definitions commonly used by Burdet and Abhari [23]. A modification of this reduced frequency is also used in Ligrani et al. [78] where a coolant Strouhal number, $St_c = 2\pi fL/U_c$ is defined. A jet can be said to be in the quasi-steady regime when, $f_c < 1$ or $St_c < 1 - 2$ according to Burdet and Abhari [23] and Ligrani et al. [78]. Typical engine conditions also satisfy the condition, $0.02 < f_c < 1$. As shown in the Tables 7.1 and 7.2, all the measurements are in the quasi-steady regime and bounds on f_c are well within the engine representative condition. However owing to the limitations on the pulsator, extreme cases of $f_c >> 1$ could not be measured. However, these conditions occur in an engine only for very low coolant Mach nos. on the pressure side of the turbine.

The effect of pulsation depends on the magnitudes of the frequency, the duty cycle of pulsation as well as the amplitude of pulsations. Some studies for the effect of these parameters on the performance of streamwise oriented holes were performed by Coulthard et al. [30, 31]. Very few measurements of a pulsating jet exist in literature. An important question with respect to such pulsating flows, is whether a quasi-steady assumption is viable for unsteady jets. This implies that a pulsating jet may be assumed to be a steady jet blowing at a BR which is averaged over all the different phases. Bernsdorf et al. [14] has shown that for high frequencies ($f_r \geq 0.01$) as long as the amplitude of pulsation is within 30% of the mean BR a quasi steady assumption is valid, however for very small frequencies ($f_r \sim 0.001$) this is no longer true as the jet flow structure itself is very momentum flux dominated during the crest and trough of the jet, but this was probably due to the fact that the pulsator had a large change in amplitude at low frequencies rather than any effect of the frequency itself. Simulations by Burdet and Abhari [23] have shown that for medium-high $BR \sim 1.25$, pulsations have a detrimental effect on the downstream effectiveness due to induced jet structure rupturing, but for smaller BR the downstream effectiveness is enhanced due to greater jet attachment. These measurements are all for streamwise oriented jets.

There is scant evidence in literature for any systematic investigation into oscillating compound angled jets. The flow velocity results shown in this chapter are some of the first examples of periodically pulsating, whole field, phase resolved, three dimensional velocity measurements of a compound angled flow. These are additions to the experimental database initiated by the pulsated streamwise jet flow field measurements shown in Bernsdorf [12]. The accompanying thermography measurements also show the effect of pulsations on the effectiveness and heat transfer coefficients. It is observed that due to the laterally oscillating movement of the compound angled injection with change in momentum flux ratio, the jet flow structure responds differently to pulsations compared to streamwise jet pulsations. It must be noted however, that two oscillating frequencies were measured, $f = 250$ Hz and 400 Hz. These result in two different f_r but in varied f_c which will also depend on the coolant velocity and hence the blowing ratio. However, owing

β	BR	DR	f [Hz]	D [mm]	$f_r = \frac{fD}{U_m}$	$f_c = \frac{fL}{U_c}$	U_m [m/s]
0°	2	1.3	0	7	0	0	125
0°	2	1.3	400	7	0.018	0.056	125
60°	2	1	250	5	0.01	0.022	115
60°	2	1.3	400	7	0.018	0.056	125

Table 7.1: A table summarizing the operating conditions of PIV flow field measurements conducted for pulsating compound angled flow. Mach no., $M = 0.3$

β	BR	DR	f [Hz]	D [mm]	$f_r = \frac{fD}{U_m}$	$f_c = \frac{fL}{U_c}$	U_m [m/s]
0°	1, 2	1.5	250	5	0.01	0.057, 0.03	125
0°	1, 2	1.5	400	5	0.017	0.088, 0.046	125
60°	1, 2	1.5	250	5	0.01	0.057, 0.03	125
60°	1, 2	1.5	400	5	0.017	0.088, 0.046	125
60°	1, 2	1.3	250	5	0.01	0.052, 0.026	125
60°	1, 2	1.3	400	5	0.017	0.08, 0.041	125

Table 7.2: A table summarizing the operating conditions of infrared thermography measurements conducted for pulsating compound angled flow. Mach no., $M = 0.3$

to the fact that the difference in the f_c for the different cases is so low, so as make them all qualitatively comparable at the same f_r.

As measuring phase resolved velocity flow field through stereoscopic PIV is expensive in terms of cost as well as time, all the operating conditions shown in previous chapters have not been measured but only certain representative ones, which could give enough insight about the principle elements of the pulsating flow field. These operating conditions are summarized in Table 7.1. Infrared thermography could be conducted for a larger number of parameters and these operating conditions are summarized in Table 7.2. Only the most relevant or insightful measurements of the total data matrix have been discussed in this chapter.

7.1 Pulsating the Jet

In a real turbine engine, the periodic pulsations to the jet structure are actually being caused by the pressure wakes from the rotor-stator interaction. In the current study the converse is done, i.e. the main flow is held steady while the injection blowing ratio is pulsated. Since the density ratio is held constant this results in an IR pulsation. The question naturally arises whether this converse pulsation is comparable to static pressure pulsations of the main flow. In the current
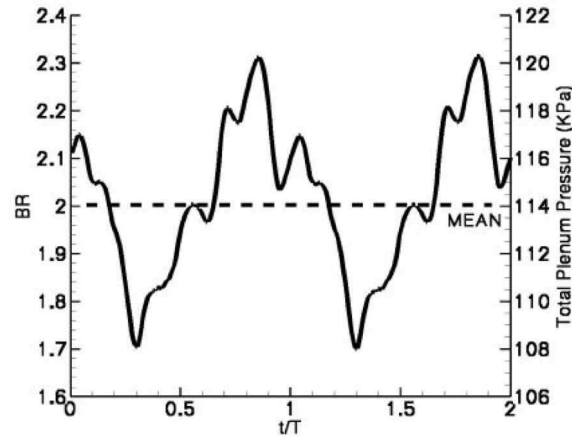
Figure 7.1: Blowing ratio variation based on pressure measurements in the plenum of the injecting hole

approach the jet is pulsated by a rotary valve thereby altering the mass flow and blowing ratio of the jet. The shape of this variation and the plenum pressure variation is shown in Fig. 7.1. The typical blowing ratio pulsation waveform caused by the pulsator are also shown in Fig. 2.3 and 2.4. The justification for pulsating the jet instead of the flow is required and previous works mainly those by Ligrani et al. [78, 79] as well as the computational works of Burdet and Abhari [23] are referenced to understand the main differences.

In the streamwise pulsating film cooling computations of Burdet and Abhari [23] a plot comparing the waveform of blowing ratio with upstream static pressure oscillations was presented. It was observed that for large frequencies, i.e. engine representative frequencies, the blowing ratio pulsation was of the same form in terms of waveform and frequency as the static pressure pulsation. The effect of traveling compression waves and pulsating the freestream boundary layer which were second order effects would understandably not be captured by only pulsating the jet. Two operating regimes both at DR=1 but at low BR=0.75 and BR=1.25 were used and the change in trajectory and coolant distribution with changing mass flow was reckoned to the be first order effect, while the pulsating boundary layer was a second order effect.

Streamwise film cooling under bulk flow pulsations were also studied by Ligrani et al. [78] and Ligrani et al. [79]. Apart from the change in blowing ratio oscillation the bulk flow pulsations were important as they created oscillations in the upstream and downstream boundary layer and at very high reduced frequencies, the oscillation in near hole static pressure was not in phase with variation in blowing ratio. Although in the end it was noted that the primary effect of the carefully generated static pressure oscillation was the change in injection flow rates. The change in trajectory and 'waviness' of the jet were the main cause of change in wall temperature behavior. These flow features stemmed from the fact that mass flow through the jet was forced to accumulate and then expand based on the exit pressure variation. This alternating accumulation and expansion are readily produced by a mass flow oscillation as well. One important distinction

that should be made between the experiments in Ligrani et al. [78] and Ligrani et al. [79] that most of the pulsation flow structure and effectiveness data corresponds to low blowing ratio regimes (BR¡1) with no density ratio for a streamwise injection. The measurements in this study are primarily for high BR and IR. At high IR, coolant proximity and vorticity become more important than alternating accumulation of bulk coolant which is prevalent for the low IR jets studies previously.

Another important observation from Ligrani et al. [78] a quasi-steady film behavior is obtained when only one pulsation or part of it is acting on all the fluid passing through the length of the cooling hole, that is, pulsation time scale is higher than the time the jet takes to travel through the metering length, $(1/2\pi f) > (L/U_c)$. For a quasi-steady regime the trajectory of the jet and the flow structure is similar to the steady injection at the instantaneous blowing rate. If this condition is maintained then there is qualitatively no difference between a flow pressure pulsation and a jet pulsation. For the current experiments the above condition is always valid. In the current case, $U_c = 120-180$ at different IR and $f = 250$ and 400 Hz, $1/2\pi f = 0.4-0.63\times10^{-3}$ whereas $L/U_c = 0.1 - 0.16 \times 10^{-3}$.

7.2 Velocity Flow Structure

The flow field of a periodically pulsating streamwise jet was discussed in detail by Bernsdorf [12], Bernsdorf et al. [14]. For a BR=1 pulsation at 250 Hz (or $f_r = 0.01$), it was observed that the flow structure was dictated by an alternating jet lift-off and reattachment as the momentum flux of the jet increased or decreased. One of the primary aims of studying the jet interaction is for the repercussions that this has on the modeling of unsteady near hole jet ejection. If a quasi-steady approach is used then a pulsating jet may be modeled by a steady jet of an equivalent blowing ratio. The amplitude of the BR variation is about ±0.3 and the duty cycle is about 50% as shown in Fig. 7.1. The pulsator is operated in the default mode without any damping effects.

The quasi-steady nature of a pulsating jet can be ascertained by comparing it to a steady jet. Figure 7.2 shows the velocity contours at a $X/D = 4$ plane for a steady jet and a pulsating one, wherein the velocity flow field is phase averaged over the 8 separate phases into which the PIV measurement was resolved. The phase-averaged flow field resembles the steady jet to a high degree. Similar observations were made previously in Bernsdorf et al. [14]. Those measurements showed that for low BR=1, the phase averaged velocity flow structure closely correlated to the steady flow. The current measurements shown in Fig. 7.2 are made for BR=2, DR=1.3, IR=3.07. They show that for a high IR, the quasi-steady assumption may be used for the high BR and moderate density ratio case as well. Based on other measures like comparisons of trajectory and circulation, it has been shown in Bernsdorf et al. [14] that a streamwise injection in the near hole may, for the most part, be assumed to be quasi-steady.

In comparison, a similar picture is shown for a canonical compound angled injection at $\beta = 60°$
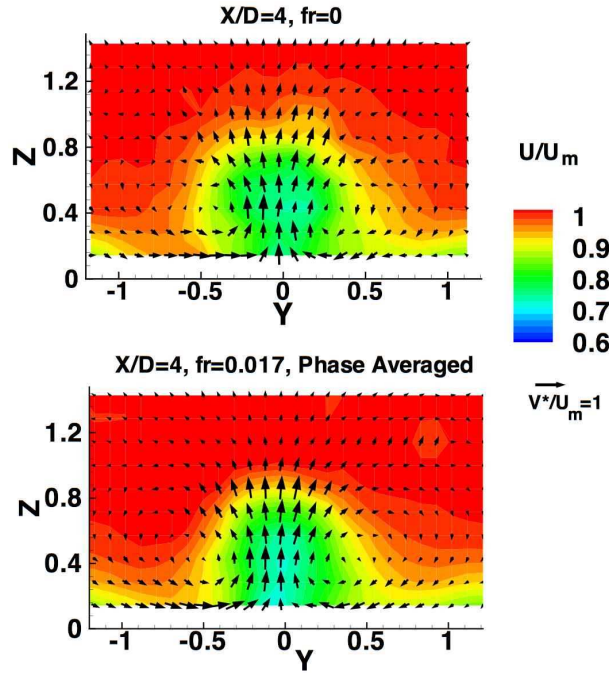
Figure 7.2: Streamwise velocity contours and plane tangential flow vectors at $X/D = 4$ for $\beta = 0°$, BR=2, DR=1.3, IR=3.07 for steady and time-averaged pulsated case, $f = 400$Hz, $f_r = 0.017$

for BR=2, DR=1.3, IR=3.07 with steady and a $f_r = 0.017$ pulsation in Fig. 7.3. The velocity contours from the phase-averaged measurements do not coincide completely with the steady injection as much as in the streamwise case. The wake zone in the pulsated case has a wider spread and is even lower in the near wall region compared to the steady case. The vortex strength is seen to be lesser in the average picture. It is not possible to select one particular point in the jet as an indicator of the jet centre for such a mixed out flow and hence tracking a trajectory for such flows is not advisable. The velocity contours show a greater jet proximity for the phase averaged unsteady compound angled jet than a steady jet.

The individual phase resolved velocity flow field for this case is shown in Fig. 7.4 at two different downstream distances $X/D = 4$ and 6. The velocity flow field is shown for three different phases, or t/T, where T represents the time taken for a single pulse. These phases are selected such that they best represent a crest, a trough and an intermediate phase. Each pulsation cycle was divided into 8 parts and phase averaged in PIV measurements. The two sets of figures shed light on the differences in pulsation for compound angled and streamwise injection flow structure. As the pulsation goes through a trough at $t/T = 2/6$ to a crest at $t/T = 6/6$, the size of the jet also correspondingly increases. However, it can be clearly seen that the movement of the wake zone laterally towards $Y = 1$ increases as the effective instantaneous momentum flux ratio reaches its peak at $t/T = 6/6$. A high momentum coolant jet is seen to the left of the boundary layer delineating velocity layer at $t/T = 6/6$ at $X/D = 4$. This shows a clear lateral oscillation of
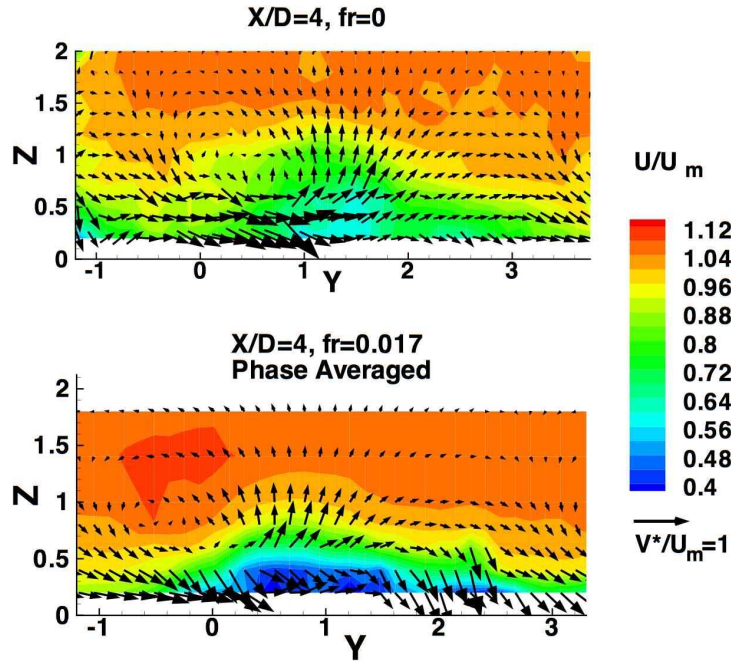
Figure 7.3: Streamwise velocity contours and plane tangential flow vectors for $\beta=60°$, BR=2, DR=1.3, IR=3.07 for steady and time-averaged pulsated case, $f = 400$Hz, $f_r = 0.017$

the injected jet with changing momentum flux. Due to this oscillation the vortex formation is weaker and the phase averaged velocity contours in Fig. 7.3 show a lesser intensity of the high momentum coolant jet and lower lateral displacement compared to the steady case. The figures for the same phases at $X/D = 6$ show a very laterally mixed out velocity zone, which does not change significantly from crest to trough. This shows another feature of oscillating compound angled jets which is, that the effect of pulsation reduces with downstream distance, as the jet is strongly mixed out and local momentum intensity differences are minor from phase to phase.

For a moderate momentum flux ratio of 2.67, a quasi-steady assumption could still be valid for downstream distances (say after $X/D = 4$), if a slight lowering of effective momentum flux ratio is accounted for. For instance the condition corresponding to a phase of 4/6 matches the steady case as well as the phase averaged results

Phase resolved measurements at a lower frequency of 250 Hz, corresponding to $f_r = 0.01$ are also carried out, but for a high momentum flux ratio of IR=4. As the frequency is lower than the previous case, it was feasible to divide a pulsation cycle into larger number of separate phases numbering 12. The effect of frequency should not be very stark as f_c is still in the quasi-steady regime. The comparison of a compound angled steady velocity plane with a phase averaged pulsated one is shown in Fig. 7.5. Even with a perfunctory glance the differences are obvious. The steady case has a strong high momentum jet core and the flow vectors indicate a strong vortex. The phase averaged case shows that the high momentum jet core is much smaller and the
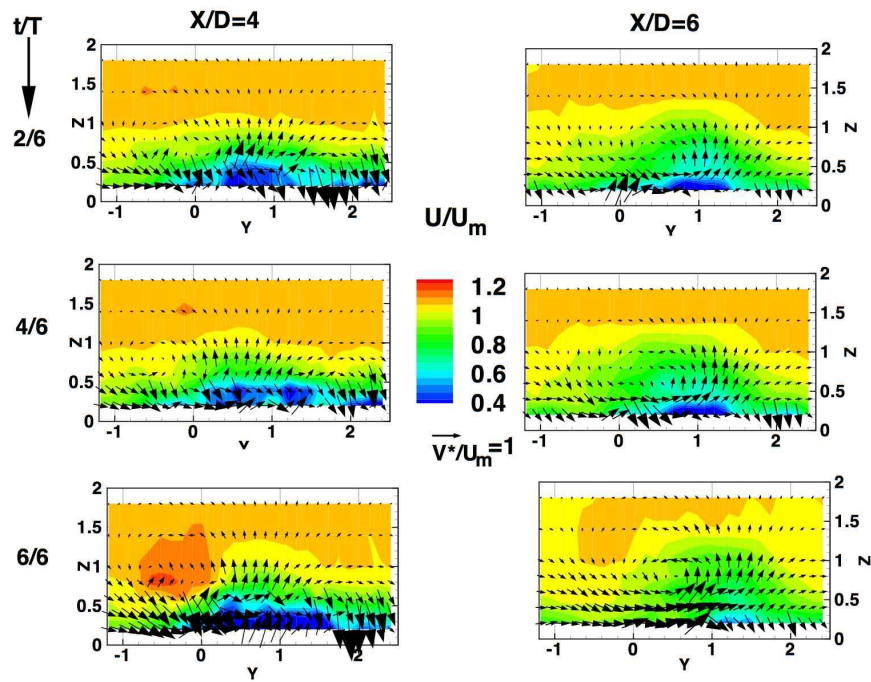
Figure 7.4: Streamwise velocity contours and plane tangential flow vectors for β=60°, BR=2, DR=1.3, IR=3.07, $f = 400$ Hz, $f_r = 0.017$ at $X/D = 4$ and 6 at three different phases in the pulsation cycle

wake region much larger. An important difference from the viewpoint of modeling these flows is the relative position of the jet cores. The lateral deviation in the steady case is almost three quarters of a hole diameter to the right of the pulsated case. Since the deviation of a compound angled jet in the lateral direction increases with the momentum flux as discussed in Chapter 5, this picture implies that for a jet pulsating with the same time averaged blowing ratio but high momentum flux ratio, the equivalent effective momentum flux ratio is much lower. The phase resolved figures are shown in detail in Fig. 7.6. At $X/D = 4$ the lateral movement of the wake zone is not very apparent but the change in jet core size is very clear. An important difference from the streamwise pulsation case is that there is no alternating aggressive attachment and detachment of the jet core but more of an increase and decrease in size. At a downstream distance $X/D = 6$, the inter-phase difference still persists albeit with significantly more mixing. Even at a high crest when the effective instantaneous momentum flux ratio is at IR=2.5, the flow structure is not similar to that observed in Fig. 7.5 for the steady jet.

These observations hint, that pulsating a compound angled jet at high IR, creates an effective momentum flux that is lower than the average BR, but the lateral movement of the jet is not as pronounced as at lower momentum flux ratios. It can also be observed that the separation of the jet core from the surface does not change significantly with phase.
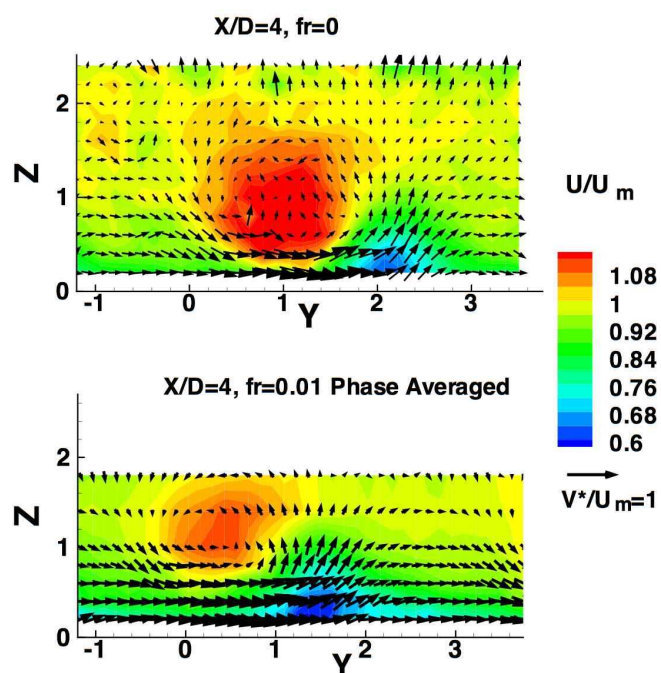
Figure 7.5: Streamwise velocity contours and plane tangential flow vectors at $X/D = 4$ for $\beta = 60°$, BR=2, DR=1, IR=4 for steady and time-averaged pulsated case, $f = 250$Hz, $f_r = 0.01$
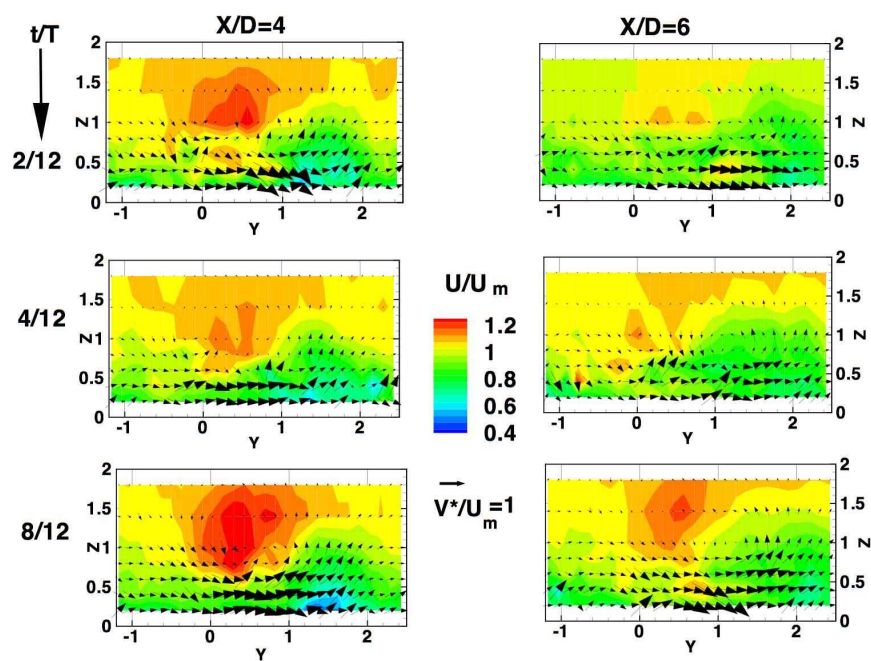

Figure 7.6: Streamwise velocity contours and plane tangential flow vectors for $60°$, BR=2, DR=1, IR=4, $f = 250$ Hz, $f_r = 0.01$ at $X/D = 4$ and 6 at three different phases in the pulsation cycle
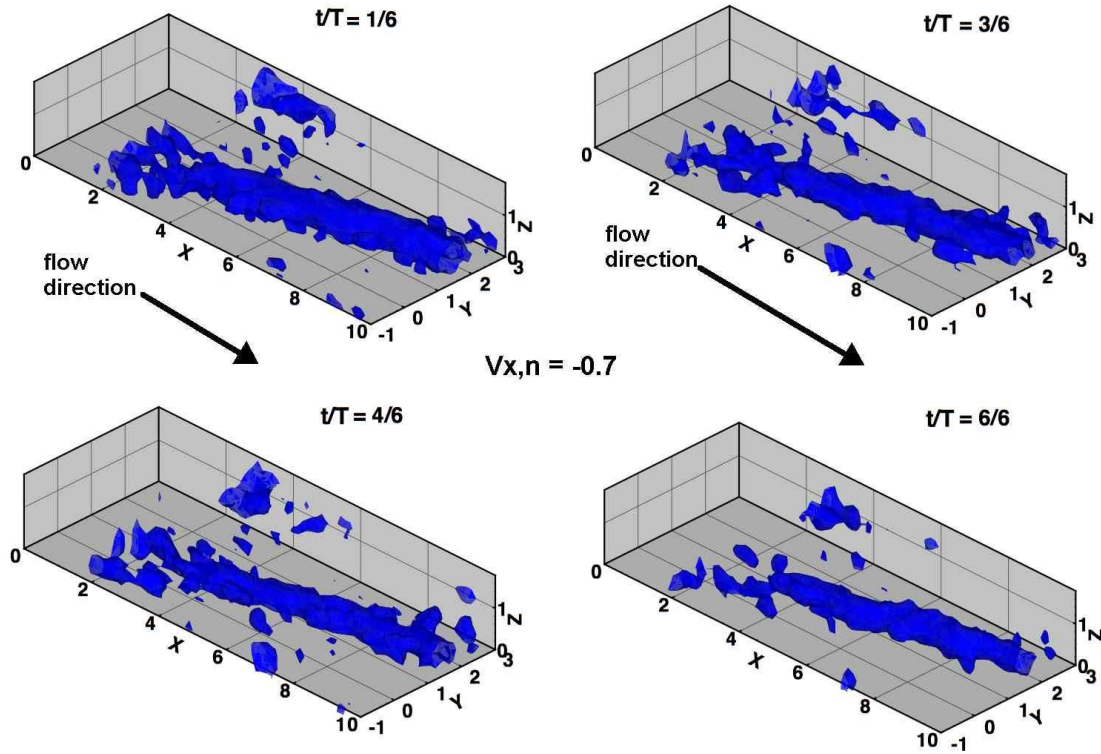
Figure 7.7: Streamwise vorticity surface iso-contours for $\beta = 60°$, BR=2, DR=1.3, IR=3.07, $f = 400$ Hz, $f_r = 0.018$ at different pulsation phases

7.3   Streamwise Vorticity

The streamwise vorticity, which is the main flow structure, is also calculated from the phase resolved velocity flow field. Figure 7.7 shows the surface iso-contours for the main streamwise vorticity emanating from the hole in blue for a BR=2, DR=1.3, IR=2.67 compound angled injection. This calculation naturally presupposes the quasi-steady nature of the pulsating jet, wherein every phase of the jet is akin to a steady jet had the instantaneous IR been imposed. The trajectory of the primary vortex core is seen to move slightly from side to side from the figure showing $t/T = 3/6$ to $t/T = 4/6$. As the instantaneous momentum flux changes, the orientation of the vorticity emanating from the jet also changes accordingly. Apart from just changing its trajectory, even the extent of the vortex core and its spatial size is seen to oscillate. However compared to the oscillation in vortex size for streamwise angled injection as shown in Bernsdorf et al. [14] this alternating size change is very less. At the pulsation crest, $t/T = 1/6$ the size of the vortex is visibly larger than in the trough at $t/T = 4/6$.

Contours of phase resolved streamwise vorticity in a plane cut at $Z = 0.5$ parallel to the wall for the two compound angled pulsated cases are shown in Fig. 7.8. The phases are so chosen that
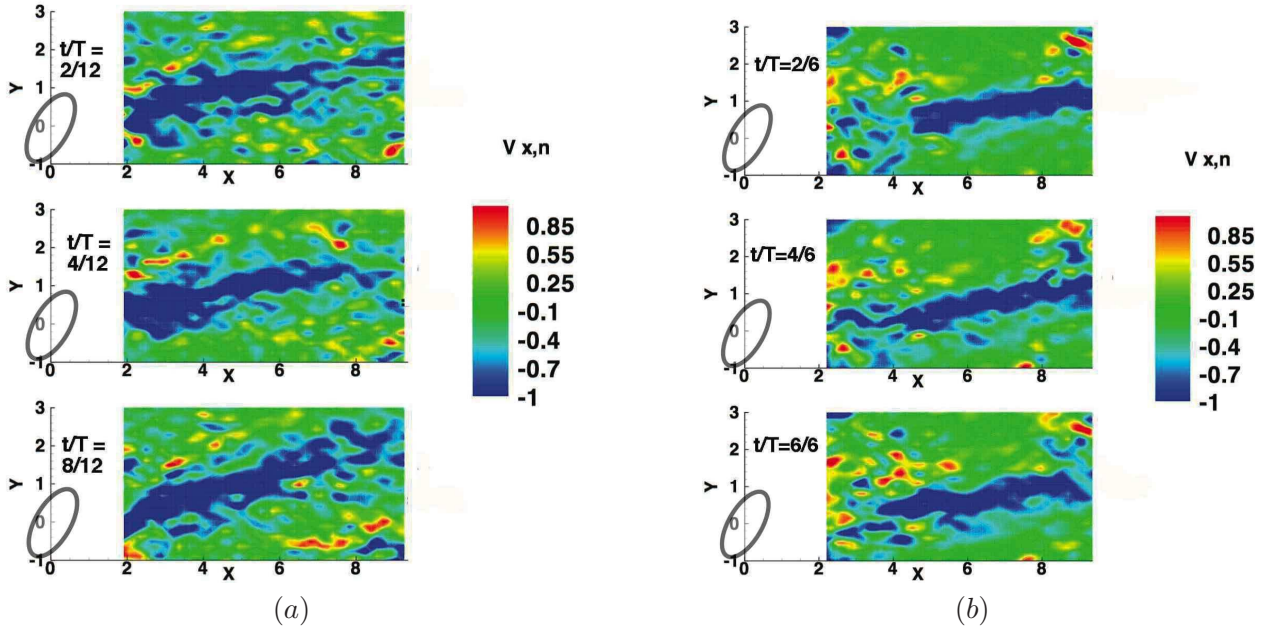
Figure 7.8: Streamwise vorticity contours for $\beta = 60°$,(a) BR=2, DR=1, IR=4, $f = 250$ Hz, $f_r = 0.01$ and (b) BR=2, DR=1.3, IR=3.07, $f = 400$ Hz, $f_r = 0.018$ at $Z = 0.5$ for three different phases

one crest, one trough and an intermediate phase are visible for both the cases. However, from the pictures it is not very clear exactly when the crest or trough in the vorticity magnitude is taking place as the average magnitude is more or less dependant on the momentum flux ratio and not affected too much by the oscillations. The lateral oscillation of the vortex core is pronounced for both the cases and the magnitude of vorticity of the higher momentum flux ratio case in (a) is higher as expected. It can be argued that if the convective time scales are lesser than the pulsation time scales, the actual value of the frequency of pulsation does not seem to have a very observable effect on the flow structure of the film cooling jet. For comparison it may be noted that assuming a speed of about 160-180 m/s for the jet it takes 0.3 milliseconds to cover 9 hole diameters downstream and the blowing ratio changes from 2.3 to 1.7 with 250 Hz which makes the time scale of pulsation to be about 4 milliseconds. It is only when there is some form of coupling between the pulsation frequency and blowing ratio amplitude that a large effect of frequency is observed or if the pulsation frequency enters the non-quasi-steady regime by having the pulsation time scale lesser than the jet convective time scale.

7.3.1 Streamwise Circulation

The area integrated streamwise vorticity or circulation defined as $\Gamma_{x,n} = \oint_A V_{x,n}.dA$ is shown in Figures 7.9 and 7.10. These plots show the evolution of total streamwise circulation with downstream distance. The non-dimensionalised IR based distance, ξ as used in previous plots in
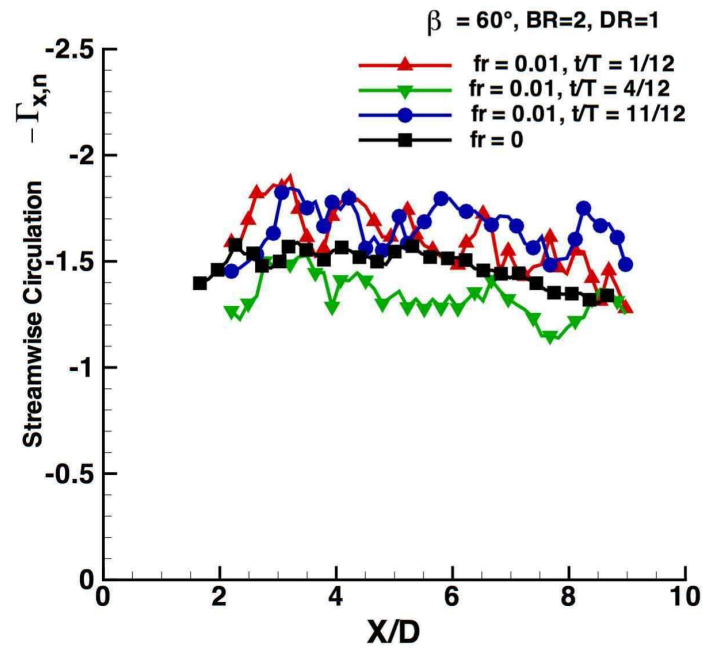
Figure 7.9: Streamwise circulation for three different phases compared to a steady jet for $\beta = 60°$, BR=2, DR=1, IR=4 and $f = 250$ Hz, $f_r = 0.01$

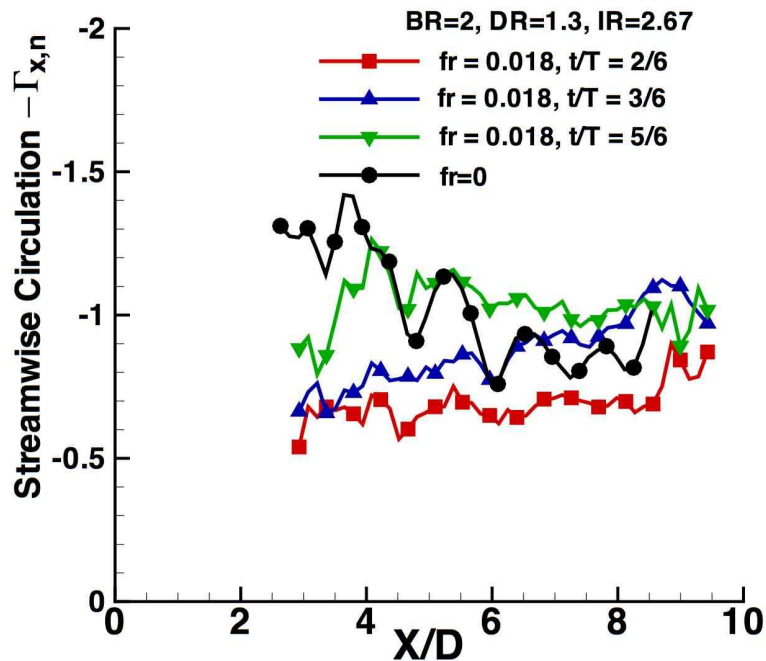**Figure 7.10:** Streamwise circulation for three different phases compared to a steady jet for $\beta = 60°$, BR=2, DR=1.3, IR=3.07 and $f = 400$ Hz, $f_r = 0.017$

Chapter 6 is not used here, as the average momentum flux ratio is more or less equal between two phases of a pulsation. Figure 7.9 shows the circulation for a BR=2, DR=1, IR=4 case with $f_r = 0.01$ pulsation. For comparison, the circulation evolution for a steady jet at the same operating condition is also shown. The phases shown in the plot are for a pulsation crest, a trough and an intermediate part.

Figure 7.9 shows 40% higher streamwise circulation for the crest of the pulsated case compared to the steady injection. This increase is primarily due to the fact that as a high momentum flux ratio jet pulsates, the exiting jet will be subject to an oscillating, momentum flux. In compound angled geometries a higher momentum flux ratio tends to not only strengthen the vorticity and increase streamwise circulation but also displace the jet laterally away from the centerline. This in turn increases the near hole asymmetry in circulation.The plot also shows that even though the magnitudes of the circulation changes with phase due to changing IR, the rate of decay for all the cases remains more or less the same as it is a function of the orientation angle.

Figure 7.10 can be contrasted with Fig. 7.9 to better understand the change in trends due to a lowering of the momentum flux ratio. For the pulsated case of $f_r = 400$, although BR=2 is maintained, the DR is increased to 1.3, thereby lowering the momentum flux ratio to 3.07. The trough at the phase of $t/T = 2/6$, the vorticity and circulation are lower due to lower momentum flux ratio, but the other phases have around the same near hole magnitude. The rate of decay slightly changes from crest to trough as the lateral movement of the jet with pulsations tends to laterally change the effective orientation angle slightly. At greater downstream positions after $X/D = 6$ the circulation curves of $f_r = 0$ case and those at the phase $t/T = 3/6$ and 4/6 are more or less similar. Hence the circulation decay is most visible only in the near hole region.

The two plots can be used to construe a fundamental argument about the mechanism of an oscillating compound angled jet. There are two main effects of the pulsation on an exiting compound angled jet. Firstly, as the momentum flux ratio increases and decreases, the magnitude of of the asymmetric streamwise circulation also changes accordingly. Secondly, as the exit conditions are modified due to the incoming momentum flux oscillation, the high momentum jet core and vorticity oscillate laterally instead of wall-normally. This is most apparent only at reduced momentum flux ratios, IR, as shown by the decay rates of the streamwise circulation.

7.4 Adiabatic Effectiveness

The surface adiabatic effectiveness may be realized byimaging the surface cooling performance of the canonical 60°compound angled geometry for the two frequencies measured at $f_r = 0.01$ and 0.0167. As, the infrared thermography equipment cannot take time resolved measurements, only time averaged measurements would be presented here.

Figure 7.11 shows the adiabatic effectiveness contours for a streamwise oriented injection at two different BR=1 and 2 at the same DR=1.5 and with the different pulsation frequencies.

(a) (b)
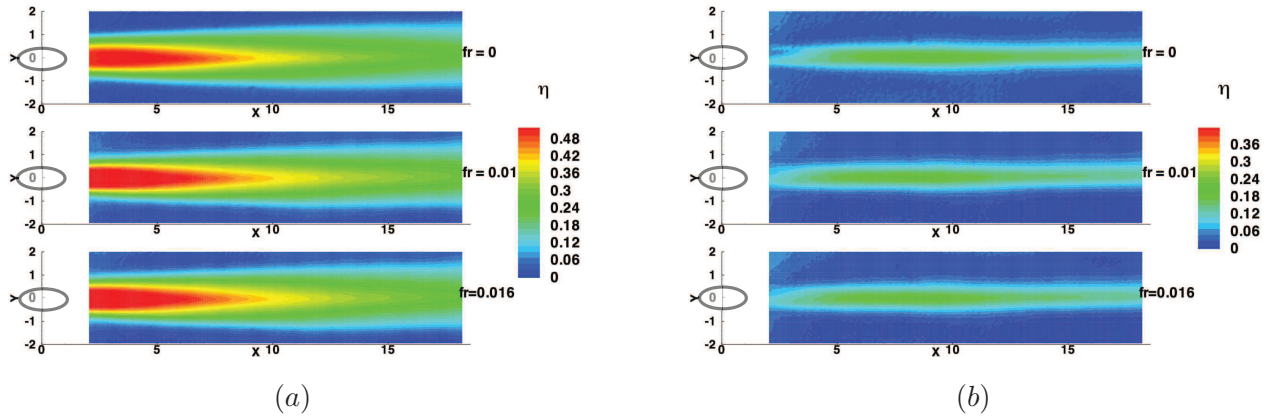
Figure 7.11: Adiabatic effectiveness contours for $\beta = 0°$,(a) BR=1, DR=1.5, IR=0.67 and (b) BR=2, DR=1.5, IR=2.67, $f = 400$Hz, $f_r = 0.018$ for $f_r = 0$, 0.01 and $f = 250$Hz, $f_r = 0.0167$
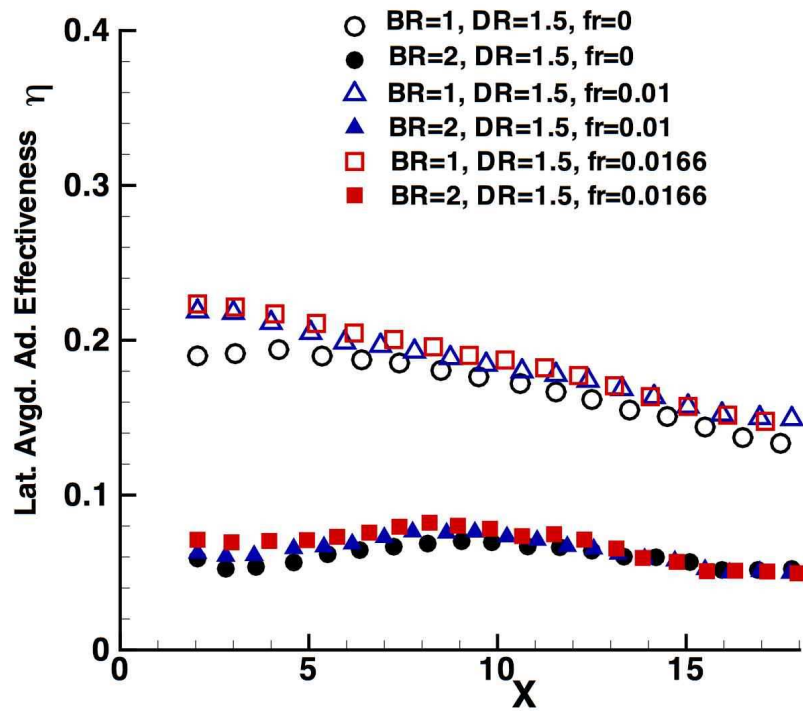
Figure 7.12: Laterally averaged adiabatic effectiveness for $\beta = 0°$ with and without pulsations at BR=1 and 2 and DR=1.5

The surface contours support the observations discussed in Bernsdorf et al. [14] that at high frequencies the quasi-steady assumption for a pulsation streamwise oriented jet is valid, as an equivalent momentum flux ratio equal to the average during the pulsation may be used to describe it as a steady jet. As is visible in Fig. 7.11 (a) for the low BR=1 case, the averaged contours
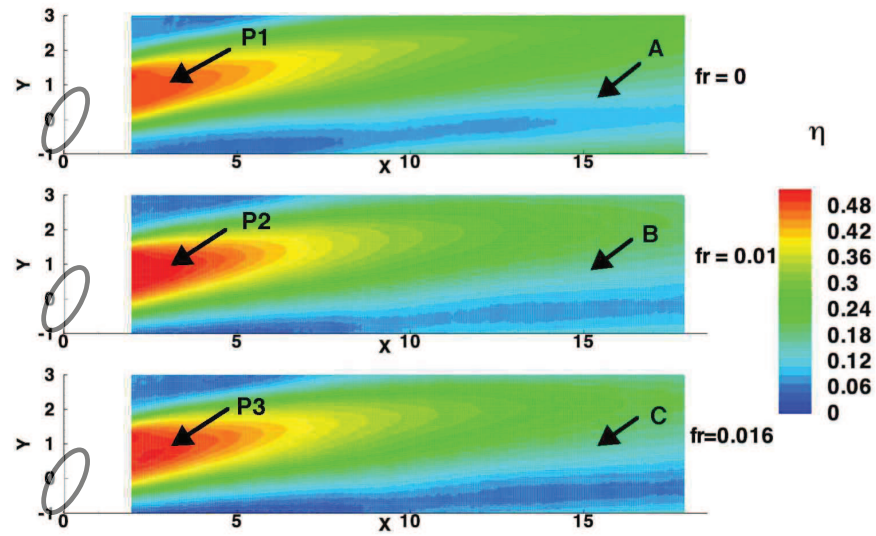
Figure 7.13: Adiabatic effectiveness contours for $\beta = 60°$, BR=1, DR=1.5, IR=0.67, $f = 0, 250, 400$ Hz, $f_r = 0$, 0.01 and 0.0167
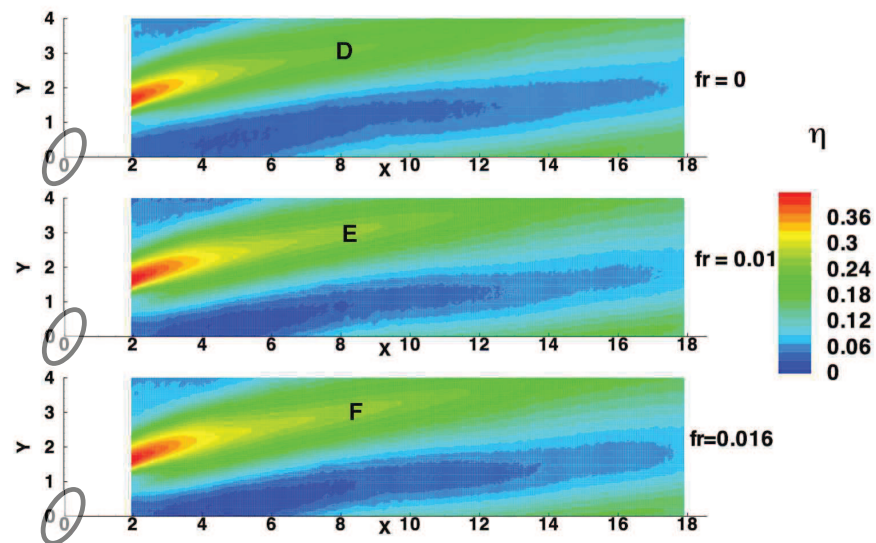
Figure 7.14: Adiabatic effectiveness contours for $\beta = 60°$,BR=2, DR=1.5, IR=2.67, $f = 0, 250, 400$ Hz, $f_r = 0$, 0.01 and 0.0167

from the two different frequencies and that due to steady jet are the same in terms of coolant lateral spread as well as penetration in the downstream distance. The local coolant peaks are also not significantly different, and any slight differences are within the uncertainty band of the measurement technique.
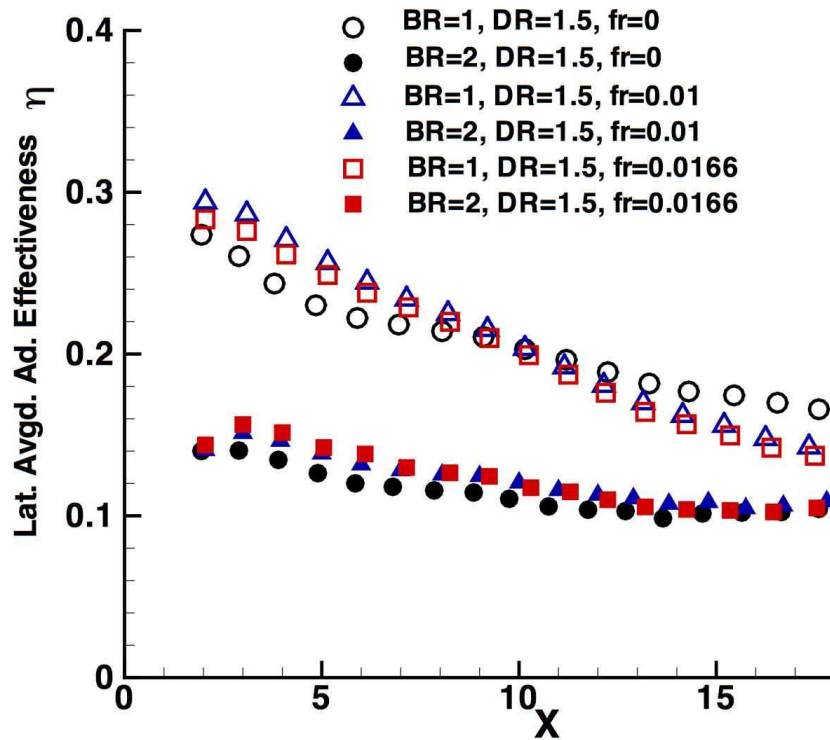
Figure 7.15: Laterally averaged adiabatic effectiveness for $\beta = 60°$ with and without pulsations at BR=1 and 2 and DR=1.5

The laterally averaged adiabatic effectiveness as shown in Fig. 7.12 clearly show the minor effect of pulsations on a streamwise injected jet. The slight increase in adiabatic effectiveness at BR=1 for both the frequencies compared to the steady case, is due to the lowering of effective momentum flux ratio and greater attachment of the jet to the wall. For the high BR=2 case, the change in adiabatic effectiveness cannot be confidently commented upon as it is within the experimental uncertainty bounds.

Figure 7.13 shows the adiabatic effectiveness for the compound angled geometry at a low BR=1, DR=1.5, IR=0.67 operating condition. The net effect of the oscillation at the low IR, is primarily to reduce the quasi-steady average IR by reducing the amount of coolant flux that exits the jet. The pulsated cases of $f_r = 0.01$ and 0.0167 can be compared with the steady case by looking at two distinct regions on the surface which are marked in the figures. These are the points where peak effectiveness occurs (P1, P2 and P3) and the downstream ones which show the extent of the coolant spread (A, B and C).

The peak effectiveness indicated by P2 and P3 is somewhat higher than in the steady case of P1. A near-hole effectiveness enhancement as seen in these cases is a ramification of a more attached jet due to lesser penetration in the freestream as well as a greater lateral movement of the jet with pulsations. The differences in effectiveness due to the changing frequency is not

very apparent. The downstream points which are used to demarcate the coolant lateral spread also show important differences. Point A, which somewhat demarcates the lateral extent of the coolant is seen to be at Y=0.5 while points B and C showing a similar effectiveness region are at Y=0.8. The lateral coolant spread in the pulsated cases is also lower than in the steady case. It can thus be observed that the lateral extent of the coolant with downstream distance reduces with pulsations. These results may be explained by previous experiments with compound angles holes, like those of Jung and Lee [63] where it was observed that for low momentum flux ratios, due to the lower ejection of bulk coolant, there is an enhancement of the effectiveness in near hole regions but the effectiveness decays rapidly with downstream distance.

Figure 7.14 shows the adiabatic effectiveness contours for the higher BR=2 case. The near hole peak effectiveness is similar for both pulsated and steady cases. The differences arises at points after X=8. The regions marked as D can be seen to have a lower effectiveness than E and F. E and F have higher effectiveness as the surface contours show a greater penetration of the coolant on the surface in the downstream direction. This penetration is direct consequence of the lateral movement of the jet which mainly spreads the coolant and hence creates greater effectiveness regions at downstream points. This coolant spread effect is not very visible at far downstream after X=12 because the mixing is anyways quite enhanced for a compound angled case even in a steady case.

The laterally averaged adiabatic effectiveness for the compound angled cases provides a good overview of the trends observed. Figure 7.15 shows that at low BR=1, there is a significant effect on downstream adiabatic effectiveness evolution due to pulsations. As visible from the contour plots, both the pulsated cases have higher effectiveness than the steady case before X=8, but as the decay in averaged effectiveness is higher for the downstream distances, the effectiveness levels fall below that of the steady case. This phenomenon is a clear indicator, that pulsations reduce the effective momentum flux ratio and the mass flow rate of the bulk coolant, thereby creating better attachment of the coolant jet at near-hole locations but a lower intensity of cooling downstream. For the high BR=2 case, the enhancement in effectiveness due to pulsation is within the experimental uncertainty of the thermal measurements and hence a clear and direct conclusion can't be made.

7.5   Boundary Layer Shape

In Section 6.4 it was shown that a compound angled injection increased the boundary layer pile up in terms of extent and size. The boundary layer pile-up as visualized by iso-contours of the non-dimensionalised horizontal velocity, $U/U_m = 0.98$ are shown for the $f_r = 0.017$ case in Fig. 7.16 for four different phases in a pulsation. The crest at $t/T = 2/6$ may be contrasted with the trough at $t/T = 4/6$. At the crest, the boundary layer pile-up is larger due to the greater entrainment from a stronger primary vortex core. The trajectory of the boundary layer pile-up is not visibly affected as it is laterally spread out due to compounding in the first place. The
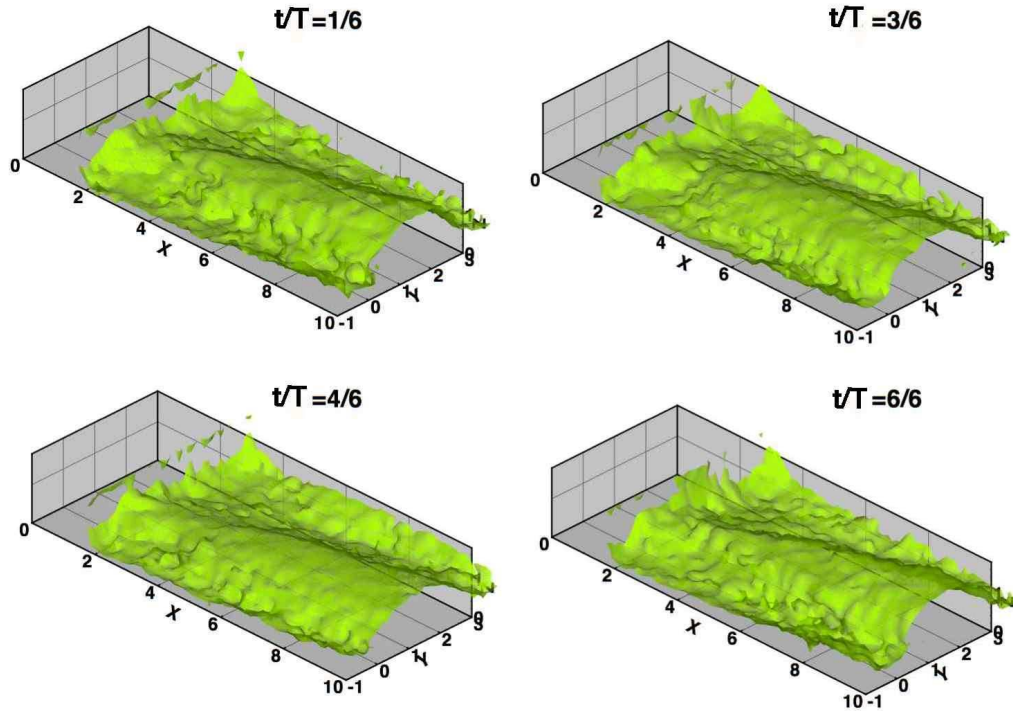
Figure 7.16: Boundary layer visualised through velocity surface iso-contours of $U/U_m = 0.98$ for $\beta = 60°$, BR=2, DR=1.3, IR=3.07, $f_r = 0.017$ at different pulsation phases

flow structure is comparable to a pile-up at the same conditions but without any pulsations.

7.6   Wall Normal Vorticity

The quantification of the coherent structures below the boundary layer which primarily affect the heat transfer coefficient is done using wall-normal vorticity. The wall-normal vorticity for $\beta = 60°$ is shown in Fig. 7.17. For both the cases, the wall-normal vorticity is more or less as expected according to their averaged momentum flux ratios. That is, the higher momentum flux ratio jet in Fig. 7.17 (a) has a greater spatial spread and extent of the wall-normal vorticity for all the phases compared to the lower momentum flux ratio shown in (b). The difference in wall-normal vorticity between any two phases is negligible for both the frequencies. It should also be noted that the figures for the wall-normal vorticity are very non-continous or patchy. This patchiness however is spread over a large extent. One reason could be that the noise in the PIV signal is high due to the phase averaging. Another reason is that the coherent unsteadiness itself is quite high. Wall-normal vortices are inherently temporally evolving vortices and hence if an attempt to capture them using averaged pictures with PIV is made, the pictures would turn out to be quite noisy.

(a)   (b)
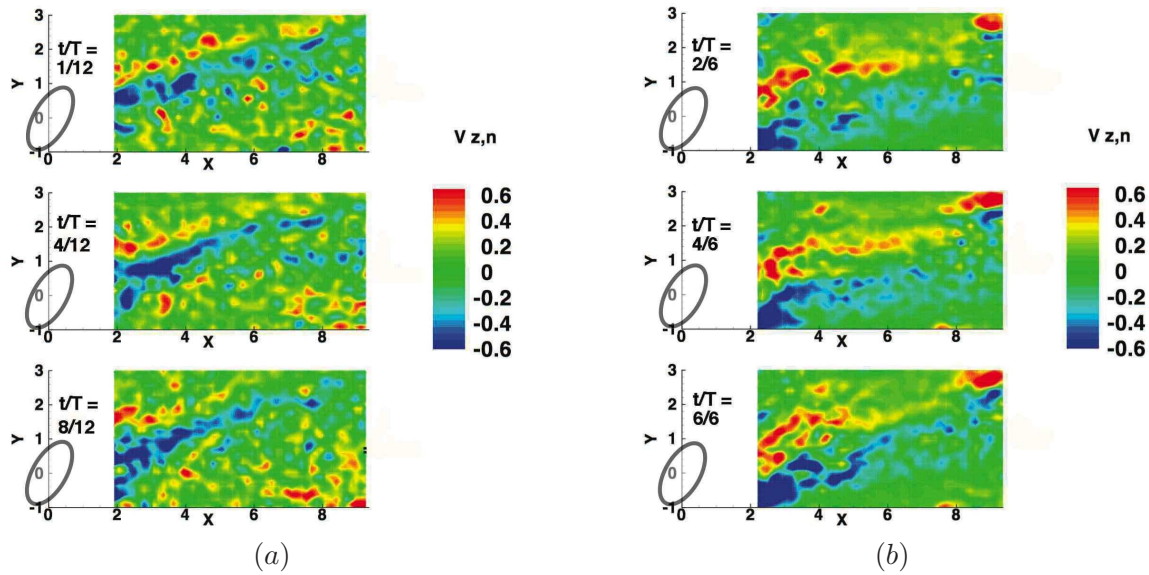
Figure 7.17: Wall normal vorticity contours for $\beta = 60°$,(a) BR=2, DR=1, IR=4, $f_r = 0.01$ and (b) BR=2, DR=1.3, IR=3.07, $f_r = 0.017$ at $Z = 0.5$ for three different phases

(a)   (b)
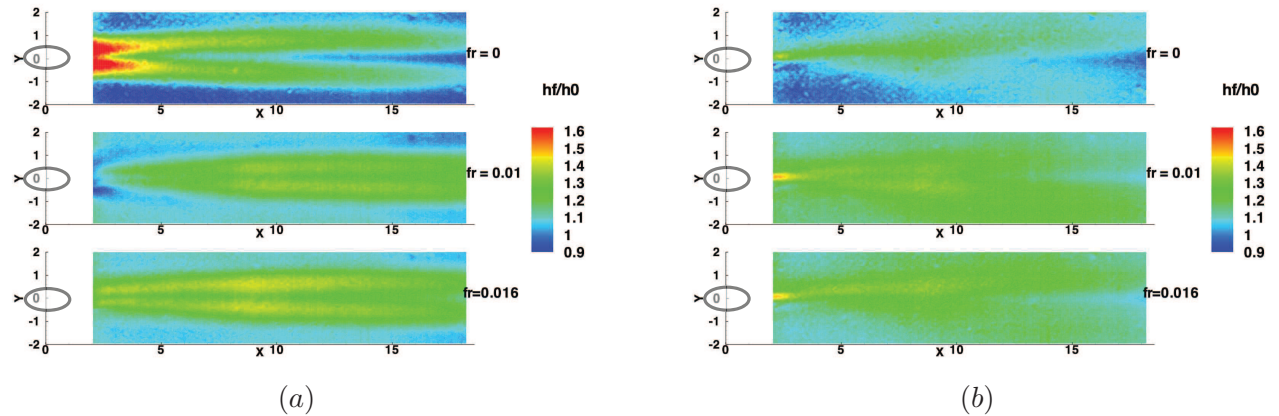
Figure 7.18: Normalised heat transfer coefficient h_f/h_0 contours for $\beta = 0°$,(a) BR=1, DR=1.5, IR=0.67 and (b) BR=2, DR=1.5, IR=2.67, for $f_r = 0$, 0.01 and 0.0167

The wall boundary layer is interspersed with many local pockets of these coherent structures as compared to a non-pulsated case where the areas outside the jet area typically have close to zero wall-normal vorticity. This could be due to the enhanced jet freestream interaction brought about by pulsations.
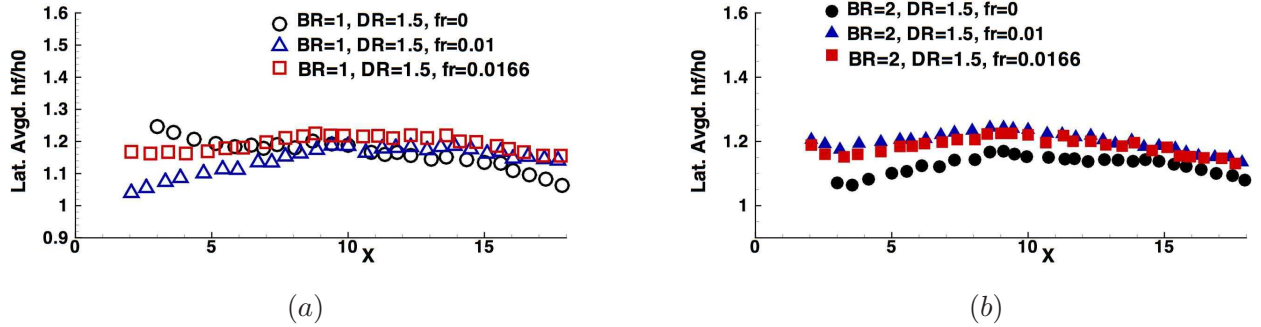
Figure 7.19: Laterally averaged normalised heat transfer coefficient h_f/h_0 for $\beta = 0°$,(a) BR=1, DR=1.5, IR=0.67 and (b) BR=2, DR=1.5, IR=2.67, for $f_r = 0$, 0.01 and 0.0167

7.7   Heat Transfer Coefficient

The heat transfer coefficient enhancement, h_f/h_0 of a streamwise injection case is plotted for the two different frequencies with a steady injection for low and high IR in Fig. 7.18 (a) and (b) respectively. The local heat transfer coefficient due to the steady case is observed to be higher in the near hole region compared to the pulsated cases for BR=1 in the plots labelled (a). As the net effect of the pulsations at the lower IR is to reduce the effective momentum flux being injected, the heat transfer enhancement is reduced in the near hole region but is mainly higher in the downstream region. This is a direct ramification of lesser bulk coolant being forced out onto the surface. For Fig. 7.18 (b) which shows the higher IR=2 case with and without pulsations, it is clearly observed that at downstream positions, the heat transfer enhancement has a high lateral spread with pulsations. Both high and low frequencies have a similar effect on the downstream enhancement of heat transfer coefficient with pulsations. This point is more readily made by comparing the laterally averaged heat transfer coefficient for the different operating conditions as shown in Fig. 7.19. The plots for the lower IR=0.67 case show that pulsations generally cause a reduction in near hole heat transfer coefficient due to the lowering of the ejected momentum flux ratio. At downstream positions as the jet attaches closely to the wall and the heat transfer coefficient is similar to the steady case. Figure 7.19 (b) shows the same comparison for the higher IR=2.67 for all three cases. As the unsteadiness generally increases the jet-freestream interaction, the heat transfer enhancement is also enhanced due to pulsations at all axial positions, although this increase above the steady case reduces with downstream distance as the effect of the jet pulsation dissipates and large mixing is then the driving factor.

It is thus seen that for a streamwise injection, pulsations affect the overall heat transfer coefficients differently depending on the momentum flux ratio regime (i.e. high or low) within which they are operating.

The local heat transfer enhancement contours for compound angled, $\beta = 60°$ injection at IR=0.67 is shown in Fig. 7.20. The difference between the steady case and pulsated cases is very clear.

Figure 7.20: Normalised heat transfer coefficient h_f/h_0 for $\beta = 60°$, BR=1, DR=1.5, IR=0.67 $f_r = 0$, 0.01 and 0.0167
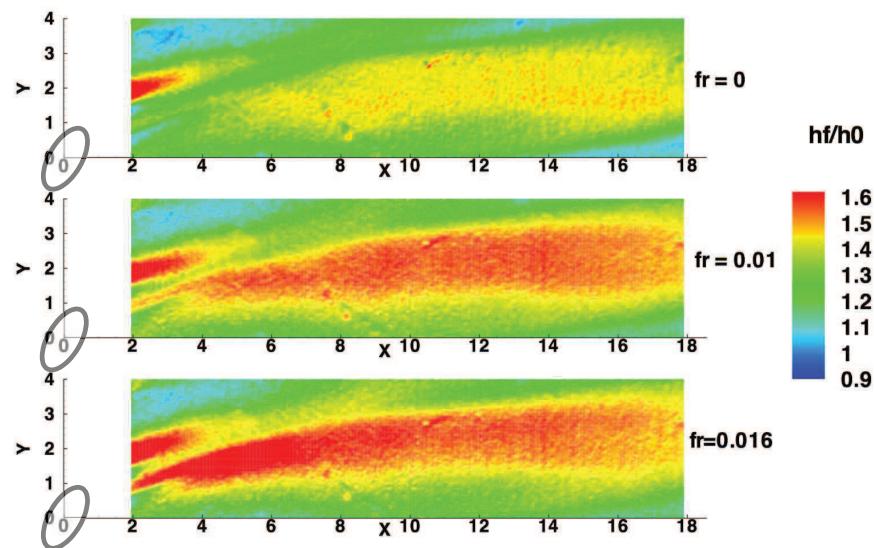
Figure 7.21: Normalised heat transfer coefficient h_f/h_0 for $\beta = 60°$, BR=2, DR=1.5, IR=2.67 $f_r = 0$, 0.01 and 0.0167

The deviation of the trajectory from the centerline is significantly reduced with pulsations. This shows the lowering of the effective momentum ejecting the jet due to pulsations. The high heat transfer enhancement regions are not as angled to the main flow as in the steady case, although at downstream distance the lateral spread is comparably the same in all three cases. There does not appear to be an apparent visible difference due to changing the frequency of pulsation for
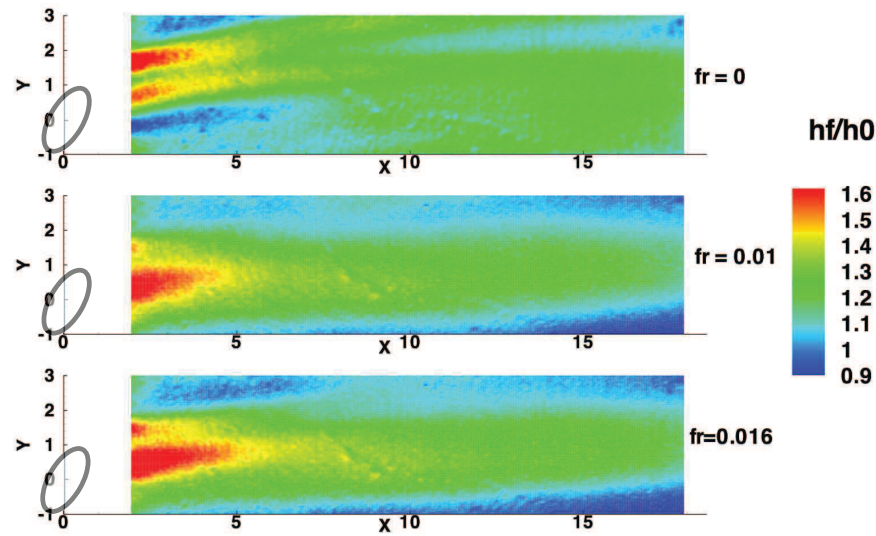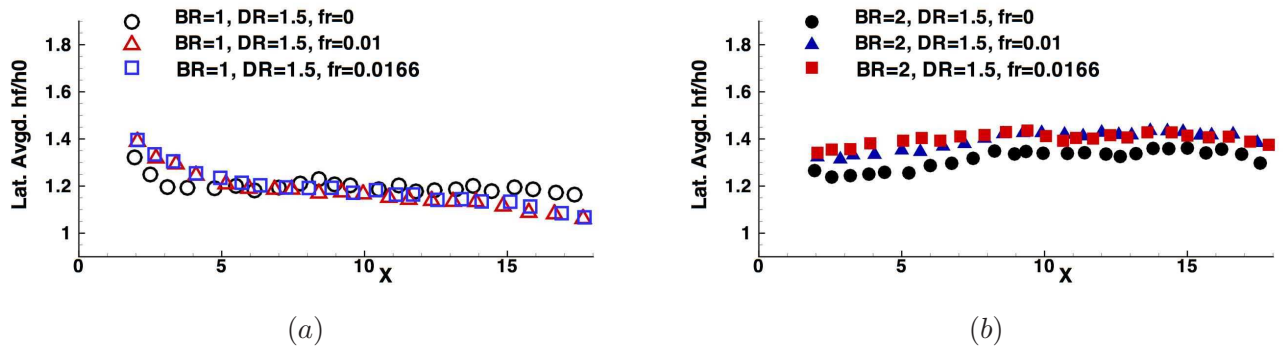
Figure 7.22: Laterally averaged normalised heat transfer coefficient h_f/h_0 for $\beta = 60°$,(a) BR=1, DR=1.5, IR=0.67 and (b) BR=2, DR=1.5, IR=2.67, for $f_r = 0$, 0.01 and 0.0167

the heat transfer enhancement. When the momentum flux ratio is increased by increasing the BR to 2, the difference between pulsated and steady cases becomes more defined. The unsteady cases are shown to have very high heat transfer coefficient augmentation at downstream positions after X=5. This augmentation although limited to the same areas as the steady case has much higher local values caused due to the higher jet freestream interaction and possibly enhanced turbulence which has not been captured by PIV. The periodic unsteadiness causes a vigorous mixing in downstream areas due to which the heat transfer is augmented.

The laterally averaged heat transfer coefficient augmentation shown in Fig. 7.22 (a) for IR=0.67 gives a concise visualization of the trends visible in the previous contours. The heat transfer coefficient for the pulsated cases is slightly higher than the steady case in the near hole region before X=5. At downstream distances the differences reduce considerably. For this low IR case, pulsations primarily reduce the effective momentum flux ratio due to the alternating release and stoppage of the emanating jets. This causes a slight increase near the hole due to a more attached jet interacting with the near wall fluid and then consequent mixing leading to slightly lower heat flux enhancements downstream. The lowering in heat transfer coefficient is about 15% due to pulsations at downstream distances whereas as visible in Fig. 7.19 (a) for a streamwise injection the heat transfer coefficient ratio is mostly the same as in a steady case.

For a high IR=2.67 injection, the effect of pulsations on laterally averaged heat transfer coefficient is shown in Fig. 7.22 (b). At all axial locations, there is a high enhancement in the heat transfer coefficient augmentation compared to a steady blowing. The greater mixing and jet-freestream interaction caused by stronger unsteady structures as well as the lateral side to side movement of the oscillating jet create a large enhancement of heat transfer coefficient. The increase due to pulsations is about 20% at all locations.

7.8 Summary

The pulsating compound angled problem is important to consider because in a real gas turbine, film cooling typically takes place in the presence of pulsations from rotor-stator interactions. A 60°compound angled pulsating jet may be modeled as a quasi-steady jet at the same momentum flux ratio as the time averaged IR for most cases. The flow structure depends on which momentum flux regime it is operating in. At low IR ($IR < 1$), the pulsations mainly affect the flow structure and heat transfer by transforming the jet into an equivalent one at a lowered effective momentum flux ratio. At high IR ($IR > 2.5$), the lowering of effective momentum flux ratio, is overshadowed by the increased jet-freestream interaction and lateral movement from side-to-side of the cooling jet. It must be noted however that the frequency effects studied here are a small, representative range of typical frequencies only and an exhaustive study is feasible only through more economical computational methods. The frequencies studied currently place the oscillating jet in a quasi-steady regime and the actual magnitude of these reduced frequencies is not wide enough to cause a stronger effect. The amplitude of oscillations would have a first order change on the cooling performance as well, which has not been varied. A very first order understanding of the effect of pulsations on compound angled injection is sought here.

1. Effect of pulsations on streamwise injection

    (a) Pulsations in streamwise jets reduce the effective momentum flux injected through the holes by alternately increasing and lowering the injected mass flux. A pulsated jet can be considered to be a steady jet at a slightly lower momentum flux ratio.

    (b) The flow structure of a phase averaged pulsated jet closely matches a steady jet at intermediate IR = 3.07. A quasi-steady assumption for streamwise injection is thus feasible as the periodic unsteadiness does not qualitatively change the flow features significantly.

    (c) At low momentum flux ratios ($IR < 2$), the pulsations mainly affect surface performance by reducing the effective momentum flux ratio and hence slightly increasing the effectiveness in near hole ($X < 6$) region compared to a steady jet.

    (d) At high momentum flux ratios ($IR > 3$) the reduction of effective momentum flux ratio in a time averaged sense by pulsations is not significant enough to cause a change in the behavior of the laterally averaged effectiveness compared to a steady jet at the same conditions.

    (e) Periodic unsteadiness decreases the near hole heat transfer augmentation akin to a lowered momentum flux injection leaving far downstream heat transfer undisturbed. At high momentum flux ratios, the pulsations significantly enhances jet-freestream interaction at downstream axial locations.This causes an enhancement of heat transfer. The laterally averaged heat transfer coefficient is augmented for all axial locations for

high IR cases, but this augmentation is just beyond the experimental uncertainty of thermal measurement.

2. Effect of pulsations on compound angled injection

   (a) The primary vortex core trajectory changes within a phase for a lower IR as borne out by the change in rate of decay of the phase resolved circulation.

   (b) The boundary layer wall-normal thickness for a pulsating compound angled jet is enhanced compared to a steady jet, but the inter-phase difference during a pulsation is minimal. The wake zone is flattened, closer to wall and has greater spread than a steady jet.

   (c) The cooling effectiveness for a pulsated low IR compound angled injection behaves akin to one at a reduced momentum flux ratio, with slightly higher near hole effectiveness but reduced cooling at downstream locations due to absence of sufficient bulk of coolant flow. These augmentations though are just beyond the limits of experimental uncertainty. Hence, only the qualitative trend of greater decay of effectiveness with downstream distance can be confidently stated.

   (d) At high IR, a pulsated compound angled injection does not show significant difference in laterally averaged adiabatic effectiveness compared to a steady jet. tem At low IR, the near hole heat transfer coefficient is increased but due to reduced coolant ejection, it reduces at downstream locations, compared to a steady jet.

   (e) The laterally averaged heat transfer coefficient is augmented by around 15% at all axial locations for a high blowing case at IR=2.67 as the increased unsteadiness increases local heat transfer coefficients.

3. Limits of Pulsation Frequency and Amplitude

   The amplitude of pulsation was not changed, but maintained at a representative value to understand the first order effects due to periodic unsteadiness. The pulsation frequencies were also not taken to their extremes of non-quasi-steady regime but maintained at a point where it was known that convective time scales of the jet would be lower than the time scales of pulsations and that there was no coupling between amplitude and frequency through the pulsating device. More exhaustive measurements exploring these parameters should be attempted.

Chapter 8

Aerothermal Performance of Film Cooling

The previous chapters have shown the influence of flow structure on cooling performance. Although, film cooling studies have almost always concentrated on the primary heat transfer issues, engine designers are also concerned with the aero-thermodynamic losses that might be produced when film cooling injection causes mixing losses. This is so because film cooling intrinsically involves mixing a hold fluid with a cold one in a turbine where small local losses could translate to large changes in overall performance. The quantification of loss is also an important part of the investigation. From, Denton [34], it is known that an entropy change parameter is the best quantification of loss. Owing to the fact that local entropy change could not be previously measured, many averaged estimates were used. The results in this chapter are the first estimates of the local changes in entropy for streamwise and compound angled film cooling jets which also take into account the losses suffered by the coolant stream. The effect of pulsations on this loss parameter is also investigated and compared with other loss parameters like pressure loss coefficient and kinetic energy loss coefficient which are often used in literature.

The results shown in this chapter are obtained by using a novel measurement technique. An in-house developed probe, the FENT (Fast response ENTropy) probe simultaneously measures pressure and temperature at high acquisition rates up to 40 kHz, details of which are explained in Section. 3.3.

8.1   Flow Conditions and Pulsations

The set of results in this chapter are all for only one blowing condition but two different geometries The Mach number of the freestream, M was held constant at 0.3 and the main flow parameters were also held constant, $BR = 2$, $DR = 1.3$, $IR = 3.07$. This resulted in typical freestream velocities of $U_h = 120$ m/s and a hole based Reynolds number, $Re_D = U_{h,\infty}D/\nu \sim 46000$.
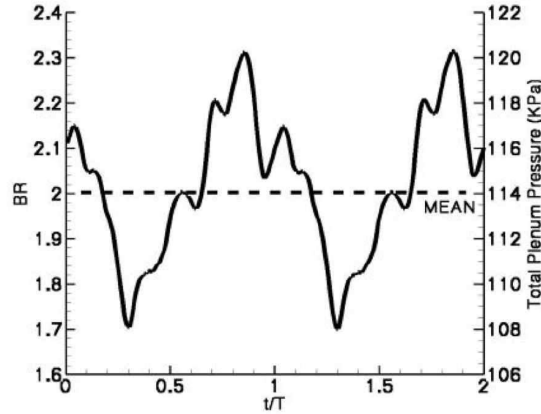
Figure 8.1: Blowing ratio and pressure variation measured in the plenum for $BR = 2$, $DR = 1.3$ and pulsation of 400 Hz, $f_r = 0.025$

The density ratios were obtained by maintaining the coolant at room temperature (298 K) and heating the freestream to about 393 K.

The results capture in detail the time-resolved and averaged temperature, pressure, entropy change and kinetic energy loss coefficient for a single operating condition, viz. BR=2, DR=1.3 for a streamwise and 60° lateral angled hole over a flat plate.

The pulsation frequencies were 0 Hz and 400 Hz corresponding to a hole-diameter based reduced frequency, $f_r = fD/U_{h,\infty} = 0.025$ which lies in the engine range according to Burdet and Abhari [22], Coulthard et al. [31, 30]. The total pressure variation in the plenum and the corresponding local BR variation is shown in Fig. 8.1 for the pulsations introduced. The duty cycle of the pulsations is a little above 0.5 as is visible in the figure. All time axes are non-dimensionalised by the time period of a single pulsation for 400 Hz.

8.2   Definition of Loss Parameters

The simultaneous pressure and temperature measurements are resolved to obtain quantities like entropy generation and a kinetic energy loss coefficient. Estimates of loss in turbomachinery applications are best described by the change in entropy, according to Denton [34]. The difficulty, however, arises in denoting a proper reference temperature and pressure to calculate this change for a jet in cross-flow situation. Ascribing the reference conditions to the freestream conditions, neglects the losses arising from the cooling hole. In this particular study using the mixed out conditions as a reference is also not possible since the domain of data acquisition did not extend far enough to record the mixed out temperatures and pressures. A logical way to take into account this two temperature, two pressure problem is to use a reference condition which is a mass weighted average of the two initial conditions of the hot freestream and the coolant in the

plenum. Such a definition was successfully applied in Wilfert and Fottner [108] to reference the pressure losses from film cooling holes in a turbine. For the purposes of creating a reference baseline, P_{ref} and T_{ref} are defined by Eq. 8.1 and 8.2 respectively. The conceptual basis for these definitions is to assume that the fluid that is measured downstream has arrived from just a single initial condition given by $P_{t,ref}$ and $T_{t,ref}$ and the difference between the two is due to the various lossy mechanisms like mixing, heat transfer and viscous dissipation between the streams and separation within the hole.

$$P_{t,ref} \quad = \quad \frac{\dot{m}_c}{\dot{m}_c + \dot{m}_h} P_{t,c} + \frac{\dot{m}_h}{\dot{m}_c + \dot{m}_h} P_{t,h} \tag{8.1}$$

$$T_{t,ref} \quad = \quad \frac{\dot{m}_c}{\dot{m}_c + \dot{m}_h} T_{t,c} + \frac{\dot{m}_h}{\dot{m}_c + \dot{m}_h} T_{t,h} \tag{8.2}$$

The reference condition in Eq. 8.1 can now be used to define a total pressure loss coefficient, $C_{P,t}$ like in Wilfert and Fottner [108] defined by Eq. 8.3, where U_∞ is the incoming freestream velocity.

$$C_{P,t} = \frac{P_{t,ref} - P_t}{\frac{1}{2}\rho U_\infty^2} \tag{8.3}$$

Since the traditional total pressure loss coefficient does not take into account the thermodynamics of the flow, the entropy change is a better indicator of mixing and separation losses Denton [34]. The entropy change $\triangle s$ at a point (P_t, T_t) is given by Eq. 8.4.

$$s_{ref} - s = \triangle s = -\mathcal{C}_p \ln\left(\frac{T_t}{T_{t,ref}}\right) + \mathcal{R} \ln\left(\frac{P_t}{P_{t,ref}}\right) \tag{8.4}$$

In order to obtain a positive number and for ease of comparison this entropy change is non-dimensionalised and plotted in subsequent figures as an entropy function, $e^{-\frac{\triangle s}{\mathcal{R}}}$. Thus, an area where this quantity, $e^{-\frac{\triangle s}{\mathcal{R}}}$ is low signifies an area of greater loss as the entropy change from the reference condition is higher. It must be noted that such a definition of entropy change depends on the viability of assuming the mass weighted averages of the reference conditions in the first place. As defined by Denton [34] an entropy loss coefficient is also defined at every measurement point using the local temperature and total velocity by Eq. 8.5 where V is the local total velocity. This value is primarily used for comparing mass-weighted averaged value for different conditions in subsequent sections.

$$\zeta = \frac{T \triangle s}{0.5 V^2} \tag{8.5}$$

Aerothermal performance of film cooling jets is most characteristically described by a film cooling loss coefficient. This is the ratio of the kinetic energy at a point downstream of injection, after some mixing has occurred, to the sum of the kinetic energy that the freestream and coolant flow would have had, were they to isentropically arrive at the point in question. This definition is explained in detail in Reiss and Boelcs [95], Wilfert and Fottner [108], Drost [37] and Young and

Horlock [109]. The loss coefficient, ξ is defined in Eq. 8.6. The advantage of using this definition is that the losses in both the freestream and the coolant holes are considered. Additionally, an ideal reference condition, as described in Eq. 8.1 and 8.2 need not be estimated.

$$\xi = 1 - \frac{\left(1 + \frac{\dot{m}_c}{\dot{m}_h}\right) T_t \left(1 - \frac{P_s}{P_t}\right)^{\frac{\gamma-1}{\gamma}}}{T_{t,h} \left(1 - \frac{P_s}{P_{t,h}}\right)^{\frac{\gamma-1}{\gamma}} + \frac{\dot{m}_c}{\dot{m}_h} T_{t,c} \left(1 - \frac{P_s}{P_{t,c}}\right)^{\frac{\gamma-1}{\gamma}}} \tag{8.6}$$

Unlike the calculation of ξ in other works like Wilfert and Fottner [108], Drost [37], there exists an engine representative temperature gradient. Previous measurements of the quantity, ξ have been primarily estimated with pressure probes in $DR = 1$ conditions. However, as will be shown later, the temperature gradients have a significant effect on the thermal mixing loss generation.

8.3   Local Loss Quantification

8.3.1   Frozen Flow Assumption for Unsteady Visualizations

As the loss generation mechanisms are visualized in an unsteady phase resolved setup in the following sections, it is important to show that the pulsating flow follows a quasi steady behavior and a frozen flow hypothesis can thus be assumed. Quantitative and qualitative measurements ascertaining the assumption of quasi-steadiness for a pulsating streamwise film cooling jet were shown by Bernsdorf et al. [14]. The ensemble averaging to resolve the loss or entropy into phases assumes that all parts of the jet follow more or less the same phase. According to Ligrani et al. [78] a pulsating jet can be considered quasi-steady and the entire part of the jet at a given moment of time is the same as a steady distribution which would exist at the same instantaneous flow condition if the condition, $1/2\pi f > L/U_c$. For the pulsating jets considered in this study the pulsation time scale is always around four times higher than the convective time scale of the jet. Further proof for this assumption may also be derived using the frozen flow hypothesis.

The criteria for verifying the frozen flow hypothesis was used in Poyneer et al. [92]. Although that work was done to detect frozen flow layers in atmospheric turbulence for corrections to astronomical objects, the quantification used could also be adapted for the current measurements. The frozen flow hypothesis may be assumed if for a measurement plane, all the points within the jet have their maximas and minimas together. This means that not only does the maximum of the frequency spectrum occurs for pulsated frequency of 400 Hz, (which is the frequency of oscillation for the measurements in this chapter) but also that the amount of power (from a power spectral density (PSD) calculation) contained in the dominant frequency as a fraction of the total PSD is more or less the same over all the jet plane. A phase angle based on the FFT may also be calculated. The temperature signal is discussed here, as it has a higher acquisition rate of 100000 Hz and hence the frequency spectrum recorded is very broad band.

A typical measurement plane has 15 horizontal and 19 vertical measurement points for the current measurements and large parts of the plane are composed of the steady freestream flow. A threshold for the power spectral density for the peak frequency is set and points where the signal is mainly non-periodic and hence the highest spectral density is four times lower than for that from the jet pulsations, are discarded and the power there is set to zero. The power spectral density for the other points within the plane is calculated and the fraction of power in the peak as compared to the total is calculated. Owing to large stochastic variations the spectrum is quite broad.

Figure 8.2 (a) shows the contour plot of a $\beta = 0°$streamwise injection at $X/D = 3$ for the fraction of the power contained in the peak at a point in the measurement plane. Figure 8.2 (b) shows the same for a compound angled jet. Within the primary jet it is observed that all the regions constituting the primary jet and which are arriving from the hole after pulsations can be considered to have a frozen flow as they all have similar power fractions in their spectrum. The mean flow obviously is not pulsated and hence after filtering does not show large peaks. The compound angled injection has more of the jet contribution spread in a larger area and the fraction of power contained in the dominant frequency is similar within the main jet zones. It is observed from both the figures that the important zones within the jet which are coming from the pulsating jet plenum are in phase with each other as the highest fraction of their power spectrum is concentrated in the dominant $f = 400$ Hz frequency. As 90% of the mass flow ejected from the jet is within the jet structure which shows up as non-zero values in these plots, it can be assumed that all the particles from within the plenum are mostly in phase.

The phase angle from the FFT of the temperature signal can also be calculated for every point. The mean is first subtracted from every signal to remove the bias and the phase angle is calculated for the dominant peak frequency at every point (which is $f = 400$ Hz for the pulsating jet). This is shown in Fig. 8.3. The calculation of phase angle is very much affected by the noise in the signal which is removed through ensemble averaging for the final measurements shown in later sections. However, for the raw signals, the phase of the max power frequency component is also not very different at different points and the picture supports the usage of a frozen flow hypothesis for unsteady visualizations for the streamwise injection case. Figure 8.2 (a) shows the spread of phase angles within the jet for streamwise injection and Figure 8.2 (b) shows the same quantification for a compound angled injection. It must be noted that a phase angle of zero in the figures implies that those zones were ignored as the power spectrum from the dominant frequency in those areas is indistinguishable from broad band noise.

8.3.2 Total Pressure Loss Coefficient, $C_{P,t}$

The total pressure loss coefficient, $C_{P,t}$, as defined in Eq. 8.3 is plotted at $X/D = 6$ for streamwise and compound angled injection, in the presence and absence of 400 Hz or $f_r = 0.025$ pulsation in Fig. 8.4. The wake shows up as a region of high total pressure loss. It should be noted that
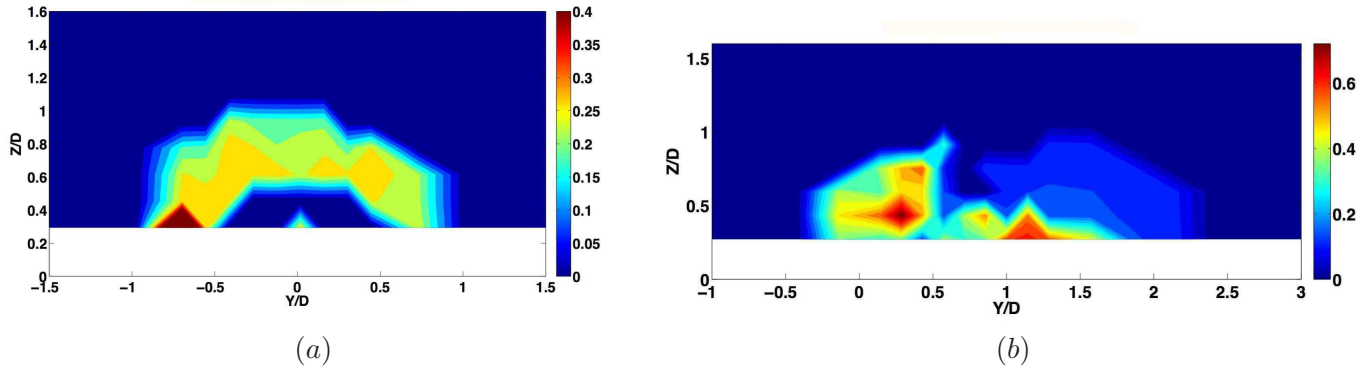
Figure 8.2: The ratio of power contained in the peak frequency of 400 Hz in the power spectrum (computed from the Fast Fourier Transform of the raw signal from the FENT probe) to that of the total power at every point for the pulsated case of $f = 400$ Hz, BR=2, DR=1.3 at $X/D = 3$ for (a) $\beta = 0°$ and (b) $\beta = 60°$
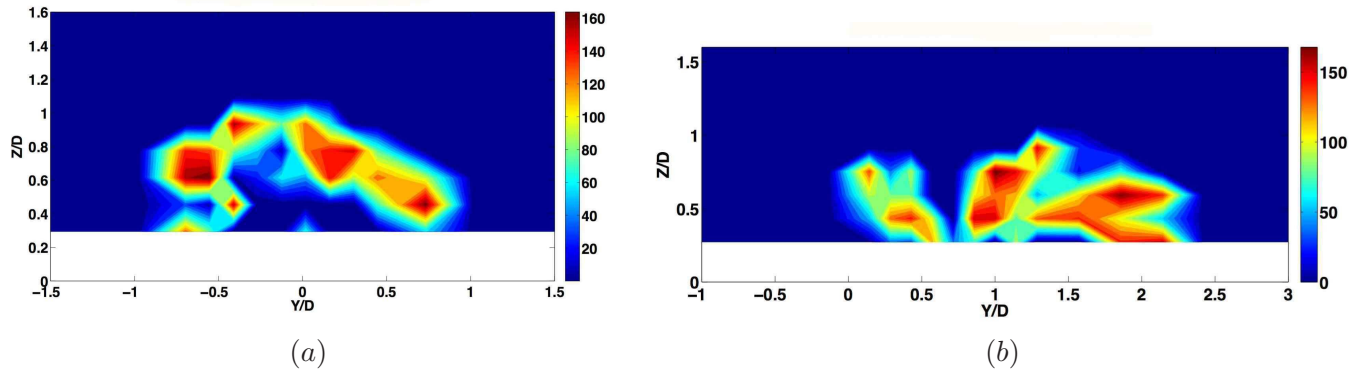
Figure 8.3: Contour of phase angle in degrees at the frequency with maximum power for $f = 400$ Hz, BR=2, DR=1.3 at $X/D = 3$ for (a) $\beta = 0°$ and (b)$\beta = 60°$

since the blowing ratio is 2, the total pressure of injection is higher than that of the freestream and unless the reference pressure, P_{ref} is mass weight-averaged as shown in Eq. 8.1, there would have been regions in this plot having negative values. The total pressure loss for a compound angled injection in Fig. 8.4 show the larger spread of the injected coolant in Fig. 8.4 (d). It can be argued that the $C_{P,t}$ plot only shows the regions of pure aerodynamic loss even though other losses are taking place. The compound angled jets, Fig. 8.4, (c) and (d), both show a greater spread of loss on the windward side of the jet due to the blockage effect, which leads to some total pressure drop in the freestream.
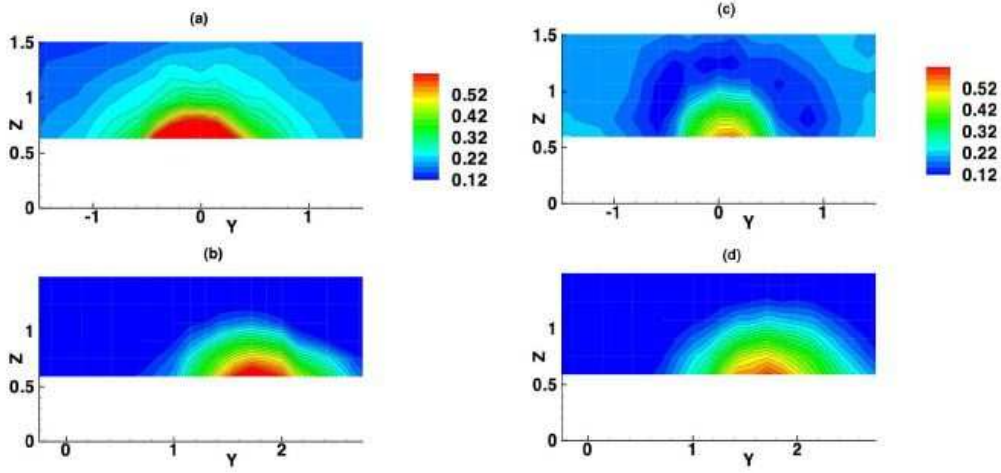
Figure 8.4: Time averaged total pressure loss coefficient, $C_{P,t}$ AT $X/D = 6$ for (a) $\beta = 0°$, $f_r = 0$ (b) $\beta = 60°$, $f_r = 0$ (c) $\beta = 0°$, $f_r = 0.025$ (d) $\beta = 60°$, $f_r = 0.025$

8.3.3 Entropy Generation and Temperature Profiles

Streamwise injection

The local temperature within a film cooling jet, T, is non-dimensionalised using, $\theta = \frac{T-T_h}{T_c-T_h}$. The entropy change is with respect to the reference conditions as described in Eq. 8.1 and 8.2. Figure 8.5 (a) and (b) shows the time averaged contours for θ for a streamwise injection at $\beta = 0°$. It is clear that due to time-averaging the Fig. 8.5, (a) and (b) are almost identical, except for part of the flow in (a) below $Z/D = 0.5$ which could not be measured due to probe access difficulties for that one case. However, at high pulsation frequency it has been shown in Bernsdorf et al. [14] that a pulsating flow is quasisteady to the point that it has almost the same flow-structure of a non-pulsating flow when viewed in time-averaged conditions. This is not strictly true for the plots of the entropy function, $e^{-\frac{\triangle s}{\mathcal{R}}}$ which shows higher losses for the pulsated case especially in the wake region. The time-averaged plots, thus give only a partial insight into the actual comparison because as visible in Fig. 8.1, the BR variation over a pulsation period is almost 0.6, which would lead to quite a bit of smearing of the temperature and pressure distribution in the wake.

Since, the entropy contours are closely correlated to the temperature contours as shown in Fig. 8.5, only the contours of the entropy function will be considered henceforth. In Fig. 8.1, the trough of the pulsation is at t/T = 0.3, but in Fig. 8.6, the jet appears smallest at t/T = 0.64. Hence the crest of the jet appears at t/T = 0.08 and the trough at t/T = 0.64. Only these two phases are shown at different downstream points as the variation is quite small at other phases. The temperature distribution downstream of the hole does not disappear completely as
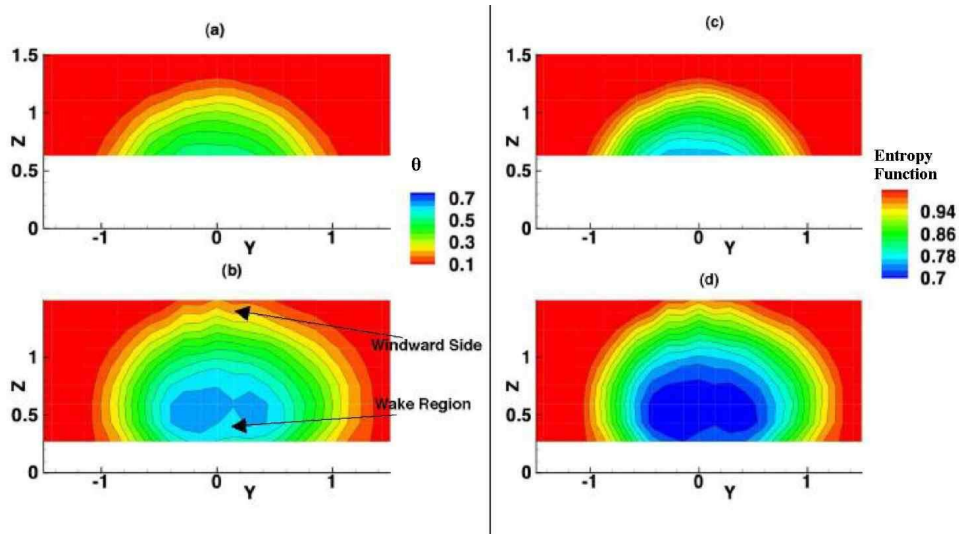
Figure 8.5: Time averaged non-dimensional temperature, $\theta = \frac{T-T_h}{T_c-T_h}$ at X/D=6 for (a) $\beta = 0°$, $f_r = 0$ (b) $\beta = 0°$, $f_r = 0.025$. Time averaged contours of the entropy function, $e^{-\frac{\triangle s}{\mathcal{R}}}$, shown for (c) $\beta = 0°$, $f_r = 0°$ (d) $\beta = 0°$, $f_r = 0.025$
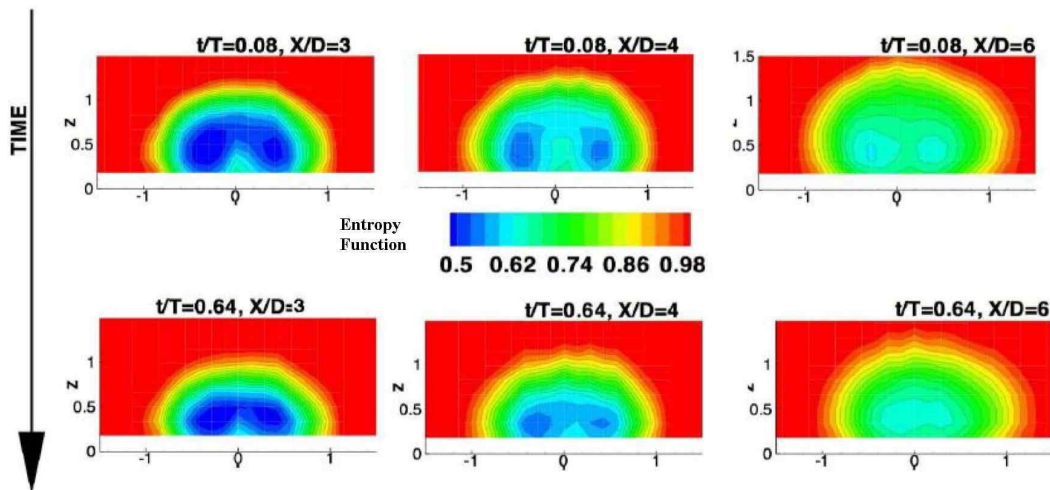
Figure 8.6:   Contours of the entropy function, $e^{-\frac{\triangle s}{\mathcal{R}}}$ of a pulsating jet at $BR = 2$, $DR = 1.3$, $\beta = 0°$, shown at X/D = 3,4,6 and at the crest t/T = 0.08 Aand the trough, t/T = 0.64 during a pulsation

the injection is not being completely switched off due to the high frequency. It simply becomes smaller and travels closer to the wall as the effect of the trough passes through.

Figure 8.6 shows the entropy function contours as they vary with time during a single pulsation and their behavior with increasing distance from the injection hole. The entropy change takes into
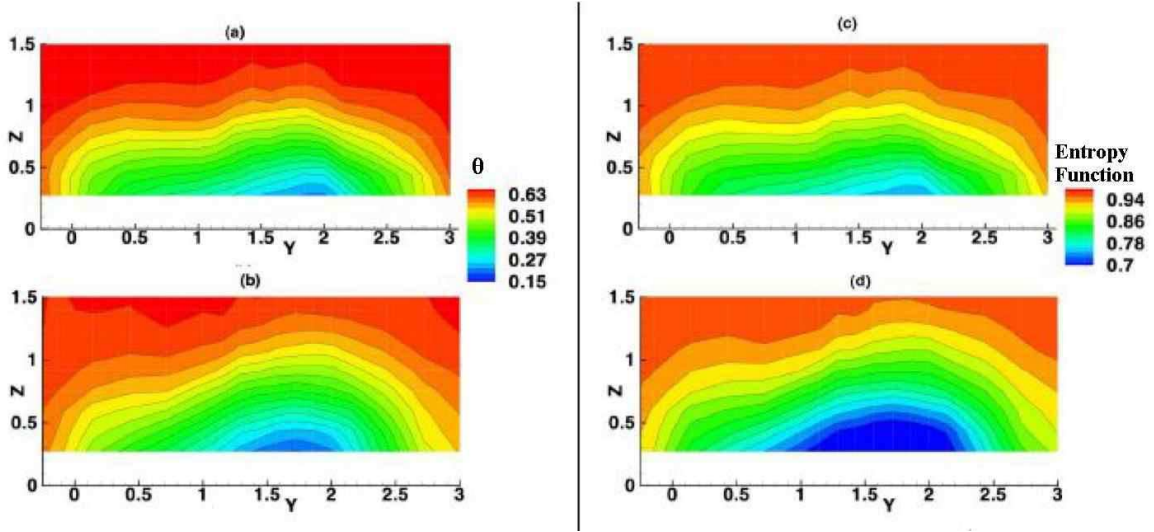
Figure 8.7: Time averaged non-dimensional temperature $\theta = \frac{T-T_h}{T_c-T_h}$ at X/D=6 for (a) $\beta = 60°$, $f_r = 0$
(b) $\beta = 60°$, $f_r = 0.025$. Time averaged contours of the entropy function $e^{-\frac{\triangle s}{\mathcal{R}}}$, shown for
(c) $\beta = 60°$, $f_r = 0°$ (d) $\beta = 60°$, $f_r = 0.025$

account the change in total temperature and total pressure. The similarity of entropy contours to the temperature contours, suggests, the preponderance of the temperature gradients over the pressure gradients in entropy generation. The sites of high entropy change are found within the coolant core. On comparing the figures at t/T = 0.08, X/D = 3 and t/T = 0.64, X/D= 3, it can be readily concluded that the as the jet becomes smaller with the pulsation trough at t/T = 0.64, the place where entropy change is maximum in both the plots is within the coolant core, where the lowest total temperature can be found.

Compound Angled Injection

The time averaged plots of θ and entropy function, $e^{-\frac{\triangle s}{\mathcal{R}}}$ for the pulsated and non-pulsated jet with a $\beta = 60°$ lateral angle are shown in Fig. 8.7. The temperature distribution of the compound angled jet has some distinct characteristics when compared to a streamwise injection. From detailed simulations of lateral angled jet of McGovern and Leylek [84], Hyams and Leylek [61], Brittingham and Leylek [18] it is known that the jet almost never lifts of even at BR = 2 and is always attached to the wall. These studies show that the CVP structure is replaced by only a single vortex which is much weaker in intensity than a corresponding CVP. The temperature profiles in Fig. 8.7 reiterate the fact as the coolant jet has a significantly lower vertical spread and is almost squashed down to the wall laterally when compared to a streamwise jet. It is suspected that part of the boundary layer wake of the lateral angled jet is not visible since it is very close to the wall which could not be accessed by the FENT probe. A single vortex core, which had been ejected at Y = 0, piles up the boundary layer mixed with the cool fluid preferentially on
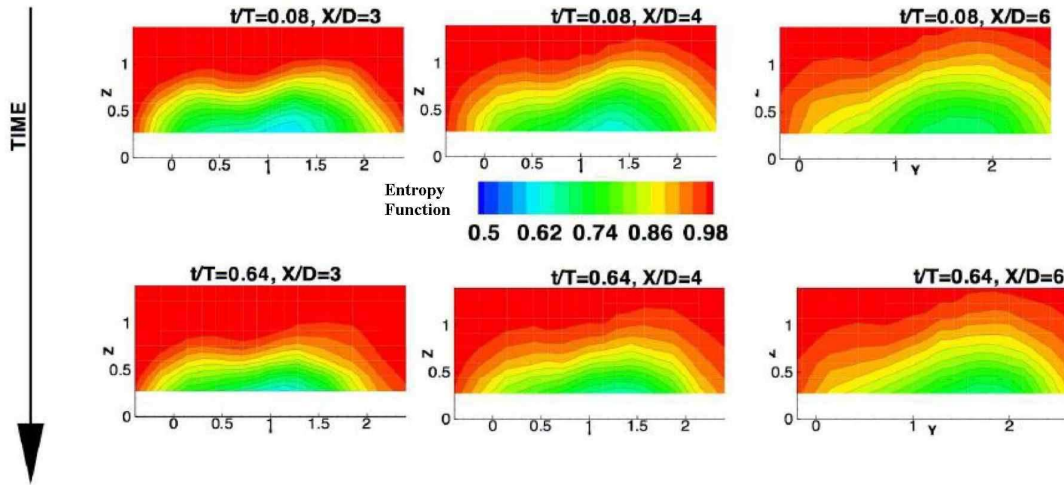
Figure 8.8: Contours of the entropy function, $e^{-\frac{\triangle s}{\mathcal{R}}}$ of a pulsating jet at $BR = 2$, $DR = 1.3$, $\beta = 60°$, shown at X/D = 3,4,6 and at the crest t/T = 0.08 and the trough, t/T = 0.64 during a pulsation

one side by entrainment, causing the shape observed. The time averaged temperature contours of the pulsated flow, Fig. 8.7 (b) shows some differences from the steady flow. This is because the lateral penetration of the jet in the Y direction increases with increasing BR, so during a pulsation, the cross-section of the jet boundary not only grows larger and then smaller with time when viewed in the Y-Z plane but also moves from left to right in the Y direction. The ramifications of these dynamics are visible in the entropy change contours where (d) shows a larger coolant wake with a pronounced single pile-up as compared to (c) which is smaller and spread closer to the wall. The pulsating jet, due to its lateral movement, does not allow the coherent pile-up of the boundary layer, but instead shows a larger coolant core which is lifted slightly higher than the steady jet. The spatial extent of the regions with greater entropy change is seen to be higher in the pulsated case. A primary conclusion from the entropy contours of Fig. 8.7, is the good correlation with the temperature distribution.

The time-resolved entropy contours in Fig. 8.8 show that during a pulsation, only the size of region at X/D = 6 changes but not its shape unlike in the plots at X/D = 3. It can thus be concluded that the lateral sweeping effect of the jet due to pulsation is not apparent after about 4 diameters downstream of the injection location. The coolant spread with the compound jet is much greater laterally than that of a streamwise case, but the spread is much closer to the wall, as is visible from Figs. 8.6 and 8.8.

These figures suggest that the thermal mixing of the jet with the hot fluid could be taking place in different ways. For a streamwise injection, it has been shown in previous literature as well as in the thermal contours of Fig. 8.5 that coolant core mixes with the hot fluid entrained from outside by the CVP thereby getting warmer. In the background of the knowledge that a

h
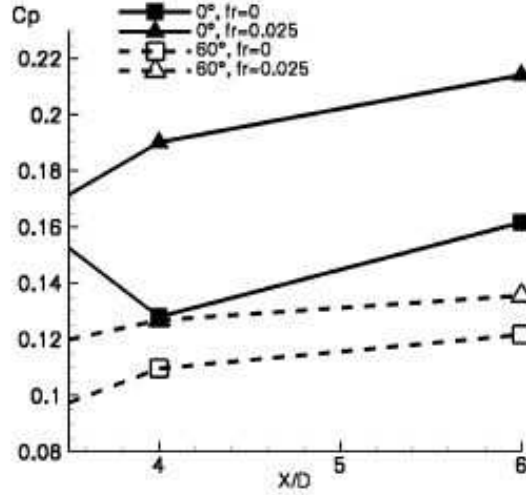
Figure 8.9: Evolution of time averaged mass flow weighted average of the total pressure loss coefficient $C_{P,t}$ with distance from hole center

compound angled jet has most of its coolant spread within the boundary layer, not only is the coolant more spread out; but due to the absence of a strong CVP, there is little entraining of hot fluid from the freestream to within the jet. Instead a better distribution of temperature within the boundary layer occurs which piles up on one side as the coolant spreads laterally rather than remaining confined within a vortex core.

8.4   Mass Averaged Loss Quantification

From Fig. 8.5 and Fig. 8.7 it appears that pulsating a compound angled jet changes the local entropy and temperature distribution much more than with a streamwise jet, however it should be noted that the momentum of a streamwise jet is much higher than a compound angled jet at the same downstream distance due to the strong entrainment of its CVP, whereas the compound angled jet loses its forward momentum in the redistribution of the coolant laterally and energizing the boundary layer. In order to get averaged quantities of performance which can be conveniently interpreted, the total pressure loss coefficient, $C_{P,t}$, entropy loss coefficient, ζ and the kinetic energy loss coefficient, ξ were mass flow averaged at the measurement planes using Eq. 8.7, where $\mathcal{F}$ represents the quantity being averaged.

$$\bar{\mathcal{F}} = \frac{\int\int \mathcal{F}\rho V \, dA}{\int\int \rho V \, dA} \tag{8.7}$$

Figure 8.10: Evolution of phase resolved mass flow weighted average of the total pressure loss coefficient $C_{P,t}$ within a single pulsation of $f_r = 0.025$

8.4.1   Total Pressure Loss Coefficient

Figure 8.9 shows the mass averaged total pressure coefficient for different conditions. It is conjectured that this quantity indicates the total pressure loss from the cooling hole as well as that suffered by the main flow during the mixing process. It must be noted however that for all cases, parts of the wake very close to the wall, where there could be significant pressure loss was not measured due to the inaccessibility of the probe. It is observed in Fig. 8.9 that the mass weighted time averaged total pressure loss increases much more for the streamwise case for successive downstream stations then for the compound angle jets in general. Pulsating jets tend to have higher pressure losses on an average than steady jets. Total pressure losses are caused due to non-isentropic momentum mixing, which are enhanced by pulsation. A compound angled injection suffers from lesser total pressure loss, even though it can be argued that the injection with its greater cross-section to the freestream, would cause a larger blockage and hence greater losses in the freestream. This is due to the fact that on mass averaging, the lower losses caused in the jet body itself tend to compensate the blockage total pressure loss. Due to the lesser effective velocity difference between jet and freestream, the losses at jet exit are lesser for a compound angled injection. Figure 8.10 shows the change in the mass-weighted pressure loss coefficient for measurement planes at X/D = 3 and 6 at different phases within a pulsation cycle for streamwise and compound angled holes. Since, the change in loss coefficient during a pulsation increases with downstream distance for the streamwise case by almost 20% but only by about 5% for the compound injection, it can be argued that the dissipation of total pressure due to mixing is higher for a streamwise injection.
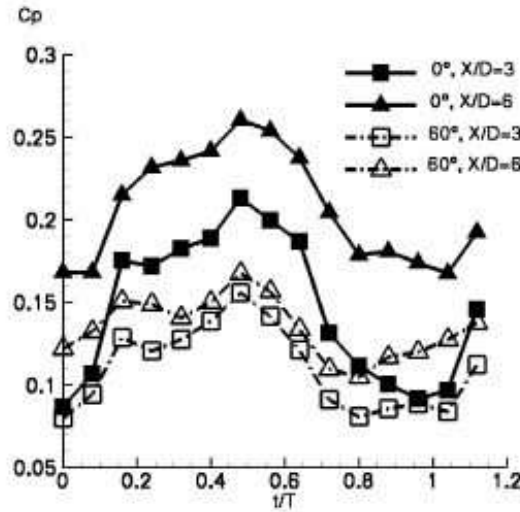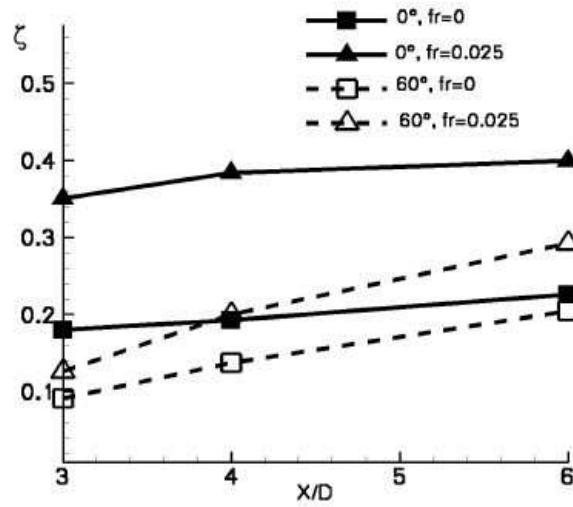
Figure 8.11: Evolution of time averaged mass flow weighted average of the entropy loss coefficient, ζ with distance from hole center with and without pulsations
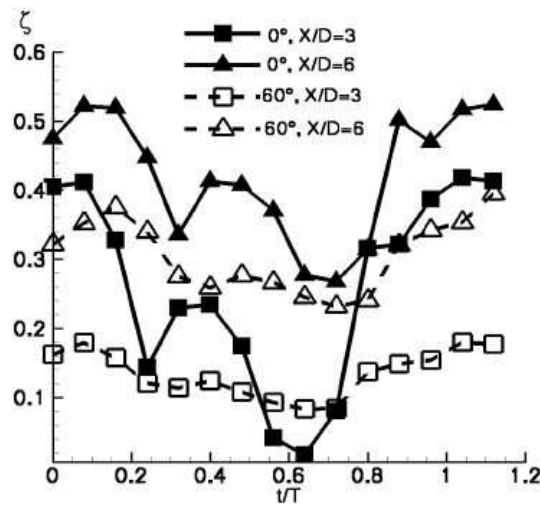
Figure 8.12: Evolution of phase resolved mass flow weighted average of the entropy loss coefficient, ζ at two distances and pulsation of $f_r = 0.025$

8.4.2 Entropy Loss Coefficient

Entropy change has been advocated as the most physically relevant loss parameter by Denton [34] for turbomachinery analysis. However, in Denton [34], the explanations and models about film cooling loss are focussed only on the loss undergone by the freestream and that too in a control volume analysis, where the final quantities are calculated after the complete mixing. The entropy

loss coefficient primarily shows the losses the freestream suffers due to (a) viscous dissipation (b) mixing of mass, momentum and energy and (c) heat transfer. Due to the modified definition of the reference quantites described by Eq. 8.1 and 8.2, this loss coefficient would also indicate the losses that the jet itself suffers within the hole and during ejection. It should be noted, that the results in this section are an attempt to understand the near-hole loss generating mechanisms with a somewhat different definition of entropy loss than that espoused in Denton [34]. Owing to probe inaccessibility to far downstream positions, the fully mixed-out averaged losses could not be calculated, but rather attention is focussed on the evolution of loss with downstream mixing as well as its variation at near-hole positions during a pulsation. These definitions seek to understand loss-generating mechanisms during the mixing process in detail.

The mass-averaged entropy loss coefficient as described in Denton [34] and given by Eq. 8.5 is shown in Fig. 8.11. One notable feature is the greater slope of the $\beta = 60°$ case with distance than of the streamwise injection. This means that the entropy loss is increasing much faster for the compound angled case spatially downstream than that of the streamwise injection. The entropy change for a compound angled injection at X/D = 6 is almost double that at X/D = 3, whereas the same ratio for streamwise injection is only about 10 to 20 percent. This is due to greater thermal mixing during compound angled injection. However, the streamwise injection has a higher loss to begin with, say at X/D = 3, which does not increase as substantially because the thermal mixing is not as prominent as the jet propagates downstream. The near-hole flow-field computations of McGovern and Leylek [84] show that the geometry of the incoming jet significantly affects the freestream-crossflow pressure field at the exit. This is manifested as the streamwise jet suffers most of its total temperature and pressure loss while being injected into the freestream and the viscous dissipation thereof due to the higher effective velocity difference between the jet and the freestream at every elemental area. The compound angled injection being injected much closer to the wall, has areas of lower momentum and therefore lower viscous dissipation due to velocity differences between the jet and freestream.

Pulsating the flow shows a marked increase in the entropy loss coefficient in both streamwise and compound angled cases. The averaged plots also show that pulsating a streamwise jet increases the entropy loss coefficient by almost 65% but only by around 10% of that for the compound angled case. Hence, it is insightful to view the change in the mass-weighted entropy loss coefficient, ζ for the pulsating flow in a time resolved manner as shown in Fig. 8.12.

A few observations are noteworthy in Fig. 8.12. Firstly, the relative variation in the entropy loss production over a cycle corresponds to the jet size as demarcated by the entropy contours in Fig. 8.6 and 8.8. Because of this, the trough of the entropy loss variation corresponds to around t/T = 0.64 at which point the jet is observed to have the smallest size and shows highest loss when the jet is at its largest. Secondly, the variation of the entropy loss coefficient for the streamwise case has a much larger range within a cycle than that of the compound angled case. This is because as the effective BR increases and decreases for the streamwise jet during a pulsation, it lifts away from the wall and comes closer to it respectively. However, the compound angled jet

h
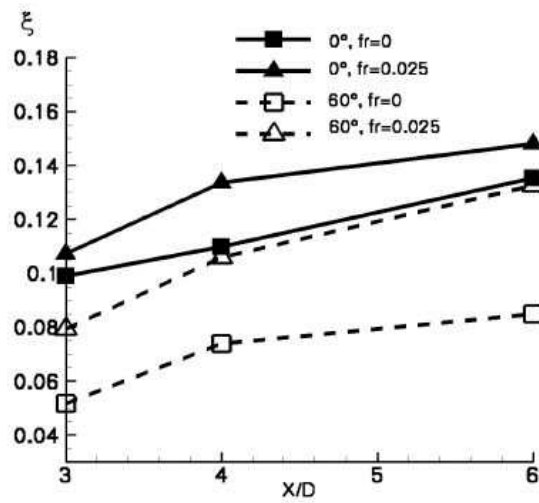
Figure 8.13: Evolution of time averaged mass flow weighted average of the kinetic energy loss coefficient, ξ with distance from hole center with and without pulsations
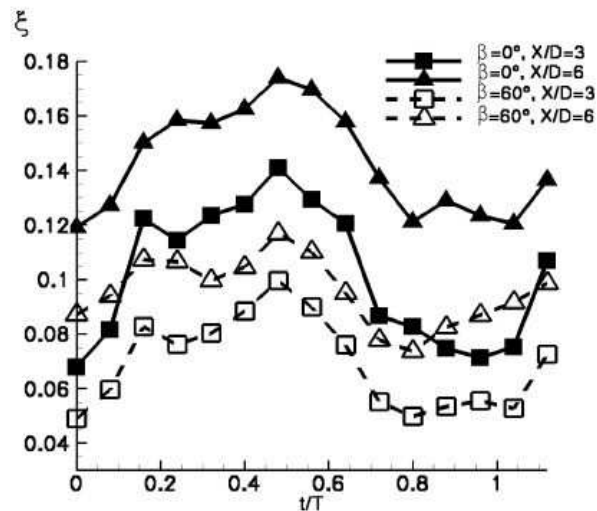
Figure 8.14: Evolution of phase resolved mass flow weighted average of the kinetic energy loss coefficient, ξ at two distances and pulsation of $f_r = 0.025$

stays more or less attached to the wall during the entire cycle but only moves laterally within a pulsation thereby not going through as big a change in jet spatial extent as the streamwise case. This is manifest quite starkly at the point $t/T = 0.64$ where for the $X/D = 3$ curve, the trough of the entropy change for $\beta = 0°$ is even lower than that of $\beta = 60°$, whereas the crest at $t/T = 1.08$ is a good two and a half times larger.

8.4.3 Kinetic Energy Loss Coefficient

The kinetic energy loss coefficient as described in Eq. 8.6 has been often used to describe the performance of film cooling geometries by taking into account losses in jet and freestream both.

Figure 8.13 shows the mass averaged kinetic energy loss coefficient, ξ, derived from the time-averaged temperatures and pressures at different downstream points for all the conditions. This loss coefficient indicates both the mixing loss and separation losses in kinetic energy suffered by the jet and freestream in a combined manner. The trends are similar to the entropy change curve, i.e. overall the streamwise injection shows higher losses than the compound angled ones and pulsation increases the losses of a steady jet. The relative increase in loss for the compound angled case from X/D = 3 to X/D = 6 is higher which could indicate the greater mixing loss contribution due to compounding. Pulsation would tend to reduce the averaged kinetic energy anyways as during part of the cycle the high BR jet becomes smaller at all planes of measurement. As far as the average loss is concerned the kinetic energy loss coefficient shows similar information to the entropy loss coefficient. However, this is only true because the entropy loss coefficient takes into account the losses in the jet itself and not only the freestream.

The time-resolved plots of the mass-averaged kinetic energy loss coefficients are shown in Fig. 8.14. The trend in the variation over a cycle is very similar to the total pressure loss coefficient variation and somewhat different to the evolution of the entropy loss coefficient. The lowest kinetic energy loss within a cycle appears just after t/T =0.88 at which point the jet is at its largest size from the time-resolved entropy contours. This trend is quite different than that of the entropy loss coefficient plot in Fig. 8.12. It appears that the kinetic energy loss coefficient variation lags the variation of the low temperature jet regions by about half a cycle. The explanation has more to do with the definition of these quantities than the mechanisms.

Through the discussions in Young and Wilcox [110] with regards to the air-cooled gas turbine, using the basic framework of an injection into a freestream, it is understood that the entropy creation is basically divided into two terms. One is the entropy change due to kinetic energy change of the jet and freestream as their velocities equilibrate. This is because of viscous dissipation as well as momentum mixing. The second contribution to entropy change is due to the thermal mixing. Figure 8.12 shows the entire loss variation, whereas Fig. 8.14 shows mainly the change in kinetic energy and not the associated thermal losses due to thermal mixing. It is for that reason that the entropy change variation within a cycle follows the jet growth and shrinkage closely whereas, the kinetic energy loss variation within a cycle shows a definite offset. The differences in the time scales with which a change in velocity propagates compared to the convective transport of temperature by the jet body are responsible for these offsets especially since the pulsation frequency is very high. Based on this reasoning, Fig. 8.14 shows that although the absolute levels of kinetic energy loss for streamwise injection is higher, the relative variation of the coefficient within a cycle is not too different for the two geometries. Compare this observation to the large difference in variation of the entropy change coefficient within a cycle. This

large variation is due to the inclusion of the thermal losses which would completely depend on the spatial extent of the low temperature fluid within the region of interest. The advantage of using compound angled jet is therefore not only to give an increased coolant coverage but also to reduce the aerothermal losses in a high blowing ratio application. Although compound angled injection has greater thermal mixing losses which increase with downstream distance, it cannot be ascertained whether at a point far downstream the mixing losses would be high enough to be higher than the losses in the streamwise injection.

8.5   Summary

Detailed measurements using a novel probe technique that allows simultaneous measurements of temperature and pressure have been performed. A novel probe access and traversing system has been used for a flexible and rapid experimental campaign. The presence of a thermal gradient between the freestream and the coolant, led to significant observations, mainly with respect to evolution of loss due to thermal mixing. Mass-weighted inlet total pressures and temperatures were used as reference conditions to better capture the entropy change within the incoming jet and the freestream simultaneously. The entropy change contours followed the same trends of the temperature contours. It was observed that the wake of a streamwise jet has areas of high entropy change and the cores of the counter rotating vortex pair showed the regions of maximum entropy change. As the jet mixes with downstream propagation, the coolant spread increases and the areas of entropy generation spread over a larger region in step with the temperature mixing. The compound angled jet in general is closely attached to the wall even at high BR. The areas of high entropy change are again mostly confined within the coolant body. One important observation during pulsation is that a streamwise jet increases and decreases in size as it rises vertically above the wall, whereas a compound angled jet has a distinct lateral movement. In light of these observations the important conclusions are as follows:

1. The compound angled jets have lower entropy losses than streamwise ones, (between 40 to 75% lesser depending on downstream distance from the hole) which increase faster with thermal mixing as the jet propagates downstream. However a streamwise jet still leads to greater entropy change primarily due to viscous dissipation and separation losses at the hole exit.

2. The usage of a compound angled hole would seem to have the benefit that kinetic energy losses suffered by the jet itself are lower, even while having a greater coolant coverage over a larger part of the metal. A possible drawback is that thermal mixing losses keep increasing with downstream distance. However, whether, at a far downstream position these losses become greater than that for a streamwise injection could not be ascertained due to limited data.

3. A pulsating jet shows a marked increase in aerothermal losses due to greater thermal mixing

and enhanced shear losses due to the changing size of the jet. A streamwise pulsating jet has around double the entropy loss than that of a steady jet due to greater penetration and effective blowing ratio variation near the hole.

4. A pulsating compound angled jet suffers only about one and a half times the loss of a steady jet at the same downstream position as the jet does not penetrate very much into the freestream but is forced to oscillate in a lateral direction against smaller shear forces.

5. It has been shown that an entropy loss coefficient incorporates the loss due to momentum mixing, thermal mixing and separation losses near the hole exit.

6. The kinetic energy loss coefficient, on the other hand would reflect the loss due to separation and momentum mixing, but the loss in thermal energy due to mixing would be underpredicted.

Chapter 9

Discussions and Conclusions

The research objectives envisaged in this work were to expand the experimental database of flow structure information for round hole film cooling as well as to understand the effect of the primary flow features of compound angled jets on the thermal cooling performance. The measurement of high resolution three dimensional velocity flow field of compound angled film cooling at different angles and operating conditions fulfilled one of the aims of the project, which was to provide high quality experimental data for computational model development and validation. In order to bring about a closer understanding between the fluid dynamics and the heat transfer parts of the problem, infrared thermography was also employed. High resolution surface temperature data at the same operating conditions as the PIV measurements helped to wean out the effects of the primary flow structure on adiabatic effectiveness and film heat transfer coefficient. Velocity measurements of pulsating compound angled flows were conducted for the first time and the effect of periodic unsteadiness on not only the flow structure but also on cooling performance was presented. Given the fact that compound angled round holes are still used extensively for cooling of gas turbine blades as they are cheaper to manufacture than most other sophisticated geometries, their in depth studies are required. This project thus, seeks to clarify the interaction between flow and cooling which may guide future designers as well as help computational researchers better their predictive tools.

9.1 Contribution of Current Work

9.1.1 Experimental Setup and Methods

The experimental study presented in this thesis was envisaged as a continuation of a previous experimental flow structure investigation of streamwise film cooling jets (Bernsdorf [12]). The particle image velocimetry system used was the same. Apart from adding extensive compound angled film cooling flow structure data at different angles and operating conditions, this study was
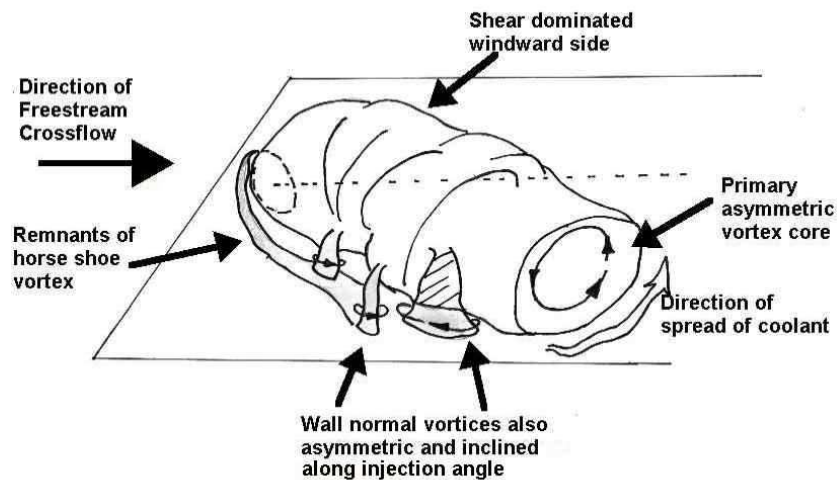
Figure 9.1: Cartoon schematic showing the main vortical elements of a compound angled film cooling jet

also designed to investigate in detail the connection between the flow physics and the observed thermal performance quantifications from other heat transfer studies. Hence, the experimental rig was suitably modified to accommodate not only heat transfer studies but also access with probes to glean a better understanding of the temperature and pressure field of the ensuing jet. An isothermal boundary wall was created by thermally managing it with a hot water system, an infrared thermography capable access window and thin film sensors for in situ calibration of temperature were also added. The usage of an entropy probe was demonstrated with a novel circle in circle access system. These rig modifications were coupled with specialized codes and post processing software which were written specifically for the current measurements. A finite element method for calculating the heat flux through the entire thermal management layer was developed and validated. The effect of radiation effects were also investigated in detail and found to be insignificant for the errors in heat flux measurements. The experimental systems and instrumentation developed as part of the current project would find further use in continuing the work towards fundamental understanding of complex flows found in turbomachinery from a combined fluid dynamics-heat transfer perspective.

9.1.2   Flow Physics and its Effect on Thermal Performance

The flow structure velocity measurements elucidated some general features which sets a compound angled film cooling flow apart from a simple jet in crossflow. A cartoon schematic of the vorticity structure is shown in Fig. 9.1. Although the finer features are dependent on the momentum flux ratio for most compound angles above 45°with respect to the freestream, the main flow features are quite similar qualitatively. The single primary vorticity emerges from the
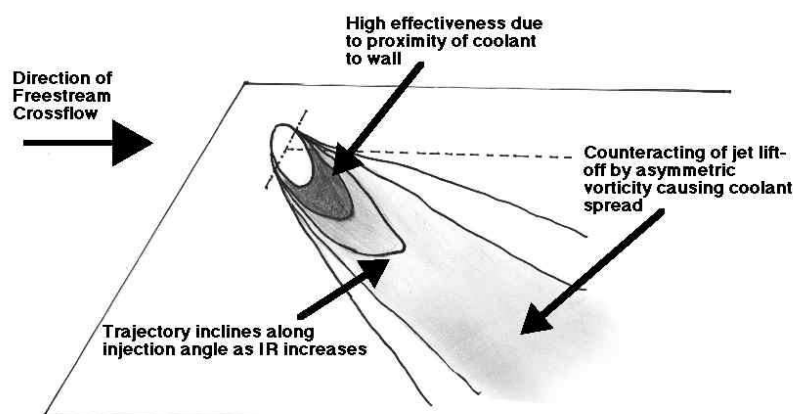
Figure 9.2: Cartoon schematic showing a typical adiabatic effectiveness distribution for a compound angled film cooling jet

injection hole and the aligning of its trajectory with the injection angle is stronger at higher momentum flux ratio. The lateral momentum of the jet orients the primary vorticity along an angle to the freestream. As the vertical momentum is thus reduced due to the redistribution; the lift-off of the jet against the freestream is reduced and in the near hole region it has greater proximity. When a vortex ring emerging from an injection hole due to the jet impulse is forced to bend towards the wall due to the crossflow, the vortex ring curves towards the wall, leading to the creation of a pair of counter rotating vortices as described in Greitzer et al. [51]. As shown in Fig. 9.1, the injected vortex ring is in a lateral direction rather than normal, due to which the single large vortex maintains itself without splitting into a counter rotating vortex pair as it is unbounded in the lateral direction. An important consequence of this vortical structure is that coolant injected by the jet is forced to be spread laterally as shown in the figure.

The wake vortices or the wall-normal vortices which are remnants of the horse shoe vortex formed as a result of the blockage offered to the freestream by the jet body are also quite prominent. As the vorticity is shed asymmetrically due to the compound alignment of the jet body, one side of the jet has smaller extent of normal vorticity whereas the other side has a larger, more spread out area of normal vorticity. This is shown in the figure as the thinner and thicker normal vorticity structures on laterally opposite sides of the jet. The absence of a counter rotating vortex pair also reduces the normal convection of the hot freestream fluid towards the wall by the concerted action of the two vortices. The main effect of increasing momentum flux ratio is to increase the size of this asymmetric vortex as well as to align the trajectory of the vortex with the original injected direction as the lateral momentum is greater. The streamwise vorticity can be quantified as an averaged quantity by observing the circulation. The circulation of the asymmetric streamwise vorticity scales with a momentum flux ratio scaled downstream distance for individual compound angles. The rate of decay increases for higher angles, whereas the overall
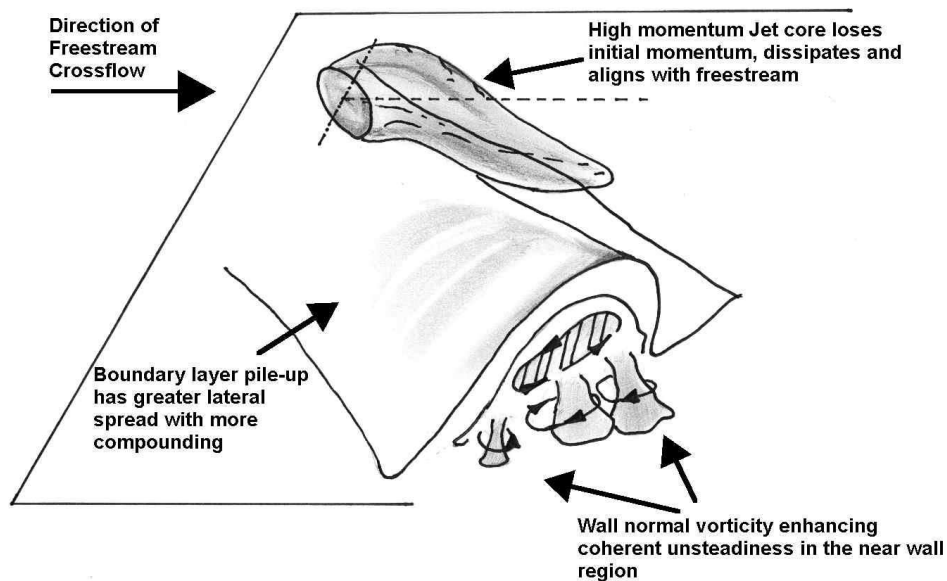
Figure 9.3: Cartoon schematic showing the evolution of the boundary layer pile-up for a compound angled film cooling jet

magnitude depends on the momentum flux ratio.

A compound angled injection is shown to have larger spread of adiabatic effectiveness. A typical large compound angled adiabatic effectiveness behavior is shown as a cartoon schematic in Fig. 9.2. As compared to a typical high momentum flux ratio streamwise injection effectiveness, there is no strong jet detachment and reattachment effect. The high effectiveness in the near hole area is due to the proximity of the coolant as the jet momentum is divided into vertical and lateral components and so the reduced vertical component results in a greater coolant proximity. For low momentum flux ratios, the coolant proximity is higher but then, in the far downstream region there might not be enough bulk mass of the coolant for keeping up the enhanced effectiveness. The advantage of a compound angled injection is clear when it is used in a high blowing ratio mode when there is greater bulk mass that is available for having coolant coverage downstream, however this also results in a stronger vertical momentum which would increase the distance between the coolant and the wall. The downstream zone shown in Fig. 9.2 is mainly due to improved coolant spread due to the streamwise vorticity shown in Fig. 9.1. In this zone although there is lesser intensity of effectiveness, the average spread of effectiveness is much more. It is thus seen that the coolant spread counteracts the increased wall distance of the jet in this case.

Another important finding from these measurements is that the sensitivity of adiabatic effectiveness to changes in momentum flux ratio decreases at higher compound angled injection, precisely due to the combined effect of the streamwise vorticity and breakup of injected momentum into
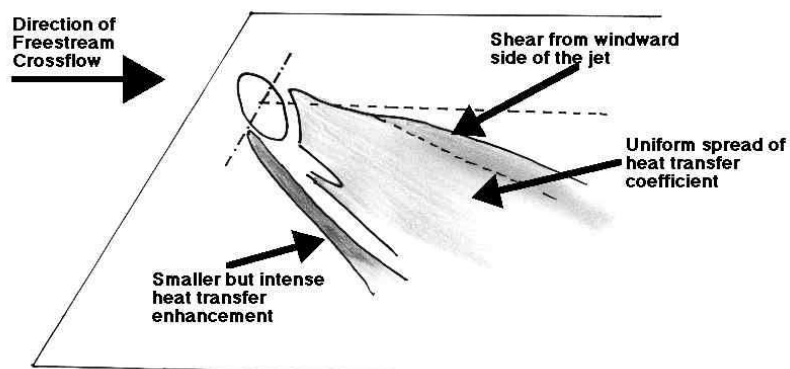
Figure 9.4: Cartoon schematic showing a typical film heat transfer coefficient enhancement downstream of a compound angled film cooling jet

vertical and lateral components.

The vorticity affects the velocity and jet core trajectories in an important way. As Fig. 9.3 shows, the high momentum jet core in the direction of the freestream emerges out of the coolant hole and its forward momentum is leached off into the lateral directions. In fact for lower momentum flux ratios and high compound angles, this high momentum jet core is hardly visible at all as the jet momentum is not concentrated in a core but spread over lateral directions and spread out. The boundary layer pile-up for high compound angled holes is large and encompasses a large wake zone which increases in lateral span with greater compounding and has a reduced sensitivity to momentum flux ratio at high compound angles. The wall normal vorticity which is enveloped under the large boundary layer pile up is a measure of the enhanced coherent unsteadiness in the large wake zone which mixes the flow strongly.

Due to the stronger vorticity, mixing and greater proximity to the wall, a compound angled injection jet produces greater averaged heat transfer coefficient enhancement compared to a simple streamwise jet. This enhancement increases with increasing compound angles but its sensitivity to momentum flux ratio decreases at higher angles too. A typical film heat transfer coefficient footprint is visible in Fig. 9.4. As the phenomenon of jet detachment and reattachment is significantly reduced for compound angled injection, the high heat transfer enhancement spots seen at downstream distances for streamwise angled jets is missing. Instead two legs of enhanced heat transfer are obtained as shown in the figure. Both are correlated to the wall-normal vorticity in size and extent. The intense but narrow enhancement leg is on one side of the jet whereas its counterpart next to it is more uniform, having lower local intensity but larger lateral spread. At the edges the heat transfer coefficient is slightly enhanced at the windward side edges of the jet which have large shear due to interaction with the crossflow. The coherent unsteadiness enhances heat transfer coefficient over large areas for larger compound angled injection. However, the trade-off between high effectiveness and high heat transfer coefficient for compound angled

holes must still be carefully considered.

9.1.3 Effect of Pulsations

The effect of periodic unsteadiness on the flow structure as well as thermal performance was also measured. The amplitude of pulsations was maintained at 30% of the average Blowing Ratio as pulsator design didn't allow a change in the amplitude for a given blowing ratio. Hence only a representative amplitude was used. For the high frequencies measured in this study the effect of frequency on cooling performance could not be ascertained. Time resolved flow structure measurements showed that with a pulsating blowing ratio a streamwise injection has an alternate increase and decrease in its counter rotating vortex pair, whereas a compound angled flow has more of a lateral movement of the jet. This is evident in the phase resolved circulation figures where the main difference in circulation between the phases is in the rate of decay which changes within a pulsation for a low IR. As the rate of decay is a function of the angle, this quantification shows that there is some lateral sweeping motion of the ensuing jet. For the most part the laterally averaged effectiveness does not significantly change with pulsations at a high IR except for a slight increase in the neat hole region. At low IR the decay in effectiveness is higher than without pulsations as the mass of bulk coolant ejecting on to the surface is reduced. A streamwise angled heat transfer coefficient is enhanced more due to pulsations as the jet alternately attaches and detaches which results in vigorous mixing. The sensitivity of heat transfer coefficient to pulsations is very less for a compound angled jets as the phenomenon of jet detachment and reattachment is not observed, but there is only a generally enhanced heat transfer coefficient due to more vigorous jet freestream interaction.

9.1.4 Aerothermal Performance of Film Cooling Jets

The entropy change during the mixing process was measured for the first time for streamwise and compound angled jets with and without pulsations. The aptness of using entropy change with regards to other aerothermal loss definitions like kinetic energy loss coefficient and total pressure loss coefficient were also compared. A novel method for taking into account temperature and pressure losses from both coolant and freestream by mass average weighting their initial conditions to use as a reference was also explored. Using a frozen flow assumption, phase resolved loss quantifications were plotted. On an average it was observed that pulsations increase aerothermal loss. Streamwise angled jets had higher loss production than compound angled injection, but due to stronger thermal mixing the rate of increase in loss with downstream distance was higher for compound angled jets. It was observed that the thermal mixing, which is an important contributor to loss is only comprehensively captured by the entropy loss definition.

9.2   Future Work

The results of this study have shed some important insight into the effect of large scale flow features on complex heat transfer performance. The vorticity information was obtained through PIV and the surface temperatures through infrared thermography. This combined knowledge was useful in understanding many important mechanisms which were previously only conjectured through educated guesses and intuitive flow visualization studies. There are two significant paths that diverge from this study for future projects depending on the research strategy. The first is of course, to continue the similar treatment of flat plate studies involving combined PIV and infrared thermography on more advanced cooling geometries like shaped holes and compound shaped holes. The effect of freestream turbulence is very significant for film cooling and heat transfer and some studies must be carried out to incorporate these effects. Diffusor shaped holes are often used on blades for their high effectiveness, but manufacturing and servicing them are expensive industrial processes. If more insight could be obtained into their flow structure, designers could also try to recreate their effects with geometries which are cheaper to manufacture. Trenched holes or film cooling geometries with shapes to create so called anti-kidney vortices would also be interesting. If these experiments are coupled with a parallel computational modeling plan, the industrial application would become much faster as capability to quickly predict complex flows without long computational times or large meshing effort can be achieved. A host of parameters affect film cooling performance and a judicious choice of exploring the parameter space should be determined.

The second research strategy would be more geared towards fundamental scaling laws, transport mechanisms and turbulence information of the flow structure as well heat transfer. The current study has thrown up many results but also many questions which need to be investigated much further. Round holed jets in crossflow are not only used for film cooling but are found in environmental flows, industrial systems, mixers, aircraft engines etc. In most cases the jets are typically aligned either with the surface or laterally with the freestream. The quantification of temperature transport, mixing and circulation for far downstream conditions would be quite important. The current studies only measured circulation until 10 hole diameters. Larger blowing ratios for these geometries and a larger extent of circulation measurement would surely help create a better scaling law with a larger body of data. Turbulence studies at industrially relevant high Reynold's number for these jets in crossflow problem are few and far between. The anisotropy of turbulence intensity as well as turbulent thermal diffusivity should be investigated for streamwise and compound angled holes. As high fidelity methods like LES (Large Eddy Simulation) and DNS (Direct Numerical Simulation) become applicable for complex flows, experimental data is essential not only to make sub-grid scale models but also for validation. The presence of negative turbulent eddy viscosity, $< u'v' > / \frac{\partial U}{\partial y}$, regions are well known from some film cooling experiments. Do these regions also exist in compound angled jets in crossflow? What do the cross-correlation of temperatures and velocity fluctuations look like in different areas of the jet? Can one construct joint probability density functions (PDFs) of velocity fluctuations through a

high resolution measurement? Joint PDFs of temperature and velocity would prove even more useful for the development of PDF methods and models of solving complex 3-D flows, not to say nothing of the immense knowledge of mixing scaling and transport mechanisms that such an investigation would bring.

The current data also revealed some interesting flow phenomena that are worthy of more investigation. It was observed that the streamwise vorticity for compound angled jets also seemed to be affected by the density ratio even if the momentum flux ratio was controlled. For high density gradient flows, baroclinic vorticity is produced. The use of temperature probes and velocity measurements should be able to detect the significance of this effect when applied at a high spatial resolution. Pulsating compound angled flows should also be looked at, in more detail especially through the impact of changing duty cycle and amplitudes on the flow structure and heat transfer. Ultimately if a pulsating film cooling hole can be studied on a real blade representative curved surface, then not only would fundamental understanding improve but also a lot of important data for computational validation would be generated. Although, many different kinds of instrumentation are available for rotating turbine blade heat transfer measurements, these are very cumbersome and give only point measurements. Full field measurements of heat transfer on a rotating turbine blade would be a future aspiration.

Bibliography

[1] R. S. Abhari. Impact of Rotor-Stator Interaction on Turbine Blade Film Cooling. *ASME J. Turbomachinery*, 118:123–133, January 1996.

[2] R. S. Abhari and A. H. Epstein. An Experimental Study of Film Cooling in a Rotating Transonic Turbine. *ASME J. Turbomachinery*, 116:63–70, January 1994.

[3] R. J. Adrian. Particle-Imaging Techniques for Experimental Fluid Mechanics. *Ann. Rev. Fluid Mech.*, 23:261–304, 1991.

[4] R. J. Adrian. Twenty Years of Particle Image Velocimetry. *Exp. Fluids*, 39(2):159–169, 2005.

[5] V. Aga, M. Rose, and R. S. Abhari. Experimental Flow Structure Investigation of Compound Angled Film Cooling. *ASME J. Turbomachinery*, 130:031005, 2008.

[6] H. Ammari, N. Hay, and D. Lampard. The Effect of Density Ratio on the Heat Transfer Coefficient From a Film-Cooled Flat Plate. *ASME J. Turbomachinery*, 112:444–450, 1990.

[7] S. Baldauf, A. Schulz, and S. Wittig. High Resolution Measurements of Heat Transfer Coefficients From Discrete Hole Film Cooling. *ASME J. Turbomachinery*, 123:749–757, 2001.

[8] S. Baldauf, A. Schulz, and S. Wittig. High Resolution Measurements of Local Effectiveness From Discrete Hole Film Cooling. *ASME J. Turbomachinery*, 123:758–765, 2001.

[9] S. Baldauf, M. Scheurlen, A. Schulz, and S. Wittig. Correlation of Film Cooling Effectiveness from Thermographic Measurements at Enginelike Conditions. *ASME J. Turbomachinery*, 124:686–698, 2002.

[10] S. Baldauf, M. Scheurlen, A. Schulz, and S. Wittig. Heat Flux Reduction From Film Cooling and Correlation of Heat Transfer Coefficients From Thermographic Measurements at Enginelike Conditions. *ASME J. Turbomachinery*, 124:699–709, 2002.

[11] A. Basset. On the Descent of a Sphere in a Viscous Fluid. *Quart. J. Mech. Appl. Math.*, 41:369–181, 1910.

[12] S. Bernsdorf. *Experimental Investigation of Film Cooling Flow Structure*. PhD Thesis, Eidgenössische Technische Hochschule Zürich, 2005. Diss. ETH No. 16355.

[13] S. Bernsdorf, M. Rose, and R. S. Abhari. Modeling of Film Cooling- Part I: Experimental Study of Flow Structure. *ASME J. Turbomachinery*, 128:141–149, 2006.

[14] S. Bernsdorf, M. Rose, and R. S. Abhari. Experimental Validation of Quasi-Steady Assumption in Modeling of Unsteady Flow. *ASME J. Turbomachinery*, 130(1):141–149, 2008.

[15] D. G. Bogard and K. A. Thole. Gas Turbine Film Cooling. *J. Propulsion and Power*, 22 (2):249–270, 2006.

[16] J. P. Bons, R. B. Rivir, C. D. MacArthur, and D. Pestian. The Effect of Unsteadiness on Film Cooling Effectiveness. *AIAA Paper 95-0306*, 1995.

[17] J. P. Bons, C. D. MacArthur, and R. B. Rivir. The Effect of High Freestream Turbulence on Film Cooling Effectiveness. *ASME J. Turbomachinery*, 118(4):814–825, 1996.

[18] R. A. Brittingham and J. H. Leylek. A Detailed Analysis of Film-Cooling Physics: Part IV -Compound Angled Injection With Shaped Holes. *ASME J. Turbomachinery*, 122:133–145, 2000.

[19] J. M. Buchlin. Infrared Thermography. In *Advanced Measurement Techniques for Aeroengines and Stationary Gas Turbines*. VKI, Belgium, 2004.

[20] R. S. Bunker. A Review of Shaped Hole Turbine Film Cooling Technology. *J. Heat Transfer*, 127:441–453, 2005.

[21] A. Burdet. *A computationally efficient feature-based jet model for prediction of film-cooling flows*. PhD Thesis, Eidgenössische Technische Hochschule Zürich, 2005. Diss. ETH No. 16163.

[22] A. Burdet and R. S. Abhari. Influence of Near Hole Pressure Fluctuation on the Thermal Protection of a Film Cooled Flat Plate. In *In Proceedings of HT2007, ASME-JSME Thermal Engg. Summer Heat Transfer Conference*, number HT2007-321812 in 1. ASME-JSME, 2007.

[23] A. Burdet and R. S. Abhari. Influence of Near Hole Pressure Fluctuation on the Thermal Protection of a Film Cooled Flat Plate. *ASME J. Heat Transfer*, 131:022202, 2009.

[24] A. Burdet, R. S. Abhari, and M. G. Rose. Modeling of Film Cooling - Part II: Model For Use in 3D CFD. *ASME J. Turbomachinery*, 129(2):221–231, 2007.

[25] C. Camci. An Experimental and Numerical Investigation of Near Hole Cooling Hole Heat Fluxes on a Film-Cooled Turbine Blade. *ASME J. Turbomachinery*, 11:63–70, 1989.

[26] H. S. Carslaw and J. C. Jaeger. *Conduction of Heat in Solids.* Oxford University Press, 1959.

[27] P. Chakraborty, S. Balachander, and R. J. Adrian. On the Relationships Betweeen Local Vortex Identification Schemes. *J. Fluid Mech.*, 535:189–214, 2005.

[28] H. Choe, W. M. Kays, and R. J. Moffat. The Superposition Approach to Film-Cooling. In *ASME Paper 74-WA/HT-27*, 1974.

[29] L. Cortelezzi and A. R. Karagozian. On the Formation of Counter-Rotating Vortex Pairs in Transverse Jets. *J. Fluid Mech.*, 446(347-373), 2001.

[30] S. Coulthard, R. J. Volino, and K. A. Flack. Effect of Jet Pulsing on Film Cooling- Part I: Effectiveness and Flow-Field Temperature Results. *ASME J. Turbomachinery*, 129:232–246, 2007.

[31] S. Coulthard, R. J. Volino, and K. A. Flack. Effect of Jet Pulsing on Film Cooling- Part II: Heat Transfer Results. *ASME J. Turbomachinery*, 129:247–257, 2007.

[32] Dantec Dynamics. *Flow Manager Software and Introduction to PIV Instrumentation.* Dantec Dynamics A/S, 2002.

[33] K. K. Deb, A. C. Ionescu, and C. Li. Protein-Base Thin Films: A New High-TCR Material. *Sensors*, 17(8):52–55, 2000.

[34] J. D. Denton. Loss Mechanisms in Turbomachinery. *ASME J. Turbomachinery*, 115: 621–656, 1993.

[35] DIN Taschenbuch 229. *Durchflussmessungen von Fluiden in geschlossen Leitungen und Drosselgeräten: Blenden, Düsen, Venturirohre.* Beuth Verlag, Berlin, 2000.

[36] J. Dittmar, A. Schulz, and S. Wittig. Assessment of Various Film-Cooling Configurations Including Shaped and Compound Angled Holes based on Large-Scale Experiments. *ASME J. Turbomachinery*, 125:57–64, 2003.

[37] U. Drost. *An Experimental Investigation of Gas Turbine Airfoil Aero-Thermal Film Cooling Performance.* PhD thesis, EPF, Lausanne, Switzerland, 1998.

[38] M. G. Dunn, W. A. Bennett, R. A. Delaney, and K. V. Rao. Investigation of Unsteady Flow Through a Transonic Turbine Stage: Data/Prediction Comparison for Time-Averaged and Phase-Resolved Pressure Data. *ASME J. Turbomachinery*, 114:91–99, 1992.

[39] E. R. G. Eckert. Analysis of Film Cooling and Full Coverage Film Cooling of Gas Turbine Blades. In *Proceedings of the 1983 International Gas Turbine Congress*, page 109, Tokyo, Japan, 1983.

[40] S. V. Ekkad, D. Zapata, and J. C. Han. Heat Transfer Coefficients Over a Flat Surface with Air and CO2 Injection Through Compound Angle Holes Using a Transiet Liquid Crystal Image Method. *ASME J. Turbomachinery*, 119(3):580–586, 1997.

[41] S. V. Ekkad, D. Zapata, and J. C. Han. Film Effectiveness Over a Flat Surface with Air and CO2 Injection Through Compound Angle Holes Using a Transiet Liquid Crystal Image Method. *ASME J. Turbomachinery*, 119(3):587–593, 1997.

[42] V. L. Eriksen and R. J. Goldstein. Heat Transfer and Film Cooling Following Injection Through Inclined Circular Tubes. *ASME J. Heat Transfer*, 96:239–245, 1974.

[43] C. Forrer. Studying the Effect of Frequency on Mass Flow Rate of the Gemini Pulsator. Master's thesis, ETH Zurich, 2006.

[44] T. F. Fric and A. Roshko. Structure in the Near Field of a Transverse Jet. *Turbulent Shear Flows*, 7:225–237, 1991.

[45] S. Friedrichs, H. P. Hodson, and W. N. Dawes. Aerodynamic Aspects of Endwall Film Cooling. *ASME J. Turbomachinery*, 119(4):786–793, 1997.

[46] C. Fuchs. *A Feature Based 3-D Film Cooling Model for Compound Angled Injection.* PhD thesis, ETH Zurich, 2009.

[47] T. L. Giang. Effect of Unsteady Cooling Flow in Heat Transfer to a Film Cooled Flat Plate. Master's thesis, The Ohio State University, Columbus, 1999.

[48] R. J. Goldstein. Film Cooling. *Advances in Heat Transfer*, 7:321–379, 1971.

[49] R. J. Goldstein and P. Jin. Film Cooling Downstream of a Row of Discrete Holes With Compound Angle. *ASME J. Turbomachinery*, 123:222–230, 2001.

[50] R. J. Goldstein, P. Jin, and R. L. Olson. Film Cooling Effectiveness and Mass/Heat Transfer Downstream of One Row of Discrete Holes. *ASME J. Turbomachinery*, 121:225–232, 1999.

[51] E. M. Greitzer, C. S. Tan, and Graf. M. B. *Internal Flow.* Cambridge University Press, 2004.

[52] M. Gritsch, S. Baldauf, M. Martiny, A. Schulz, and S. Wittig. The Superposition Approach to Local Heat Transfer Coefficients in High Density Ratio Film Cooling Flows. In *ASME Paper No. 99-GT-168*, 1999.

[53] M. Gritsch, A. Schulz, and S. Wittig. Effect of Crossflows on the Discharge Coefficient of Film Cooling Holes With Varying Angles of Inclination and Orientation. *ASME J. Turbomachinery*, 123:781–787, 2001.

[54] E. F. Jr. Hasselbrink and M. G. Mungal. Transvers Jets and Jet Flames. Part 1: Scaling Laws for Strong Transverse Jets. *J. Fluid Mech.*, 443:1–25, 2001.

[55] B. A. Haven and M. Kurosaka. The Effect of Hole Geometry on Lift-off Behavior of Coolant Jets. In *AIAA 34th Aerospace Sci. Meeting and Exhibit, Reno*, volume Jan 1996, 1996.

[56] B. A. Haven and M. Kurosaka. Kidney and Anti-Kidney Vortices in Crossflow Jets. *J. Fluid Mech.*, 352:27–64, 1997.

[57] J. D. Heidmann and S. V. Ekkad. A Novel Antivortex Turbine Film-Cooling Hole Concept. *ASME J. Turbomachinery*, 130:031020, 2009.

[58] J. O. Hinze. *Turbulence*. McGraw-Hill Book Inc., New York, 1959.

[59] S. Honami, T. Shizawa, and A. Uchiyama. Behavior of the Laterally Injected Jet in Film Cooling Measurements of Surface Temperature and Velocity-Temperature Field Within the Jet. *ASME J. Turbomachinery*, 116(1):106–112, 1994.

[60] M. S. Hung, P. P. Ding, and P. H. Chen. Effects of Injection Angle Orientation on Concave and Convex Surfaces Film Cooling. *Expt. Therm. Fluid Sc.*, 33(2):292–305, 2009.

[61] D. G. Hyams and J. H. Leylek. A Detailed Analysis of Film-Cooling Physics: Part III - Streamwise Injection With Shaped Holes. *ASME J. Turbomachinery*, 122:122–132, 2000.

[62] S. Ito, R. J. Goldstein, and E. R. G. Eckert. Film Cooling of a Gas Turbine Blade. *J. Engg. Power*, 100:476–481, 1978.

[63] I. S. Jung and J. S. Lee. Effects of Orientation Angles on Film Cooling over a Flat Plate: Boundary Layer Temperature Distributions and Adiabatic Film Cooling Effectiveness. *ASME J. Turbomachinery*, 122(1):153–160, 2000.

[64] H. Kaplan. *Practical Applications of Infrared Thermal Sensing and Imaging Equipment*. SPIE Optical Engineering Press, 1999.

[65] R. M. Kelso, T. T. Lim, and A. E. Perry. An Experimental Study of Round Jets in Cross-Flow. *J. Fluid Mech.*, 306:111–144, 1996.

[66] S. J. Kline and F. A. McClintock. Describing Uncertainties in Single-Sample Experiments. *J. Mech. Eng.*, pages 3–8, 1953.

[67] A. Kohli and D. G. Bogard. Adiabatic Effectiveness, Thermal Fields and Velocity Fields for Film Cooling With Large Angle Ejection. *ASME J. Turbomachinery*, 119:352–358, 1997.

[68] V. Kumar and B. S. R. Sastry. Thermal Expansion Coefficient of Binary Semiconductors. *Cryst. Res. Technol.*, 36(6):565–569, 2001.

[69] P. Kupferschmied, P. Koeppel, W. Gizzi, C. Roduner, and G. Gyarmathy. Time-Resolved Flow Measurements with Fast-Response Aerodynamic Probes in Turbomachines. *Meas. Sci. Technology*, 11:1036–1054, 2000.

[70] P. Kupferschmied, P. Köppel, C. Roduner, and G. Gyarmathy. On the Development and Application of the FRAP (Fast-Response Aerodynamic Probe) System for Turbomachines - Part 1: The Measurement System. *ASME J. Turbomachinery*, 122:517–522, 2000.

[71] B. Lakshminarayana. *Fluid Dynamics and Heat Transfer of Turbomachinery.* John Wiley and Sons, 1996.

[72] H. Lamb. *Hydrodynamics.* Cambridge University Press, 1892.

[73] J. S. Lee and I. S. Jung. Effect of Bulk Flow Pulsations on Film Cooling With Compound Angle Holes. *Int. J. Heat Mass Transfer*, 45(1):113–123, 2001.

[74] S. W. Lee, Y. B. Kim, and J. S. Lee. Flow Characteristics and Aerodynamic Losses of Film Cooling Jets with Compound Angle Orientations. *ASME J. Turbomachinery*, 119(2): 310–319, 1997.

[75] P. M. Ligrani and J. S. Lee. Film Cooling from Two Staggered Rows of Compound Angle Holes at High Blowing Ratios. *Int. J. Rotating Machinery*, 2(3):201–208, 1996.

[76] P. M. Ligrani and A. E. Ramsey. Film Cooling from Spanwise-oriented holes in Two Staggered Rows. *ASME J. Turbomachinery*, 119:562–567, 1997.

[77] P. M. Ligrani, S. Ciriello, and D. T. Bishop. Heat Transfer, Adiabatic Effectiveness and Injectant Distributions Downstream of a Single Row and Two Staggered Rows of Compound Angle Film Cooling Holes. *ASME J. Turbomachinery*, 114:687–700, 1992.

[78] P. M. Ligrani, R. Gong, J. M. Cuthrell, and J. S. Lee. Bulk Flow Pulsations and Film Cooling - I. Injectant Behavior. *Int. J. Heat Mass Transfer*, 39(11):2271–2282, 1996.

[79] P. M. Ligrani, R. Gong, J. M. Cuthrell, and J. S. Lee. Bulk Flow Pulsations and Film Cooling - II. Flow Structure and Film Effectiveness. *Int. J. Heat Mass Transfer*, 39(11): 2283–2292, 1996.

[80] W. Liu and B. Yang. Thermography Techniques for Integrated Circuits and Semiconductor Devices. *Sensor Review*, 27(4):298–309, 2007.

[81] Y. Lu, A. Dhungel, S. V. Ekkad, and R. S. Bunker. Effect of Trench Width and Depth on Film Cooling From Cylindrical Holes Embedded in Trenches. *ASME J. Turbomachinery*, 131:011003, 2009.

[82] B. Maerklin. Design, Manufacturing and Commissioning of a Pulsator. Master's thesis, ETH Zurich, 2002.

[83] M. Mansour. *A 48kHz Bandwidth, 1.8mm Diameter Entropy Probe for Aerothermal Loss Measurements in Turbomachinery Flows.* PhD thesis, ETH Zurich, 2008.

[84] K. T McGovern and J. H. Leylek. A Detailed Analysis of Film-Cooling Physics: Part II-Compound Angled Injection With Cylindrical Holes. *ASME J. Turbomachinery*, 122: 113–121, 2000.

[85] A. Melling, F. Durst, and J. H. Whitelaw. *Principles and Practise of Laser-Doppler Anemometry*. Academic Press, 1981.

[86] K. E. Meyer, J. M. Pedersen, and O. Oezcan. A Turbulent Jet in Crossflow Analysed With Proper Orthogonal Decomposition. *J. Fluid Mech.*, 583:199–227, 2007.

[87] R. J. Moffat. Describing the Uncertainties in Experimental Results. *Expt. Therm. Fluid Sc.*, 1:3–17, 1988.

[88] Z. M. Moussa, J. W. Trischka, and S. Eskinazi. The Near Field in the Mixing of a Round Jet With a Cross-stream. *J. Fluid Mech.*, 80:49–80, 1977.

[89] H. Nasir, S. V. Ekkad, and S. Acharya. Effect of Compound Angle Injection On Flat Surface Film Cooling With Large Streamwise Injection Angle. *Expt. Therm. Fluid Sc.*, 25: 23–29, 2001.

[90] A. Pfau. *Loss Mechanisms in Labyrinth Seals of Shrouded Axial Turbines*. PhD thesis, ETH Zurich, 2003.

[91] J. R. Pietrzyk, D. G. Bogard, and M. E. Crawford. Hydrodynamics Measurements of Jets in Crossflow for Gas Turbine Film Cooling Applications. *ASME J. Turbomachinery*, 111 (2):139–145, 1989.

[92] L. Poyneer, M. van Dam, and J-.P. Veran. Experimental Verification of the Frozen Flow Atmospheric Turbulence Assumption with Use of Astronomical Adaptive Optics Telemetry. *J. Opt. Soc. Am. A*, 26(4):833–846, 2009.

[93] A. K. Prasad. Sterescopic Particle Image Velocimetry. *Exp. Fluids*, 29(2):103–116, 2000.

[94] M. Raffel, C. Willert, and J. Kompenhans. *Particle Image Velocimetry*. Springer, 1998.

[95] H. Reiss and A. Boelcs. Experimental Study of Showerhead Cooling on a Cylinder Comparing Several Configurations using Cylindrical and Shaped Holes. *ASME J. Turbomachinery*, 122:162–169, 2000.

[96] O. Reynolds. On the Resistance Encountered by Vortex Rings and the Relation between the Vortex Rings and the Streamlines of a Disc. *Nature*, 14:477, 1876.

[97] H. A. Rydholm. An experimental investigation of the velocity and temperature fields of cold jets injected into a hot crossflow. *ASME J. Turbomachinery*, 120(2):320–326, 1998.

[98] J. P. Schlienger. *Evolution of Unsteady Secondary Flows in a Multistage Shrouded Axial Turbine*. PhD thesis, ETH Zurich, 2003.

[99] D. L. Schmidt, B. Sen, and D. G. Bogard. Film Cooling With Compound Angle Holes: Adiabatic Effectiveness. *ASME J. Turbomachinery*, 118:807–813, 1996.

[100] B. Sen, D. L. Schmidt, and D. G. Bogard. Film Cooling With Compound Angle Holes: Heat Transfer. *ASME J. Turbomachinery*, 118:800–806, 1996.

[101] R. Siegel and J. R. Howell. *Thermal Radiation Heat Transfer*. Taylor and Francis, 2002.

[102] S. H. Smith and M. G. Mungal. Mixing, Structure and Scaling of the Jet in Crossflow. *J. Fluid Mech.*, 357:83–122, 1998.

[103] A. Teekaram, C. Forth, and R. Jones. Film Cooling in the Presence of Mainstream Pressure Gradients. *J. Turbomachinery*, 113:484–492, 1991.

[104] Z. Vidakovic. Estimating The Radiation Correction On Heat Transfer Measurements For A Film Cooling Experiment . Master's thesis, ETH Zurich, Switzerland, 2007.

[105] D. K. Walters and J. H. Leylek. A Detailed Analysis of Film-Cooling Physics: Part I – Streamwise Injection With Cylindrical Holes. *J. Turbomachinery*, 122(1):102–112, January 2000.

[106] S. K. Waye and D. G. Bogard. High-Resolution Film Cooling Effectiveness Comparison of Axial and Compound Angle Holes on the Suction Side of a Turbine Vane. *ASME J. Turbomachinery*, 129(2):202–211, 2007.

[107] K. Wieghardt. On the Blowing of Warm Air for De-Icing Devices. *FB 1900, Reports and Translations No. 315*, 1944.

[108] G. Wilfert and L. Fottner. The Aerodynamic Mixing Effect of Discrete Film Cooling Jets with Mainstream Flow on a Highly Loaded Turbine Blade. *ASME J. Turbomachinery*, 118 (3):468–478, 1996.

[109] J. B. Young and J. H. Horlock. Defining the Effeciency of a Cooled Turbine. *ASME J. Turbomachinery*, 128:659–667, 2006.

[110] J. B. Young and R. C. Wilcox. Modeling the Air-Cooled Gas Turbine: Part II - Coolant Flows and Losses. *ASME J. Turbomachinery*, 124:214–221, 2002.

[111] C. H. N. Yuen and R. F. Martinez-Bothas. Film Cooling Characteristics of a Single Round Hole at Various Streamwise Angles in a Crossflow: Part I - Effectiveness. *Int. J. Heat Mass Transfer*, 46:221–235, 2003.

[112] C. H. N. Yuen and R. F. Martinez-Bothas. Film Cooling Characteristics of a Single Round Hole at Various Streamwise Angles in a Crossflow: Part II - Heat Transfer Coefficient. *Int. J. Heat Mass Transfer*, 46:237–249, 2003.

Appendix A

Nomenclature

X	Streamwise coordinate normalised by hole diameter
Y	Lateral distance normalised by hole diameter
Z	Wall-normal distance normalised by hole diameter
U, V, W	Mean velocity components
M	Mach Number
P	Pressure
T	Temperature
D	Hole diameter
Re_D	Reynolds Number based on hole diameter, $U_\infty D/\nu$
S	Pitch distance between two holes
L	Length of the hole pipe
Tu	Turbulence Intensity
BR	Blowing Ratio, $\rho_c U_c / \rho_f U_f$
DR	Density Ratio, ρ_c / ρ_f
IR	Momentum flux ratio, BR^2/DR
V_x	Streamwise vorticity, $\frac{\partial W}{\partial Y} - \frac{\partial V}{\partial Z}$
V_y	Cross-stream vorticity, $\frac{\partial U}{\partial Z} - \frac{\partial W}{\partial X}$
V_z	Wall normal vorticity, $\frac{\partial V}{\partial X} - \frac{\partial U}{\partial Y}$
h_{conv}	Convective heat transfer coefficient
h_f	Temperature independent film heat transfer coefficient
h_P	Planck's constant, $6.63 \times 10^{-34} m^2 kg/s$
f	Frequency of pulsation in Hz
f_r	Reduced frequency, fD/U_∞
$\dot{m}$	Mass flow rate
t/T	Time non-dimensionalised by the pulsation period
$\mathcal{R}$	Specific gas constant of dry air
$\mathcal{C_P}$	Specific heat capacity at constant pressure

s Entropy

Greek

ρ Density

δ Boundary Layer Thickness

ϕ Injection angle with respect to surface of the flat plate

β Lateral angle of hole axis with freestream

$\Gamma_{x,n}$ Normalised Streamwise Circulation, $\oint_A V_{x,n} dA$

ξ Momentum flux ratio scaled downstream distance, $\frac{4X(S/D)}{IR\pi}$

ϵ Emissivity

σ Stefan-Boltzmann Constant, $5.67 \times 10^{-8} \frac{W}{m^2 K^4}$

θ Non-dimensional wall temperature, $\frac{T_h - T_w}{T_h - T_c}$

η Adiabatic effectiveness, $(T_h - T_{aw})/(T_h - T_c)$

λ Wavelength of radiation

Subscripts

c Coolant fluid

h, m (Hot) Freestream fluid

0 No injection baseline

aw Adiabatic Wall

$conv$ Convective

f Film

iso Isothermal plate

w Wall

n Normalised

ref Reference value

D Hole diameter based

t Total quantity

s Static quantity

∞ Averaged reference value

Abbreviations

ETH Swiss Federal Institute of Technology

PIV Particle Image Velocimetry

CFD Computational Fluid Dynamics

CCD Charge Coupled Device

$Nd:YAG$ Neodymium doped Yttrium Aluminum Garnet

$DEHS$ Diethyl Hexyl Sebacat

TCP/IP Transfer Control Protocol/Internet Protocol

PC Personal Computer

CVP	Counter rotating Vortex Pair
FCM	Film Cooling Model
$NHFR$	Net Heat Flux Reduction
LES	Large Eddy Simulation
DNS	Direct Numerical Simulation
$RANS$	Reynolds Averaged Navier Stokes
PDF	Probability Density Function
PSD	Power Spectral Density
FFT	Fast Fourier Transform

Appendix B

Operating Conditions

The operating conditions with respect to pressures and temperatures are described for every case according to the diagram shown in Fig. B.1. The tables show the raw temperatures and pressures for every geometry and operating condition based on the test section and points in Fig. B.1.

PIV Measurements

The PIV measurements are carried out for 15°, 60°and 90°compound angled holes with a surface angle of 30°. For ease of comparison the the BR and DR values are reported as 1, 2, 1.5 etc. The precise and accurate values required especially for computational verification will vary slightly according to the values shown in the tables. It must be noted that for most cases the pressure
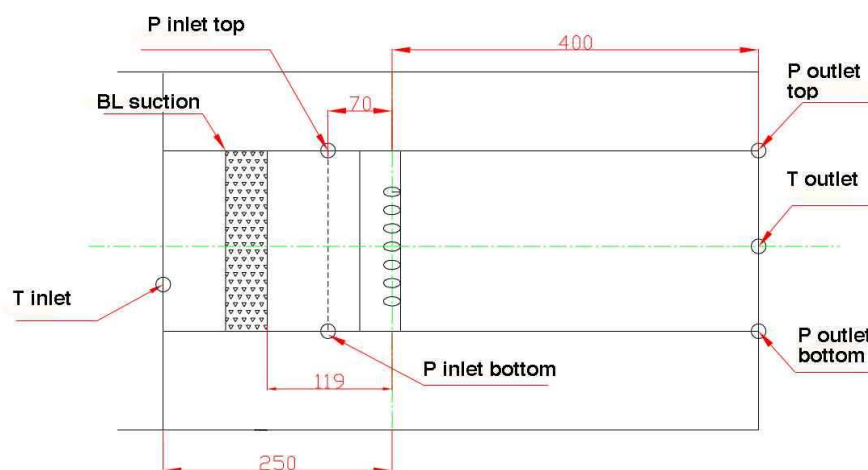
Figure B.1: Test section schematic showing locations of inlet and outlet pressure and temperature measurement

and temperature values are quite similar and depend primarily on the blowing or density ratio that is being set.

Quantity (static)	BR=1, DR=1 IR=1	BR=1, DR=1.5 IR=0.67	BR=2, DR=1 IR=4	BR=2, DR=1.5 IR=2.67
P inlet (Pa)	95807.5	95592	96187	95975
P outlet (Pa)	95542	95262	95925	95656
P plenum (Pa)	106538	103942	123049	114071
T inlet (K)	289.3	381.2	289.3	370.9
T outlet (K)	293.4	377.4	293.4	364.2
T plenum (K)	300.3	256.2	300.3	244.7

Table B.1: Operating conditions for 15°PIV measurements

Quantity (static)	BR=1, DR=1 IR=1	BR=1, DR=1.5 IR=0.67	BR=2, DR=1 IR=4	BR=2, DR=1.5 IR=2.67
P inlet (Pa)	97481	95608	97546	95832
P outlet (Pa)	97224	95330	97321	95584
P plenum (Pa)	110397	105489	129470	117500
T inlet (K)	288.7	369.8	288.4	367.5
T outlet (K)	288.7	382.9	288.7	376.9
T plenum (K)	299.1	253.29	299.3	240.7

Table B.2: Operating conditions for 60°PIV measurements

Quantity (static)	BR=1, DR=1 IR=1	BR=1, DR=1.5 IR=0.67	BR=2, DR=1 IR=4	BR=2, DR=1.5 IR=2.67
P inlet (Pa)	96922	96135	97375	96750
P outlet (Pa)	95530	95175	95826	95660
P plenum (Pa)	106432	108698	117901	112019
T inlet (K)	290.3	380.9	289.6	378.9
T outlet (K)	293.7	380.7	292.8	379.3
T plenum (K)	300.6	258.9	300.3	250.2

Table B.3: Operating conditions for 90°PIV measurements

Quantity (static)	BR=2, DR=1.3 IR=3.67, f=0	BR=2, DR=1.3 IR=3.67, f=400 Hz
P inlet (Pa)	96737	95979
P outlet (Pa)	95948	94808
P plenum (Pa)	114309	11425
T inlet (K)	356.3	357.8
T outlet (K)	355.6	357.7
T plenum (K)	271.9	272.6

Table B.4: Steady state operating conditions for 0°PIV measurements with pulsations. Amplitude of Pulsations is ±0.3 in blowing ratio. The detailed pulsation waveform is shown in Fig. 2.3 and 2.4

Quantity (static)	BR=2, DR=1 IR=4, f=250 Hz	BR=2, DR=1.3 IR=3.67, f=400 Hz
P inlet (Pa)	97574	96451
P outlet (Pa)	95964	95628
P plenum (Pa)	121261	115966
T inlet (K)	289.2	358.1
T outlet (K)	292.7	358.5
T plenum (K)	301.7	275.5

Table B.5: Steady state operating conditions for 60°PIV measurements with pulsations. Amplitude of Pulsations is ±0.3 in blowing ratio. The detailed pulsation waveform is shown in Fig. 2.3 and 2.4

Infrared Thermography Measurements

For infrared thermography only a single DR=1.5 was maintained. The pressures and temperatures for the different cases are as shown in the following tables.

Quantity (static)	BR=1, DR=1.5 IR=0.67	BR=2, DR=1.5 IR=2.67
	$\beta = 0°$	
P inlet (Pa)	96427	96854
P outlet (Pa)	95557	96006
P plenum (Pa)	101945	121978
T inlet (K)	387	387.6
T outlet (K)	374	374
T plenum (K)	257.5	258.3
	$\beta = 15°$	
P inlet (Pa)	96333	96819
P outlet (Pa)	94570	95070
P plenum (Pa)	102056	121613
T inlet (K)	386.6	386.3
T outlet (K)	373	372
T plenum (K)	257.3	257.7
	$\beta = 60°$	
P inlet (Pa)	96674	97111
P outlet (Pa)	95746	95929
P plenum (Pa)	102902	122705
T inlet (K)	386.5	386.5
T outlet (K)	375.9	379.4
T plenum (K)	257.7	257.8
	$\beta = 90°$	
P inlet (Pa)	96537	96319
P outlet (Pa)	95723	95019
P plenum (Pa)	102318	122031
T inlet (K)	387.3	387.4
T outlet (K)	382.1	383
T plenum (K)	259	258.6

Table B.6: Steady state operating conditions for steady jet streamwise and compound angled infrared thermography measurements

Quantity (static)	BR=1, DR=1.5 IR=0.67, f=250 Hz	BR=2, DR=1.5 IR=2.67, f=250 Hz
	$\beta = 0°$	
P inlet (Pa)	96140	96739
P outlet (Pa)	95310	95895
P plenum (Pa)	101753	121586
T inlet (K)	388.7	388.8
T outlet (K)	377.9	381
T plenum (K)	261	257.8
	$\beta = 60°$	
P inlet (Pa)	95575	96137
P outlet (Pa)	94713	94807
P plenum (Pa)	102818	121323
T inlet (K)	385.3	385.5
T outlet (K)	380	381.4
T plenum (K)	258.2	255

Table B.7: Steady state operating conditions for 0°and 60°IR thermography measurements with pulsations of 250 Hz. Amplitude of Pulsations is ±0.3 in blowing ratio. The detailed pulsation waveform is shown in Fig. 2.3 and 2.4

Quantity (static)	BR=1, DR=1.5 IR=0.67, f=400 Hz	BR=2, DR=1.5 IR=2.67, f=400 Hz
	$\beta = 0°$	
P inlet (Pa)	95194	95586
P outlet (Pa)	94211	94514
P plenum (Pa)	102575	121587
T inlet (K)	389.4	389.8
T outlet (K)	378.5	381.5
T plenum (K)	258.6	258.7
	$\beta = 60°$	
P inlet (Pa)	95778	96190
P outlet (Pa)	94815	94909
P plenum (Pa)	102354	122158
T inlet (K)	385.6	385.5
T outlet (K)	376.6	381
T plenum (K)	257.9	256.5

Table B.8: Steady state operating conditions for 0°and 60°IR thermography measurements with pulsations of 400 Hz. Amplitude of Pulsations is ±0.3 in blowing ratio. The detailed pulsation waveform is shown in Fig. 2.3 and 2.4

Appendix C

Publications

1. Aga, V., Mansour, M. and Abhari, R. S., (2008) Aerothermal Performance of Streamwise and Compound Angled Pulsating Film Cooling Jets, *ASME J. Turbomachinery*, **131**, pp 041015

2. Aga, V., Rose, M. and Abhari, R. S., (2008) Experimental Flow Structure Investigation of Compound Angled Film Cooling, *ASME J. Turbomachinery*, **130**, pp 031005

3. Aga, V. and Abhari, R. S. (2009) Influence of Streamwise Vorticity on Adiabatic Effectiveness of Compound Angled Film Cooling, *In Proc. 19th ISABE Conference, Montreal, Canada*, Paper No. ISABE-2009-1182

4. Aga, V., Mansour, M. and Abhari, R. S., (2008) Aerothermal Performance of Streamwise and Compound Angled Pulsating Film Cooling Jets, *In. Proc. ASME Turb Expo 2008, Berlin Germany*, Paper No. GT-08-50678

5. Aga V., Mansour M. and Abhari, R. S. (2008) Turbulent Thermal Diffusivity in Streamwise and Compound Angled Film Cooling Jets. *In Proc., 19th Int. Symp. on Transport Phenomena, Reykjavik, Iceland*, August 2008

6. Aga, V., Feliciani. C., Chokani, N. and Abhari, R. S. (2007) Turbulence Measurements of a High Reynolds Number Jet in Crossflow using PIV and FRAP. *60th Ann. Meeting of the Div. of Fluid Dynamics, APS, Salt Lake City, UT, USA*, Nov. 2007.

7. Fuchs, C., Aga, V. and Abhari, R. S. (2008) An Improved Feature Based Jet Model For Modeling of Film-Cooled Turbine Blade Flows, *In Proc., 19th Int. Symp. on Transport Phenomena, Reykjavik, Iceland*, August 2008

8. Mansour M., Aga V., Chokani, N and Abhari, R. S. (2008) Aerothermal Aspects of Pulsated Inclined Film Cooling Jets in Crossflow. *In Proc., 38th Fluid Dynamics Conference and Exhibit, Seattle, Washington, USA*, Paper No. AIAA 2008-4298. June 2008

Appendix D

Curriculum Vitae

Personal Data

Name	Vipluv Aga
Born	20 September 1981, Mumbai, India
Citizenship	Indian

Education

1999	Higher Secondary Certificate, Maharashtra from Jai Hind College, Mumbai, India
2000-2005	Bachelor's and Master's studies in Aerospace Engineering at Indian Institute of Technology (IIT) Madras, India
2005	Dual Degree, Bachelor of Technology and Master of Technology in Aerospace Engineering from Indian Institute of Technology Madras, India. Winner of the Institute Blues Award
2005-2009	Doctoral studies at the Laboratory of Energy Conversion (formerly, Turbomachinery Lab) in the Department of Mechanical and Process Engineering at the Swiss Federal Institute of Technology Zurich, (ETH Zurich)